Chemical Vapour Deposition of *p*-type First Row Transition Metal Oxides for Use in Sensing Volatile Organic Carbon Species

by

Jone-him Tsang

A thesis presented for the degree of

Doctorate of Engineering (EngD)

School of Mathematical and Physical Sciences

University College of London

September 2022

Declaration

I hereby declare that this thesis has not been, and will not be, submitted in whole or in part to another University for the award of any other degree.

University College London

Jone-him Tsang

Submitted for the degree of Doctor of Engineering

Chemical Vapour Deposition of *p*-type First Row Transition Metal Oxides for Use in Sensing Volatile Organic Carbon Species

Abstract

There has been an increased attention towards gas detection due to levels of toxic and hazardous gases to which humans are exposed to everyday. Semiconductor gas sensors, mainly metal oxide sensors have good sensitivity due to difference in conductivity even at low concentrations. Metal oxide are desirable materials for sensors due to their low cost, robust structure, relatively low energy consumption and good response to a variety of gases and vapours. Several metal oxides have been used for gas sensor devices, including but not limited to SnO_2, WO_3 and TiO_2. Since the discovery for its use as gas sensors, SnO_2, a *n*-type material is one of the most widely used gas sensor material. However, there are drawbacks such as poor baseline stability, interference from humid conditions and low selectivity.[1,2]

Recently $Cr_{2-x}Ti_xO_3$, a *n*-type doped *p*-type material has improved properties compared to SnO_2, a pure *n*-type MOS. It displays better stability towards relative humidity, a low baseline drift, higher selectivity and better stability.[3] Since its discovery as a gas sensing material by Moseley and Williams, it has been widely used in research and commercially with the ability to detect various gases and vapours such as NH_3, CO, H_2S and different alcohols.[4,5]

Ceramic substrate are still commonly used as the based for MOS sensors due to its low cost, ease of fabrication, chemical stability and robustness of the substrate (sensor can be made via screen-printing). However, there are certain limitation, which is why Micro-electro-mechanical system (MEMS) technologys have been extensively researched upon over recent years. Some of the reasons for such drive is because MEMS miniaturised

heating element (micro-hotplates) can operate at high temperatures quickly and preserve power consumption (mW ranges) due to its low thermal mass.[6] However, due the MEMS substrate brittleness, certain synthetic techniques are not viable such as screen printing. Therefore, one aspect of the project is to directly and successfully deposit CTO sensing material onto the MEMS substrate via AACVD. Once deposited, its sensitivity and selectivity towards VOCs will be investigated and compared to ceramic screen printed sensors. This project is carried out in collaboration with Alphasense Ltd (http://www.alphasense.com/), a leading UK gas sensor manufacturer.

The mechanism of gas sensing has long been debated and described. Here two models are described, band bending model and surface trap limited model. The latter was used to explain the mechanism and interaction of the sensors tested in this project.

Another aspect of this project is to find optimum parameters to generate *n*-type doped CWO and *p*-type doped CNO thin films via AACVD. Detailed analysis (elemental composition, oxidation state, structural information and morphology) of the deposited thin films were studied using XRD, EDX and XPS. These materials sensing abilities were tested towards various different VOCs.

This project was carried out in collaboration with Alphasense Ltd, a leading UK gas sensor company. The project was divided into the following main sections:

- Synthesis of CTO thin films onto glass, alumina and gas sensing substrates
- Characterisation of CTO thin films
- Synthesis of CTO on MEMS platforms
- Gas sensor tests at Alphasense

Challenges and Achievements

Some of the challenges that were faced during the four years of study were as follow: Covid-19 interrupted my final year of study which made it very difficult / near impossible to go to Alphasense to build new sensors and to conduct gas sensing experiments. During

the deposition of substrate onto sensing platforms (ceramics substrates), a masked were first used to protect the sensing layers detection pad so that it would not affect the welding process. This however caused an imbalance of sensing substrate on each sensor, i.e. the masked had 9 holes to deposit onto 9 substrates but each hole were not the same size. Therefore after discussion with an engineer at Alphasense, it was concluded that a mask was not necessary as the sensing layer was thin enough to not affect the welding process on the detection pad. Another challenge was the availability of the equipment for gas sensing analysis at Alphasense. Due to this equipment and experiments needed to be booked and thought of weeks in advance.

Some of the achievements that was accomplished within this thesis were as follow: Successfully depositing various doped chromium oxide sensors onto ceramic sensing platform (both *n*-type and *p*-type dopants). These sensors were tested to a wide range of VOCs and displayed different levels of sensitivity and selectivity towards them. CTO was also successfully deposited onto MEMs platform and were tested to again a variety of VOCs and displayed different levels of sensitivity and selectivity towards them. Finally, two papers were published during the work of this thesis; 10.3390/proceedings2019014050 and 10.1109/SENSORS47125.2020.9278881.

Acknowledgements

I would like to thank Professor Chris Blackman for the opportunity to work in his research laboratory. The guidance and undying support he has provided throughout the years has been greatly appreciated especially during the pandemic. My time at the University College London was an unforgettable experience. The research I have been working on has been very interesting and hope it has contributed towards the science community. I would also like to thank Professor David Scanlon for the help and support as a secondary supervisor throughout the years.

I would like to also give a special thanks to Dr Francesco Di Maggio during my first few years at UCL. The guidance and willingness in teaching new laboratory skill are what made this report possible. He has provided daily support and helpful tips, I could not have hoped for a friendlier postdoc supervisor to work under. Thank you for pushing me through this year.

I would like to give thanks to Mr Martin Vickers for XRD pattern data, Dr Steven Firth for SEM images and Raman analysis, Dr Tom Gregory for EDX analysis and Mr Martyn Towner for XPS training and analysis. I would also like to thank Dr Ehsan Danesh for gas sensing training, data analysis, scientific knowledge and practical skills that has been bestowed upon me.

I would like to write a few words to my friends and colleagues; thank you for making this a wonderful and enjoyable year full of drinks, food and laughter. I would like to thank the Blackman group, Thank you Dr Yiyun Zhu, Dr Yaomin Li and Dr Xueming Xua for the help and knowledge in CVD and sensing materials. Thank you Juhun Shin, Yuting Yao and Xinyue Zhang for the ideas and help you have given over the years. I would also

like to thank those in Prof Rob Palgraves group, for sharing offices and having a great time over the years.

In particular, I would like to thank Dr Shane Lo Fan Hin, a mentor and a dear friend who has continuously pushed me into pursuing a doctorate in chemistry and motivating me into finishing this thesis. I would also like to thank Dr Frances Heale, since joining back in 2016 you have kept me company in the rather cold, dead and gloomy office during my Masters. The discussions about the holidays we wanted to go whenever life hit us hard, the 'banters' we had and for the amazing outings over the course of the year. The coffee and lunch breaks we take to go switch ourselves off for an hour will truly be missed. I could not have asked for a better friend to support me throughout these years. Thank you to these true and trustworthy friends who has supported me, cheered me up and pulled a happy smile out of me during the grim and toughest moments.

Last in order of mention or occurrence but not of importance, I would like to thank my family: my parents and my brothers for supporting me mentally throughout these years and my life in general. Their unwavering encouragement has been phenomenal and I am proud to call them my parents and brothers and I hope that they enjoy this as some light bedtime reading.

Contents

Abstract ii

Acknowledgements v

List of Figures x

List of Tables xx

Abbreviations xxii

1 General Introduction **1**

1.1 Volatile Organic Compounds 2

1.2 Gas Sensors 6

1.3 Recent Advances in *p*-type MOS Gas Sensors 13

1.4 Recent Advances in *n*-type MOS Gas Sensors 26

1.5 Engineering of MOS Sensors 31

1.5.1 Screen-printing 32

1.5.2 Sol-gel Techniques 32

1.5.3 Microwave-assisted and Solvothermal Techniques 33

1.5.4 Physical Vapour Deposition (PVD) 34

1.5.5 Chemical Vapour Deposition (CVD) 37

1.6 Micro-electro-mechanical systems (MEMS) 40

2 Gas Sensing Mechanism **43**

2.1 Band Bending Model 45

2.2 Surface-trap Limited Model 49

3 Experimental 59

3.1 Methodology of Characterisation 59

3.2 Deposition Parameter 64

3.3 Metal Oxide Thin Films Synthesis 65

3.3.1 Synthesis of Chromium Oxide Thin Films 65

3.3.2 Synthesis of Tungsten Oxide Thin Films 65

3.3.3 Synthesis of Nickel Oxide Thin Films 65

3.3.4 Synthesis of Tungsten-doped Chromium Oxide Thin Films 66

3.3.5 Synthesis of Titanium-doped Chromium Oxide Thin Films 66

3.3.6 Synthesis of Nickel-doped Chromium Oxide Thin Films 66

3.3.7 Gas Sensing Methodology 67

4 *P*-type Metal Oxide Thin Films 70

4.1 Chromium Oxide (Cr_2O_3) Film Characterisation 72

4.2 Nickel Oxide (NiO) Film Characterisation 82

4.3 Summary 88

5 Mixed Metal Oxide Thin Films 90

5.1 Chromium Titanium Oxide (CTO) 90

5.1.1 Introduction 90

5.1.2 Film Characterisation 90

5.2 Tungsten Doped-chromium Oxide (CWO) 104

5.2.1 Introduction 104

5.2.2 Film Characterisation 105

5.3 Nickel Doped-chromium Oxide 118

5.3.1 Film Characterisation 118

5.4 Summary 128

6 Thin Films Gas Sensing Analysis 130

6.1 Sensitivity towards isobutylene, ammonia and hydrogen sulfide 130

6.1.1 Chromium Oxide 130

6.1.2 Nickel Oxide 134

6.1.3 Chromium Titanium Oxide (CTO) 136

6.1.4 Tungsten Doped-chromium Oxide 141

6.1.5 Summary 144

6.2 Sensitivity towards VOCs 145

6.2.1 Toluene 145

6.2.2 Formaldehyde 149

6.2.3 Isopropanol 152

6.2.4 Benzene and 2-Butanone 156

6.2.5 Summary 158

6.3 MEMs Devices 159

6.3.1 Summary of MEMs Devices 164

7 Conclusion and Future Work 166

7.1 Conclusion 166

7.2 Future Work 168

References 169

List of Figures

1.1 Schematic diagram of a commercial pellistor sensor 7

1.2 Schematic diagram of a QCM mass sensitive gas sensor 8

1.3 Schematic diagram of a electrochemical gas sensor 9

1.4 Number of publications from 1973 to 2019 on metal oxide gas sensors . . 10

1.5 Schematic diagram of single and double sided sensor on a wafer substrate 12

1.6 Schematic diagram of FET and impedance sensor 13

1.7 Ball and stick unit cell model of (a) Cu_2O and (b) CuO 13

1.8 Ellingham diagram displaying the standard Gibbs energy of formation for a number of metal oxides 14

1.9 (a) Response towards 5 ppm to 1000 ppm formaldehyde; (b) Response towards 5 ppm to 100 ppm formaldehyde; (c) Reproducibility test; (d) Schematic diagram of Cu_2O sphere with quadruple shells 15

1.10 Response of CuO thick films on MEMS sensors towards hydrogen sulfide in a hygrogen environment 17

1.11 Normalised response towards different concentrations of H_2S in dry and humid hydrogen conditions at 350 °C 18

1.12 SEM Images of (a). CuO NWs; (b.) CuO NTs and (c). CuO NCs 18

1.13 a)CuO NTs and b) CuO NCs displays the response towards 1000 ppm of CO at different annealing temperatures; c) Response towards 1000 ppm of CO at different operating temperatures with 2.5 mg of CuO NTs and CuO NCs; d) CuO NTs response and recovery towards different concentrations of CO, where the NTs were annealed at 500 °C and at a operating temperature of 175 °C; e) CuO NTs and CuO NCs sensing response at a operating temperature of 175 °C and different concentrations of CO in terms of R_g/R_a; f) linear fitting of CuO NTs and CuO NCs response as a function of CO concentration at at a operating temperature of 175 °C . . . 20
1.14 CuO nanowire in sensing performance towards toluene, hexane, acetone, and ethanol at operating temperatures of a) 200 °C; b) 250 °C; c) 300 °C. d) Bar graphs of the sensor responses the four VOCs at 1000 ppm concentration at various operating temperatures 21
1.15 a)NiO and b) Cr_2O_3 nanowires SEM images, c) and d) XRD patterns of Ni and Cr nanowire arrays before and after thermal oxidation. e) and f) are Gas sensing response towards various hexane concentrations 22
1.16 Spinel structure of Co_3O_4 23
1.17 Response of mesoporous Co_3O_4 nanochains towards increasing concentration of H_2S 24
1.18 Response of mesoporous Co_3O_4 nanochains towards increasing concentration of NH_3, CO and H_2 25
1.19 ZnO sensitvity response towards CO at room temperature and at a concentration of 250 ppm and 500 ppm 27
1.20 (a) In_2O_3 NFs and TNTs sensor response towards 50 ppm of H_2S as a function of working temperature and (b) In_2O_3 NFs and TNTs sensor response towards 50 ppm of H_2S as a function of time 28
1.21 (a). Response towards 100 ppm ethanol at varying operating temperatures; (b). Response towards varying concentrations of ethanol at optimum operating temperatures 29

1.22 (a). Resistance of TiO_2 NWs at room temperature and 100 ppm NO_2; (b). Response of TiO_2 NWs towards at room temperature and varying concentrations of NO_2 30
1.23 (a). V_2O_5 response towards different VOCs at room temperature and concentration of 100 ppm; (b). Sensitivity of V_2O_5 towards 100 ppm of xylene at room temperature 31
1.24 Schematic diagram of the sol gel technique: A. the colloidal suspension in the sol, and B. sol spun to form gel. 33
1.25 Schematic diagram of the solvothermal technique, where the red arrows represent external heating 34
1.26 SEM images of CuO nanostructures 35
1.27 Schematic diagram of vapour evaporation 35
1.28 Types of sputtering processes 36
1.29 Schematic diagram of A. DC sputtering and B. Magnetron Sputtering . . 36
1.30 Schematic diagram of a simple thermal CVD reactor 38
1.31 Schematic diagram of an aerosol-assisted CVD 39
1.32 Schematic diagram of a simple MEMs sensor structure 41

2.1 Schematic model of grain size effect on MOS sensors: a) Boundary controlling ()$D >> 2L$; b) Neck controlling ($D \geq 2L$); c) Grain controlling ($D < 2L$) 44
2.2 Schematic diagram of porous sensing layer 46
2.3 Schematic diagram of band bending model reaction mechanism towards formaldehyde for a *n*-type material, where: a) Flat bend prior to any surface reaction; b) In air; c) In gas 47
2.4 Schematic diagram of energy band representation for *p*-type material where: a) Flat bend prior to any surface reaction; b) Trapping of electrons due to oxygen adsorption and formation of the holes accumulation layer 49

2.5 Schematic diagram of energy band representation for *p*-type material with decrease in band bending where: a) Trapping of electrons due to oxygen adsorption and formation of the holes accumulation layer ; b) After interaction with reducing gas 49

2.6 Schematic diagram of surface-trap limited compensated semiconductor model 50

2.7 Schematic diagram of three curves with decreasing bulk donor density. Where N_A is equal to the surface acceptor density which is described as N_S in the equations above. The x-axis is the surface acceptor density; and the y-axis is the conductivity 54

3.1 Contact resistances and the resistivity of the silicon sample. 62

3.2 Field and voltage polarities of a *p*-type semiconductor for Hall measurement 63

3.3 Schematic diagram of sensors connected to pins via platinum wires 67

3.4 Image of SMS board system used for controlling and analysing the sensors resistance and operating temperature in idle and when exposed to gases. a). Side on view; b). Top down view 68

4.1 a) Relative sensor response as function of operating temperatures towards 150 ppm ammonia; b) Resistance response towards 25 ppm, 50 ppm, 100 ppm and 150 ppm of ammonia at 300 °C for different precursors; c) Relative sensor response comparison for different precursors towards NH_3 71

4.2 pXRD pattern of chromium oxide on: Glass, quartz, alumina and alumina sensors substrates. Where the orange stick pattern and * equates to corundum (Al_2O_3) and the blue stick pattern and + equates to eskolaite (Cr_2O_3) 72

4.3 Chromium 2*p* spectra of chromium oxide on different substrates. The inset plot is a close up spectra for samples on quartz and sensor substrates . . . 74

4.4 Chromium 2*p* spectra of chromium oxide displaying Cr(III) and Cr(VI) peaks where; a) Glass substrate; b) Quartz; c) Sensor annealed at 500 °C; d) Sensor annealed at 600 °C and f) Sensor annealed at 700 °C 75

4.5 Survey scan spectrum of chromium oxide on different substrates 76
4.6 Normalised raman spectrum of chromium oxide on various substrates . . 76
4.7 Cross section SEM image of Cr_2O_3 on FTO glass 79
4.8 Arrhenius plots for the resistivity of Cr_2O_3 thin film under pure nitrogen . 80
4.9 Chromium oxide activation energy against temperature under nitrogen . . 81
4.10 Deposition of NiO on glass using $Ni(acac)_2$ (left) and $Ni(TMHD)_2$ (right) 82
4.11 pXRD pattern of NiO, with $Ni(acac)_2$ as the starting material on glass substrate 83
4.12 Nickel 2*p* spectra of nickel oxide 84
4.13 Raman specta of nickel oxide 85
4.14 Cross section SEM image of NiO on FTO glass 86
4.15 Arrhenius plots for the resistivity of NiO thin film under nitrogen 87
4.16 Nickel oxide activation energy against temperature under nitrogen 88

5.1 pXRD patterns of commercial screen printed CTO sensors, different titanium loading AACVD deposited CTO sensors annealed at 600 °C for 24 h, TiO_2 and Cr_2O_3 91
5.2 Low angle plot of pXRD patterns for commercial screen printed CTO sensors, different titanium loading AACVD deposited CTO sensors annealed at 600 °C for 24 h, TiO_2 and Cr_2O_3 92
5.3 XPS survey spectrum of AACVD and screen printed CTO 95
5.4 XPS survey spectrum of AACVD CTO on FTO and miniature alumina substrate 96
5.5 Cr 2*p* and Ti 2*p* spectra of AACVD CTO 97
5.6 Cr 2*p* and Ti 2*p* spectra of screen printed CTO 97
5.7 O 1*s* spectra of AACVD and screen printed CTO 98
5.8 Raman spectra of Cr_2O_3, TiO_2, AACVD and screen printed CTO films . . 101
5.9 Cr_2O_3 raman spectra reported by Li 101
5.10 TiO_2 raman spectra reported by Challagulla 102
5.11 Cross section SEM image of CTO on quartz substrate 103

5.12 Chromium titanium oxide Arrhenius plot 104
5.13 Chromium titanium oxide activation energy against temperature under nitrogen 105
5.14 pXRD pattern of AACVD deposited CWO at various deposition temperature and flow rates. 106
5.15 EDS elemental surface analysis of CWO at different deposition temperature and flow rate 107
5.16 Cr 2*p* and W 4*f* spectra of CWO on glass substrate at different parameter deposition 108
5.17 XRD pattern of CWO at different compositions and annealing temperatures. 109
5.18 Raman spectra of CWO deposited on at different compositions and annealing temperatures. 110
5.19 Raman spectra of WO_3 reported by Huirache-Acuna. 112
5.20 CWO pXRD pattern deposited on quartz substrate annealed at 600 °C . . 114
5.21 Cr 2*p* and W 4*f* spectra of CWO on quartz 114
5.22 Raman spectra of CWO deposited on quartz substrate. 116
5.23 Cross section SEM image of CWO on quartz substrate 116
5.24 Tungsten doped-chromium oxide activation energy against temperature under pure nitrogen 117
5.25 Tungsten doped-chromium oxide activation energy against temperature under pure nitrogen 118
5.26 XRD pattern of CNO deposited onto glass and alumina 119
5.27 EDS elemental surface analysis of CNO 120
5.28 Chromium and nickel 2*p* spectra of nickel doped-chromium oxide 122
5.29 Raman specta of nickel doped chromium oxide 124
5.30 Raman spectra of nickel doped chromium oxide reported by Verma 124
5.31 Cross section SEM image of CNO on quartz substrate 126
5.32 Nickel doped-chromium oxide activation energy against temperature under nitrogen 127

5.33 Nickel doped-chromium oxide activation energy against temperature under nitrogen 128

6.1 AACVD Cr_2O_3 gas sensor response towards isobutylene (20 ppm-5 ppm-20 ppm pulse) and working temperature of 400 °C and 450 °C 131
6.2 ZnO sensor response towards isobutylene 132
6.3 AACVD Cr_2O_3 gas sensor response towards ammonia (75 ppm-25 ppm-75 ppm pulse) and working temperature of 400 °C and 450 °C 133
6.4 Cr_2O_3 response towards ammonia reported by Almaev 134
6.5 Indium and tin coated indium oxide response reported by Qi 135
6.6 NiO sensor response (resistance in Ω) towards isobutylene at variable operating temperatures 135
6.7 NiO sensor response (resistance in Ω) towards different gases reported by Ayyala 136
6.8 AACVD and screen printed CTO sensor gas response towards isobutylene (20 ppm-5 ppm-20 ppm pulse) and working temperature of 400 °C and 450 °C 137
6.9 AACVD CTO sensor gas response towards isobutylene (20 ppm-5 ppm-20 ppm pulse) and working temperature of 400 °C and 450 °C in comparison with sensors previously made 138
6.10 AACVD and screen printed CTO sensor gas response towards ammonia (75 ppm-25 ppm-75 ppm pulse) and working temperature of 400 °C and 450 °C 139
6.11 AACVD and screen printed CTO sensor gas response towards hydrogen sulfide (24 ppm-8 ppm-24 ppm pulse) and working temperature of 400 °C and 450 °C 141
6.12 AACVD CWO gas sensor response towards isobutylene (20 ppm-5 ppm-20 ppm pulse) and working temperature of 400 °C and 450 °C; where a). Resistance response and b). R_g/R_a response 142

6.13 AACVD CWO gas sensor response towards ammonia (75 ppm-25 ppm-75 ppm pulse) and working temperature of 400 °C and 450 °C; where a). Resistance response and b). R_g/R_a response 143
6.14 AACVD NiO sensors resistance response (Ω) against time (minutes) towards two pulses of toluene (225 ppb and 112.5 ppb) at operating temperature of 300 °C and 50 % relative humidity 145
6.15 CTO sensor response (resistance in Ω) and operating temperature (°C) against time (minutes) when exposed to 210 ppb toluene at 50 % relative humidity 146
6.16 AACVD CWO sensors resistance response (Ω) against time (minutes) towards two pulses of toluene (225 ppb and 112.5 ppb) at operating temperature of 300 °C and 50 % relative humidity 147
6.17 AACVD CNO sensors resistance response (Ω) against time (minutes) towards two pulses of toluene (225 ppb and 112.5 ppb) at operating temperature of 300 °C and 50 % relative humidity 148
6.18 AACVD Cr_2O_3 sensors resistance response (Ω) against time (minutes) towards two pulses of formaldehyde (95 ppb and 47.5 ppb) at operating temperature of 300 °C and 50 % relative humidity 149
6.19 AACVD NiO sensors resistance response (Ω) against time (minutes) towards two pulses of formaldehyde (95 ppb and 47.5 ppb) at operating temperature of 300 °C and 50 % relative humidity 150
6.20 Typical dynamic response curves of gas sensors fabricated from (A) NiO-40, (B) NiO-80, (C) NiO-130 and (D) bulk NiO particle, during cycling between increasing concentration of HCHO and ambient air at 300 °C . . 151
6.21 Screen printed and AACVD CTO sensors resistance response (Ω) against time (minutes) towards one pulse of formaldehyde (95 ppb) at operating temperature of 300 °C and 50 % relative humidity 152

6.22 AACVD CWO sensors resistance response (Ω) against time (minutes) towards two pulses of formaldehyde (95 ppb and 47.5 ppb) at operating temperature of 300 °C and 50 % relative humidity 152
6.23 AACVD CNO sensors resistance response (Ω) against time (minutes) towards two pulses of formaldehyde (95 ppb and 47.5 ppb) at operating temperature of 300 °C and 50 % relative humidity 153
6.24 AACVD NiO sensors resistance response (Ω) against time (minutes) towards two pulses of isopropanol (500 ppb and 250 ppb) at operating temperature of 300 °C and 50 % relative humidity 154
6.25 Sensor response (resistance in Ω) against time (minutes) when exposed to propan-2-ol at 350 °C and 50% relative humidity, 450 ppb and 225 ppb concentration, where a. Screen printed sensor response and b. AACVD sensor response. 155
6.26 AACVD CWO sensors resistance response (Ω) against time (minutes) towards two pulses of isopropanol (500 ppb and 250 ppb) at operating temperature of 300 °C and 50 % relative humidity 155
6.27 AACVD CNO sensors resistance response (Ω) against time (minutes) towards two pulses of isopropanol (500 ppb and 250 ppb) at operating temperature of 300 °C and 50 % relative humidity 156
6.28 Sensor response (resistance in Ω) against time (minutes) when exposed to benzene at 50% relative humidity, 210 ppb and variable temperatures. . . 157
6.29 AACVD sensor response (resistance in Ω) against time (minutes) when exposed to 2-butanone at 350 °C and 50% relative humidity, 500 ppb and 250 ppb concentration. 157
6.30 Schematic diagram of three curves with decreasing bulk donor density. Where N_A is equal to the surface acceptor density which is described as N_S in the equations above. The x-axis is the surface acceptor density; and the y-axis is the conductivity 158
6.31 Microscopic images of AACVD deposited CTO thin films on MEMs devices 159

6.32 Resistance response to 200 ppb toluene in 50% relative humidity. 160
6.33 MEMs, screen printed and ceramic AACVD sensors response to 200 ppb of toluene in increasing relative humidity 161
6.34 Resistance response to 900 ppb acetone in 50% relative humidity. 162
6.35 Resistance response to 900 ppb acetone in 50% relative humidity day two test. 162
6.36 MEMs response to 400 ppb ethanol in 50% relative humidity. 163
6.37 MEM sensors response towards 500 ppb dichlorobenzene in 50% relative humidity. 163

List of Tables

1.1 VOC concentration in mobile cabins 3

1.2 Types of gas sensors 6

1.3 Materials and analytes used for gas sensors 11

1.4 Change in resistance for different gases 11

1.5 Sensing performance of multishelled Cu_2O sensors towards 200 ppm formaldehyde at 120 °C operating temperature 16

1.6 Specification of commercial MOS MEMs-based sensors 42

4.1 pXRD 2θ peaks and lattice planes of Cr_2O_3 on different substrates 73

4.2 Binding energies (eV) of Cr_2O_3 annealed on different substrates ([a]literature values) and the calculated composition ratio 77

4.3 Raman shift assignment for Cr_2O_3 on different substrates 78

4.4 Hall effect measurements of Cr_2O_3 at room temperature 79

4.5 Film deposition parameters using $Ni(acac)_2$ 83

4.6 Binding energies (eV) of NiO using $Ni(acac)_2$ compared to [a]literature values 85

4.7 Hall effect measurements of NiO at room temperature 86

5.1 pXRD 2θ peaks and lattice planes of $Cr_{2\text{-}x}Ti_x$ annealed at 600 °C and screen printed CTO sensors 93

5.2 EDS analysis and atomic percentage comparison of CTO sensors 94

5.3 Theoretical and actual composition of AACVD CTO sensors. 95

5.4 Binding energies (eV) of $Cr_{2\text{-}x}Ti_xO_3$ annealed at 600 °C ([a,b]literature values) 99

5.5 Composition Ratio of CTO sensor substrates and screen printed sensors . 99

5.6 Raman shift assignment for AACVD and screen printed CTO sensors . . 100
5.7 Hall effect measurement of CTO sensors 103
5.8 Atomic percentage of sodium in CWO on glass substrate 109
5.9 pXRD 2θ peaks and lattice planes of $Cr_{2-x}W_xO$ on alumina and annealed at different temperatures 111
5.10 Raman shift assignment of CWO on alumina 113
5.11 Binding energies (eV) of CWO on quartz ([a,b]literature values) 115
5.12 Hall effect measurements of CWO on quartz substrates 117
5.13 pXRD 2θ peaks and lattice planes of CNO on different substrates 121
5.14 Binding energies (eV) of CNO compared to literature values 123
5.15 Raman shift assignment for CNO thin films 125
5.16 Hall effect measurements of CNO at room temperature 127

6.1 MEMs gas response towards VOCs 165

Abbreviations

AACVD	Aerosol Assisted Chemical Vapour Deposition
CVD	Chemical Vapour Deposition
CNO	Nickel Doped Chromium Oxide
CTO	Titanium Doped Chromium Oxide
CWO	Tungsten Doped Chromium Oxide
DC	Direct Current
e^-	Electron
E_F	Fermi level
E_g	Band gap
EDX	Energy-dispersive X-ray spectroscopy
FTO	Fluorine Doped Tin Oxide
h^+	Hole
MEMs	Micro Electro Mechanical Systems
MOS	Metal Oxide Semiconductor
pXRD	Powder X-ray diffraction
PVD	Physical Vapour Deposition
R_a	Baseline Resistance of Air
R_g	Baseline Resistance of Gas Analyte
SEM	Scanning eletron microscopy
TDBAA	Titanium Diisopropoxide Bis(Acetyl-acetonate)
VOC	Volatile Organic Compound
XPS	X-ray Photoelectron Spectroscopy
XRD	Single Crystal X-ray Diffraction

Chapter 1

General Introduction

The air on planet Earth contains a number of different chemical species, natural and artificial, some of which are vital to living organisms and others harmful to vary degrees.[7] Industrial processes have increased the use and manufacture of harmful substances (e.g. toxic and combustible gases) leading to the occasional leakage of gas, creating potential hazards for living organisms such as acid rain, greenhouse effect and ozone depletion. Hence gas sensors have assumed increasing importance in modern society for monitoring the environment, chemical processes, space and agricultural applications.[8]

Due to the dramatic growth in modern society, in particular the advancement of technology which has created an increase in standard of living, there has been an increase in environmental pollution. Environmental pollution can be split into three categories: air, water and soil pollution. Both air and water pollution can cause major harm over a short period of time as these types can rapidly diffuse over large areas.[9] By definition, an air pollutant is any substance which can harm humans, animals or vegetation. Pollutants can be classed into four categories: Gaseous pollutants (e.g. volatile organic compounds (VOCs), ozone, NO_x), persistent organic pollutants (e.g. furans), heavy metals (e.g. mercury) and aerosol particles. The next section will discuss VOCs in depth.[10]

1.1 Volatile Organic Compounds

Organic compounds can be categorised into three sections according to volatility: volatile organic compounds (VOCs), non-volatile organic compounds (NVOCs) and semi-volatile organic compounds (SVOCs). According to the World Health Organisation (WHO), VOCs are defined as all organic compounds in the boiling point range of 50 °C to 260 °C. Since the 1970s, there has been an increase amount of studies and reviews towards the concentrations of VOCs in indoor air.[11] VOCs are common in everyday life activities such as cooking, driving, house painting, food, beverages etc. resulting in the emission of various organic compounds such as alcohols, aromatics, alkenes, alkanes and esters.[12,13] It has also been shown that certain hazardous VOCs are highly toxic and carcinogenic, which may cause both short and long term health issues (e.g. allergy or cancer) as well as impacts on the ecosystem.[14] It has been found that indoor air contains a larger number of VOCs ($50-300$) and at higher concentrations than outdoor air, where concentration is dependent on the environment.[13] Indoor air is defined as the air in non-industrial areas of dwelling, office, school and hospital. The largest source of indoor air pollution is due to building materials, although occasional leakages of pollutants from outdoor air could be a contribution towards this high concentration.[15,16] VOCs have been shown to cause an adverse effect on people (usually office workers) known as ’sick building syndrome’. Typical symptoms are headaches and respiratory problems, the main cause of this is due to poor ventilation in the working environment.[13]

Another aspect to consider is the air quality in mobile cabins such as trains, air planes, buses and tubes as these types of transports are heavily used in modern society which may cause harm to the general public. Table 1.1 displays some of the VOCs found in public transport and the concentrations levels. It can be seen that most of the VOCs exposed in the air of these cabins are relatively comparable to one another with acetone and ethanol displaying a higher concentration in airplanes. 2-butanone which is usually used in coating and adhesives have similar concentrations across all modes of transport.[17]

Formaldehyde, the simplest of aldehydes, is used in building material such as plywood,

Table 1.1. VOC concentration in mobile cabins.[17]

VOC	Airplane	Train	Bus	Tube
Acetone ppm	8.84 – 70.6	20.63 – 38.73	12.63 – 30.73	12.63 – 38.73
Benzene ppm	0 – 2.29	0.63 – 1.25	0.63 – 1.88	1.25 – 2.19
2-Butanone ppm	1.15 – 6.07	1.02 – 3.73	1.36 – 6.1	1.36 – 5.76
Ethanol ppm	81.73 – 1923.84	90.22 – 902.21	26.54 – 137.99	68.99 – 159.21
Formaldehyde ppm	1.38 – 7.73	7.73 – 13.84	–	–
2-propanol ppm	4.89 – 37.77	0 – 13.45	2.85 – 25.67	3.67 – 9.37
Toluene ppm	12.4 – 22.95	1.86 – 14.33	3.98 – 10.35	3.45 – 7.16

resins, adhesives and carpeting.[18] It is a colourless and flammable gas at room temperature. Humans are usually exposed to this via inhalation; with low levels of exposure, it can lead to dizziness, fatigue, sore eyes and nausea. Upon high levels of formaldehyde exposure, breathing difficulties may result and ultimately pulmonary edema.[19] Although highly toxic, formaldehyde is still used industrially due to its low cost and high reactivity in the production of urea and phenolic resin.[20] The Occupational Safety and Health Administration (OSHA) set a threshold limit value of 0.75 ppm over a 8 h workday.[13]

Benzene is the simplest of aromatic compounds with a distinct odour. It is a colourless and highly flammable liquid with a boiling point of 80.1 °C and density of 0.878 g ml^{-1} at 20 °C.[21] It is a by-product of petrochemical process such as oil refining and is widely used in the industrial area as a solvent and cleaning agent. Benzene can be released from motor vehicles in exhaust fumes, which is of particular hazard due to its toxic and carcinogenic properties. High concentration level of exposure can lead to sudden seizures and respiratory failure. It is also a major cause of leukaemia and lymphomas.[22] The OSHA has set a threshold limit value of 1 ppm over a 8 h workday.[13]

Toluene is a colourless and flammable liquid with a distinct aromatic odour. It is insoluble in water, but soluble in both ethanol and acetone with a boiling point of 110.7 °C and density of 0.866 g ml^{-1} at 20 °C.[21,23] Toluene is a widely used aromatic hydrocarbon in adhesive, dyes, medicines, pesticides, explosive materials, fingernail polish etc. .[24] It is usually emitted from gasoline processes and crude oil as well as from the making of coke from coal. Toluene has similar toxicity to that of benzene and is an irritant to the skin and mucus membrane. High concentration levels of exposure can cause rapid heart beat and nervousness, it also damages organs such as the liver and kidneys and central nervous system. The National Institute for Occupational Safety and Health (NIOSH) has set a threshold limit value of 100 ppm over a 10 h workday and WHO has set a guideline value for indoor air of 0.07 ppm at 25 °C.[12,13]

Propan-2-ol or isoproyl alcohol is a colourless and flammable liquid with a boiling point of 82.3 °C, melting point of −89.5 °C and density of 0.785 g ml^{-1} at 20 °C. It is used for the production of acetone and isopropyl hailide and is used in paints, polishes,

antiseptics and insecticides. It causes irritation to eyes and nose when inhaled and when ingested, it causes dizziness, drowsiness and nausea. The American Conference of Governmental Industrial Hygienists (ACGIH) has set a threshold limit value of 200 ppm over a 10 h workday.[13]

2-butanone or methyl ethyl ketone (MEK) is a colourless liquid with a butterscotch like scent. It has a boiling point of 79.6 °C, melting point of −86.7 °C and density of 0.805 g ml^{-1} at 20 °C.[25] It is used in products such as protective coatings and adhesives, plastics, textiles, paints and medicine. The vapour inhaled could result in coma or even death. The ACGIH has set a threshold limit value of 300 ppm over a 8 h workday.[13]

Ethanol is a clear, colourless, volatile liquid with a boiling and melting point of 78.3 °C and −114 °C respectively and density of 0.789 g ml^{-1} at 20 °C.[21] Ethanol is a flammable compound and is the most widely used alcohol and a wide spectrum of applications such as food, chemical industries, biomedical and health and safety. Ethanol vapours are harmful and could lead to health problems such as headaches, drowsiness, eye irritations and breathing difficulties.[26] Therefore the need of quantitative detection of ethanol vapour at ppm levels is not only of medical but also social importance. The NIOSH has set a threshold limit of 1000 ppm over a 10 h workday.[13]

Acetylene is a flammable unsaturated colourless gas with a very distinct odour. It is an extremely volatile liquid with a boiling point of −84.7 °C. It is commonly used as a fuel in oxyacetylene welding, metal cutting and as a raw material used for the synthesis of chemicals such as acetylaldehyde, acetic acid and benzene. It is also used in synthetic rubber, paints, fabric, floor coverings, dry cleaning solvents and insecticide sprays. Acetylene is extremyl hazardous due to it being intrinsically unstable, especially when pressurised, it can cause an explosion, producing a large amount of heat. It also has a weak narcotic effect, where it prevent cells from oxygenating. Exposure to high levels of acetylene can lead to suffocation.The NIOSH has set a exposure limit value of 2500 ppm over a 8 h workday.[13]

Acetone, the simplest of ketone is a clear, colourless liquid with a pungent smell. It has a boiling point of 56.5 °C, melting point of −94 °C and a density of 0.788 g ml^{-1} at room temperature.[21] Acetone is a commonly used reagent in both industry and laboratories as

a cleaning agent, to dissolve plastics, purify paraffin and dehydrate tissues. It is also an important material for organic synthesis where it is used to make epoxy resin, polymethyl methacrylate and pharmaceutics. Acetone can cause irritation of the throat, nose and eye. Short term exposure towards acetone (five minutes to 300 ppm to 500 ppm) can cause slight irritations. Exposure to high concentrations can lead to headache, dryness in mouth, nausea, dizziness and drowsiness. However, long term exposures can lead to pharyngitis, bronchitis and dermatitis. The ACGIH has set a threshold limit value of 500 ppm over a 8 h workday.[13]

1.2 Gas Sensors

Humans use their nose as a gas sensor, which is a powerful tool used to measure the quality of various different products (e.g. food, drinks, perfumes and chemical products) from the odour it releases via 'sensory panels'. However, these panels are shown to be affected by many factors such as physical and mental health.[27] It is also near impossible to smell trace amounts of odourless gases. Therefore techniques such as gas chromatography and mass spectrometry have been used to help in gas analysis. However, these techniques are typically not portable, are expensive and have a relatively slow performance.[28] Therefore mobile gas sensors have been intensely researched over the last decade. There are many different types of gas sensors that operate using different principles and materials, which have different selectivity and sensitivity to gases, lifetime and price as listed in table 1.2.

Table 1.2. Types of gas sensors.[29]

Types of sensors	Functionality
Calorimetric	Change in temperature, heat flow or heat content
Mass Sensitive	Change in the weight, amplitude, frequency, size or shape
Magnetic	Change of paramagnetic properties
Optical	Change in light intensity, colour, or emission
Electrochemical	Change in current, voltage or capacitance
Electrical	Change in conductivity

Calorimetric sensors, also known as thermometric sensors convert temperature changes generated by chemical reactions to electrical signals (e.g. change in current or voltage).[30] These sensors are widely used for the detection of explosive combustible gases due to its high stability, reliability, accuracy and long lifetime.[31] However, they operate at high temperature and are sensitive towards oxygen containing compounds.[32] Temperature change is recorded when the gaseous compound is burnt in the presence of oxygen (mainly air) on the surface of a small bead or film of an active metal catalyst (e.g. Pt, Pd, Rh).[33,34] An example of this are pellistor (catalytic bead) sensors (illustrated in figure 1.1).

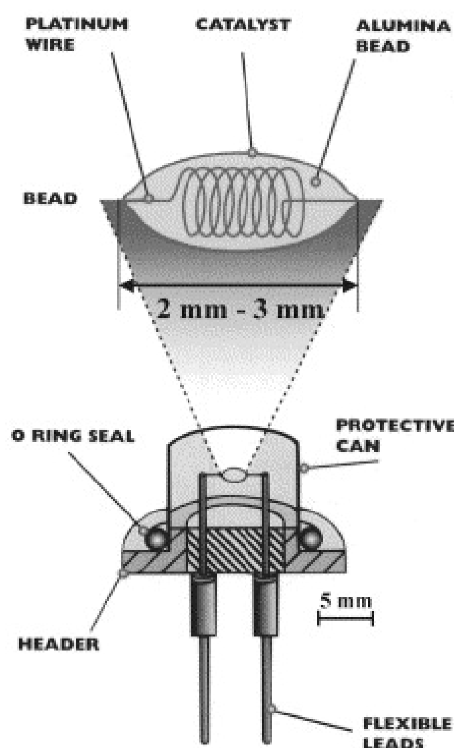

Figure 1.1. Schematic diagram of a commercial pellistor sensor.[35]

Mass sensitive gas sensors rely on changes on the surface of the sensor during interaction with analytes. Mass change happens from the accumulation of analyte on the sensing layer (e.g. polymer) during its interaction.[36] Quartz crystal microbalance (figure 1.2) are classed as mass sensitive gas sensor, containing a metal electrode deposited on a piezoelectric quartz crystal wafer. The sensor measures the frequency shift with respect to mass loading via electromechanical oscillators.[37] These sensors generally have good precision, diverse surface functionalisation and high sensitivity; however, they have poor signal to

noise ratio, and are sensitive to humidity and temperature.[32]

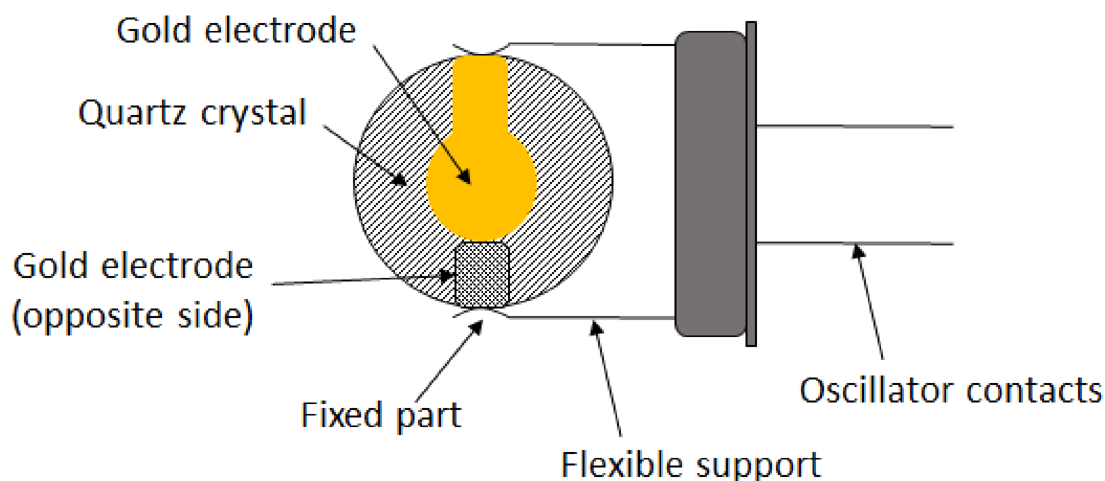

Figure 1.2. Schematic diagram of a QCM mass sensitive gas sensor.[38]

Magnetic gas sensors looks at the change in paramagnetic properties of the gas being analysed, whilst optical gas sensors detect changes in the visible region of the spectra or other electromagnetic waves during chemical interaction.[39] These devices consist of a light source, wavelength selector, identification and interaction unit, a transducer to convert it to traceable signals and a detector.[40] Optical sensors are very sensitive, and are capable of identifying individual compounds in mixtures. However, the downside is the complex sensor array system, which makes it more expensive to operate and are typically not portable due to delicate optics and electrical components.[32]

Electrochemical gas sensors ionises gas molecules via a three phase boundary layer (atmosphere -electrode of catalytic active material- electrolyte). An example of an electrode material is Au-Nafion with sulfuric acid as an internal electrolyte solution. However, due to corrosion and contamination, these sensors only have a lifetime of one to two years.[41,42] Figure 1.3 illustrates a simple schematic diagram of a electrochemical gas sensor where cations and anions move in the electrolyte.

Metal oxides electronic properties ranges from metals conductors to semiconductors and through to insulators. Semiconductors can be divided into two categories; intrinsic and extrinsic semiconductors. These are related to the purity of semiconductors. Intrin-

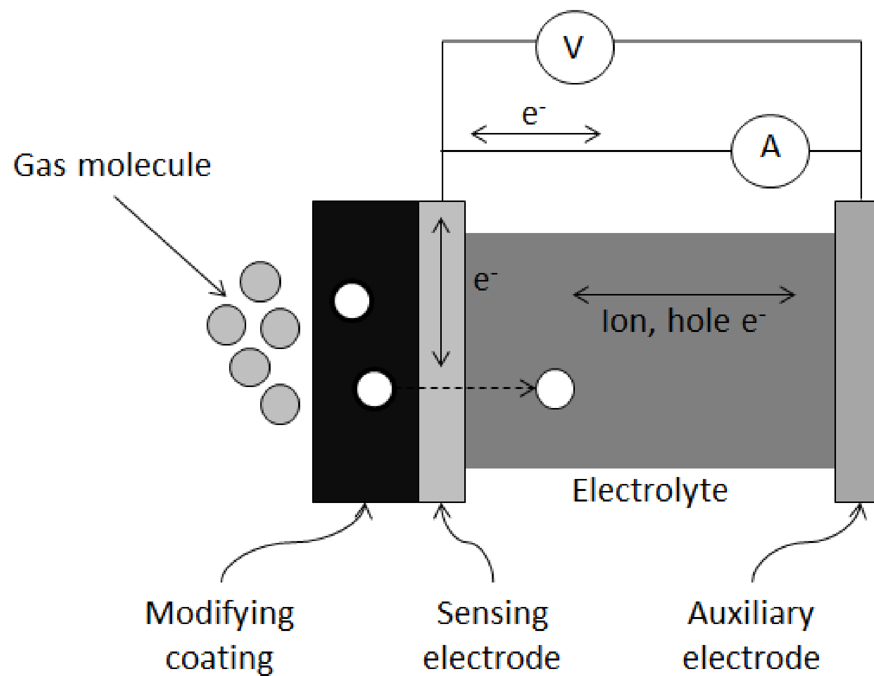

Figure 1.3. Schematic diagram of a electrochemical gas sensor.[43]

sic semiconductors, also known as pure semiconductors contain very low concentrations of defects and external impurities. The conductivity of these materials are temperature dependent. There are similarities between intrinsic semiconductors and insulators; the only difference between the two is the size of the bandgap energy. Intrinsic semiconductors have smaller band gaps which in turn allows greater electron concentration in the conduction band, therefore providing material with lower electrical resistance. Extrinsic semiconductors have some impurities added to modify their electronic properties. These defects in the crystal lattice of semiconductors can be a source of either electrons or holes and are generally lattice vacancies.[44,45]

The first semiconducting metal oxide sensor was pioneered by Seiyama *et al*. in 1962 for gas sensors based on zinc oxide, as they discovered a change in resistance of the material when a gas was absorbed onto the surface.[2] Since then, there has been a sharp increase in the development of semiconducting gas sensors, as shown in figure 1.4. Table 1.3 shows a small example of different metal oxides with different affinities of gases which detect combustible, reducing, or oxidising gases via their conductivity, with ZnO and SnO_2 being the most common material for sensing.[46–48]

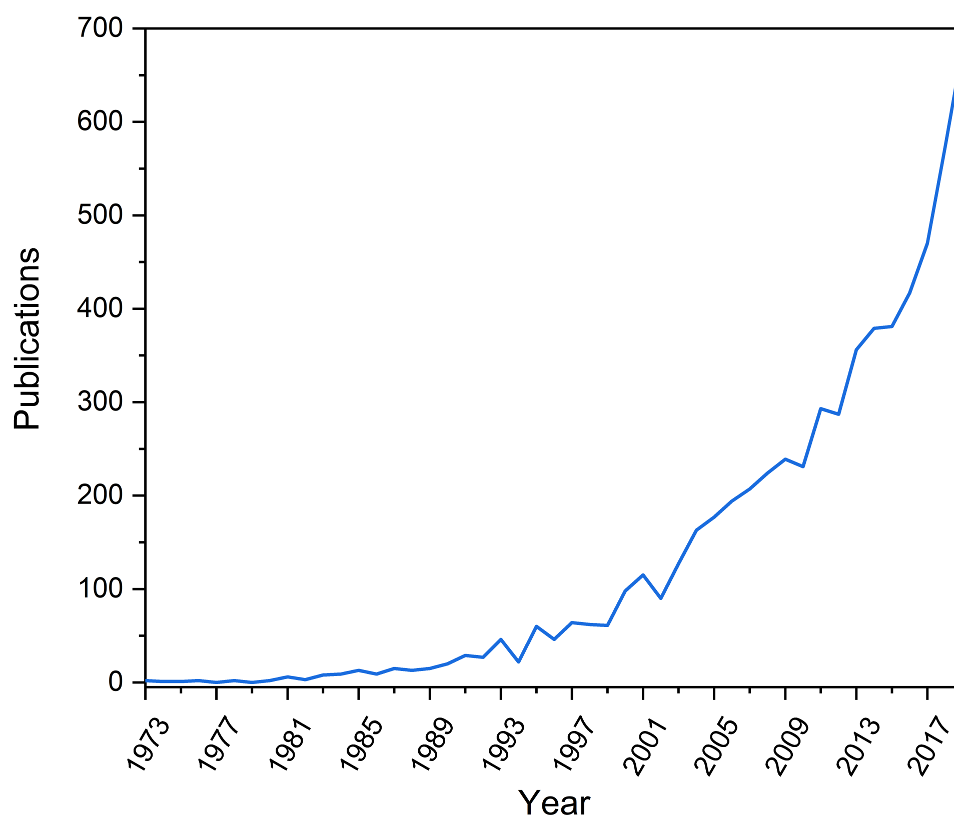

Figure 1.4. Number of publications from 1973 to 2019 on metal oxide gas sensors (source from Scopus).

Gas sensors based on metal oxide semiconductors (MOS) are commercially available and have been widely used in the detection and monitoring of flammable and toxic gases. MOS are cheap, reliable, low power consuming, have good sensitivity due to a wide range in conductivity and robust structure which make them ideal as a gas sensing material. Due to this, there has been an increase in demand for better gas sensors with higher sensitivity and selectivity (ability to discriminate the target from the interference analyte and display a target specific sensor response). Table 1.4 displays the change in resistance seen for a a typical *n*-type (electron charge carriers) and *p*-type (hole charge carriers) MOS sensor when exposed to a reducing and oxidising gas. A change in resistance is due to combustion reactions occurring on the surface of the metal oxide with the lattice oxygen species and the output signal of these 'transducers'.[48,55,56]

The output signal of these transducers is usually dependent on operating temperature. Response and recovery times of chemiresistive gas sensors are also shown to be operating

Table 1.3. Materials and analytes used for gas sensors.

Material	Analytes	Detection limit (ppm)
SnO_2	CO	5.0[49]
	EtOH	100[50]
ZnO	NH_3	5.0[51]
	CH_4	50.0[52]
TiO_2	CH_2O	0.04[53]
	NO_2	0.16[54]

Table 1.4. Change in resistance for different gases.[55]

MOS Type	Reducing Gas	Oxidising Gas
n-type	Decrease in resistance	Increase in resistance
p-type	Increase in resistance	Decrease in resistance

temperature dependent, i.e. temperatures over 200 °C is needed for good chemisorption and desorption of detected gas which rapidly increases the power consumption.[57]

MOS gas sensors consist of three parts, a sensing layer/film, electrode and heater. When the metal oxide interacts with a gas, a change in resistance occurs upon exposure to target gases which is measured by a pair of electrodes. These sensors are usually equipped with a heater so the sensor can reach its optimum operating temperature. There are three different operating principle for MOS: conductometric, field effect transistor (FET) and impedance change.[58]

Conductometric is the most common sensing modality for MOS gas sensors. There are two types of structures for conductometric sensing platform, direct heating and indirect heating. For direct heating the heater is in contact with the sensing material, however, this is less stable and prone to interference. Therefore most gas sensors use indirect heating, an example of this is wafer detectors. There are two types of wafers; single and double sided illustrated in figure 1.5. Single sided wafer has the heater and detection pads exposed on the same surface of the device, whereas with double sided the detection pads are on the surface device and the heater pad faces the bottom surface of the device. The advantage

of single sided wafer is better control of operating temperatures and ease of assembly due to the simplistic design. However, constructing this device requires the use of insulating layers.[59] Double sided sensors are easier to construct but are more difficult to assemble into sensor devices. The substrate used are usually silica or alumina as they have good mechanical strength and stable to elevated temperature and corrosive chemicals.[60,61]

In addition to this, conductometric sensors have three main designs: (i) thin film, (ii) thick film and (iii) sintered pellet. Thin and thick film sensors are the more common type and are produced by depositing a sensing layer onto a substrate (e.g. Al_2O_3) equipped with gold and platinum electrodes (as shown in figure 1.5). The electrodes are used to measure the resistance of the sensor and to control the temperature of the sensors heater.[62]

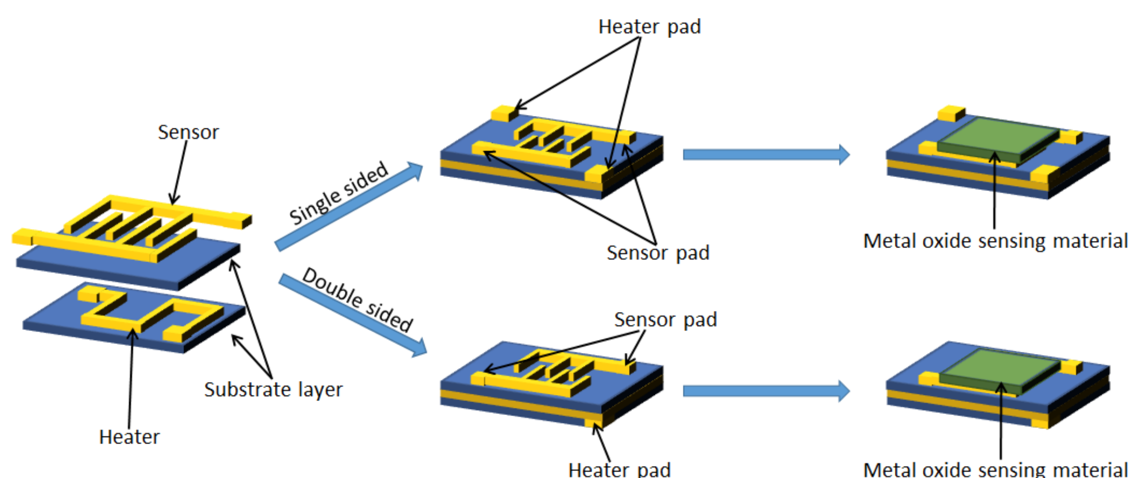

Figure 1.5. Schematic diagram of a single and double sided sensor on a wafer substrate.[60,61,63]

FET type sensors and impedance sensors are illustrated in figure 1.6. FET sensors are used for single or arrays of one dimensional semiconducting nanomaterials with a complex fabrication process. FET sensors are based on changes in the parameters due to exposure to target gases on sensing channels. The advantage of using FETs include: ability to operate at room temperature, enhances the generation of sensitive and selective sensing surface due to a variety of sensing material available and they are small in dimension and compatible with micro-fabrication techniques which can be made into sensor arrays.[64,65] Impedance change type sensors operates under alternating voltage upon exposure to target species.[60] These sensors are non-invasive and contactless due to the adjustable penetration

of the electric field and charge induction.[66]

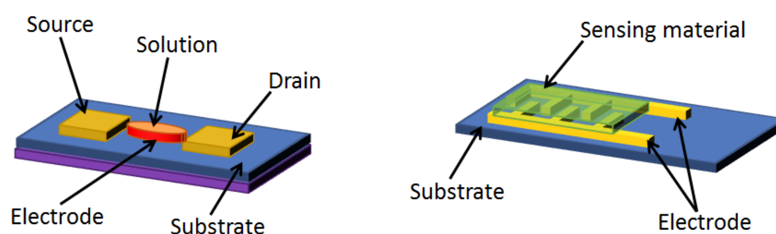

Figure 1.6. Schematic diagram of a FET and impedance sensor (from left to right).[67,68]

1.3 Recent Advances in *p*-type MOS Gas Sensors

This section explores different MOS gas sensors that have been researched for the past 10 to 15 years, for *p*-types. The sensitivity and selectivity of these sensors are examined towards VOCs in particular.

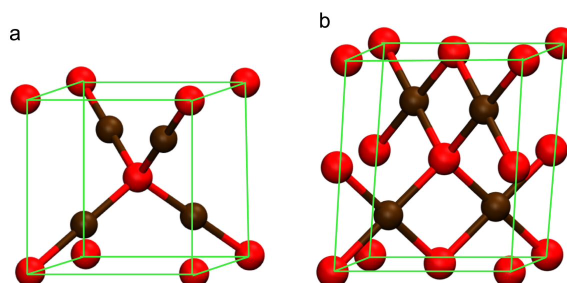

Figure 1.7. Ball and stick unit cell model of (a) Cu_2O and (b) CuO.[69]

Copper oxides are an abundant material which are non-toxic and environmentally friendly.[70] Copper (II) oxide (CuO), a black colour material also known as cupric oxide is a *p*-type MOS, with a narrow band gap energy of 1.2 eV. Cu_2O, also known as cuprous oxide is reddish in colour and has a bandgap of 2 eV to 2.17 eV.[71,72] CuO has a complex monoclinic structure, whereas Cu_2O has a cubic structure.[69] Thermal oxidation of copper metal is a widely used method in synthesising CuO and Cu_2O due to coppers high oxygen affinity.[73] Figure 1.8 illustrates the Ellingham diagram for various metal oxides where it depicts the relative thermodynamic stability of the different oxides. The lines which are lower in the diagram possess a more negative standard Gibbs energy of formation, indicating the more stable a metal oxide is.[74]

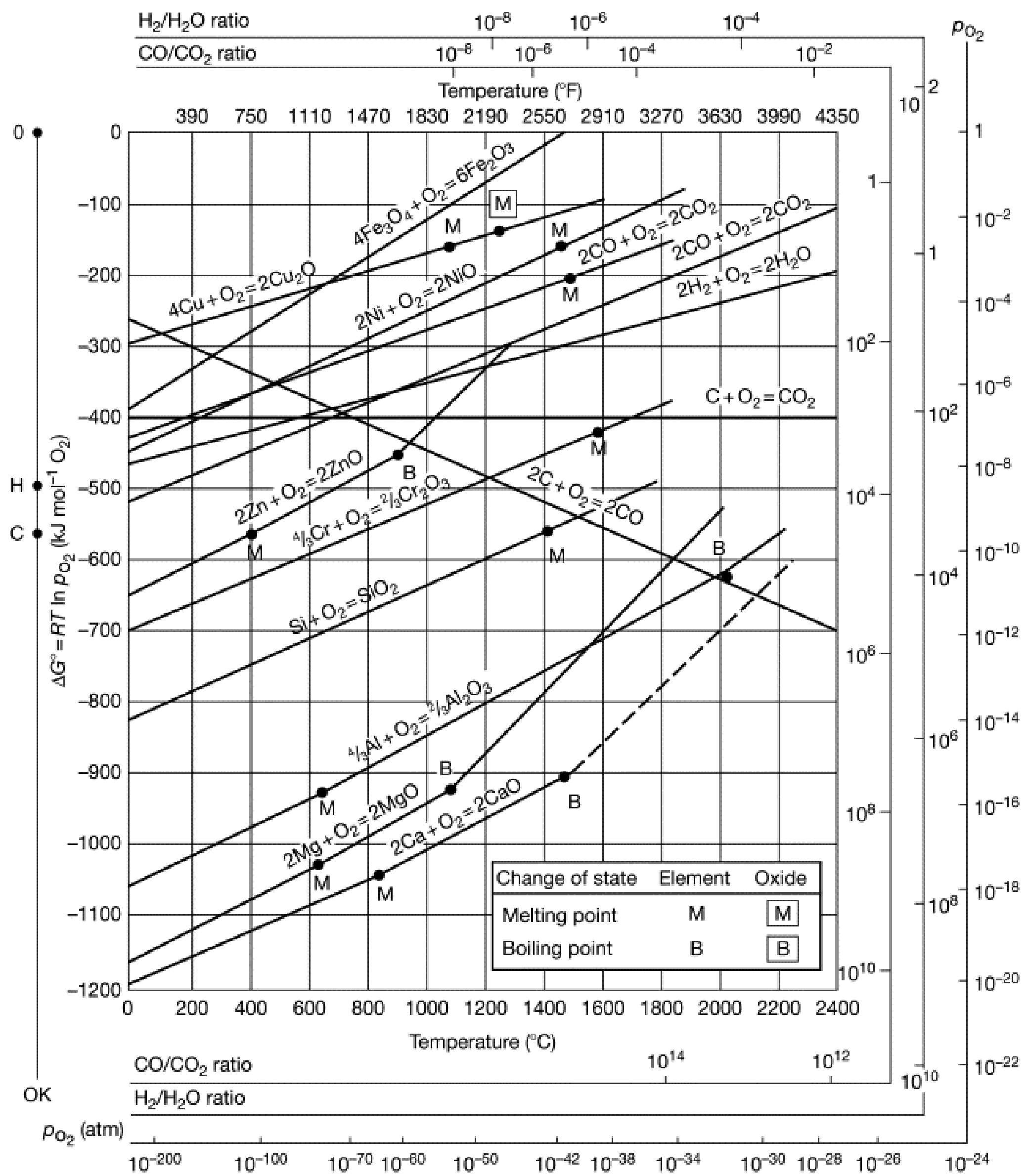

Figure 1.8. Ellingham diagram displaying the standard Gibbs energy of formation for a number of metal oxides.[74]

Thermal oxidation for the formation of Cu_2O and CuO is simple, low cost and produces high purity, however, it is time consuming. Other synthetic techniques have been used for the formation of copper oxides such as; solvothermal, hydrothermal, microwave, sol-gel, spray pyrolysis, sputtering etc. Several types of nanostructures have been reported for both copper oxide materials.[75–77] CuO and Cu_2O has been used in a wide range of applications such as; catalysis, lithium-ion batteries, film transistors, sensors and solar cells.[78–81] Due to their due to their intrinsic *p*-type properties, the use of CuO as a gas sensor have been extensively studied but less so for Cu_2O. CuO nanostructure gas sensors have shown to

have sensitivity towards a variety of both oxidising and reducing gases such as: H_2S, H_2, CO, CO_2, ethanol and so on.[82]

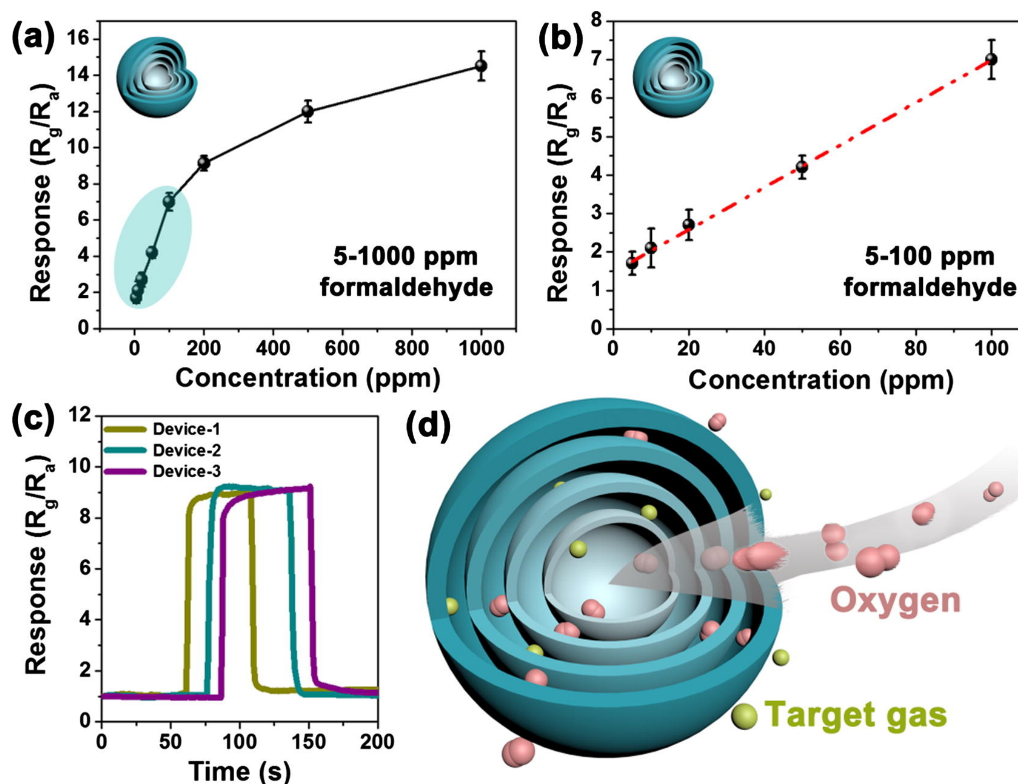

Figure 1.9. (a) Response towards 5 ppm to 1000 ppm formaldehyde; (b) Response towards 5 ppm to 100 ppm formaldehyde; (c) Reproducibility test; (d) Diagram of Cu_2O sphere with quadruple shells.[81]

Zhang *et al.*[81] recently reported the fabrication of a multishelled *p*-type cuprous oxide (Cu_2O) with enhanced formaldehyde sensitivity (illustrated in figure 1.9). It was hypothesised that a tunable hollow multishelled Cu_2O sphere with enough void space should supply effective active sites for gas adsorption. Zhang explained the response of all four types of multishelled Cu_2O (single, double, triple and quadruple) towards formaldehyde increased when operating temperature increased from 90 °C to 120 °C and a decrease in response is seen when temperature increases past 120 °C. Out of the four types of multishelled Cu_2O, the quadruple-shelled sensor exhibits a higher response of 9.6 R_g/R_a when exposed to 200 ppm of the reducing gas, where R_g/R_a is the calculated response of the sensor i.e. the sensitivity. It also desplayed a response and recovery time (5 s and 3 s) compared to the other multishelled sensor (a comparison is illustrated in table 1.5). Figure 1.9a) shows the responses of the quadruple- shelled sensor as a function of formalde-

hyde concentration at optimum working temperature. The response of the sensor increased rapidly between 0 ppm and 100 ppm but slowly after 100 ppm and remained steady and slowly becoming saturated above 200 ppm . This could be attributed to formaldehyde occupying on all surface active sites or the lack of surface adsorbed oxygen species for gas sensing reaction.[81]

Table 1.5. Sensing performance of multishelled Cu_2O sensors towards 200 ppm formaldehyde at 120 °C operating temperature.[81]

Structure	Response (R_g/R_a)	Response Time (s)	Recovery Time (s)
Single	2.1 ± 0.2	8.0 ± 1.4	31.0 ± 5.0
Double	4.6 ± 0.3	8.0 ± 1.5	12.5 ± 1.2
Triple	7.5 ± 0.5	6.5 ± 1.2	7.0 ± 0.7
Quadruple	9.6 ± 0.5	5.0 ± 1.0	3.0 ± 0.4

Urasinska-Wojcik and Gardner[83] reported a detailed analysis of thick film copper oxide CuO, onto MEMs sensors via drop casting for the detection of low levels of hydrogen sulfide (H_2S) in a pure hydrogen environment and under various operating conditions. The sensors displayed a relatively stable response towards H_2S in both dry and humid hydrogen conditions. Operating temperature was a significant factor of the performance of CuO layer towards the analyte and humidity. The optimal temperature was determined to be 350 °C in the absence of humidity and similar response was seen at lower temperature (150 °C to 200 °C) in a humid environment.

Figure 1.10a illustrates the change in resistance for CuO sensors towards different pulses of H_2S in a proportional amount of dry hydrogen environment at the optimal working temperature of 350 °C. The average response values towards H_2S was 1.27 and 1.19 for 10 ppm and 1 ppm respectively. Figure 1.10b displays the average response towards different concentrations of H_2S in a dry H_2 environment at working temperatures between 150 °C to 400 °C. The sensors response were remained relatively unchanged at low temperatures (150 °C to 250 °C), with a gradual increase between 300 °C to 400 °C where the optimal temperature was at 350 °C.

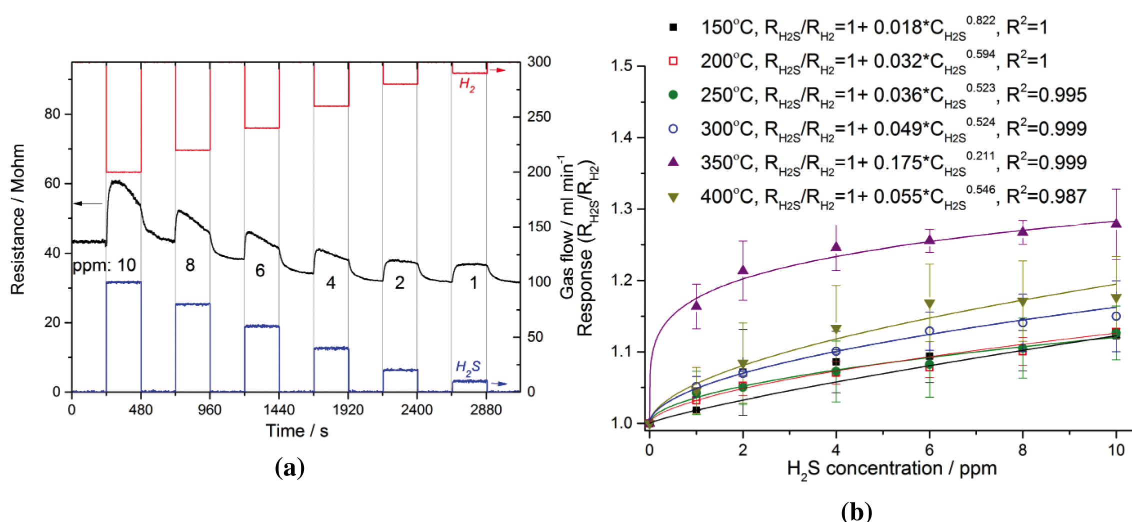

Figure 1.10. Response of CuO thick films on MEMS sensors towards H_2S in H_2 environment, where (a) Dynamic response of CuO towards decreasing concentration of H_2S (10 ppm to 1 ppm) in dry H_2 at 350 °C; (b) Sensor response at a working temperature range between 150 °C to 400 °C towards H_2S in dry H_2.[83]

Urasinska-Wojcik also describes the influence of humidity in an H_2 environment towards the sensors as depicted in figure 1.11. The sensors were tested in the presence of 0 %, 25 %, 50 %, 60 % and 75 % relative humidity at a working temperature of 350 °C. The response displayed no significant change towards all five concentrations of H_2S between dry H_2 and in 25 % relative humidity. However, at higher humidity levels, the response were greater, displaying similar response to one another at all five concentrations. Looking at the response for 6 ppm a percentage increase of 13.5 %, 18.7 % and 19.3 % was recorded for 50 %, 60 % and 75 % relative humidity respectively compared to when the sensors were exposed in a dry H_2 environment.

Chen *et al.*[84] reported in 2018 the synthesis of copper oxide (CuO) nanocubes (NCs) and nanotubes (NTs) and studied their sensing performance towards carbon monoxide (CO). CuO NTs were synthesised via the oxidation of Cu nanowires. Heat treatment at 500 °C for CuO NTs and 400 °C for CuO NCs exhibited the greatest response towards CO in terms of R_g/R_a as illustrated in figures 1.13a) and 1.13b).

Figure 1.13c examines the response of the two sensors as a function of operating temperature at a gas concentraion of 1000 ppm where CuO NTs displayed the greatest response at an operating temperature of 175 °C with an R_g/R_a of $\sim$ 3.25; and for CuO NCs

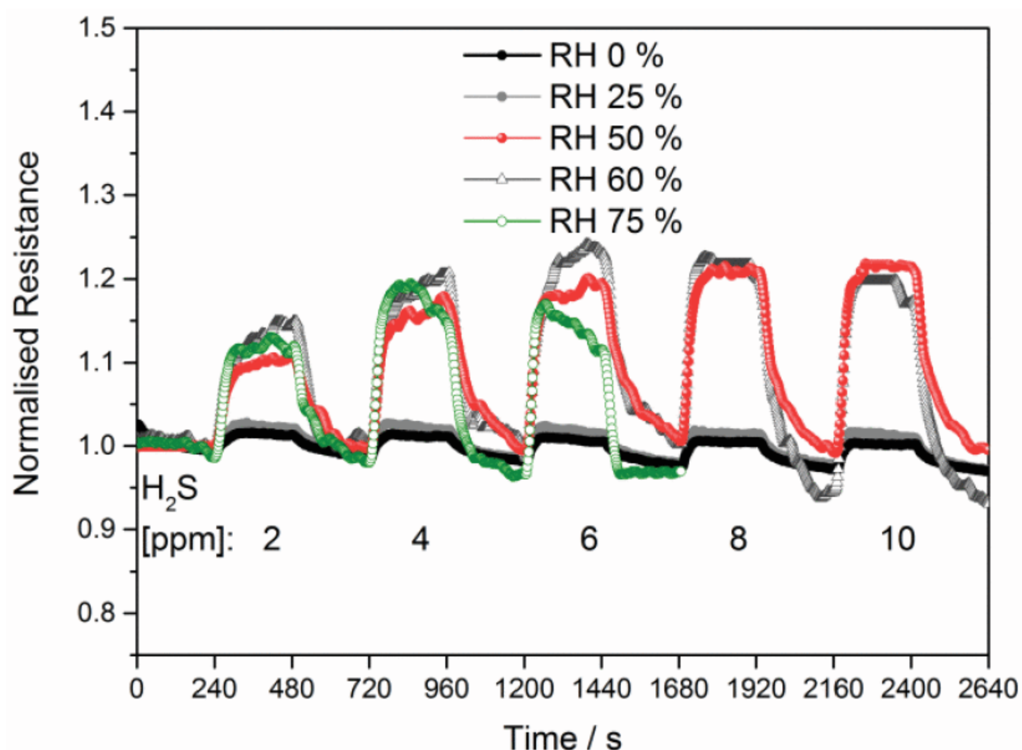

Figure 1.11. Normalised response towards different concentrations of H_2S in dry and humid hydrogen conditions at 350 °C.[83]

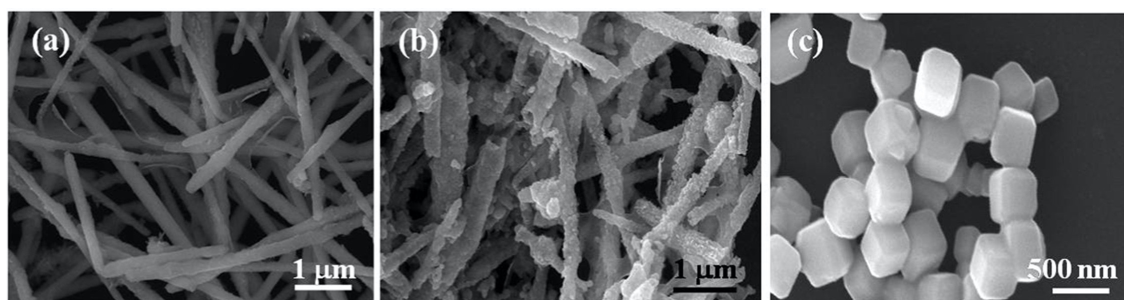

Figure 1.12. SEM Images of a) CuO NWs; b) CuO NTs and c) CuO NCs.[84]

the optimum operating temperature was at 250 °C giving a R_g/R_a response of ∼ 2.0. The sensitivitvty of both CuO NCs and NTs where investigated towards various concentrations of CO (50 ppm to 1000 ppm) at an operating temperature of 175 °C which is depicted in figure 1.13d and figure 1.13e. In terms of R_g/R_a response, both CuO NCs and NTs show a increase in response as CO concentration increases. However, CuO NTs exhibited a higher response performance and lower detection limit than CuO NCs. The main factors could be due to the difference in surface area, CuO NTs had a larger surface area (143.2 m g^{-2}) than CuO NTs (82.4 m g^{-2}). Different surface planes of CuO NTs and CuO NCs are exposed

which may have an effect on their gas adsorption and sensing capabilities. Figure 1.13f displays the linear fitting of CuO NCs and NTs to different CO concentrations, where both sensing material shows good linear fits in two concentration ranges. At low CO concentration range 0 ppm to 200 ppm, the response intensity increases rapidly. Whereas above 200 ppm response intensity increases slowly.[84]

Cho *et al.*[85] in 2016 developed a high resolution *p*-type MOS nanowires as an ultrasensitive sensor for the detection of VOCs. In the report, Cho looked into the use of CuO, NiO and Cr_2O_3 for the detection of VOCs. The sensing performance for CuO nanowires were examined and a variety of non-polar (toluene and hexane) and oxygen based (acetone and ethanol) VOCs were tested at concentration levels of 1000 ppm at three different operating temperatures 200 °C, 250 °C and 300 °C. It was seen that CuO nanowires displayed a rapid response towards acetone and ethanol at temperatures of 250 °C and 300 °C as seen in figure 1.14.[85]

In the case of NiO and Cr_2O_3 nanowires, the two materials displayed a response towards hexane at an operating temperature of 280 °C for NiO and 350 °C for Cr_2O_3 as depicted in figure 1.15. Figures 1.15a) and b) illusatrates the SEM image of NiO and Cr_2O_3 nanowires. Figures 1.15c) and d) displays the pXRD patterns of nickel and chromium pre and post annealing. Figures 1.15e) and f) displays the gas response of NiO and Cr_2O_3 nanowire sensors towards hexane. NiO exhibited high sensitivity towards hexane ($\Delta R/R_a$ = 30 at 1 ppm) and also displayed rapid response and short recovery time even at low concentration exposure (R_a (ΔR denotes the baseline resistance of the sensor exposed to dry air and the change in resistance after exposure to analytes respectively). The reason explained was due to the morphology for the fabrication of the ultrathin pattern which resulted in the formation of a hole accumulation layer. For Cr_2O_3, the sensors displayed a large change in response at all concentrations of hexane, however due to equipment limitation, resistance above the detection limit was not recorded and hence unable to calculate the response.[85]

Cobalt oxide (Co_3O_4) containing 2+ and 3+ oxidation states, is a *p*-type MOS with a bandgap of 1.6 eV to 2.2 eV and has a spinel structure. In the cubic spinel structure, Co^{2+}

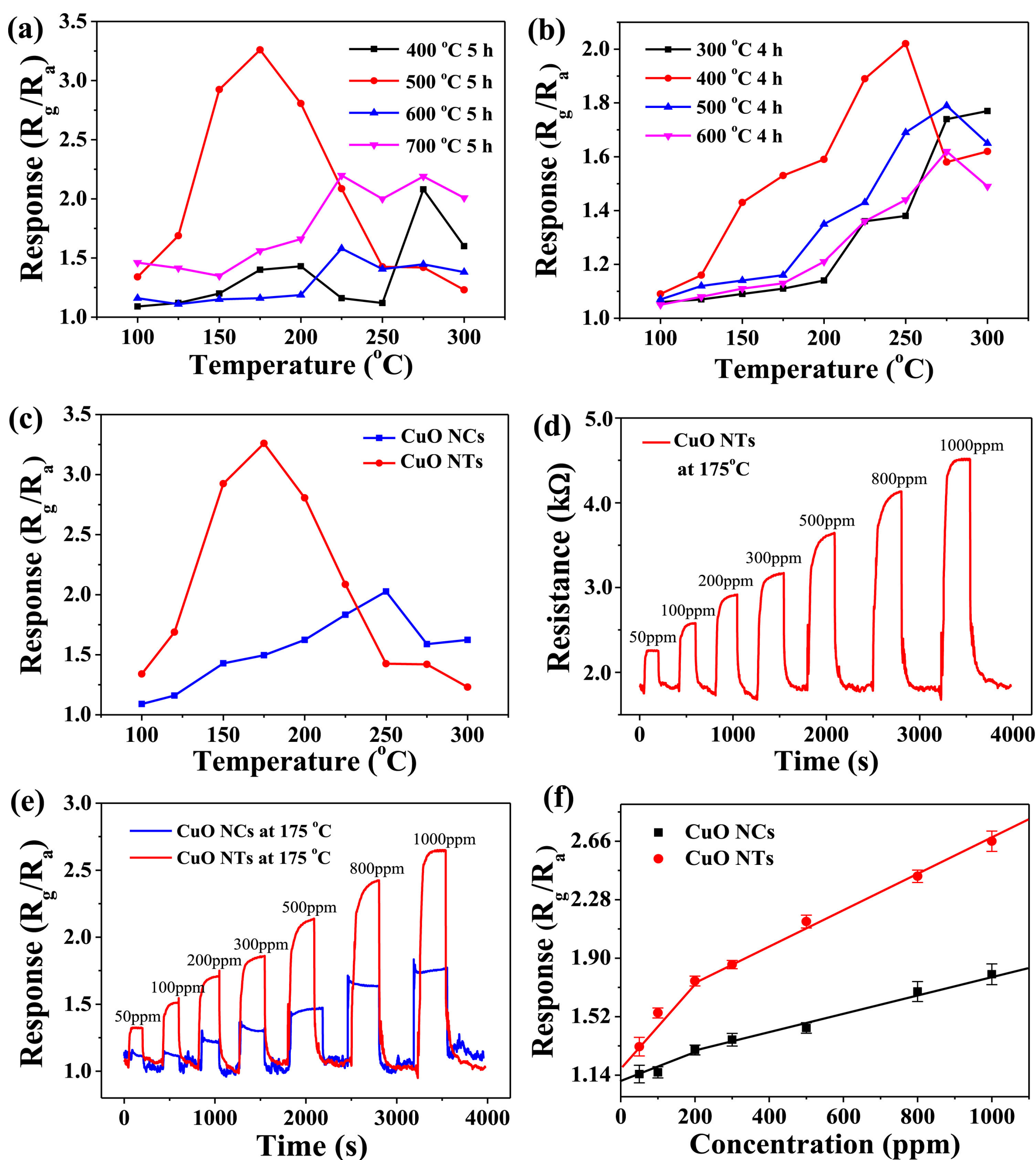

Figure 1.13. a)CuO NTs and b) CuO NCs displays the response towards 1000 ppm of CO at different annealing temperatures; c) Response towards 1000 ppm of CO at different operating temperatures with 2.5 mg of CuO NTs and CuO NCs; d) CuO NTs response and recovery towards different concentrations of CO, where the NTs were annealed at 500 °C and at a operating temperature of 175 °C; e) CuO NTs and CuO NCs sensing response at a operating temperature of 175 °C and different concentrations of CO in terms of R_g/R_a; f) linear fitting of CuO NTs and CuO NCs response as a function of CO concentration at at a operating temperature of 175 °C.[84]

ions occupies one eighth of the tetrahedral sites and Co^{3+} ions occupies half of the octahedral sites (displayed in figure 1.16).[87] Various methods have been used to deposit Co_3O_4 such as sputtering, hydrothermal, pyrolysis, sol-gel, CVD, atomic layer deposition (ALD)

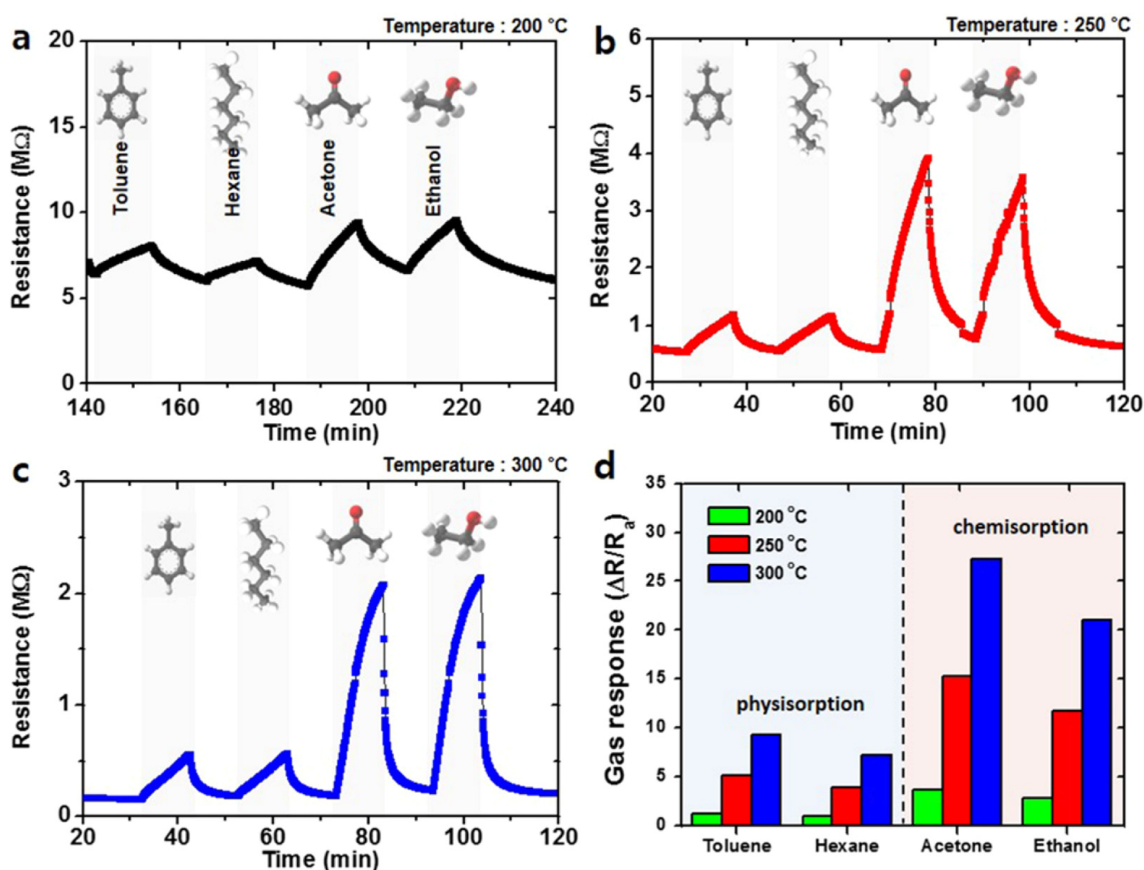

Figure 1.14. CuO nanowire in sensing performance towards toluene, hexane, acetone, and ethanol at operating temperatures of a) 200 °C; b) 250 °C; c) 300 °C. d) Bar graphs of the sensor responses the four VOCs at 1000 ppm concentration at various operating temperatures.[85]

and thermal oxidative decomposition, each forming different nanostructures.[88–90] Co_3O_4 have been extensively studied for the applications of photovoltaics, sensors, lithium-ion batteries, catalysis and supercapacitors due to its high abundance, low cost and high stability under ambient coniditons. Co_3O_4 have shown to be a growing interesting in gas sensing applications due to its high catalytic activity for the oxidation of reducing gases.[91,92]

Hieu and Cuong *et al.*[93] reported the synthesis of mesoporous Co_3O_4 nanochains for the detection of H_2S. The mesoporous nanochains were synthesised via hydrothermal conditions using hydrated cobalt nitrate as starting material and annealed at 600 °C for five hours. Co_3O_4 sensor were exposed to 1 ppm to 100 ppm of H_2S in air at three different operating temperatures (250 °C, 300 °C and 350 °C), as shown in figure 1.17a), b) and c). Figure 1.17 demonstrates an increase in resistance towards H_2S as a reducing gas, at a concentration as low as 1 ppm, showing a typical *p*-type MOS sensing behaviour. Co_3O_4

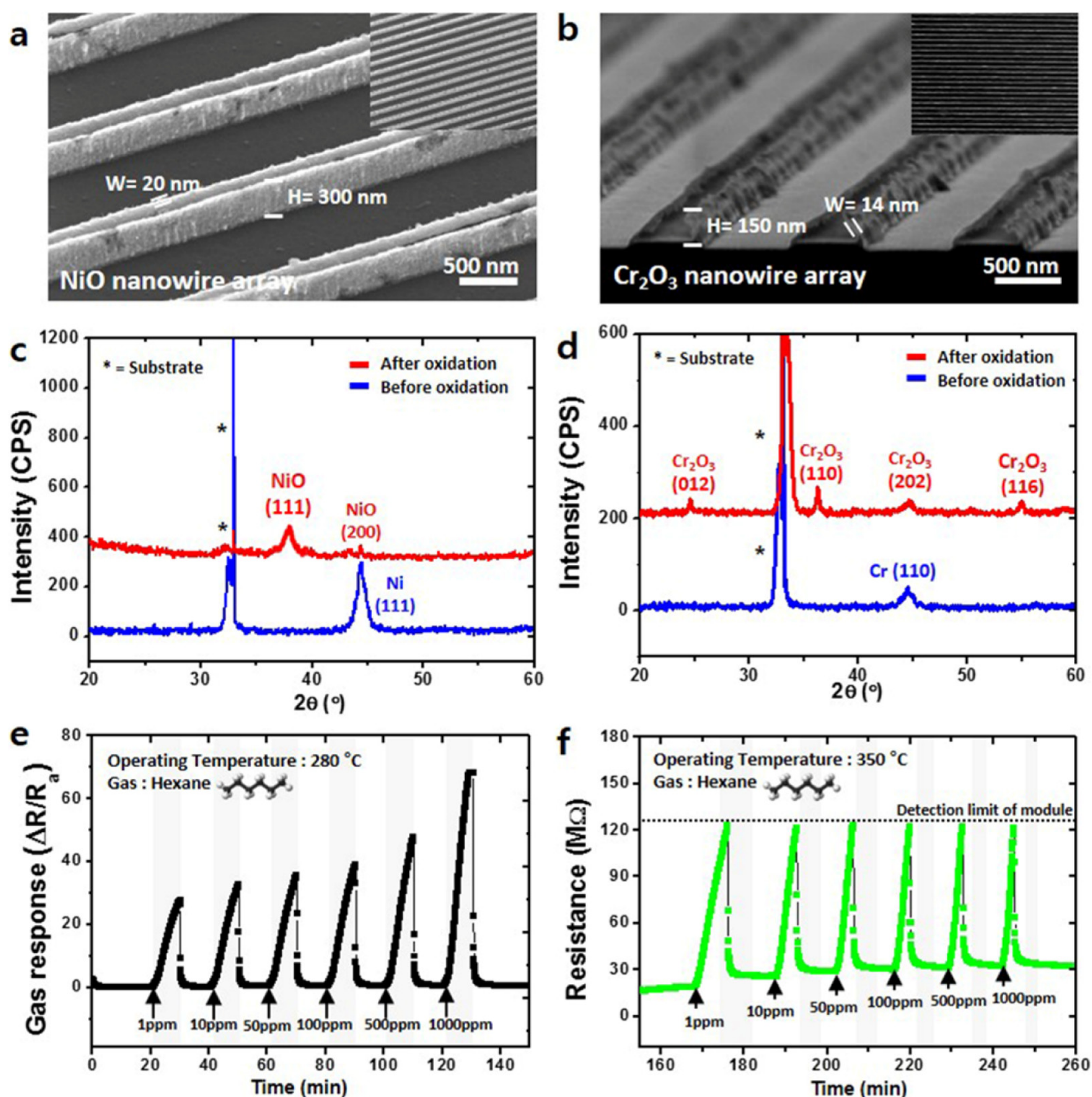

Figure 1.15. a)NiO and b) Cr_2O_3 nanowires SEM images, c) and d) XRD patterns of Ni and Cr nanowire arrays before and after thermal oxidation. e) and f) are Gas sensing response towards various hexane concentrations.[84]

sensors displayed stable sensing and recovery independent of operating temperatures. The optimum operating temperature for Co_3O_4 sensors towards H_2S was found to be at 300 °C as shown in figure 1.17d). The response and recovery times were found to be at 46 s and 24 s respectively.[93]

Hieu and Cuong *et al*. also reported the sensitivity and selectivity of mesoporous Co_3O_4 nanonchains towards NH_3, CO, and H_2 at an operating temperature of 300 °C. Figure 1.18a) illustrates the the sensors response towards an increasing concentration of NH_3 (10 ppm to 1000 ppm) and showed a trend similar to that of H_2S; response increases as

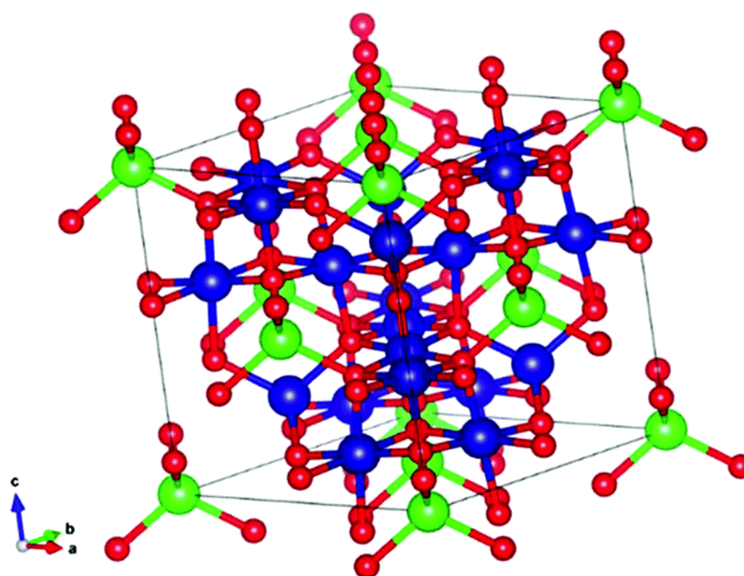

Figure 1.16. Spinel structure of Co_3O_4 where the blue atoms denote Co^{3+} in octahedral site, green atoms denote Co^{2+} in tetrahedral sites and red atoms denote oxygen.[86]

the concentration of analyte increases. Figure 1.18b) shows response towards CO from 2.5 ppm to 200 ppm. Response between 2.5 ppm to 50 ppm showed little to no change; the response towards 200 ppm of CO was slightly higher. Figure 1.18c) represents the response towards H_2 at a concentration of 25 ppm to 1000 ppm. Response increases as concentration increases; however, as shown in Figure 1.18d), sensitivity towards CO and H_2 is comparatively lower than that of both H_2S and NH_3, whihc demonstrates selectivity towards the latter two gases.[93]

Since its discovery in 1990 by Moseley and Williams, chromium titanate ($Cr_{2-x}Ti_xO_3$,CTO), a *p*-type material has been extensively used in gas sensing due to its desirable characteristics such as tolerance towards relative humidity, a good baseline stability and good sensitivity.[94,95] It was the first new MOS material since the discovery of SnO_2 in the 1960's to be commericallised and maufactured in large quanities and is used for the detection of VOCs and CO.[96]

CTO is generally prepared by solid-state synthesis between chromium and titanium oxides at temperatures above 900 °C.[97] However, there are disadvantages for this method such as high temperature synthesis, poor chemical homogeneity of the material and components contamination which influences the sensing layer. Commercialised CTO sensor

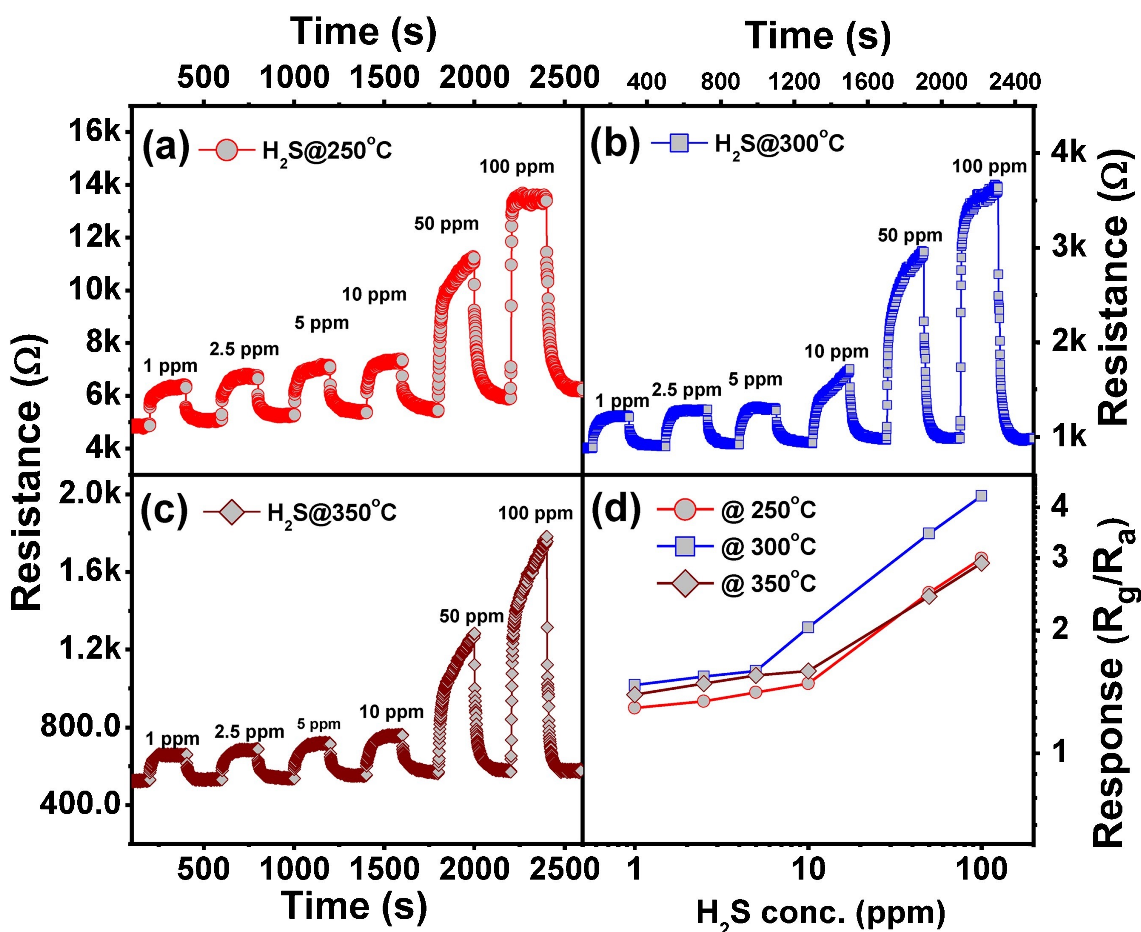

Figure 1.17. Response of mesoporous Co_3O_4 nanochains towards increasing concentration of H_2S and operating temperature of (a) 250 °C; (b) 300 °C and (c) 350 °C.(d) Response as a function of H_2S concentration.[93]

are manufactured via screen printing which results in porous thick films. However, this process is time consuming and requires multiple coatings to achieve a sufficient thickness for the film to function effectively as a gas sensor. In addition to this, the ink used contains organic compounds which have to be burnt out, which decreases the sensing ability due to carbon residues on the sensing layer. It is also difficult to control the microstructure and chemical composition of the material.[95,98]

Atkinson *et al.*[99] reported the doping of Cr_2O_3 with TiO_2 produced a solid solution with minimal changes in unit cell volume. The difference in measured density with Ti concentration was consistent with the Ti being dissolved as Ti^{4+} compensated by Cr vacancies. This results in Ti^{4+} acting as *n*-type dopant to a *p*-type chromium oxide. The observation correlated with atomistic simulations of the solid solution which indicated

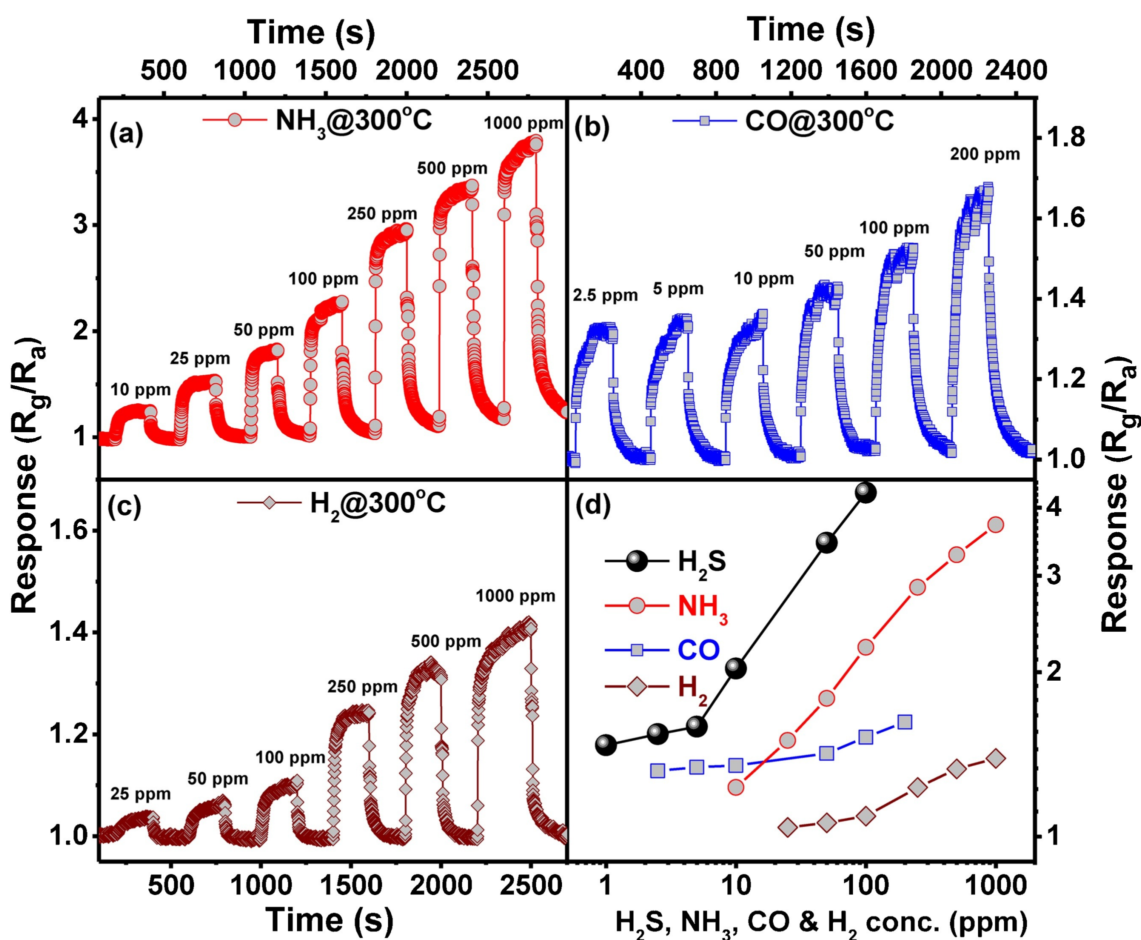

Figure 1.18. Response of mesoporous Co_3O_4 nanochains towards increasing concentration of (a) NH_3; (b) CO and (c) H_2. (d) Response as a function of gas concentration.[93]

that the Ti^{4+} ions and Cr vacancies form low energy complex defects.[99]

Pokhrel *et al.*[100] investigated the sensitivity of $C_{2-x}Ti_xO$ powders ($x \leqslant 0.5$) towards acetone. The sensor displayed a linear increase in response as a function of analyte concentration as well as quick response and recovery time. The stability of the sensor was tested by placing them into a test chamber with 1 ppm of acetone for 144 h. The change in resistance was measured every 24 h and displayed a decrease in relative response was in the form of first order exponential decay. After 144 h, all sensors demonstrated a constant response towards acetone.[100]

1.4 Recent Advances in *n*-type MOS Gas Sensors

In this section, recent *n*-type MOS sensors are explored to look into the sensitivity and selectivity towards VOCs and compare those sensing ability to *p*-type MOS that was explored in the previous section (section 1.3) with same or similar gases that was used to test these sensing material.

Zinc oxide (ZnO) has been extensively researched upon since 1935 and has been a good material to use in the gas sensing industry as it has a good sensing response, good selectivity, is easy to synthesise, low cost, good thermal and chemical stability and non-toxic. ZnO is an *n*-type MOS with a wide bandgap of 3.2 eV to 3.4 eV and a large exciton binding energy of 60 meV at room temperature.[101,102] Heiland discovered in 1954 the correlation between electrical resistance of ZnO and H_2 gas. However it was not until 1962 Seiyama *et al.* used ZnO as a gas sensor towards various VOCs: toluene, benzene, propane, CO_2, ethyl ether and ethyl alcohol.[2,103]

Zhao *et al.*[104] reported in 2015 CVD synthesis of a highly sensitive on-chip zinc oxide (ZnO) nanocomb sensor for the detection of CO at room temperature. Figure 1.19 displays the sensitivity of ZnO nanocombs in air towards a CO concentration of 250 ppm and 500 ppm at room temperature with a relative humidity of less than 10%. The ZnO sensor exhibited similar response at both concentrations; $\sim$ 7.5 at 250 ppm and $\sim$ 8.8 at 500 ppm and also display short response and recovery time.[105] As previously stated in the section above, CuO NCs and NTs were used in the detection of CO and was reported to have a response of just above 2.1 and just below 1.5 for the NTs and NCs respectively to an exposure of 500 ppm of CO. One point to bare in mind is that Hubner *et al.* proposed that the response of a *p*-type MOS sensor to the same concentration of gas analyte is equal to the square root of the response of a *n*-type MOS sensor when the morphology of the sensing material is the same.[104]

Indium oxide (In_2O_3) is a *n*-type MOS with a bandgap of 3.5 eV to 3.7 eV.[106] In_2O_3 has two types of crystalline phases, cubic and rhombohedral. Cubic In_2O_3 has relatively high conductivity and has been used in microelectronic fields, solar cells and flat panel dis-

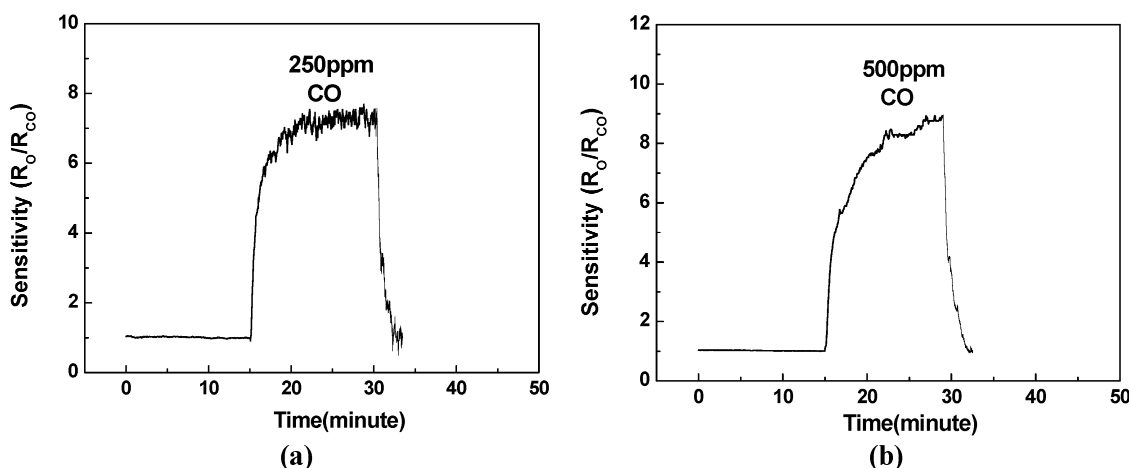

Figure 1.19. ZnO sensitvity response towards CO at room temperature and at a concentration of 250 ppm and 500 ppm.[105]

played units. Various techniques has been used to synthesise In_2O_3 such as; sol-gel, vapour deposition, spin coating, solvothermal, etc.[75] As a gas sensor, In_2O_3 has been widely used for the detection of O_3, NO_2, CO and H_2.[107]

Duan *et al.*[107] reported the fabrication of indium oxide (In_2O_3) nanofibers (NFs) and toruloid nanotubes (TNTs) and their gas sensing properties towards hydrogen sulfide at room temperature. The In_2O_3 nanomaterials were fabricated via a conventional electrospinning process and was calcined in air at 550 °C for two hours. Figure 1.20a) displays both NFs and TNTs sensors response towards 50 ppm H_2S at an operating temperature between 25 °C to 300 °C in dry air. At room temperature, the sensors exhibited a high response towards H_2S with an R_a/R_g of ~ 230 for NFs and ~ 280 and ~ 330 for TNTs one and two respectively. As operating temperature rises towards 300 °C, sensitivity dramatically decreases. Figure 1.20b) displays the response and recovery times of the In_2O_3 NFs and TNTs at room temperature. The response times of In_2O_3 NFs, TNTs one and two were 78 s, 62 s and 45 s respectively and the recovery times were found to be about 90 s, 107 s and 127 s respectively. In_2O_3 TNTs demonstrated a higher and more rapid response at room temperature towards 50 ppm H_2S; which could be due to the difference in surface area as TNTs have both inner and outer surface which could provide more active sites.[107,108] Co_3O_4 Nanochains that were explored previously demonstrated a response of roughly between 2.5 and 3.5 R_g/R_a, with an operating temperature between 250 °C to

350 °C towards 50 ppm of hydrogen sulfide.

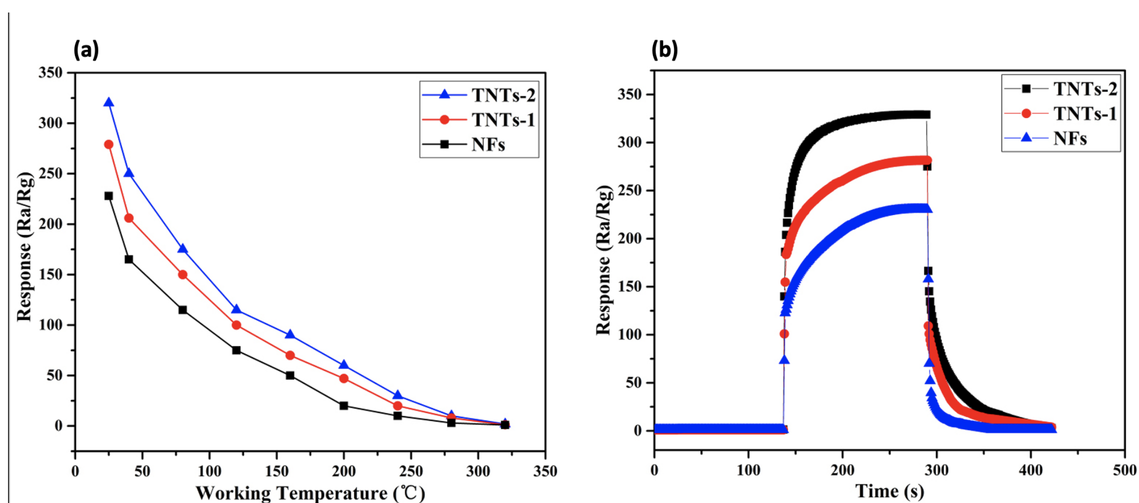

Figure 1.20. (a) In_2O_3 NFs and TNTs sensor response towards 50 ppm of H_2S as a function of working temperature and (b) In_2O_3 NFs and TNTs sensor response towards 50 ppm of H_2S as a function of time.[107]

Cerium oxide (CeO_2), an *n*-type semiconductor has a wide bandgap, high temperature stability, low redox potential to easily change oxidation states (Ce^{4+} and Ce^{3+}) and low cost.[109,110] Due to these properties, it has been used in several areas of research such as organic free dye solar cells, photoelectrode, energy and enviromental process and catalysis.[111,112] CeO_2 has recently been explored as a gas sensing material and has shown some promising results, displaying sensitivity towards to a range of reducing and oxidising gases such as: CO, SO_2, H_2S, EtOH, H_2 and NO.[113–115]

Yu and Lee *et al.*[116] recently reported the synthesis of CeO_2 nanoparticles (NPs) and its enhanced ethanol gas sensing capabilities. CeO_2 was synthesised via hydrothermal conditions with the use of ionic liquids and calcined at 600 °C for two hours. Ionic liquids have low surface tension causing high nucleation rates, which reduces the size of the particles leading to an increase in surface area. Ionic liquids can also act as an electrostatic and a steric stabilising agent, slowing down particle growth. Commerically bought CeO_2 and synthesised CeO_2 NPs were exposed to ethanol and compared. Figure 1.21a depicts the sensors reponse as a function of operating temperature towards 100 ppm of ethanol. the graph also demonstrates CeO_2 NPs produce a better response than commerical CeO_2 towards ethanol at all operating temperature tested. The optimum operating

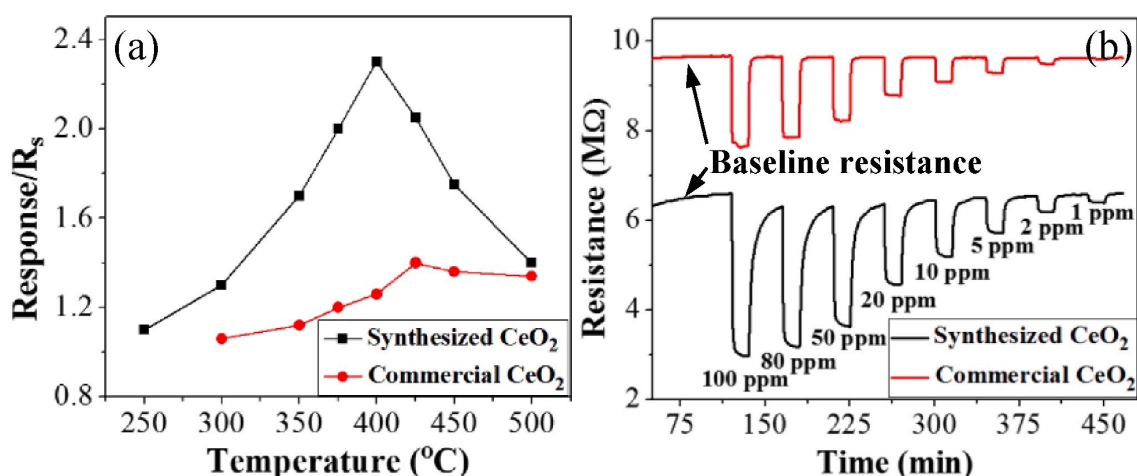

Figure 1.21. (a). Response towards 100 ppm ethanol at varying operating temperatures; (b). Response towards varying concentrations of ethanol at optimum operating temperatures.[116]

temperature was shown to be at 400 °C for CeO_2 NPs and 425 °C for commerical CeO_2, with a response of 2.3 and 1.4. When operating temperature passes 400 °C, response towards ethanol decreases dramatically. The reason for this could be a decrease in concentration of oxygen vacancies as temperature increases. Figure 1.21b depicts both sensors response at their respective optimum temperature at a decreasing concentration of ethanol (100 ppm to 1 ppm). Both sensors displayed the same trend in response, high reponse towards high concentration of ethanol and a decrease in response as concentration drops towards 1 ppm. As reported, synthesised CeO_2 NPs outperformed commerical CeO_2 in at varying concentrations of ethanol. At 1 ppm CeO_2 NPs displayed a change in resistance, whereas commerical CeO_2 displayed little to no change in resistance at low levels of ethanol.[116]

Titanium dioxide (TiO_2), an *n*-type MOS has three different crystalline phases; rutile, anatase and brookite with a bandgap of 3.0 eV, 3.2 eV and 3.13 eV to 3.40 eV respectively. The three polymorph displays different gas sensing properties with a decrease in sensitivity upon a change in phase from anatase to rutile. Anatase and brookite phases are thermodynamically metastable and irreversibly convert to rutile at high temperatures (600 °C to 1000 °C).[117] In its rutile phase, it is metastable above 800 °C and is used as an oxygen gas sensor for automotive air:fuel reatio control.[118] TiO_2 is very abundant in earth,

making it an inexpensive material, it is also non-toxic, chemically stable and environmentally friendly.[119,120] It is one of the most studied materials and is widely used in various applications such as sensors, photocatalyst, reduction of CO_2, production of H_2 and solar cells.[121–124]

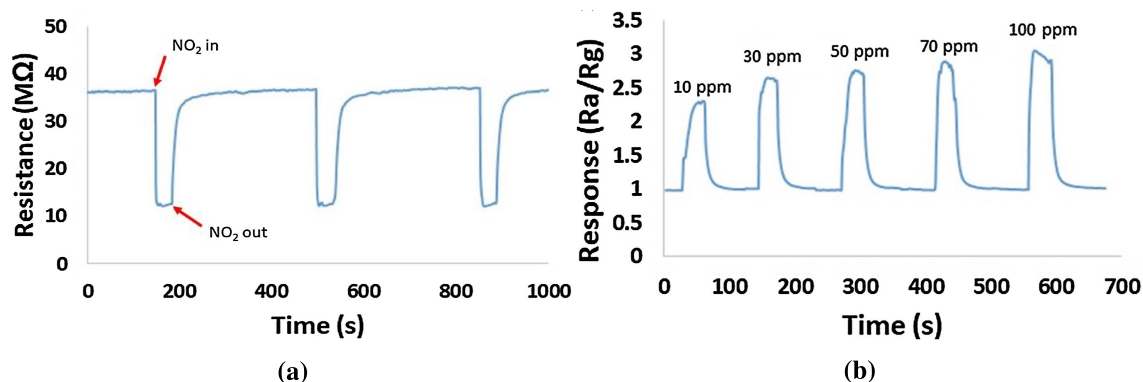

Figure 1.22. (a). Resistance of TiO_2 NWs at room temperature and 100 ppm NO_2; (b). Response of TiO_2 NWs towards at room temperature and varying concentrations of NO_2.[125]

Wu *et al.*[125] prepared titanium dioxide (TiO_2) nanowires (NWs) for the detection of nitrogen dioxide (NO_2). TiO_2 NWs were prepared via hydrothermal process and sintered at 500 °C for one hour in air. The NWs were shown to have a high response towards 100 ppm of NO_2, relatively humidity of 50% and at room temperature. The sensor gave a response of ~ 3 R_a/R_g. The response and recovery times were 10 s and 19 s respectively. Different levels of NO_2 concentrations were investigated from 10 ppm to 100 ppm; the response did increase as the concentration of analyte increased but the changes in response was small, suggesting that the TiO_2 NWs sensor can be reliably used to monitor the concentration of NO_2 within this range with minimal changes in response.[125]

Vanadium oxide, a transition metal has different oxidation states ($2^+ – 5^+$) and forms a variety of oxides.[102] Out of all the oxides, V_2O_5 is the most frequently studied oxide for the detection of combustible and toxic gases.[126,127] Chemically speaking, V_2O_5 is a great catalyst candidate due to the variety of oxidation states vanadium has to offer and the different oxygen coordination geometries it has. V_2O_5 thin films have been prepared on different substrates by a wide range of techniques, such as; CVD, spray pyrolysis, sol-gel and spin coating.[128]

Rayappan *et al.*[129] reported the synthesis of flower-liked nanostructured V_2O_5 thin

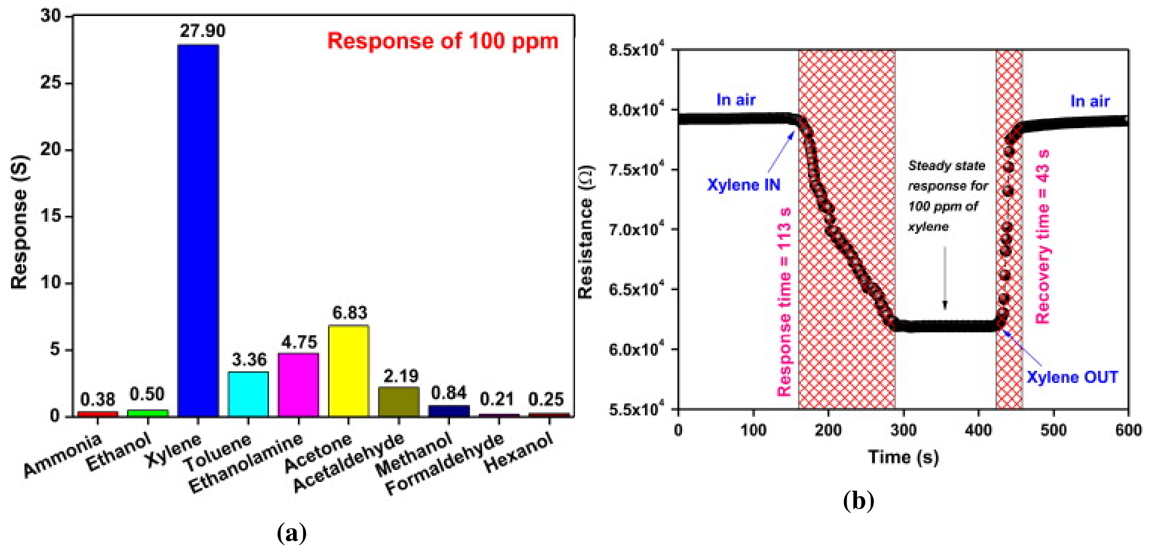

Figure 1.23. (a). V_2O_5 response towards different VOCs at room temperature and concentration of 100 ppm; (b). Resistance of V_2O_5 towards 100 ppm of xylene at room temperature.[129]

films and its sensing capabilities at room temperature; the thin films were deposited via spray pyrolysis. Figure 1.23a displays the response of V_2O_5 thin films at room temperature and dry air towards various VOC vapours at a concentration of 100 ppm. The film has shown to be highly sensitive and selectivie towards xylene at room temperature. It also shows promising response towards other VOCs such as toluene, ETA and acetone. Figure 1.23b illustrates the response and recovery time of V_2O_5 towards 100 ppm of xylene at room temperature, displaying a response and recovery time of 113 s and 43 s respectively. Response $(S) = R_a/R_g$ if $R_a > R_g$.[129]

1.5 Engineering of MOS Sensors

There are a wide range of techniques to produce semiconducting metal oxide gas sensors, such as screen printing, sol-gel techniques, physical vapour deposition (PVD), microwave-assisted and solvothermal techniques and chemical vapour deposition (CVD). However, certain factors must be considered upon the selection process which is listed below:[130]

1. Cost – If the material is expensive then the demand for it will be considerably lower and hence will have limited application.

2. Purity – A slight change in the materials compositions may lead to a significant effect on the performance of the sensor.

3. Porisity – A highly porous material will have a greater surface area for gas interaction, leading to a better response.

1.5.1 Screen-printing

Screen-printing technique is an inexpensive, highly reliable and reproducable method to produce sensors and is mainly used in industry to produce commerical metal oxide semiconducting gas sensors.[131] The process involves pushing ink through a porous mesh or layer which matches the layout of the substrate. The ink contains the metal oxide material in a viscous vehicle and injected on to the surface of the substrate. Once the ink has been injected, the print is heated to remove the viscous vehicle, leaving the metal oxide only on the surface.[130,132]

1.5.2 Sol-gel Techniques

Sol-gel technique (diagram displayed in figure 1.24) is a wet-chemistry process, widely used in glass and ceramics sector. The system uses the formation of collodial suspension of starting material particles (sol), which goes under gelation (gel) where cross linkage happens between the other particles giving rise to new material with various different properties.[133,134] For example, with ceramic film formation, the sol evaporates which gives highly porous xerogel film. When this is heated, the film forms a dense material on the surface of the substrate.[130] Tungsten oxide thin films embedded on a gold electrode were made via this method and was shown to have sensing properties towards gaseous trimethylamine (TMA) (100 ppm) at low operating temperatures (70 °C) with a R_g/R_a value of roughly three.[135]

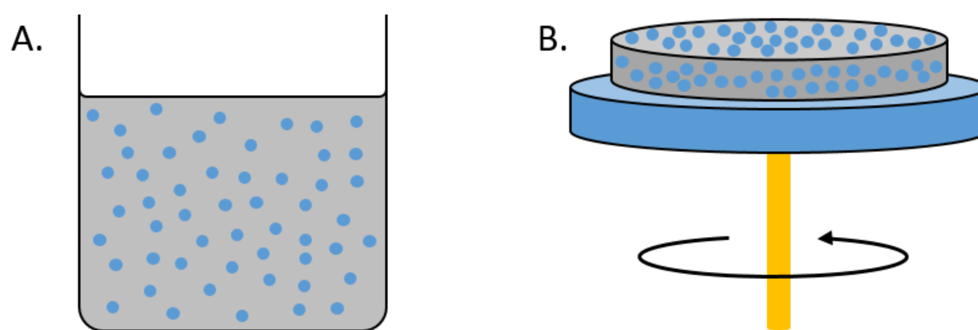

Figure 1.24. Schematic diagram of the sol gel technique: A. the colloidal suspension in the sol, and B. sol spun to form gel.[136]

1.5.3 Microwave-assisted and Solvothermal Techniques

Microwave-assisted system has been slowly gaining interest due to the rapid rate of synthesis (i.e. due to the easiness of elevating the temperature beyond the boiling point of the solvent) and a more efficient internal heating the reaction as heat is generated throughout the volume of materials.[137] The advantage of using this method is it can synthesise materials with small size, high purity and no negative effect such as thermal gradient effect when scaling-up the reaction.[138,139] Cirera *et al.* reported the formation of gas sensors based on SnO_2 via microwave-asssisted synthesis and has indicated the feasibilty of the gas sensor has improved with the use of microwave-assisted SnO_2.[140]

Solvothermal method (diagram displayed in figure 1.25), is similar to that of hydrothermal and is carried out in a closed vessel under an autogenous pressure, usually above the boiling point of the solvent. Many starting materials can undergo quite unexpected chemical changes under solvothermal conditions, which are often accompanied by the formation of nanoscale morphologies. High boiling organic solvents have been used for solvothemal reactions and mixtures of solvents have been used to avoid the problem of solubility of different starting materials.[77,141] An example of this is CuO nanoparticles and cloudlike nanostructures. These nanostructures were formed in conditions of either 12 or 24 hours and either 120 °C or 150 °C. Figure 1.26 illustrates the nanostructures that were formed. These nanostructures displayed gas sensing abilities towards CO, which show a sensivity of about 9 R_a/R_g and a working temperature of 300 °C and 400 ppm concentration of CO.[77]

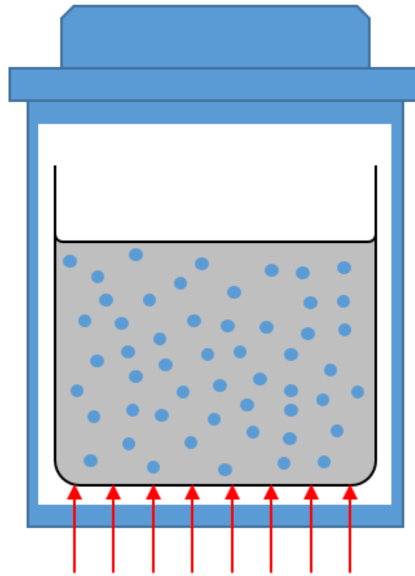

Figure 1.25. Schematic diagram of the solvothermal technique, where the red arrows represent external heating.[136]

1.5.4 Physical Vapour Deposition (PVD)

Physical vapour deposition (PVD) is commonly used for metals and semiconducting metal oxide processes under high vacuum, using evaporation or sputtering techniques to remove materials from the sputter target or crucible, depositing it onto a substrate. This technique is particlularly useful due to its properties:[142]

- Thickness layer ranges from tens of nanometres to tens of micrometres.
- Layers are uniform and reproducible.
- Multilayer systems can be done in one process and there is no limitation in choice of starting material.
- Operating temperatures are kept low (room temperature) and rarely exceeds 350 °C during deposition process.
- The properties of the layers can be modified by altering the parameters used in this technique.

Vapour evaporation is when the starting material is heated at high temperature either via resistive heating or by electron beam kept under vacuum until a sufficient amount

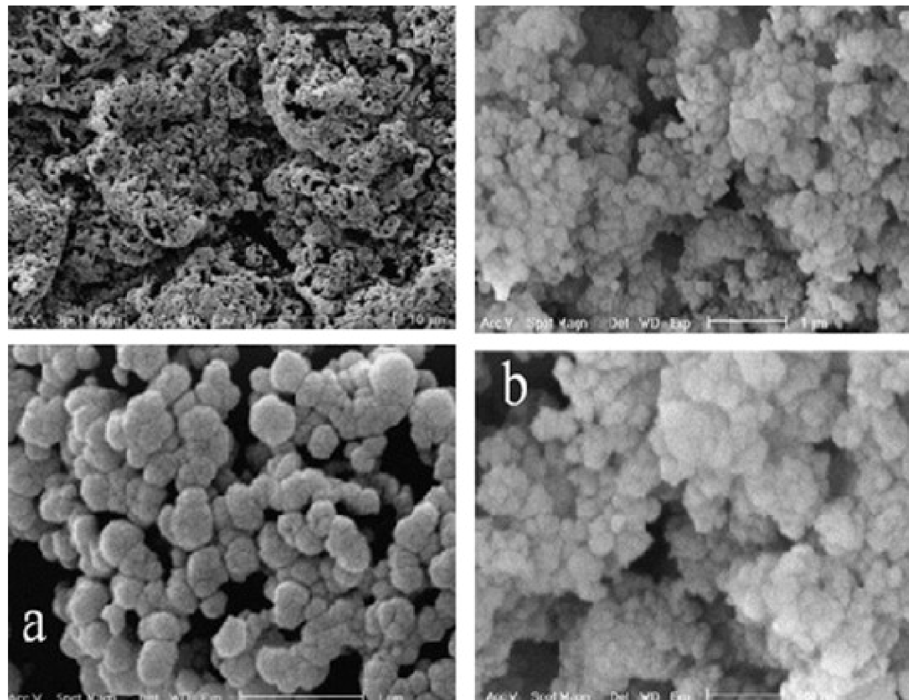

Figure 1.26. SEM images of CuO nanostructures.[77]

of vapour pressure is reached; the particles are then transported and condensed onto the substrate. Problems arise with the use of resistive heating such as contamination of the layer and limited thickness; whereas with electron beam, it is highly efficient in heating the starting material and has good thickness and uniform layers.[143,144]

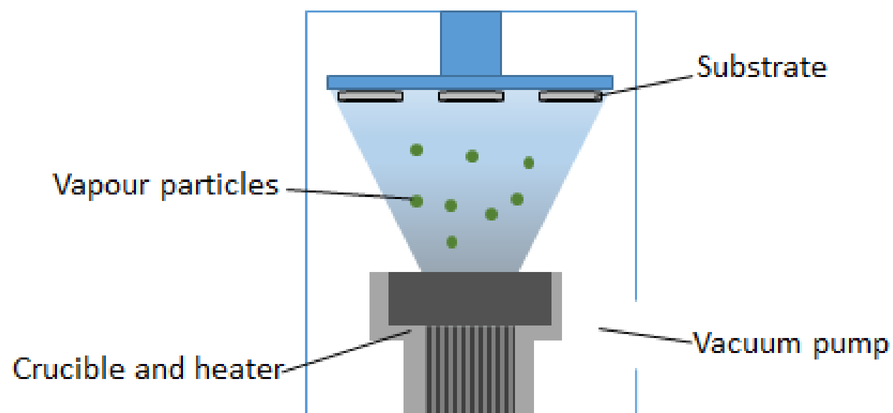

Figure 1.27. Schematic diagram of vapour evaporation.[142]

Sputtering is a plasma process which accelerates Ar^{+} gas ions towards the cathode target, removing the particles from the materials as vapours. The particles then condense onto the substrate. There are many different types of sputtering as shown in figure 1.28.

The main difference between evaporation and sputtering are that sputter atoms have a impact energy of 3 eV to 10 eV compared to 0.2 eV to 0.26 eV for evaporation.[142,145]

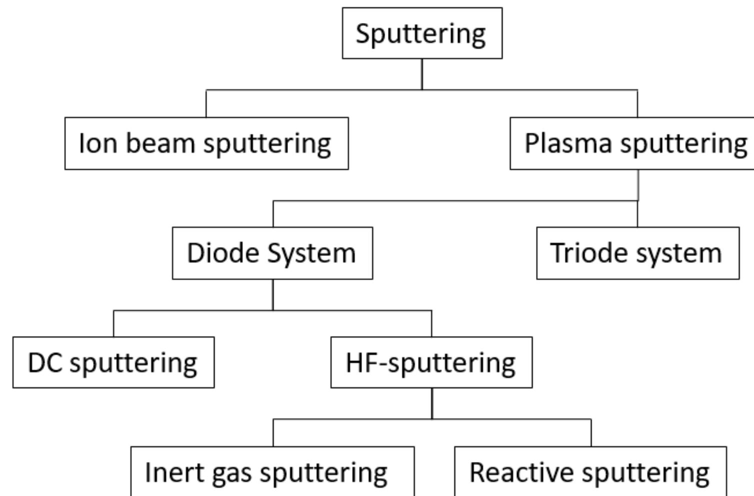

Figure 1.28. Types of sputtering processes.[142]

Direct Current (DC) sputtering is widely used for semiconducting metal oxide materials whereas this is not in the case of non-conducting material due to a reduction of negative potential. Therefore, the acceleration potential for Ar^+ ion breaks down. Magnetron sputtering can be used with DC sputtering side by side, it increases the number of electron via an electromagnetic field which contributesd to the ionisation of Ar^+ ions. As the electrons deflect at a less of an angle than the ions, the electrons has a closer target which leads to a increase probability of ionisation and higher sputter rate.[146,147]

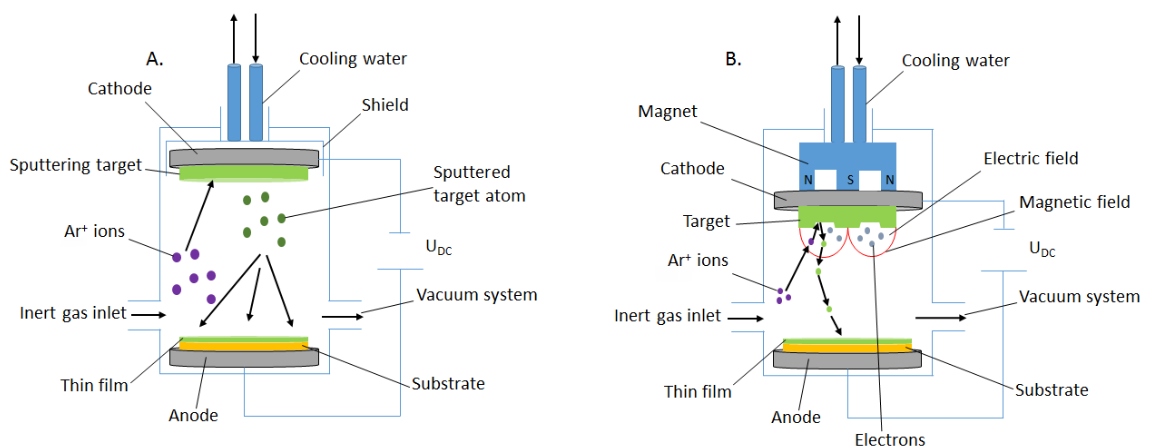

Figure 1.29. Schematic diagram of A. DC sputtering and B. Magnetron Sputtering.[142]

1.5.5 Chemical Vapour Deposition (CVD)

Chemical vapour deopsition (CVD) is the dissociation or chemical reaction of gaseous starting material in an activated environment to form a stable solid product. Deposition occurs either in a homogeneous gas phase reaction or heterogeneous chemical reaction in the proximity of a heated surface. CVD can be used in various applications such as electronic materials, coating and ceramic fibres due to the following advantages:[148]

- Produces highly dense, uniform and pure materials which are reproducible.
- Good control over the crystal structure and surface morphology by altering the CVD parameters.
- Inexpensive for conventional CVD process.
- Can use a wide range of precursors.
- Low deposition temperatures.

However there are certain drawbacks as well:

- The use of corrosive and toxic materials that are harmful to the environment.
- Difficult to deposit multiple materials in stoichiometric amounts as they have different properties.
- Sophisticated reactor and vacuum system such as plasma assisted CVD increases the cost of production.

A different type of CVD process known as aerosol-assisted CVD (AACVD), provides a method of synthesising metal oxide nanostructures for gas sensors. AACVD have the same advantages as conventional CVD and also overcomes the drawback of depositing multicomponent materials in stoichiometric amounts as AACVD relies on precursor solution concentrations and hence the stoichiometric amount can be calculated. Other advantages include; low cost of deposition due to the a simplistic vapour precursor generation and rapid formation at low temperatures due to small diffusion distance.[132,150,151]

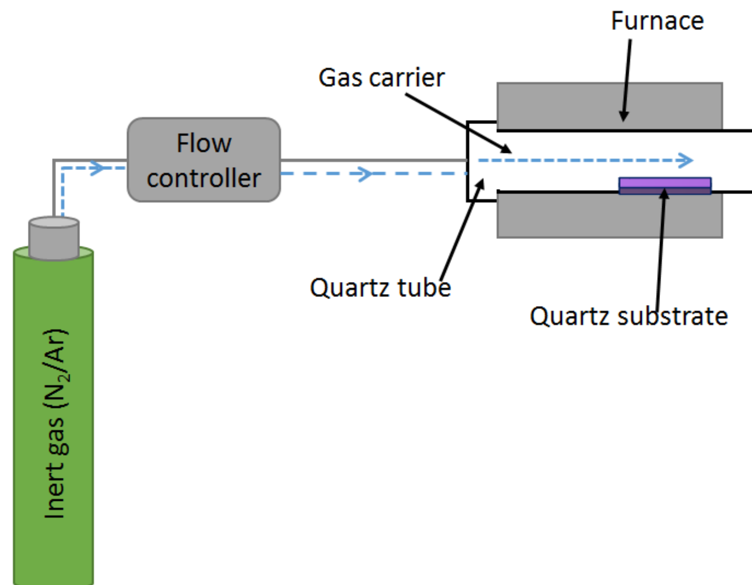

Figure 1.30. Schematic diagram of a simple thermal CVD reactor.[149]

AACVD, as shown above have many advantages which makes it an attractive technique industrially. As the system can be carried out under atmospheric pressure, the rate of deposition can be several magnitudes higher than that of high vacuum techniques. AACVD also reduces the importance of the requirement for high volatility precursors.[150]

The basis of AACVD is the atomisation of a precursor solution which is transported by a flow of inert carrier gas to the substrate. The solvent then undergoes rapid diffusion, forming precursor vapours; at elevated temperatures, the vapours starts to react and decompose forming a thin film on the substrate. If the aerosol droplet reaches the substrate before it evaporates and vaporises, a spray pyrolysis process occurs rather than a CVD reaction. Suitable solvents for atomisation provides high solubility of the precursor, low vapour pressure and viscosity. The atomisation of the precursor solution can be achieved by using different types of aerosol generators such as pneumatic aerosol jet, electrostatic atomisation and ultrasonic aerosol generation.[150,151]

Two different types of reaction (homogeneous and heterogeneous) can occur in the CVD reactor depending on the parameters. Heterogeneous reaction is when the vapourised precursor is absorbed onto the surface of the substrate, forming thin films; whereas a homogeneous reaction occurs when temperture is too high, the precursor decomposes too

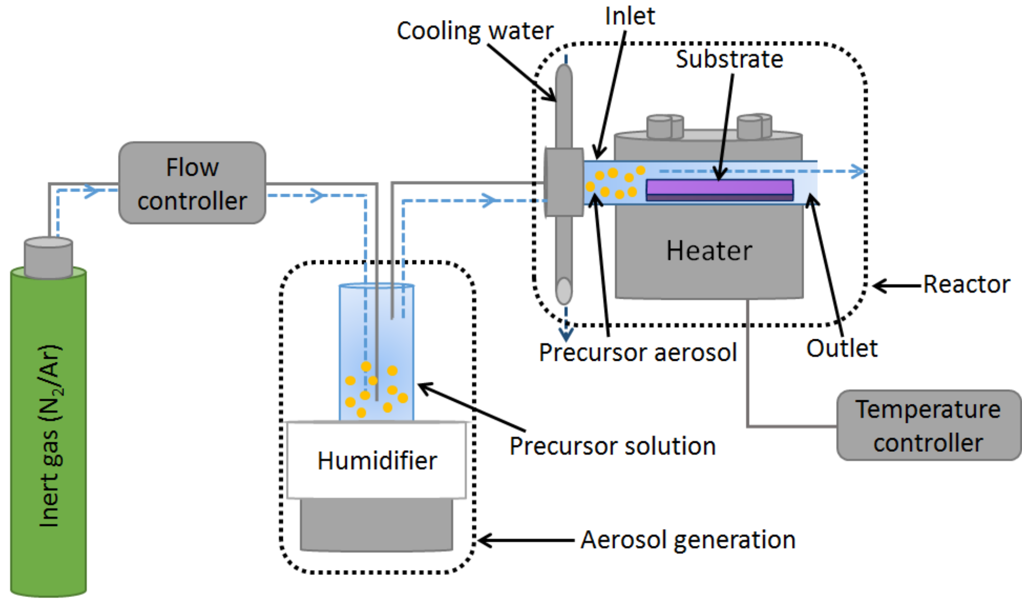

Figure 1.31. Schematic diagram of an aerosol-assisted CVD.[152–155]

early causing homogeneous nucleation forcing fine particles, leading to the formation of porous films.[150]

There are various methods for aerosol generation producing different size of droplets which effects the production rate. One method is ultrasonic aerosol generation which uses a piezoelectric transducer underneath a liquid precursor. The properties of this method is dependent on the nature of the precursor, the intensity and frequency of the ultrasonic beam.[156] The wavelength (λ) is described using Kevin's formula (equation (1.1)), where f, ρ and γ are the exication frequency, density and surface tension respectively. The diameter of the droplet was defined by R. Lang in 1962 using a empiric formula (k = constant) shown in equation (1.2), where the diameter of droplet is a function of $\lambda(d_{\mathrm{d}} = k'\lambda)$.[157]

$$\lambda^3 = \frac{2\pi\gamma}{\rho f^2} \tag{1.1}$$

$$d_{\mathrm{d}} = k[\frac{2\pi\gamma}{\rho f^2}]^{\frac{1}{3}} \tag{1.2}$$

Electrostatic atomisation is another method to generate aerosol which is done by applying an electrical potential to a cylinderical spray nozzle causing fine charged spray

droplets, forming stable spray cones (Taylor cones). These cones are formed when the surface tension of the precursor balances with an electric force under an electric field.[158]

1.6 Micro-electro-mechanical systems (MEMS)

Ceramic substrate (commonly alumina) based MOS sensors still has a large commercial market due to low cost, ease of fabrication, chemical stability and robustness of the substrate (sensor can be made via screen-printing). However, there are two main limitations of ceramic sensors which are, complicated mounting process of the sensor and power dissipation (∼0.5 W to 1.0 W) which restricts their usage in portable, battery driven and high temperature applications.[159] Therefore, Micro-electro-mechanical system (MEMS) technologys have been a hot topic of discussion and research over the last decade, in particular MEMS based gas sensors, which have been extensively researched. This is due to the continuous drive to advance miniaturised gas sensors for the development of electronic nose devices (E-nose) in various fields such as food quality, health and indoor air contaminants and hence the design and assembly of miniaturised gas sensors are crucial.[160–162] MEMS miniaturised heating element (micro-hotplates) can operate at high temperatures quickly and preserve power consumption (mW ranges) due to its low thermal mass.[6]

Table 1.6 shows a list of companies (Ams AG, Bosch Sensortec, Figaro and Sensirion) and their successfully developed MEMS based MOS sensors for the detection of VOCs and indoor air quality. It also depicts the size of each device, target gas, power consumption, the type of package and interface it uses. The demand for continuous reduction in power usage and miniaturisation have driven the research of MOS sensors towards direct integration of the MEMS sensing layer/structure with integrated circuits for signal conditioning circuits.[6] The integration can happen via multi-chip approach, where the sensor and circuits are designed and generated on separate chips. This method can enable independent optimisation of the MEMS sensor and the MOS sensing layer circuit. Another advantage of this method is its less time consuming on the development side and can have a more flexible design. However, due to the complex packaging and wire bonding, it is

expensive. Another option is the monolithic approach; a more advanced way to integrate MOS circuits and MEMS sensors where both the sensor and circuits are designed and generated on a single substrate. This approach enhances the sensors peformance by reducing its size and power usage.[163]

The structure of a traditional screen printed ceramic MOS sensor was briefly described in section 1.2 and illustrated in figure 1.5. The MOS sensor consist of a sensing layer, gold electrode layer on a ceramic or alumina substrate. If the sensor was a double sided wafer, the heating electrode would be at the bottom and is usually made of platinum. For MOS MEMS sensors, they usually consist of a thin suspended membrane which contains the sensing material on top, micro-electrodes for electrical resistance changes of the sensing material and a micro-heating element. The thin membrane is an insulating layer which is made of either silicon dioxide (SiO_2 or nitride (Si_3N_4). This insulating layer also helps prevents catalytic interaction between the heater material and target gas. A simple structure of a MEMs sensor is depicted below in figure 1.32.[6,164]

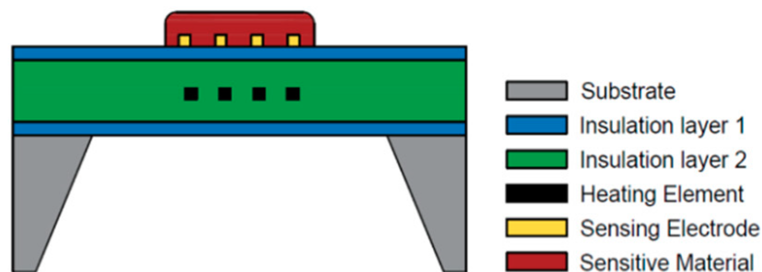

Figure 1.32. SSchematic diagram of a simple MEMs sensor structure.[6]

Table 1.6. Specification of commercial MOS MEMs-based sensors.[6]

Comnpany	ams AG			Bosch Sensortec	Figaro	Sensirion
Product Number	iAQ/core P	CCS811	AS/MLV/P2	BME680	TGS8100	SGPC2
Device Diameter (mm)	15.24×17.78	$2.7 \times 4 \times 1.1$	$9.1 \times 9.1 \times 4.5$	$3.0 \times 3.0 \times 0.93$	$3.2 \times 2.5 \times 0.99$	$2.45 \times 2.45 \times 0.9$
Target Gas	CO_2, TVOCs [a]	CO_2, TVOCs	VOCs	TVOCs	H_2, EtOH	TVOCs
Power Usage	9 mW	1.2 mW to 46 mW	34 mW	<0.1 mA [b]	15 mW	1 mA [c]
Voltage (V)	3.3	1.8 to 3.6	2.7	1.2 to 3.6	1.8	1.62 to 1.98
Package	SMD [d]	LGA [e]	–	LGA	Ceramic	DFN[f]
Interface	I^2C [g]	I^2C	Analog	606	I^2C and SPI [h]	I^2C

[a] Total concentration of VOCs in ambient conditions
[b] Sleep mode
[c] Low power mode
[d] Surface-mounted Device
[e] Land Grid Array
[f] Dual Flat No-leads
[g] Inter-integrated circuit
[h] Serial Peripheral Interface

Chapter 2

Gas Sensing Mechanism

In ambient air, oxygen gas is absorbed onto the surface of the oxide, which serves as a trap for electrons from the conduction band for *n*-types and from the valence band for *p*-types, resulting in the formation of chemisorbed oxygen species (O_2^-, O^- and O^{2-}). The oxygen ion species O_2^-, O^- and O^{2-} are stable below 100 °C, between 100 °C to 300 °C and above 300 °C respectively.[165,166] The proposed reactions forming these species are shown below:

$$O_{2(g)} \longleftrightarrow O_{2(abs)} \quad (2.1)$$

$$O_{2(abs)} + e^- \longleftrightarrow O_2^- \quad (2.2)$$

$$O_2^- + e^- \longleftrightarrow 2\,O^- \quad (2.3)$$

$$O^- + e^- \longleftrightarrow O^{2-} \quad (2.4)$$

As previously discussed, MOSs based gas sensors are promising materials due to their high sensitivity, low cost and large number of gases detected.[47,64,167] So far, *n*-type MOS such as SnO_2, ZnO, TiO_2 and WO_3 have been used for the detection of gases due to their high sensitivity and rapid response time.[168–170] Currently, *p*-type MOSs are less used and developed than *n*-types; even though *p*-types exhibit advantages over *n*-type materials in gas sensing applications, for instance *p*-types have a characteristic oxygen adsorption property which can be used to design high performance gas sensing showing rapid recovery

kinetics and humidity tolerance.[171–173] They also show less temperature dependence for their conduction at high temperature ranges. *P*-type materials exhibit relatively high ambient or thermal stability, this is due to their tendency to exchange oxygen from its lattice with air as they have multiple stable oxidation states and high positive hole concentration. These characteristics are desirable for the development of high performance VOC sensors. However, several issues needs to be addressed for the use of *p*-type MOSs in VOC sensing, including optimising sensitivity, response and recovery time.[64,174]

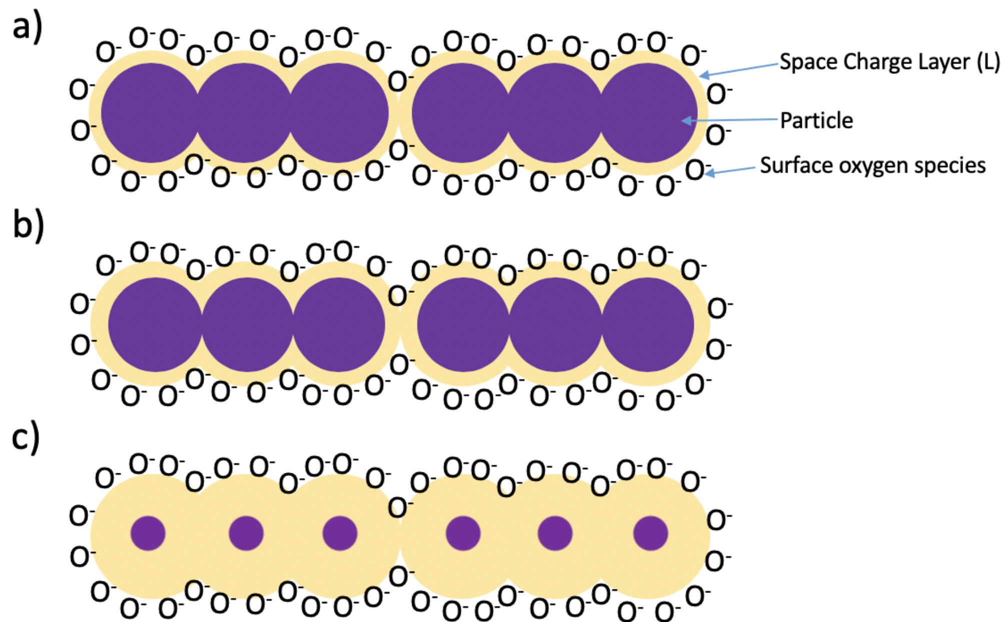

Figure 2.1. Schematic model of grain size effect on MOS sensors: a) Boundary controlling ($D >> 2L$); b) Neck controlling ($D \geq 2L$); c) Grain controlling ($D < 2L$).[12,55,175]

A way to improve the sensitivity for MOSs would be to reduce the grain size to the nanoscale. Figure 2.1 depicts a schematic grain model of three different types: $D >> 2L$, $D \geq 2L$ and $D < 2L$ where D is is the particle size and L is the space charge layer. When the grain size is large ($D >> 2L$), the grain are unaffected by surface interaction of the gas and the conductance is limited by the schottky barrier. This is known as boundary controlling model. When $D \geq 2L$, the space charge layer around the necks forms a conduction channel. The conductivity is limited by the cross sectional area of necks between the grains which leads to an enhanced sensitivity. This is known as neck control model. For $D < 2L$, the space charge layer is fully extended throughout the whole grain, which

leads them to a almost full depletion of mobile charge carriers. This causes a dramatic decrease in conductivity as there is a lack of significant barriers for the interconnected grain charge transport. This is known as grain controlling model. Sensitivity becomes dependent in the grain size, sensivity increases as grain size becomes smaller, however dramatic decrease in grain size leads to a decrease in structrual stability.[12,55,175] However, the manufacture of a stable MOS nanostructure smaller than a couple of nanometres is still a challenge as it is difficult to precisely controlling grain growth to within a few nanometres whilst maintaining porosity and thermal stability.[85,176]

The mechanism of gas sensing have long been debated and described. Herein, two different models are explored below, band bending and surface trap limited model. The concept of band bending was first developed by Schottky and Mott.[177–180] Band bending is when there is an upwards bend on the surface of the MOS causing a electron depletion layer for *n*-types and holes accumulation layer for *p*-types. For surface trap limited model, the sensing mechanism is described in terms of kinetics and in a equilibrium process.

2.1 Band Bending Model

In this section, the mechanism is described as a change in conductivity via band bending, using SnO_2 as an example, to understand the influence of morphology and how conduction occurs in the sensing layer. Interaction of gases may happen on different sites of the structure depending on type of morphology. There are two distinct types, compact layers which takes place only at geometric surfaces which are typically obtained with thin films and porous layers which takes place throughout the volume of the layer such as the surface of individual grains, grain to grain boundaries, between grains and electrodes and grains and substrates. Porous layers are typically obtained with thick films.

For compact layers, there are another few possibilities, completely and partially depleted layer which are dependent on the ratio of layer thickness and Debye length. For a partially depleted layer, when the surface reactions do not affect the conduction of the entire layer, i.e. the layer thickness is greater than the depleted surface layer, the conduction

process will take place in the bulk region as it's more conductive for an n-type material like SnO_2.

The assumption for compact layers are that the constant material properties do not depend on the process by which the layer is formed and hence ensures a surface layer and a bulk layer. The electrical current will therefore flow parallel to the surface and the conduction process takes place in the lower resistive bulk area. However, this is then indirectly influenced by the modulation of the low resistive cross section area and explains why the relative resistance changes for such kinds of layer are low.

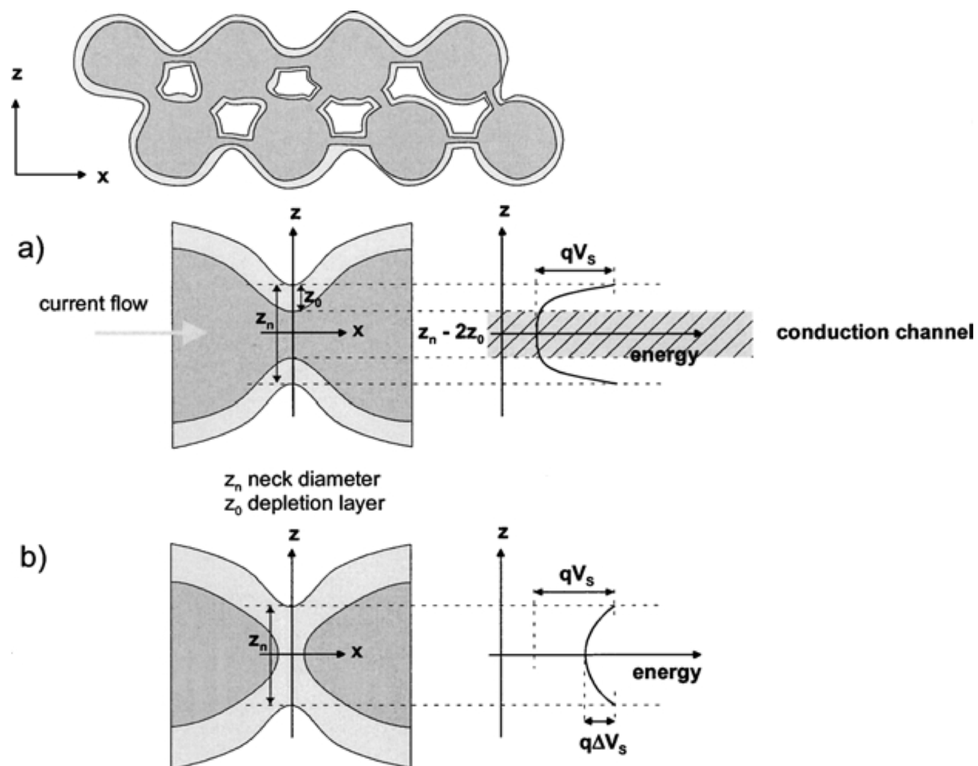

Figure 2.2. Schematic diagram of porous sensing layer, where a). Open neck, where its partially depleted and b). Closed neck where its fully depleted. z_n is the neck diameter[181]

For porous layers (figure 2.2), the gas species can penetrate into the bulk, which makes the active surface much deeper and hence it is possible for the porous layer to have contributions from; surface or bulk i.e when the neck diameter is greater than the depletion layer, grain boundaries for large grains not sintered together and finally flat bands for small grains and necks. For small grains and necks, when the mean free path and free charge carriers becomes carriers, one has to take surface influence on mobility into consideration.

This occurs as the number of collisions by free charge carriers in the bulk becomes comparable with surface collision. The electrical current is forced to cross the surface, passing from one grain to another and is directly influenced by the energy barriers between the grains. These are the few reasons why *n*-type MOS sensors are obtained by using porous thick film layers displays some of the best sensing results.

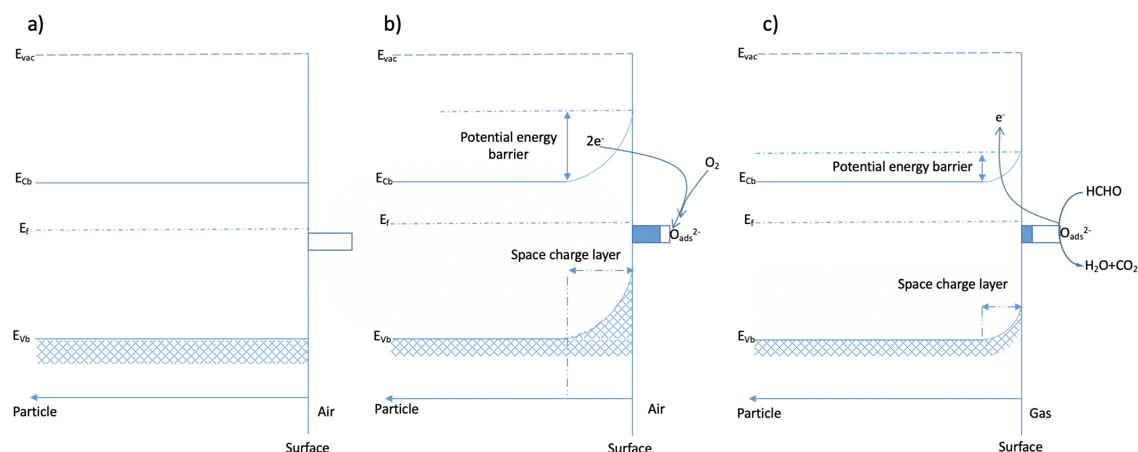

Figure 2.3. Schematic diagram of band bending model reaction mechanism towards formaldehyde for a *n*-type material, where: a) Flat bend prior to any surface reaction; b) In air; c) In gas.[181–183]

For an *n*-type semiconductor, when sensors are exposed to air, oxygen is adsorbed onto the surface of the oxide which creates a potential barrier. The oxygen molecule interacts with the surface of the oxide, forming charged oxygen species (O_2^-) via redox reaction from the conduction band. This leads to a space charge layer (electron depletion region) and band bending on the surface of the MOS. The resistance of the sensors is dependent on the size of the potential barrier formed on band bending, i.e. an increase in band bending leads to a increase in resistance.[12,181]

Figure 2.3 illustrates the detection of formaldehyde (HCHO). When formaldehyde is exposed to the sensor, it reacts with adsorbed oxygen species on the surface of the MOS, and releases the trapped electrons back into the conduction band of the sensing material. This increases the charge carrier density and hence reduces the thickness of the space charge layer and decreases the potential barrier and resistance.[182,184–186] This is described below:

$$HCHO_{(g)} \longrightarrow HCHO_{(ads)} \quad (2.5)$$

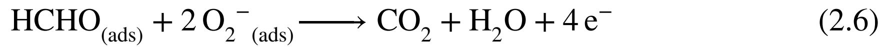

$$HCHO_{(ads)} + 2\,O_2^-{}_{(ads)} \longrightarrow CO_2 + H_2O + 4\,e^- \quad (2.6)$$

All modelling such as sensing and transduction has been based on experimental and theoretical knowledge of tin dioxide, an inherent *n*-type material. Whereas for *p*-type materials, there has been limited knowledge in how sensing arises. Pokhrel *et al.* has recently investigated how surface reaction induced electrical changes affect the sensors signal of *p*-type thick porous layer of chromium oxide. In general, upon exposure to a reducing gas, *p*-type sensors would display an increase in resistances. This correlates accordingly to the mechanism in which ionosorbed oxygen acts as a surface acceptor. These oxygen species determines the appearance of an accumulation layer for holes that has a lower resistivity if compared to the bulk. The changes on the surface sites are due to the interaction between the surface acceptor and the electrons from the valence band. These electrons will be trapped on the surface, causing additional holes. In terms of energy band representation as shown in figure 2.4, this is described as an upwards band bending governed by the overall negative charge present on the surface as the electron are trapped there. This overall charge is in turn compensated by the overall holes present on in the accumulation layer. E_{CS} is the energy of surface condution, E_{AS} is the energy of surface acceptor, E_{VS} is the energy of surface valence.[183,187]

In general, when a metal oxide is exposed to a reducing gas (e.g. ethanol), a decrease in the concentration of ionosorbed oxygen is observed, the freed electrons will go back to the valence band and decrease the concentration of holes. In terms of energy band representation (shown in figure 2.5), a decrease in the overall surface negative charge leads to a decrease in band bending and hence the resistivity in the accumulation layer will also decrease. Therefore, when exposed to ethanol in air the total sensors resistance will increase. Two aspects can be affected by surface reactions, electron affinity and band bending. Where the former can be influenced by changes in surface dipole such as hydroxyl group and for the latter, it can be influenced by surface charges.

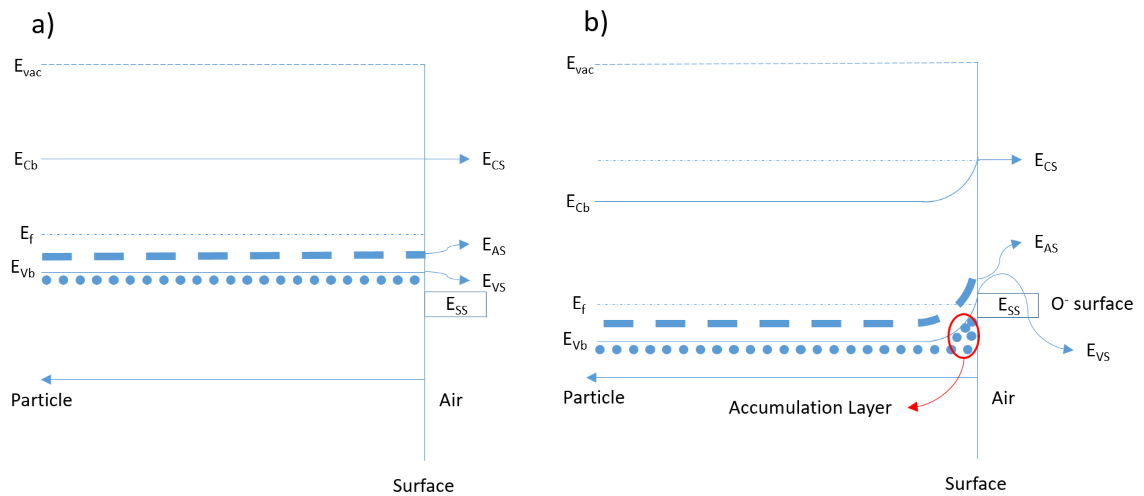

Figure 2.4. Schematic diagram of energy band representation for *p*-type material where: a) Flat bend prior to any surface reaction; b) Trapping of electrons due to oxygen adsorption and formation of the holes accumulation layer.[187]

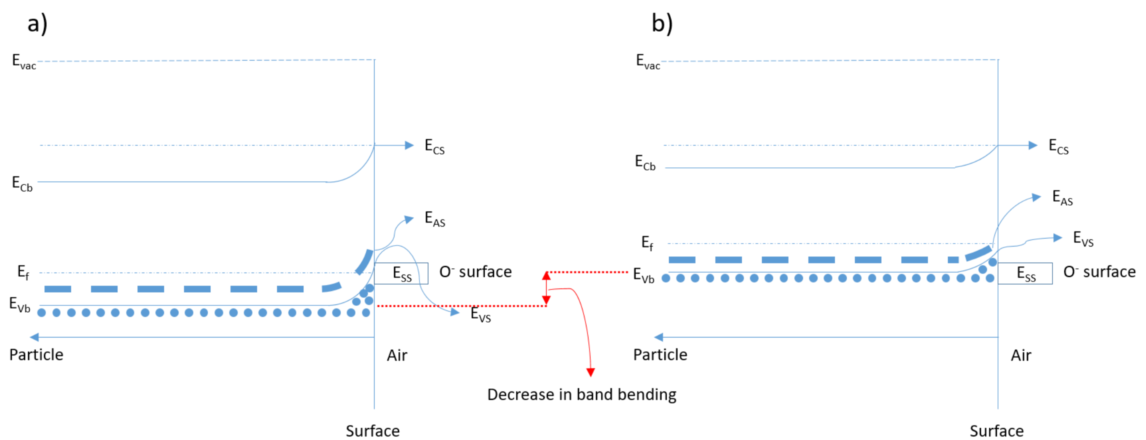

Figure 2.5. Schematic diagram of energy band representation for *p*-type material with decrease in band bending where: a) Trapping of electrons due to oxygen adsorption and formation of the holes accumulation layer ; b) After interaction with reducing gas.[187]

2.2 Surface-trap Limited Model

As explained above the response towards gas detection for *n*-type oxides focuses on the surface state formed by chemisorption of oxygen from ambient air. Reaction with a reducing gas such as hydrogen or carbon monoxide at a suitable temperature is related to a decrease of density of surface oxygen species and replenishing the charge carrier density. The decrease in resistance of tin dioxide due to the introduction of a reducing gas is entirely consistent with such a model, as is the resistance increase that occurs when *p*-type materials are exposed to traces of reducing gases in air.

Analysis of different conductivities of tin dioxide pellets have shown the charge transport being controlled by Schottky barriers at grain junctions. In the surface trap limited model this barrier is ascribed to electron transfer from bulk donor states to surface acceptor states, i.e. chemisorbed oxygen species. If the bulk donor density is low enough, the grains can be fully depleted of conduction electrons and a surface-trap limited conductivity would occur. This model was investigated by Williams *et al.*; however, this model presented is for a non-equilibrium process where the oxide material observed are at temperatures at which the bulk of the oxide equilibrates with the atmosphere at any rate. Figure 2.6 illustrates the surface-trap limited compensated semiconductor model, where; E_D is the ionisation donor energy, E_A is the acceptor ionisation energy, ΔE_D is the energy difference between donor and conduction band, $\Delta E_A$is the energy difference between acceptor and valence band, E_{S1} and E_{S2} are the surface acceptor ionisation energy one and two.

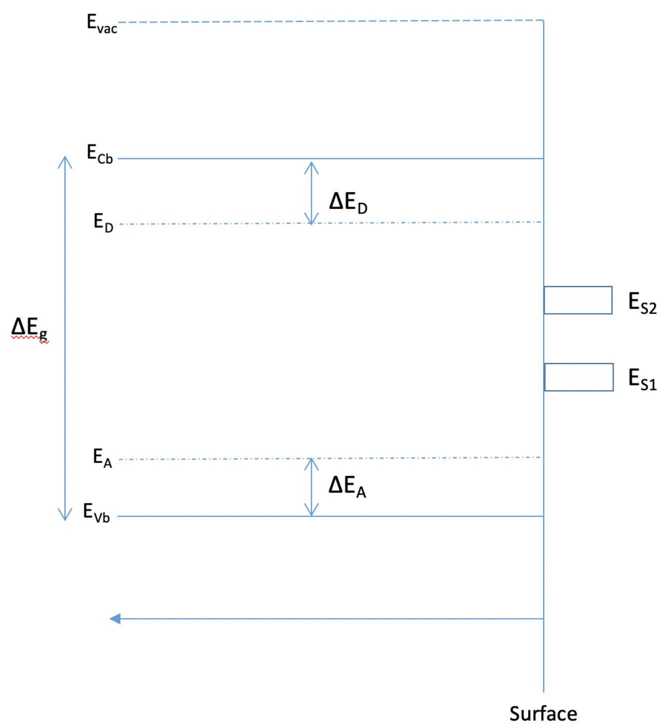

Figure 2.6. Schematic diagram of surface-trap limited compensated semiconductor model.[5]

For this model to be applicable, a sufficiently fine grained material with sufficiently low donor density is required in order to be considered completely depleted and therefore conductivity to be surface-trap limited. As tin dioxide does not behave in this manner, but

rather displays limited conductivity by Schottky barriers between grains, i.e. the grains are not fully depleted. The model is only applicable for fine grained porous materials with significantly lower donor density than SnO_2.[188] If this is the case and surface-trap limited conductivity dominates, then the carrier concentrations can be calculated from the following: for thermal excitation of carriers, $X \rightleftharpoons p + n$;

$$\therefore K_1 = N_C \exp(\frac{-\Delta E_g}{K_B T}) = p.n \tag{2.7}$$

Where K_1 is the equilibrium constant of the number of carrier concentration thermally excited, N_c is the density of state at the conduction band edge, E_g is the bandgap, K_B Boltzman constant, T is temperature (K), p is concentration of holes and n is the concentration of electrons.

For the ionisation of donors, $D \rightleftharpoons D^+ + n$;

$$\therefore K_2 = N_C \exp(\frac{-\Delta E_D}{K_B T}) = \frac{[D^+][n]}{[D]} = \frac{n f_D}{(1 - f_D)} \tag{2.8}$$

Where K_2 is the equilibrium constant of the number of ionised donor, E_D is the donor ionisation energy and f_D is the fraction of donor ionised. Therefore as the fraction of donor ionised increases, the concentration of electrons increases.

For the deionisation of surface acceptors, $S^- \rightleftharpoons S + n$;

$$\therefore K_3 = N_C \exp(\frac{-\Delta E_S}{K_B T}) = \frac{[S][n]}{[S^-]} = \frac{n(1 - f_S)}{f_S} \tag{2.9}$$

Where K_3 is the number of ionised acceptors, E_S is the surface acceptor ionisation energy and f_S is the fraction of surface acceptors with trapped electrons. Therefore as the fraction of surface acceptors with trapped electrons increases, the concentration of electrons decreases.

For charge balance;

$$p + f_D N_D = n + f_S N_S \tag{2.10}$$

where N_S and N_D are the surface acceptor and donor state densities respectively. It was assumed that $N_S \gg N_D$ for a surface trap limited conduction i.e. the surface acceptor state density is far greater than donor state densities, n is so small and $K_2 \gg K_3 \gg K_1$ i.e. the ionisation of surface acceptors is far greater than the ionisation of donors which in turn is far greater than the total number of carriers thermally excited. Hence the donor state lies just below the conduction band and the surface acceptor state lies below the donor state. Substituting the terms; f_S and f_D in equation (2.10) for the rearranged terms from equations (2.7) to (2.9) gives the equation:

$$\frac{K_1}{n} + \frac{N_D K_2}{(n + K_2)} = n + \frac{N_S n}{(K_3 + n)} \tag{2.11}$$

After some rearrangement, equation (2.11) can be expressed as:

$$K_1(n + K_2)(K_3 + n) + nN_D K_2(K_3 + n) = n^2(n + K_2)(K_3 + n) + n^2 N_S(n + K_2) \tag{2.12}$$

It was assumed that $N_S \gg N_D$, n is so small and $K_2 \gg K_3 \gg K_1$, n^x where $x \geq 3$ and any terms with K_1 becomes zero; therefore, equation (2.11) simplifies to:

$$N_S K_2 n^2 - N_D K_2 K_3 n \approx 0 \tag{2.13}$$

Therefore:

$$n \approx \frac{K_3 N_D}{N_S} \tag{2.14}$$

And:

$$p \approx \frac{K_1 N_S}{K_3 N_D} \tag{2.15}$$

For conductivity:

$$\sigma = \mu_e en + \mu_p ep \tag{2.16}$$

Where μ_e is electron mobility, μ_p is hole mobility and e is electron charge. Therefore, by substituting equations (2.14) and (2.15) into equation (2.16), the conducitivity can be expressed in terms of acceptor state density, which yields:

$$\sigma = \mu_e e \frac{K_3 N_D}{N_S} + \mu_p e \frac{K_1 N_S}{K_3 N_D} \tag{2.17}$$

Which could be expressed as:

$$\frac{\sigma}{e} = \mu_e \frac{K_3 N_D}{N_S} + \mu_p \frac{K_1 N_S}{K_3 N_D} \tag{2.18}$$

It was considered that the effect of a non-equilibrium process interaction on the surface of analyte gas at low concentration in air cause changes in acceptor state density; i.e. as N_S increases, conductivity will decrease to a point where it reaches a minima and increases again. Therefore, if the first expression is large the charge carriers are electron dominated (n-type response) and if the second expression is large, charge carriers are dominated by holes (p-type response).

By differentiating equation (2.18) with respect to N_S and $\frac{\partial \frac{\sigma}{e}}{\partial N_S} = 0$ to calculate the minimum;

$$\frac{\partial \frac{\sigma}{e}}{\partial N_S} = 0 = -\mu_e \frac{K_3 N_D}{N_S^2} + \mu_p \frac{K_1}{K_3 N_D} \tag{2.19}$$

Therefore;

$$\mu_e \frac{K_3 N_D}{N_S^2} = \mu_p \frac{K_1}{K_3 N_D} \tag{2.20}$$

And hence;

$$N_S = N_D \left(\frac{\mu_e}{\mu_p} \frac{K_3}{K_1}\right)^{\frac{1}{2}} \tag{2.21}$$

If N_D were too large or too small, then the minimum would move out of the range of N_S achievable by varying the trace gas concentration in air and hence a purely n-type or p-type response would be observed. If N_D is in an appropriate range, a change in sign for conductivity can occur with increasing gas concentration. There can also be a point where a gas analyte could decrease conductivity, but another (stronger reducing/oxidising gas) may move N_S below the minimum value for conductivity which results in a increase in conductivity, which is described in figure 2.7. For this figure, N_A is equal to the surface acceptor density which is described as N_S in the equations above. The x-axis is the surface acceptor density; and the y-axis is the conductivity.

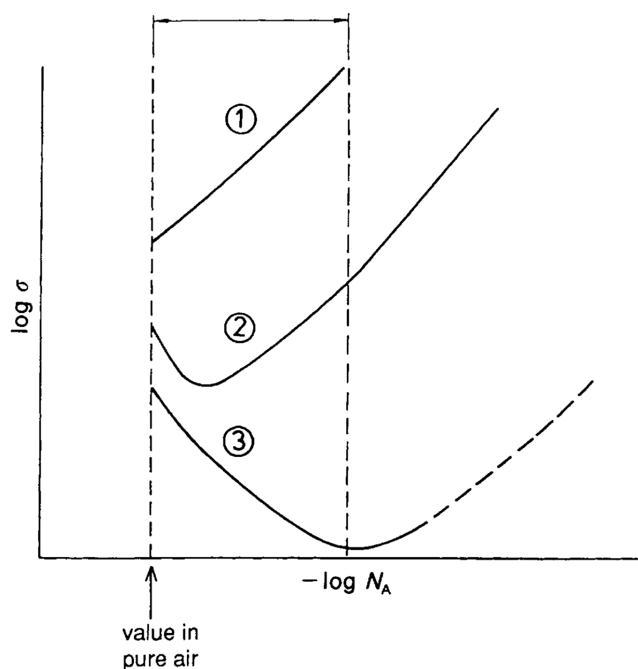

Figure 2.7. Schematic diagram of three curves with decreasing bulk donor density. Where N_A is equal to the surface acceptor density which is described as N_S in the equations above. The x-axis is the surface acceptor density; and the y-axis is the conductivity.[188]

Figure 2.7 depicts three curves with progressive decreasing donor density. Curve one describes a pure n-type behaviour i.e. increase in conductivity in the presence of a reducing gas which decreases N_S, and hence increases $-logN_S$ from value in pure air. Therefore S^- represents ionosorbed oxygen and that a reducing gas (R) reacts with the adsorbed oxygen ($R + S^- \longrightarrow RS + e^-$) and hence the fraction of surface acceptors decreases. Curve three demonstrates a pure p-type behaviour i.e. decrease in conductivity in the presence of a

reducing gas and therefore increases N_S, and hence decrease $-logN_S$ from value in pure air. Curve two describes a *p*-type behaviour at first, a decrease in conductivity to a point of minima (As the concentration of reducing gas increases) where then *n*-type behaviour occurs (increase in conductivity).

In 1995, Henshaw *et al.* extended the model by considering the calculation of carrier concentration for a surface-trap limited compensated semiconducting oxide system.[5] Two new terms are introduced, where the equilibrium of valence band holes with surface oxygen, $S \rightleftharpoons S^- + p$ is expressed as;

$$\therefore K_4 = N_V \exp(\frac{-\Delta E_G - \Delta E_S}{K_B T}) = \frac{[S^-][p]}{[S]} = \frac{f_S}{(1 - f_S)} \tag{2.22}$$

Where N_V is the density of state at the valence band edge, and the ionisation of bulk acceptors, $A^+ \rightleftharpoons A + p$ can be expressed as;

$$\therefore K_5 = N_V \exp(\frac{-\Delta E_G - \Delta E_A}{K_B T}) = \frac{[A][p]}{[A^+]} = \frac{(1 - f_A)}{f_A} \tag{2.23}$$

Where ΔE_A is the bulk acceptor ionisation energy and f_A is the fraction of acceptors ionised. Hence the new charge balance can be expressed as;

$$p + f_A N_A + f_D N_D = n + f_S N_S \tag{2.24}$$

By substituting the terms p, f_A, f_D and f_S using equations (2.7) to (2.9) and (2.23), equation (2.24) can be written as;

$$\frac{K_1}{n} + \frac{N_A K_1}{(K_5 n + K_1)} + \frac{N_D K_2}{(n + K_2)} = n + \frac{N_S n}{(K_3 + n)} \tag{2.25}$$

Equation (2.25) can be further rearranged and can be expressed as;

LHS;

$$K_1(K_5n+K_1)(n+K_2)(K_3+n)+N_A K_1 n(n+K_2)(K_3+n)+N_D K_2 n(K_5n+K_1)(K_3+n) \tag{2.26}$$

RHS;

$$n^2(K_5n + K_1)(n + K_2)(K_3 + n) + N_Sn^2(K_5n + K_1)(n + K_2) \tag{2.27}$$

Again it was assumed that $N_S \gg N_D, N_A$ for surface trap limited conduction so n is small and $K_2, K_5 \gg K_3 \gg K_1$, n^x where $x \geq 3$ and any terms with K_1^y where $y \geq 2$ becomes zero. Therefore;

$$\begin{aligned} &K_1K_2K_5n^2 + K_1K_3K_5n^2 + K_1K_2K_3K_5n + K_1K_2N_An^2 + K_1K_3N_An^2 + K_1K_2K_3N_An \\ &+ K_2K_3K_5N_Dn^2 + K_1K_2N_Dn^2 + K_1K_2K_3N_Dn = K_1K_2K_3n^2 + K_1K_2N_Sn^2 \end{aligned} \tag{2.28}$$

Equation (2.28) can be rearranged as;

$$\begin{aligned} &n^2(K_1K_2K_5 + K_1K_3K_5 + K_1K_2N_A + K_1K_3N_A + K_2K_3K_5N_D + K_1K_2N_D - K_1K_2K_3 \\ &- K_1K_2N_S) + n(K_1K_2K_3K_5 + K_1K_2K_3N_A + K_1K_2K_3N_D) \approx 0 \end{aligned} \tag{2.29}$$

As $K_2, K_5 \gg K_3 \gg K_1$, $n^2(K_1K_3K_5 + K_1K_3N_A - K_1K_2K_3)$ can be ignored. Therefore;

$$\begin{aligned} &n^2(K_1K_2K_5 + K_1K_2N_A + K_2K_3K_5N_D + K_1K_2N_D - K_1K_2N_S) \\ &+ n(K_1K_2K_3K_5 + K_1K_2K_3N_A + K_1K_2K_3N_D) \approx 0 \end{aligned} \tag{2.30}$$

Which could be rewritten as;

$$n^2(K_1K_2(N_A + N_D - N_S) + K_2K_3K_5(N_D + \frac{K_1}{K_3})) + n(K_1K_2K_3(N_A + N_D + K_5)) \approx 0 \tag{2.31}$$

As $N_S \gg N_D, N_A$ and $N_D \gg \frac{K_1}{K_3}$ as $K_1 = np$; the donor density is greater than the carrier density and K_1 is small in comparison to K_3. Therefore;

$$n^2(K_2K_3K_5N_D - K_1K_2N_S) + n(K_1K_2K_3(N_A + N_D + K_5)) \approx 0 \tag{2.32}$$

$N_D, N_A \gg K_5$, therefore;

$$n^2(K_2K_3K_5N_D - K_1K_2N_S) + n(K_1K_2K_3(N_A + N_D)) \approx 0 \tag{2.33}$$

And hence;

$$nK_1K_2K_3(N_A + N_D) \approx n^2(K_1K_2N_S - K_2K_3K_5N_D) \tag{2.34}$$

$K_1K_2N_S \gg K_2K_3K_5N_D$, therefore;

$$nK_1K_2K_3(N_A + N_D) \approx n^2K_1K_2N_S \tag{2.35}$$

Therefore;

$$nN_S \approx K_3(N_A + N_D) \tag{2.36}$$

Hence;

$$n \approx K_3\frac{(N_A + N_D)}{N_S} \tag{2.37}$$

As $K_1 = np$, therefore;

$$\frac{K_1}{p} \approx K_3\frac{(N_A + N_D)}{N_S} \tag{2.38}$$

$$\therefore K_1 \approx pK_3\frac{(N_A + N_D)}{N_S} \tag{2.39}$$

$$\therefore p \approx \frac{K_1}{K_3}\frac{N_S}{(N_A + N_D)} \tag{2.40}$$

Since $\frac{K_1}{K_3} \approx \frac{K_4}{K_1}$;

$$\therefore p \approx \frac{K_4}{K_1}\frac{N_S}{(N_A + N_D)} \tag{2.41}$$

The conductivity can be expressed in terms of surface acceptor state density;

$$\frac{\sigma}{e} = \mu_e K_3\frac{(N_A + N_D)}{N_S} + \mu_p\frac{K_4}{K_1}\frac{N_S}{(N_A + N_D)} \tag{2.42}$$

If the majority charge carriers are electrons then the first term dominates and if holes are the majority, the second term dominates. Differentiating equation (2.42) with respect to N_S gives the sensitivity of the material.

$$\frac{\partial \frac{\sigma}{e}}{\partial N_S} = 0 = \mu_e K_3 \frac{(N_A + N_D)}{N_S^2} + \mu_p \frac{K_4}{K_1} \frac{1}{(N_A + N_D)} \tag{2.43}$$

The sensitivity from this surface-trap limited compensated model for an n-type oxide is determined by the first term and show strong dependence to the surface acceptor state density. However the sensitivity of a p-type oxide is determined by the second term and is independent of the surface acceptor state density. Therefore, when a solid solution displays n to p-type conduction switching at some levels of stoichiometry, the sensitivity of the n-type material will be stronger than that of p-type; with the assumption that there are no changes in the microstructure, N_S is small and $K_3 \gg K_4/K_1$. K_3 and K_4 magnitudes are determined by the surface acceptor state energy as shown in equations (2.9) and (2.22) and the conditions above are met when the energy of the surface acceptor state is close to the conduction band. As the values of K_3 and K_4 vary with ΔE_S, small changes to the surface acceptor state energy may have a large effect of the sensitivity.

Henshaw also explains the change in resistance sign associated with adsorption of water by the oxides material can be rationalised by surface hydroxide trap energy, in particular it positioning relative to the O_{ads}^- trap state. When n-type oxides are exposed to moisture resistance decreases, this assumes that the dissociative adsorption, OH_{ads} trap state lies higher in energy than the O_{ads}^- trap state.

Chapter 3

Experimental

3.1 Methodology of Characterisation

Unless stated otherwise, reactions were conducted in a fume hood. All chemicals and solvents used were purchased from either Fisher Scientific or Sigma Aldrich. All glassware were cleaned with soap, acetone and deionised water before use. Substrates were washed with soap and rinsed with deionised water, acetone, isopropanol (IPA) and methanol. Substrates used were either microscope slides, alumina, FTO, quartz, alumina sensors or microelectromechanical system hotplates (MEMS).

Microscope slides were purchased. They were 1.0 mm thick with a squared shape of 25.0 mm by 25.0 mm. Energy dispersive x-ray spectroscopy (EDX) analysis showed the presence of oxygen 58.0%, silicon 26.5%, sodium 10.0%, and magnesium and calcium both at 2.5%. Alumina sensors were manufactured at University of Warwick. They were 2.5 mm by 2.5 mm in size, and 0.55 mm thick. Detection and heater tracks were made with gold and platinum materials respectively. The material comprised of 58.0% of oxygen, 13.0% of aluminium, 12.0% of silicon, 3.0% of calcium, 6.0% of barium, 5.0% of chromium and other trace elements.

Elemental dispersive x-ray spectroscopy analysis (EDX) were conducted using a Philips XL30 ESEM and a JEOL JXA-8600 superprobe. EDX measurements were carried out using an acceleration voltage of 20.0 kV, spot size 6.0, magnification of 1000 and acquisition

live time of 45 seconds under high vacuum. The samples were coated with a thin layer of carbon and connected to the metal stage by copper tape.

Scanning Electron Microscopy (SEM) were collected on a Jeol 6310F microscope using an acceleration voltage of 10.0 μA and a probe current of 8.0 A. All the sample images were collected using a secondary electron detector. The samples were coated with thin layer of sputtered gold and connected to the metal stage by copper tape. SEM images were collected using 'imagej' software. EDX and SEM were also conducted using a Carl Ziess SEM with the EHT set at 20 kV, current of 1.5 nA and a working distance of 8.5 mm.

X-ray diffraction (XRD) pattern for glass substrates were analysed using Bruker, Linx-Eye D8 X-ray diffractometer in reflection mode using Cu K_α radiation ($\lambda = 1.5406$ Å) operated at 40.0 kV and 40.0 mA. Scans were performed using a glancing incident angle (θ) of 0.8° and detection range angles from 10.0° to 66.0° 2θ degree, with a scanning parameter of 0.05 ° / $step$ and 3.0 s / scan. For alumina and microhotplate sensors, patterns were collected using a Bruker, D8 Discover X-ray diffractometer equipped with a Vantec-500 two dimension detector, in reflection mode using a Cu K_α radiation operated at 50.0 kV and 1.0 mA. The diffraction patterns were obtained in a three frame scan collected at detector angles of 25.0°, 40.0° and 55.0° (the 2θ range analysed was approximately between 18.0° and 66.0°) by integrating the Debye-Scherrer cones of the three frames. The acquisition time was 60 s / $frame$ with a step width of 0.5°. Identification of the crystal phases was achieved by comparing patterns with the ICSD Web database.

X-ray Photoelectron Spectroscopy (XPS) measurements was performed using a Thermo K_α spectrometer with monochromatic Al K_α radiation, a dual beam charge compensation system and constant pass energy of 50 eV. Survey scans were collected in the range 0 -1350 eV (binding energy). High resolution scans were carried out for Cr, W, Ni, Al, Au, O and C. The data collected was studied using CasaXPS software and binding energies were calibrated with respect to C 1s peak at 284.6 eV.

X-ray fluorescence (XRF) measurements was performed using a PANalytical epsilon4 spectrometer. Scan were conducted under helium and at six different voltages and current. The current varied, dependent on the thin film, the voltages were at 5 kV, 9 kV,

12 kV, 20 kV and 50 kV. Elemental analysis were given in weight percentage which were converted to atomic percentages.

Raman spectroscopy analyses were carried out using a Renishaw 1000 spectrometer equipped with a 532 nm laser. The Raman system was calibrated using a silicon reference. All films were placed in the spectrometer using an X-Y stage and analysed in between the ranges of100 cm^{-1} to 2000 cm^{-1}, with a laser power of 10 %, an exposure time of 45 seconds and an accumulation of three times per sample.

The Hall effect demonstrates the direct measurement of majority carrier density. To calculate the Hall effect a four point probe method called the van der Pauw method is used. Van der Pauw demonstrated that the resistivity of an arbitrarily shaped sample could be estimated from measurements of its resistance provided the sample satisfies the following conditions: contacts are at the boundary, contacts are small, sample is uniformly doped and uniformly thick and that there are no holes in the sample. A correction factor (f) was derived to use for estimation.

This method allows a current to be forced between two contacts (A and B in this case) while the voltage is measured between two different contacts (C and D). Voltage is not measured by contacts A and B as you get an incorrect resistance value. This is because when resistance is calculated (V_{AB}/I_{AB}) for AB, the resistance is too large due to contact resistance, where the resistance sits exactly at the contact between the metal probe (the contact) and the semiconductor (a schematic diagram is shown in figure 3.1). As this resistance has a voltage drop across it whenever there is current flowing through it (i.e. $V_{contact} = I_{AB}.R_{contact}$). The contact resistance plays no part on the conductivity of semiconductors and therefore shouldn't be part of the measured voltage. By measuring V_{CD} on contacts with zero current flowing through them, no voltage drop across $R_{contact}$ occurs and as a result only the voltage due to resistivity is measured.[189]

For Hall measurements, a uniform magnetic field B_z (T), is applied perpendicular to the direction of a electric field. For a *p*-type semiconductor, a voltage V_x is applied to the ohmic contacts on the front and back (B and D) of the sample which causes holes to flow in the positive x-direction, where $E_x = V_x/l$. The current density is given by;[189,190]

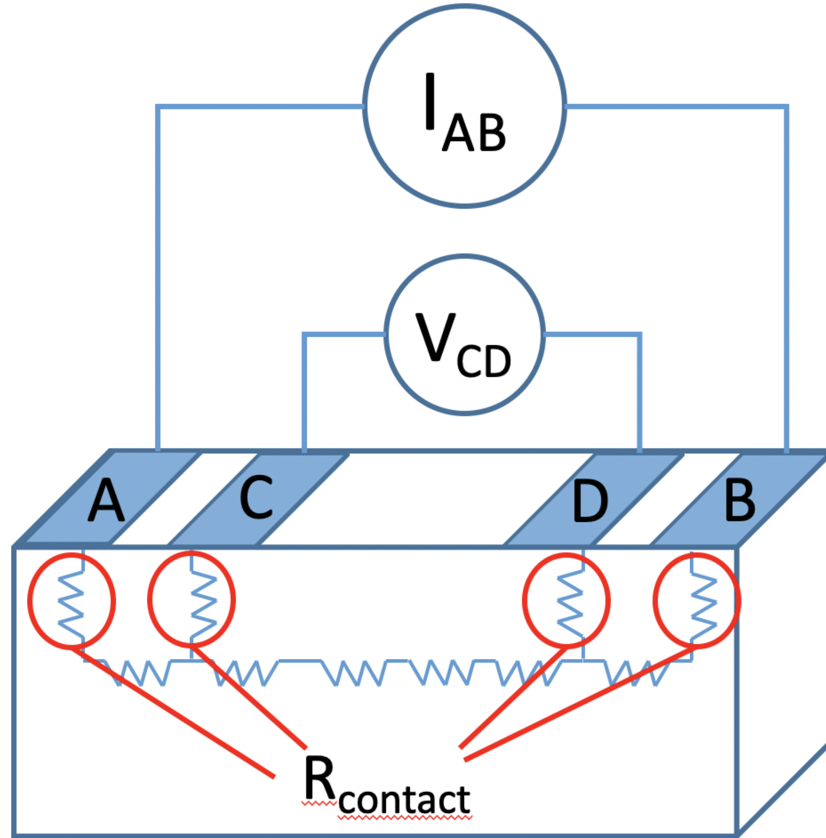

Figure 3.1. Contact resistances and the resistivity of the silicon sample.

$$J_x = \frac{I_x}{w.t} \tag{3.1}$$

Where w is the width, t is the thickness of the sample and I_x is the applied current. $\sigma \sim \sigma_p$ as $p \gg n$ in *p*-type materials. Therefore the average hole drift velocity is;

$$v_x = \mu_p E_x \tag{3.2}$$

Where μ_p is the hole mobility. In a magnetic field, in the positive z-direction, the holes experience an additional force $F_B = qV_x.B_z$ which pushes the holes in the negative y-direction. The holes thus collect at the left side of the structure, on surface A and leave behind negatively charged acceptors at the right contact C. These charges induce an electric field directed in the positive y-direction that creates an electric field induced force opposite to the magnetic force. No current can flow in the y-direction, because nothing is connected

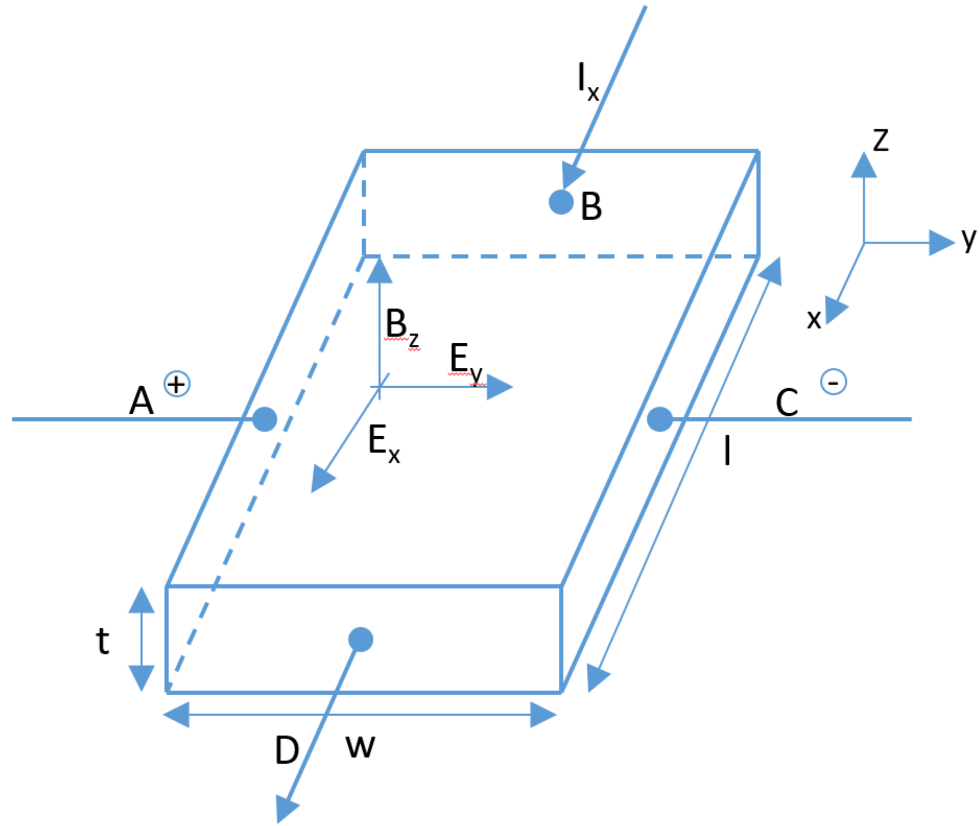

Figure 3.2. Field and voltage polarities of a *p*-type semiconductor for Hall measurement.

to contacts A and C. No current flow, means that the semiconductor must have no net force in that direction. Therefore, the two opposite forces B_z and the induced Hall field (E_y) must have equal magnitudes and;

$$qE_y = qV_x \times B_z \tag{3.3}$$

Where q is the elementary charge constant. Equation (3.3) can also be rewritten as;

$$E_y = \frac{1}{qp}J_x B_z \qquad as \qquad V_x = \frac{J_x}{qp} \tag{3.4}$$

Where p is the holes carrier concentration. The Hall coefficient is defined as;

$$R_H = \frac{1}{qp} \tag{3.5}$$

Therefore equation (3.4) can be rewritten as;

$$E_y = R_H J_x B_z \quad (3.6)$$

The induced voltage between contacts A and C is known as Hall voltage (V_H), which describes the nature of the material i.e. whether it is an n-type or p-type. This can be defined as;

$$V_H = E_y w \quad (3.7)$$

Therefore the holes carrier concentration can be solved by using equations (3.5) to (3.7);

$$p = \frac{I_x B_z}{qtV_H} \quad (3.8)$$

The Hall mobility can also be calculated as;

$$R_H = \frac{V_H t}{I_x B_z} \qquad and \qquad \sigma_p = q\mu_p p \quad (3.9)$$

Therefore hole mobility can be expressed as;

$$\mu_p = \frac{\sigma_p}{qp} = R_H \sigma_p \quad (3.10)$$

3.2 Deposition Parameter

Deposition of metal oxide thin films was achieved via AACVD in a CVD reactor equipped with a water cooling system in proximity of the inlet to minimise pre-reaction of precursors. Aerosols were formed using an ultrasonic humidifier operated at 2 MHz and transported to the reactor by N_2 gas carrier. Films was deposited on different substrates at various temperatures between 330 °C and 380 °C. The flow rate of the gas carrier were varied between 0.75 L min^{-1} and 2.0 L min^{-1}. The thin films were annealed between 500 and 700 °C in air for at least six hours.

3.3 Metal Oxide Thin Films Synthesis

3.3.1 Synthesis of Chromium Oxide Thin Films

A flat bottom flask was charged with chromium hexacarbonyl (0.05 g, 0.227 mmol) in methanol (15.0 ml) and sonicated until solvated. The glass substrates were cleaned, placed into the reactor and heated to 340 °C. Aerosols were generated via a humidifier and transported by N_2 gas carrier with a flow rate of $1.0\,L\,min^{-1}$. Once completed, the temperature and flow rate were reduced to 100 °C and $0.3\,L\,min^{-1}$ respectively. This yielded a dark green thin film, which was annealed at 500 °C for two hours. A similar method was use to deposit Cr_2O_3 onto a alumina sensing platform. Chromium hexacarbonyl (0.1 g, 0.454 mmol) in methanol (40.0 ml) was used. The alumina sensors were annealed at 600 °C for 24 hours.

3.3.2 Synthesis of Tungsten Oxide Thin Films

A flat bottom flask was charged with tungsten hexacarbonyl (0.1 g, 0.284 mmol) in methanol (15.0 ml) and stirred at room temperature until solvated. The substrates were cleaned, placed into the CVD reactor and heated to 340 °C. Aerosols were generated via a humidifier and transported by N_2 gas carrier with a flow rate of $1.0\,L\,min^{-1}$. Once the reaction was complete, the temperature and flow rate were reduced to 100 °C and $0.3\,L\,min^{-1}$ respectively. This was annealed at 500 °C for two hours.

3.3.3 Synthesis of Nickel Oxide Thin Films

A flat bottom flask was charged with nickel bis(2,2,6,6-tetramethyl-3,5-heptanedionate) (0.1 g, 0.284 mmol) in methanol (15.0 ml) and stirred at room temperature until solvated. The substrates were cleaned, placed into the CVD reactor and heated to 340 °C. Aerosols were generated via a humidifier and transported by N_2 gas carrier with a flow rate of $1.0\,L\,min^{-1}$. Once the reaction was complete, the temperature and flow rate were reduced to 100 °C and $0.3\,L\,min^{-1}$ respectively. This was annealed at 500 °C for two hours.

3.3.4 Synthesis of Tungsten-doped Chromium Oxide Thin Films

A flat bottom flask was charged with chromium hexacarbonyl (0.10 g, 0.454 mmol) in methanol (23.0 ml) and sonicated until it was dissolved. In a separate flask, a stock solution of tungsten hexacarbonyl was made, dissolving 0.843 g (2.396 mmol) in 70 ml of methanol. 7.0 ml (0.024 mmol) of the solution was added to the first flask with a molar ratio of $Cr_{1.85}W_{0.15}$. The substrates was cleaned, placed into the reactor and heated to 360 °C. Aerosols were generated via a humidifier and transported by N_2 gas carrier with a flow rate of 1.5 L min^{-1}. Once the reaction was completed the temperature and flow rate was reduced to 100 °C and 0.3 L min^{-1} respectively, which yielded a dark green thin film. This was annealed at 600 °C for 24 hours.

3.3.5 Synthesis of Titanium-doped Chromium Oxide Thin Films

A flat bottom flask was charged with chromium hexacarbonyl (0.10 g, 0.454 mmol) in methanol (37.0 ml) and sonicated until it was solvated. Titanium diisopropoxide bis(acetylacetonate) (TDBAA) was prepared in a different flask, 0.22 g was weighed out and methanol (15.0 ml) was added. 3.0 ml of the TiDBAA methanol solution was added to the chromium solution and stirred. The with a molar ratio of the solution is $Cr_{1.85}Ti_{0.15}$. The substrates (2.0 mm by 2.0 mm alumina sensor) was set onto a base and covered with a mask. This was placed into the reactor and heated to 340 °C. Aerosols were generated via a humidifier and transported by N_2 gas carrier with a flow rate of 1.5 L min^{-1}. Once the reaction was complete, the temperature and flow rate was reduced to 100 °C and 0.3 L min^{-1} respectively, yielding a dark green thin film. This was annealed at 600 °C for 24 hours.

3.3.6 Synthesis of Nickel-doped Chromium Oxide Thin Films

A flat bottom flask was charged with chromium hexacarbonyl (0.10 g, 0.454 mmol) and nickel(II) bis(2,2,6,6-tetramethyl-3,5-heptanedionate) ($Ni(thd)_2$) in methanol (40.0 ml) and sonicated until solvated. The with a molar ratio of the solution is $Cr_{1.85}Ni_{0.15}$. This was placed into the reactor and heated to 350 °C. Aerosols were generated via a humidifier and

transported by N_2 gas carrier with a flow rate of 1.5 L min^{-1}. Once the reaction was complete, the temperature and flow rate was reduced to 100 °C and 0.3 L min^{-1} respectively, yielding a dark green thin film. This was annealed at 600 °C for 24 hours.

3.3.7 Gas Sensing Methodology

Once the AACVD deposited sensors were made, platinum wires were used to connect the alumina sensors onto a pin stage as shown in figure 3.3. The wires were 50 μm thick, which were annealed beforehand at 100 °C for one hour with a temperature ramping of 15 °C min^{-1}. Four platinum wires were used to connect to the nickel pins, two were welded to the gold ink detection track pads and two to the heater track pads, using a welder powered to 27 W.

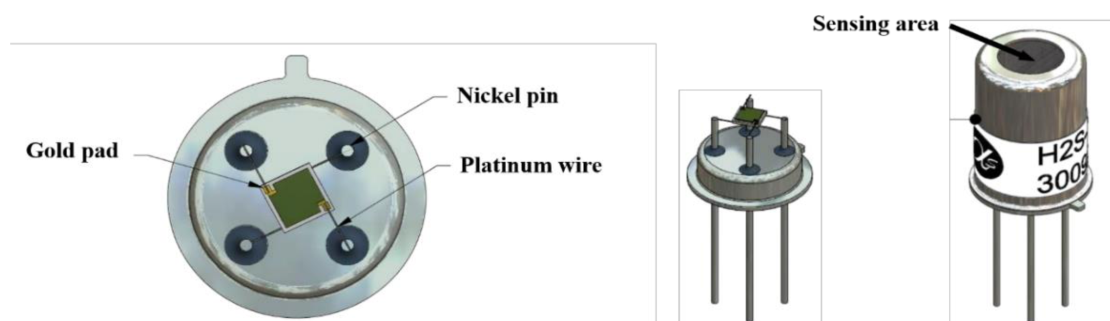

Figure 3.3. Schematic diagram of sensors connected to pins via platinum wires. First image is a top view of the uncapped device, second image is a side-on view on the uncapped device and the last image is a front view of the capped device.

Gas sensing analysis of AACVD fabricated metal oxide thin film sensors were tested at Alphasense Ltd both by myself and Dr Eshan Danesh (employee of Alphasense), where they ran the experiments that was designed. The sensitivity, selectivity and optimum parameters of metal oxide sensors towards various VOCs were briefly examined and compared to Alphasense's screen printed CTO thick film sensors. The sensors working temperature and resistance were measured and controlled by a Sensor Management System (SMS), which is designed to work with up to eight metal oxide gas sensors. It has circuits to accurately control sensor heater temperature based on digital control loops. The individual sensor heater 0 °C resistance and temperature coefficients can be set as parameters,

and there are a number of heater set-point algorithms that can be selected as parameters. These include temperature ramps and timed temperature schedules that are controlled via an external RS485 interface to a PC (figure 3.4).

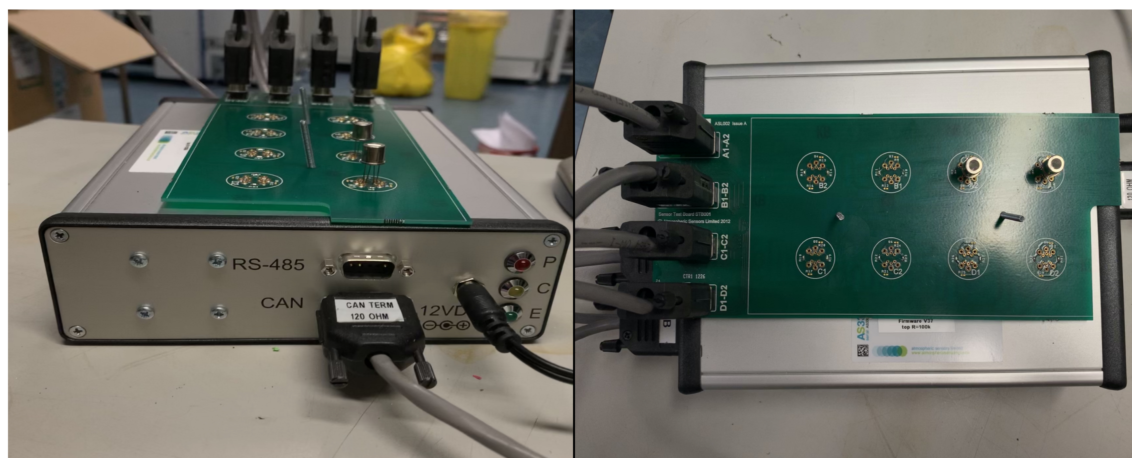

(a) **(b)**

Figure 3.4. Image of SMS board system used for controlling and analysing the sensors resistance and operating temperature in idle and when exposed to gases. a). Side on view; b). Top down view.

VOC gas tests were examined via permeation tubes which enables generation of precise and repeatable calibration gas standards, with concentrations ranging from part per trillion to high part per million. A permeation tube is a polymer tube, typically made of PTFE, that contains a solid, liquid or gas analyte, sealed and crimped at both ends. The calibration chemical permeates through the walls of the tube at a constant rate for a given temperature; it then mixes with and is carried away by a diluent or make-up flow.

A standard experimental procedure for the analysis of VOCs consist of examining the sensitivity and selectivity of different AACVD metal oxide sensors at working temperature of 300 °C, two different concentrations (part per million/parts per billion) and a relative humidity of 50 %. Relative humidity was calculated by dividing the wet air flow by the total flow rate (in this case 500 ml min^{-1}) which was kept constant during the experiment. Therefore, for a relative humidity of 50 %, 250 ml min^{-1} of wet air is needed and 250 ml min^{-1} of dry air or mixture of dry air and gas analyte. A relative humidity of 50 % was chosen as this was used to mimic the humidity of the environment. The enclosed system containing the sensors was first purged with 50 % humid air for ten minutes, after-

wards a flow of highly concentrated gas analyte passed through for 15 minutes, then a flow of just humid air passed for 5 minutes, lastly the gas analyte at a lower concentration was flown through again for 15 minutes. The performance of these sensors were compared to commercial screen printed CTO sensors and / or literature values.

Chapter 4

P-type Metal Oxide Thin Films

This chapter looks into the synthesis of two types of *p*-type metal oxides; chromium oxide and nickel oxide. The main focus is to look into the characteristics of the two metal oxides such as its chemical structure, chemical state and electronic properties in order to gain a better insight of how it works as a gas sensor and a better understanding of how the mechanism of *p*-type metal oxides gas sensors work.

Chromium oxide, a *p*-type semiconductor has a band gap of 3.4 eV.[191] The most stable oxide of chromium is Cr_2O_3 with an oxidation state of 3+; a magnetic insulator which adopts the corundum structure. Cr_2O_3 have shown to be sensitive to H_2, CO_2 and O_2 gases at 450 °C. M. Egashira *et al*. have shown by using decoration with noble metals, Cr_2O_3 displays sensitivity towards CH_4 and H_2 over a temperature range of 300 °C to 600 °C.[192]

Nickel oxide (NiO), a *p*-type semiconductor with a cubic phase crystal structure displays the same crystal structure of NaCl and is an antiferromagnetic material with a band gap energy between 3.6 eV to 4.0 eV which displays good thermal and chemical stability.[136,193] NiO is known as a Mott-Hubbard insulator due to its electron-electron interaction which explains it poor conductivity as a semiconductor.[194] Different deposition methods such as sol-gel, spray pyrolysis, spin coating, sputtering, spray pyrolysis and chemical vapour deposition (CVD) have been used to deposit thin films of nickel oxide with each method offering different advantages depending on the specific application of interest.[195–198]

Due to the increase in gas sensing applications i.e. agricultural, industrial and environmental monitoring, there has been an constant search for new sensitive material which are stable under ambient conditions.[199] NiO is not a popular gas sensing material due to its strong *p*-type characteristic and poor conductivity. However, recent reports have shown that NiO thins films can detect VOCs (formaldehyde), reducing gases such as H_2, CH_4 and NH_3 as well as NO_2, an oxidising gas.[200–204]

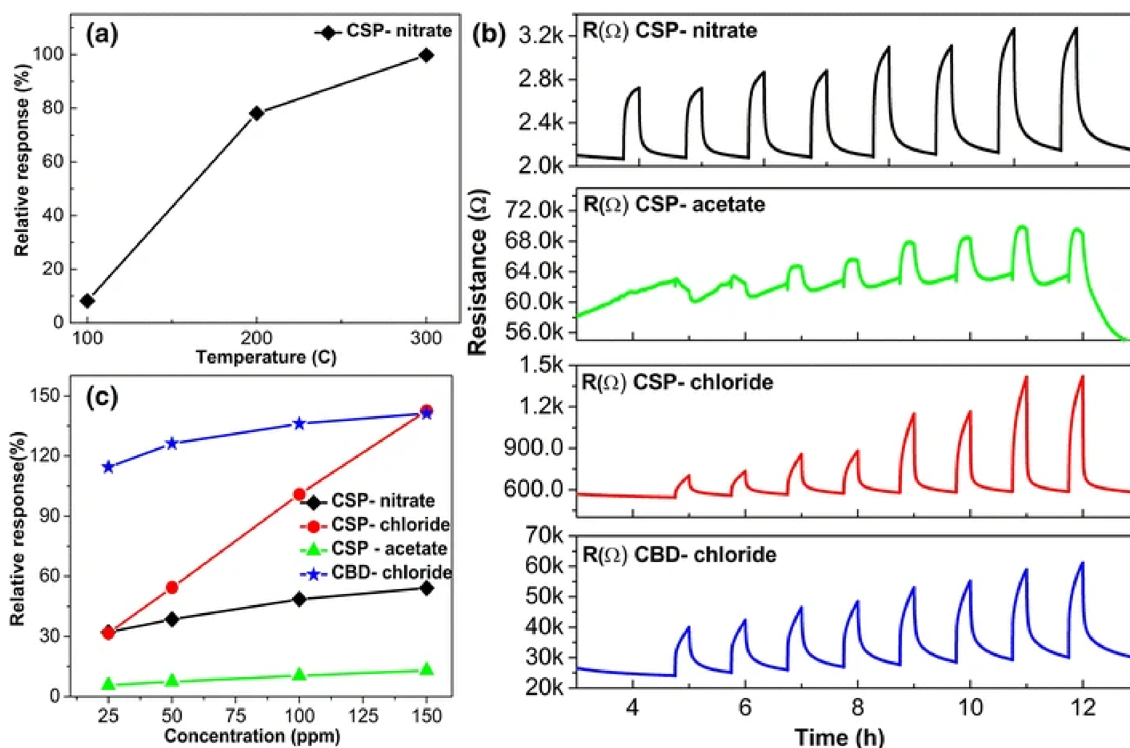

Figure 4.1. a) Relative sensor response as function of operating temperatures towards 150 ppm ammonia; b) Resistance response towards 25 ppm, 50 ppm, 100 ppm and 150 ppm of ammonia at 300 °C for different precursors; c) Relative sensor response comparison for different precursors towards NH_3.[199]

Gomaa[199] compared different deposition techniques (spray pyrolysis and chemical bath deposition) for the growth of NiO nanostructured films to obtain highly developed surface area. Different precursors were also used to understand if the morphology affects the materials sensing capabilities toward ammonia. NiO sensors deposited via spray pyrolysis and chemical bath deposition formed nanocubes and nanoflakes respectively. Nickel acetate, nickel chloride and nickel nitrate were used to form NiO nanocubes and has an affect on the morphology and crystallites average size of the deposited films. Illustrated in figure 4.1, both NiO nanocubes and nanoflakes demonstrates different levels

of sensitivity towards ammonia, where in figure 4.1c nanoflakes made using nickel chloride gives a high and stable relative response towards ammonia compared to the others across all concentration levels. The relative response (S) is calculated by $S = ((R_{Gas} - R_{Background})/R_{Background}) \times 100$.[199]

4.1 Chromium Oxide (Cr_2O_3) Film Characterisation

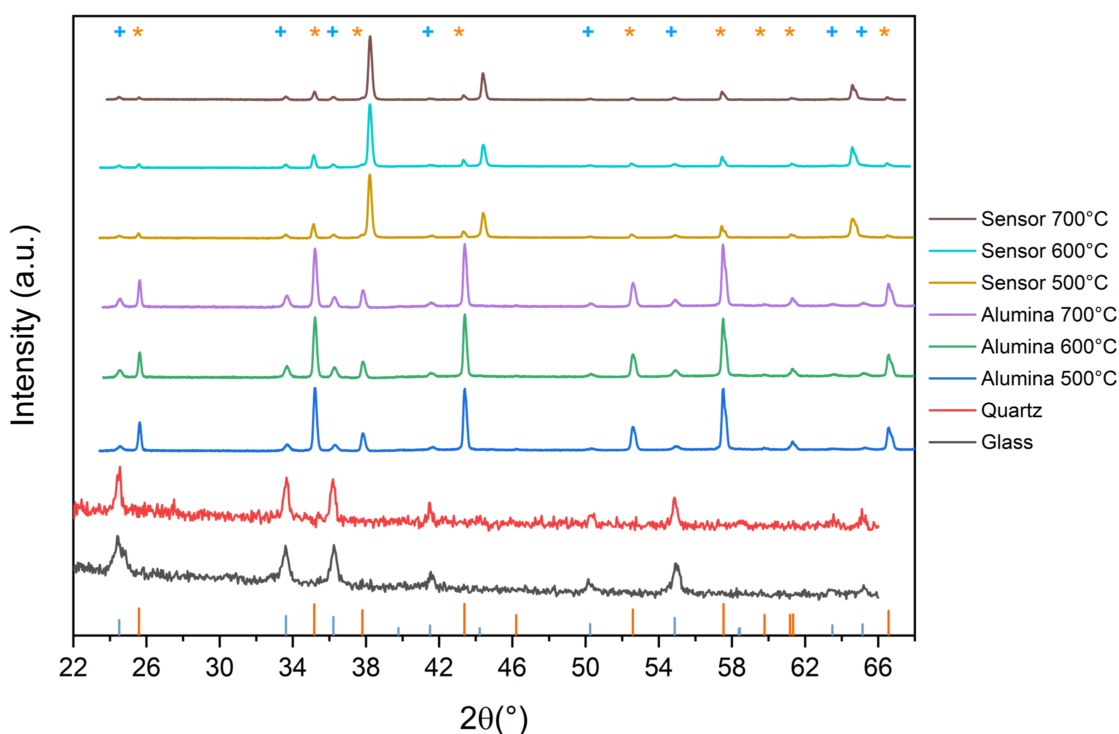

Figure 4.2. XRD pattern of chromium oxide on: Glass, quartz, alumina and alumina sensors substrates. Where the orange stick pattern and * equates to corundum (Al_2O_3) and the blue stick pattern and + equates to eskolaite (Cr_2O_3).

Structural analysis (pXRD) of chromium oxide thin films were conducted. The films was deposited onto various substrates; microscope glass, alumina, alumina sensors and quartz. The films were annealed at a range of different temperatures (500 °C to 700 °C). The 2θ peaks displayed in figure 4.2 for samples on glass and quartz corresponds to the crystal structure of eskolaite, the mineral ore of Cr_2O_3 which is depicted in the figure as the blue stick pattern. For the samples deposited onto alumina and sensor substrate, whilst displaying the peaks for eskolaite, peaks for corundum was also present (Al_2O_3 is illustrated as the orange stick pattern) which was expected as the substrates are made from

alumina. For the sensor substrates, gold was also detected which comes from the ink used for the sensing electrodes. The 2θ peak for (300) lattice plane for chromium oxide was not observed on the sensor substrate. The reason for this is because the peak for gold (211) also lies within that 2θ region and hence is merged into one peak. When chromium oxide thin films were annealed at different temperatures (500 °C to 700 °C) on alumina and sensor substrates, no 2θ peak shift were observed. Table 5.1 below depicts the peaks for chromium oxide and its corresponding lattice planes.

Table 4.1. pXRD 2θ peaks and lattice planes of Cr_2O_3 on different substrates.

pXRD 2θ peak (°)								Lattice Plane
Glass	Quartz	Alumina			Alumina sensor			
		500 °C	600 °C	700 °C	500 °C	600 °C	700 °C	
24.4	24.5	24.5	24.5	24.6	24.5	24.5	24.5	(012)
33.6	33.6	33.6	33.7	33.7	33.6	33.6	33.6	(104)
36.2	36.2	36.3	36.3	36.3	36.3	36.2	36.2	(110)
41.6	41.5	41.6	41.6	41.6	41.6	41.5	41.5	(113)
50.1	50.3	50.3	50.3	50.3	50.3	50.2	50.2	(024)
54.9	54.9	54.9	54.9	54.9	54.9	54.8	54.8	(116)
–	–	63.6	63.5	63.5	–	–	63.4	(214)
65.2	65.1	66.6	65.2	65.2	–	–	–	(300)

X-ray photoelectron spectroscopy (XPS) surface analysis was conducted using carbon $1s$ as calibration at 284.6 eV for charge shift corrections. Figure 4.3 depicts the chromium $2p$ spectra for chromium oxide deposited onto several different substrate. Analysis on alumina substrates were not characterised due to charging issues with the substrate that caused peak shifts of about 5 eV. The spectras on glass and quartz substrates were annealed at 500 °C and 600 °C respectively. The values of 574.9 eV and 576.8 eV were recorded for the $2p_{\frac{3}{2}}$ and $2p_{\frac{1}{2}}$ band on glass and quartz substrate respectively. However, two different peak environments were indicated in the $2p_{\frac{3}{2}}$ region for samples on glass (a deconvolution of these peaks are represented in figure 4.4a), whereas samples on quartz only a single environment was present.

The two different environments seen on the glass substrate sample are related to the

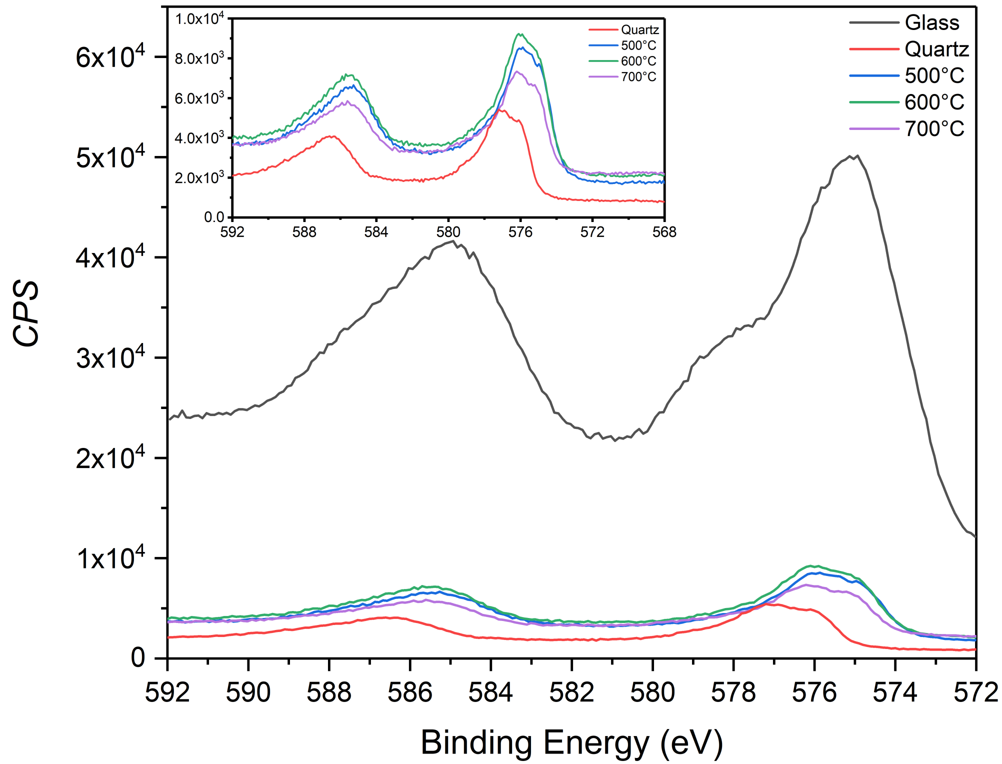

Figure 4.3. Chromium $2p$ spectra of chromium oxide on different substrates. The inset plot is a close up spectra for samples on quartz and sensor substrates.

binding energies of different oxidation states of chromium; Cr(III) and Cr(VI) at roughly 576 eV and 579 eV respectively. The survey spectrum was inspected (as illustrated in figure 4.5) and indicated the presence of sodium at roughly 1070 eV. For quartz and alumina sensor substrates, the sodium peak was not present. A reasonable assumption for different oxidation states observed for chromium is due to the formation of Cr(III) → Cr(VI) during the annealing process; where sodium ions from the glass substrate migrate onto the deposition layer and diffuse into the film when heated at high temperatures under the presence of oxygen rich environment, forming sodium dichromate ($Na_2Cr_2O_7$) as shown in equation (5.1).

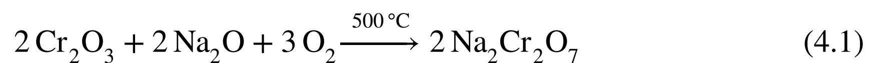

$$2\,Cr_2O_3 + 2\,Na_2O + 3\,O_2 \xrightarrow{500\,^{\circ}C} 2\,Na_2Cr_2O_7 \tag{4.1}$$

Figure 4.3 also illustrates the chromium $2p$ spectra for alumina sensors annealed at 500 °C, 600 °C and 700 °C. All three samples displays one distinct peak in the $2p_{\frac{3}{2}}$ region which refers to the oxidation state Cr(III) which is illustrated in figure 4.4. No major peak

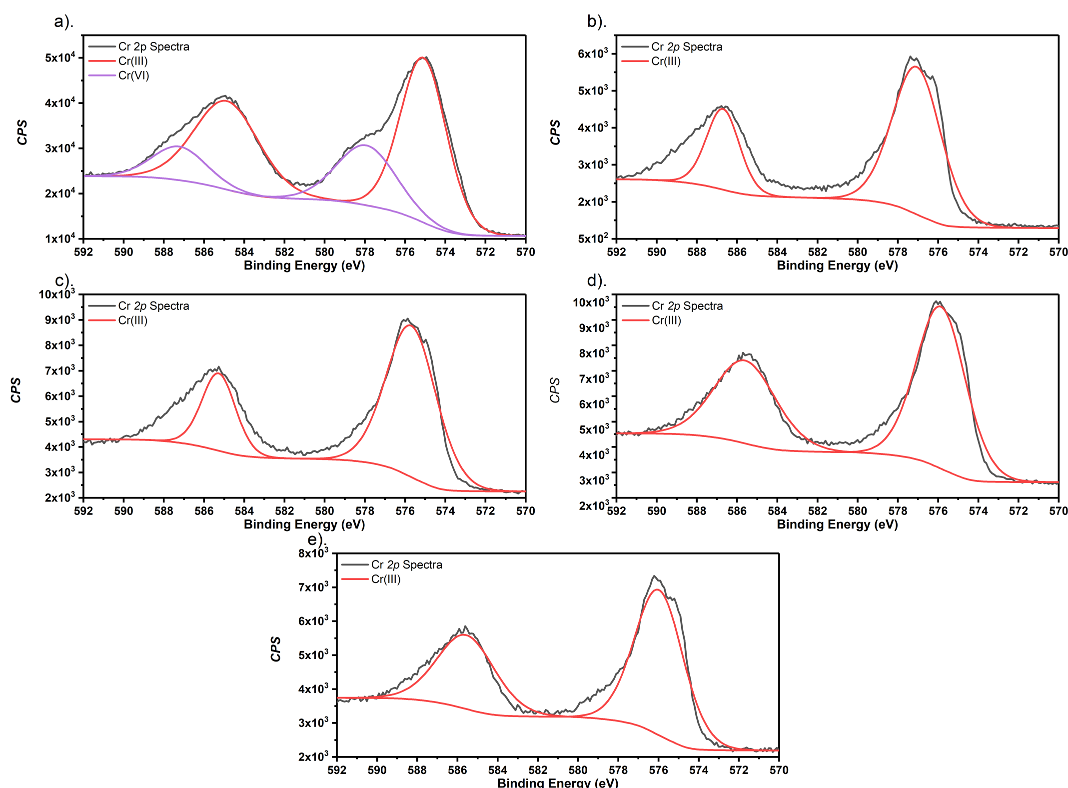

Figure 4.4. Chromium 2*p* spectra of chromium oxide displaying Cr(III) and Cr(VI) peaks where; a) Glass substrate; b) Quartz; c) Sensor annealed at 500 °C; d) Sensor annealed at 600 °C and f) Sensor annealed at 700 °C.

shift was seen when annealing temperature changed from 500 °C to 600 °C and to 700 °C (575.9 eV, 575.9 eV and 576.2 eV). Table 4.2 depicts the binding energies of chromium and oxygen for the samples analysed and its comparison to literature values. The table also contains the calculation for the composition ratio. The composition ratio of deposited chromium oxide was calculated by peak intensity ratio and RSF values (7.69 for Cr 2*p* and 2.93 for O 1*s*). The calculations showed that the films analysed contained a consistent amount of oxygen on quartz and alumina substrates. But on glass there was a slightly higher concentration of oxygen which is due to dichromate formation. Another reason for the slightly higher oxygen concentration is due to contaminants such as hydroxyls from water, silicates and carbon containing species.

Raman analysis was conducted on the various chromium oxide samples which is illustrateed in figure 4.6. Chromium oxide (Cr_2O_3), has a eskolaite structure with a space group $R\bar{3}c$ and point group D^6_{3d}. The irreducible representation determined via group the-

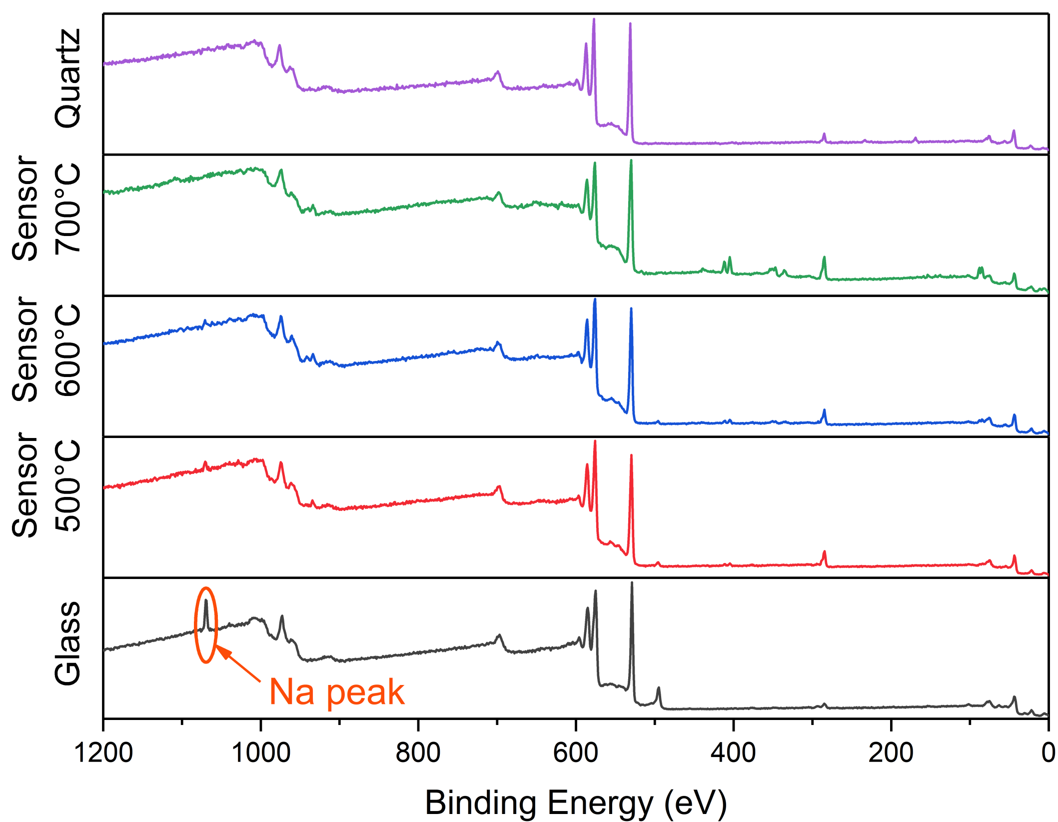

Figure 4.5. Survey scan spectrum of chromium oxide on different substrates.

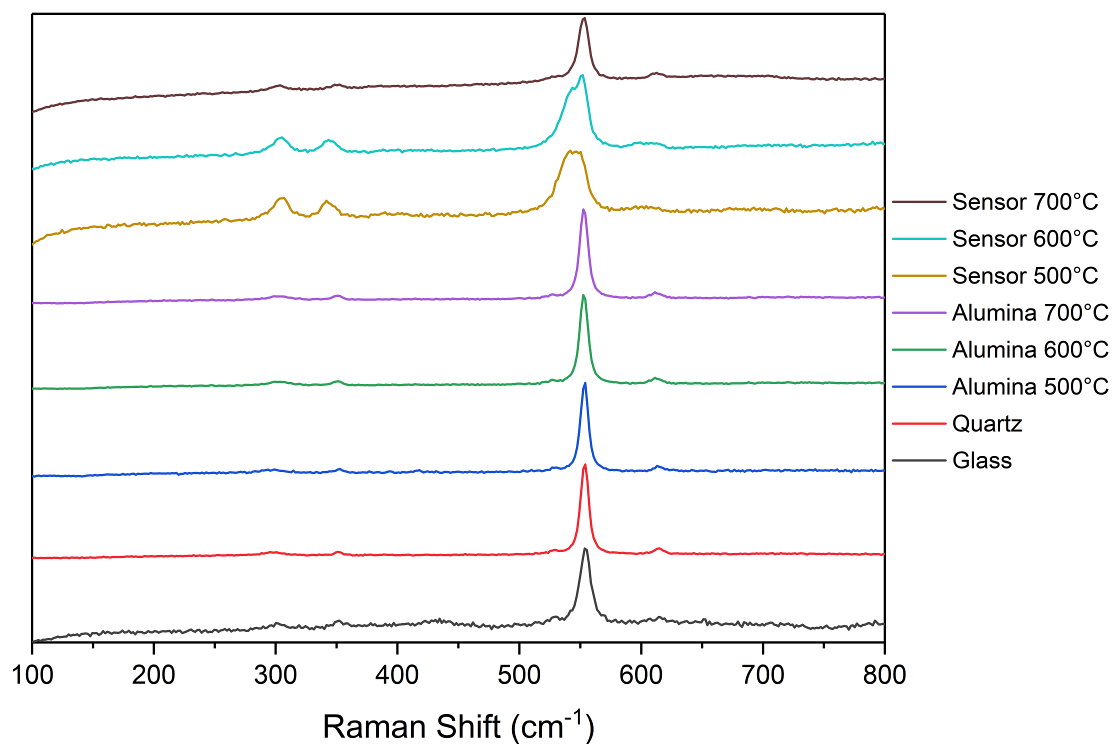

Figure 4.6. Normalised raman spectrum of chromium oxide on various substrates.

Table 4.2. Binding energies (eV) of Cr_2O_3 annealed on different substrates ([a]literature values) and the calculated composition ratio.

Sample	Cr $2p_{\frac{3}{2}}$	O $1s$	Peak Intensity		Atomic Ratio
			Cr $2p_{\frac{3}{2}}$	O $1s$	
Glass	574.9	529.1	106933.8	124966.4	Cr(1) : O(3)
Quartz	576.8	530.5	10497.1	7479.3	Cr(1) : O(1.9)
Sensor (500 °C)	575.9	529.4	18245	11890.4	Cr(1) : O(1.7)
Sensor (600 °C)	575.9	529.6	20015.3	12670.4	Cr(1) : O(1.7)
Sensor (700 °C)	576.2	529.7	14036.1	11480.2	Cr(1) : O(2.1)
Cr_2O_3[a]	576.1	–	–	–	–

[a] Biesinger *et al.* referenced to Au $4f_{\frac{3}{2}}$ at 83.95 eV.[205]

ory was shown to be $\Gamma_{red} = 2A_{1g}+2A_{1u}+3A_{2g}+2A_{2u}+5E_g+4E_u$.[206,207] Seven modes are raman active ($2A_{1g} + 5E_g$) and six are infared active ($2A_{2u} + 4E_u$). The other five modes ($3A_{2g} + 2A_{1u}$) are both raman and infared inactive. Raman spectrum of chromium oxide on various different substrates were analysed and closely compared to literature values of Cr_2O_3. The peaks observed closely coincide with literature sources reported by Beattie *et al.* and shown in table 4.3. The intense peak which corresponds to the A_{1g} assignment at 553 cm^{-1}, 552 cm^{-1}, 554 cm^{-1}, 552 cm^{-1}, 545 cm^{-1}, 551 cm^{-1} and 553 cm^{-1} for glass, quartz, alumina and alumina sensor substrates (at three different annealing temperature) respectively. The peak expected at 530 cm^{-1} was not present in some of the samples analysed. A reasonable assumption for this is the peak may have merged into the the much higher intensity A_{1g} peak.

Cross section SEM imaging was conducted on chromium oxide deposited onto FTO substrate. This was used to determine the thickness of the thin film layer from AACVD fabrication. The thickness of chromium oxide was determined to be approximately 33 µm. The film thickness was used for Hall effect measurement and conducted under ambient conditions where the Hall voltage was calculated.

Table 4.4 describes the resistance, Hall mobility, bulk carrier concentration, Hall co-

Table 4.3. Raman shift assignment for Cr_2O_3 on different substrates.

Observed Raman Shift (cm^{-1})								Assignment	Literature [a] (cm^{-1})
Glass	Quartz	Alumina			Alumina Sensors				
		500 °C	600 °C	700 °C	500 °C	600 °C	700 °C		
300	296	300	297	302	303	305	304	E_g	303
350	351	349	352	351	341	343	352	E_g	351
530	527	–	527	527	–	–	526	E_g	530
553	554	552	554	552	545	551	553	A_{1g}	551
614	613	613	611	611	604	604	612	E_g	612

[a] Beattie *et al.*[208]

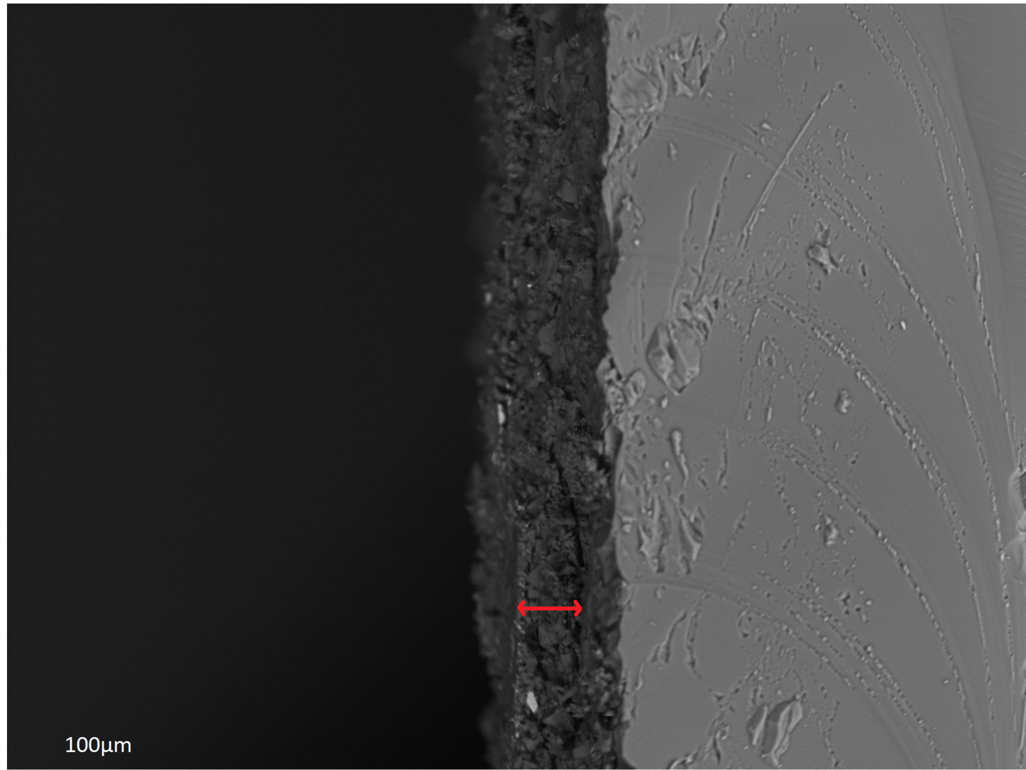

Figure 4.7. Cross section SEM image of Cr_2O_3 on FTO glass.

efficient and Hall voltage of chromium oxide thin films on quartz respectively. The Hall effect was measured three times using each sample. At a current of 1.0 nA and thickness of 33 µm, the Hall voltage was calculated. In general, a positive Hall coefficient indicates that the material is *p*-type and a negative Hall coefficient indicates the material is of *n*-type nature. In the measurements conducted here, it can be seen that the Hall coefficient is a positive value and hence suggest that the material is *p*-type.[209] Khan[210] reported for a thin film Cr_2O_3 of 300 nm, the Hall coefficient was roughly 1.7×10^{-2} cm^3 C^{-1} which is significantly smaller than the values displayed in table 4.4. However, the bulk carrier concen-

Table 4.4. Hall effect measurements of Cr_2O_3 on quartz at room temperature.

Measurements	ρ (Ω cm^3)	μ ((cm^2 V^{-1} s^{-1})	N_B (cm^{-3})	R_H (cm^3 C^{-1})	V_H (mV)
A	5.39×10^6	101.2	1.15×10^{10}	5.45×10^8	8.43
B	1.03×10^7	226	2.68×10^9	2.33×10^9	36.1
C	1.34×10^8	15.03	3.10×10^9	2.01×10^9	31.1

tration obtained via Hall measurement is considerably lower when compared to literature (Khan *et al*. reported carrier concentration value between 2.55×10^{26} and $2.0 \times 10^{27} \mathrm{m^{-3}}$). It was also reported that as temperature increases so does the carrier concentration, however due to limitations, Hall measurement was only carried out at 300 K.[210] The reasons for the difference in value measured as compared to literature sources may include ohmic contact geometry, sample uniformity and accuracy of thickness determination for an ideal sample to show a true Hall voltage. If this is the case, the measured voltage is then shifted due to ohmic drop.

Activation energy profile was calculated by measuring baseline resistance of three different samples of chromium oxide sensors under pure nitrogen at elevated temperatures (100 °C to 450 °C). An arrhenius plot shown in figure 4.8 was generated from the resistance values and lines of best fit were plotted.

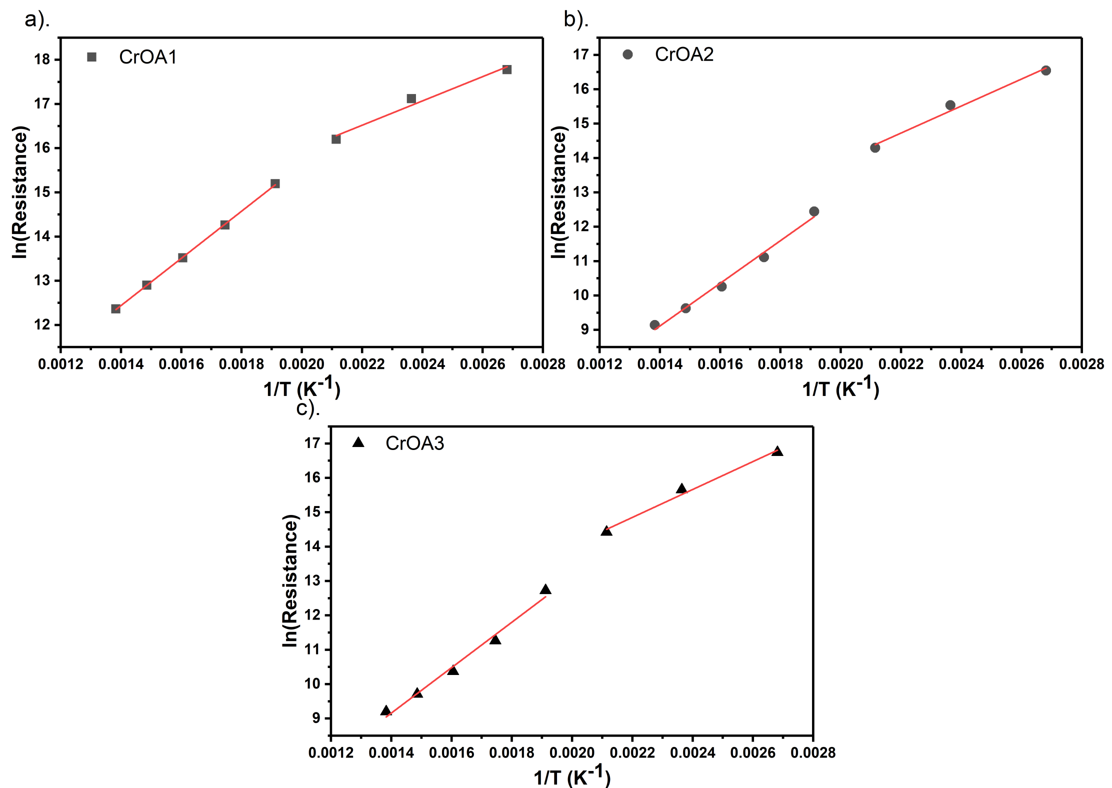

Figure 4.8. Arrhenius plots for the resistivity of Cr_2O_3 thin film under pure nitrogen.

Using the lines of best fit, the activation energy can be calculated as;

$$\rho = A \exp(\frac{-Ea}{K_B T}) \tag{4.2}$$

Where ρ is the resistance, Ea is the activation energy, K_B is the Boltzman constant and T is temperature in kelvin. Therefore;

$$ln\rho = lnA - \frac{Ea}{K_B}\frac{1}{T} \tag{4.3}$$

Where $y = ln\rho$, $c = lnA$, $m = -\frac{Ea}{K_B}$ and $x = \frac{1}{T}$. The activation energy at an given temperature can therefore be expressed as;

$$Ea = K_B T(lnA - ln\rho) \tag{4.4}$$

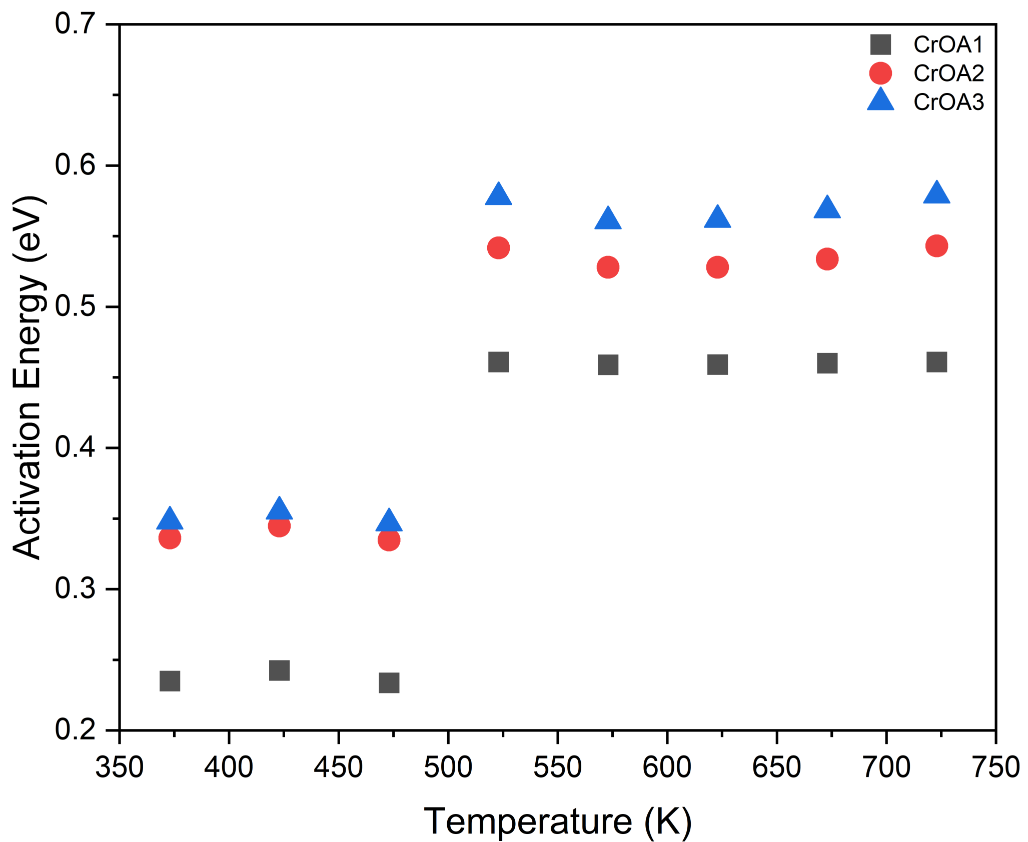

Figure 4.9. Chromium oxide activation energy against temperature under nitrogen.

Figure 4.9 illustrates the activation energy of chromium oxide where three different sensor were tested. The three samples demonstrated two different activation energies,

ones at low temperature and another at a high temperature range. Between 475 K to 525 K, the activation energy increases exponentially, from 0.24 to 0.46 eV for the CrOA1, and from 0.35 to 0.54 and 0.58 eV for CrOA2 and CrOA3 sample respectively. Kofstad *et al*. had observed a value of 1.87 eV for the activation energy of porous chromium oxide when heated at high temperature (greater than 1000 °C). Kofstad also demonstrated a compacted sample of chromium oxide showed a temperature dependent resistance decrease as temperature decreased from 1200 °C to 700 °C with an obsevered activation energy of around 0.2 eV at 700 °C which conincides with the values seen in figure 4.9.[211] There has also been reports of the activation energy of conductance for chromium oxide ranging from 0.26 eV to 0.6 eV dependant on how the chromium oxide samples were prepared.[212–214]

4.2 Nickel Oxide (NiO) Film Characterisation

Figure 4.10. Deposition of NiO on glass using $Ni(acac)_2$ (left) and $Ni(TMHD)_2$ (right).

Anhydrous $Ni(TMHD)_2$, a deep purple solid and hydrated $Ni(acac)_2$ a turquoise green coloured powder were selected as precursors for the deposition of nickel oxide thin films. Work previously conducted within our group demonstrated good film deposition using the two precursors described above. The NiO deposited onto glass produced a silver mirror like film as shown in figure 4.10 using hydrated $Ni(acac)_2$ and anhydrous $Ni(TMHD)_2$. The films prior to annealing demonstrates the precursor $Ni(acac)_2$ used produced a uniform film compared to $Ni(TMHD)_2$. When the films are annealed at 500 °C for 24 hours, they become transparent. Therefore, $Ni(acac)_2$ was chosen as the sole precursor for the deposition of nickel oxide thin films.

Table 4.5. Film deposition parameters using $Ni(acac)_2$.

Sample	Temperature (°C)	Flow Rate ($L\,min^{-1}$)	Solvent
NiO^1	340	1.5	EtOH:MeOH (1:1)
NiO^2	340	1.5	MeOH

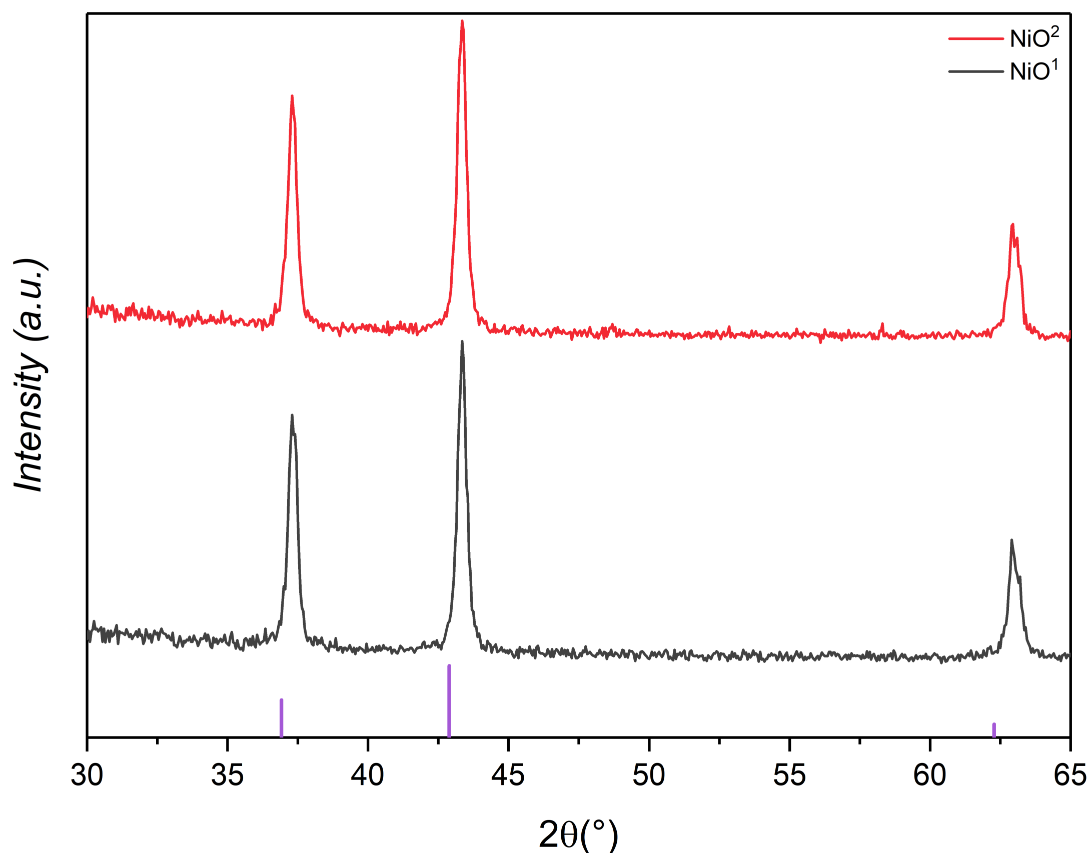

Figure 4.11. pXRD pattern of NiO, with $Ni(acac)_2$ as the starting material on glass substrate.

pXRD, structural analysis was performed on the thin films labelled in table 4.5, which were deposited onto glass substrates. NiO^1 used a methanol ethanol 1:1 ratio solvent solution and NiO^2 used only methanol as the solvent. The patterns illustrated in figure 4.11 resembles the crystal structure of bunsenite, the mineral of nickel oxide which is displayed by the stick pattern in the figure. The slight difference between the stick pattern and the analysed XRD could be due to misalignment of the diffractometer. Parameters similar to chromium oxide were chosen for the deposition as $Ni(acac)_2$ was intended for use as a dopant for chromium oxide. Two types of solvent mixture were tested, a one to one ethanol, methanol mixture and one with only methanol. The film using only methanol as

solvent produced a better homogeneous film and was therefore chosen as the solvent of choice.

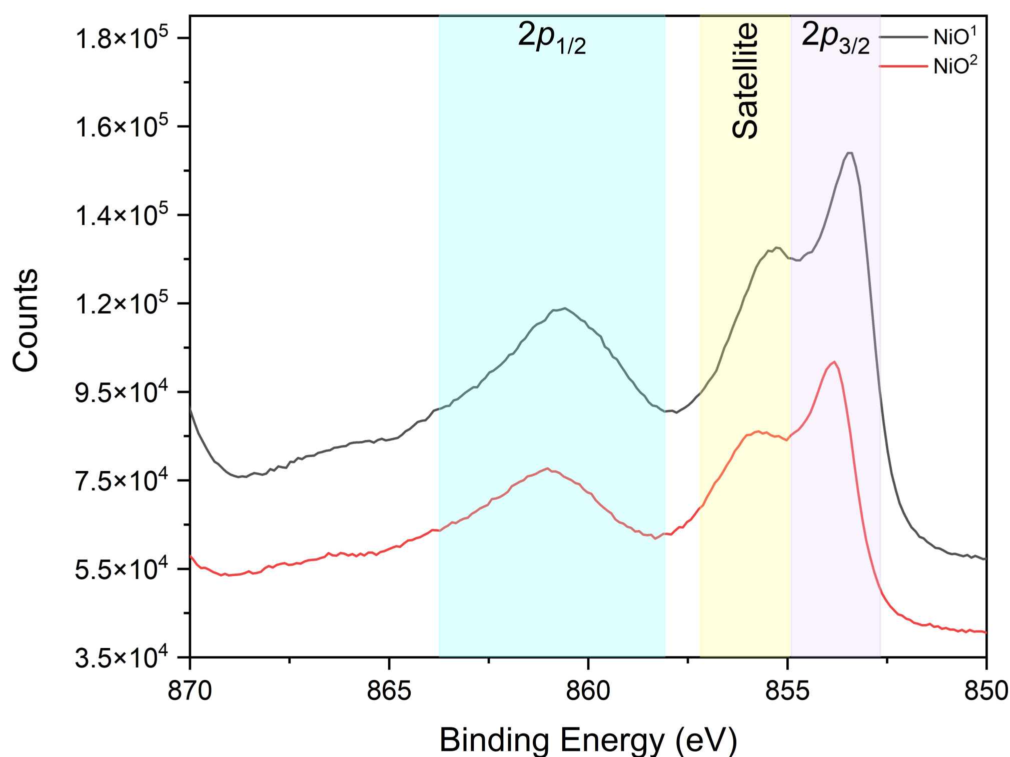

Figure 4.12. Nickel 2*p* spectra of nickel oxide.

XPS surface analysis was conducted using carbon 1*s* as calibration at 284.6 eV. Nickel 2*p* spectrum was generated (figure 4.12) and compared to literature sources. The nickel $2p_{\frac{3}{2}}$ peak demonstrates a multiplet splitting for both samples on glass substrate which is frequently seen for NiO and the peak binding energy are in good agree with literature value illustrated in table 4.6 at 853.7 eV reported by Venezia.[215] The peak also corresponds to the oxidation state Ni(II).[215] No other oxidation states where observed within the detection limit. Table 4.6 illustrates the binding energies of nickel oxide thin films deposited and its literature value.

Raman spectra of different nickel oxide samples at room temperature are shown in figure 4.13 between a frequency range of 100 cm^{-1} to 1700 cm^{-1}. The spectrum shows a main strong broad band at 510 cm^{-1}. Two other weak broad bands were present on the sample that used only methanol as the solvent. The band values of the nickel oxide thin

Table 4.6. Binding energies (eV) of NiO using $Ni(acac)_2$ compared to [a]literature values.

Sample	Ni $2p_{\frac{3}{2}}$	O 1s
NiO[1]	853.4	528.9
NiO[2]	853.8	529.3
NiO[a]	853.7	–

[a] Venezia *et al.*[215]

films are similar with those reported in literature by Mironova-Ulmane[216] for NiO where the bands were reported at roughly 570 cm^{-1}, 1090 cm^{-1} and 1490 cm^{-1}.[216] These bands were not as intense as those described by Mironova-Ulmane, which could be due to the material used for the measurement; i.e. transparent thin films were used here for Raman analysis whereas nanopowders were used in the literature.

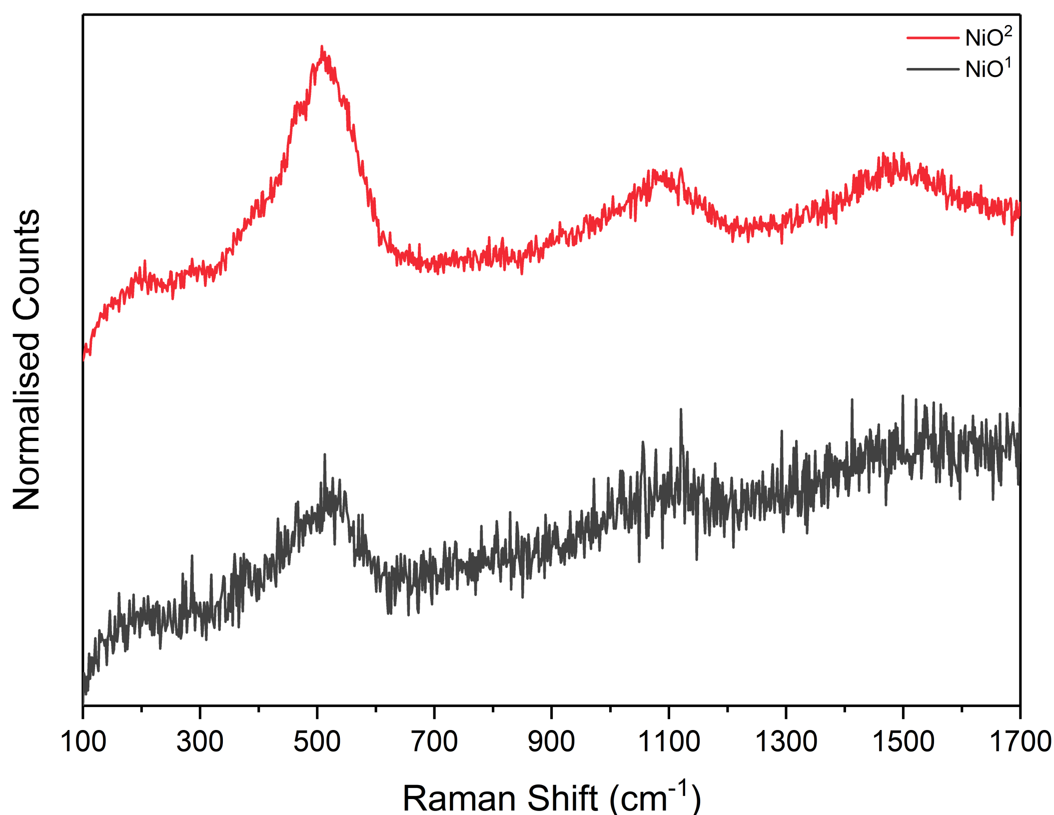

Figure 4.13. Raman spectra of nickel oxide.

Cross section SEM analysis was conducted on nickel oxide films on FTO substrate to measure the thickness of the deposited film which was found to be 13.2 µm thick. Hall

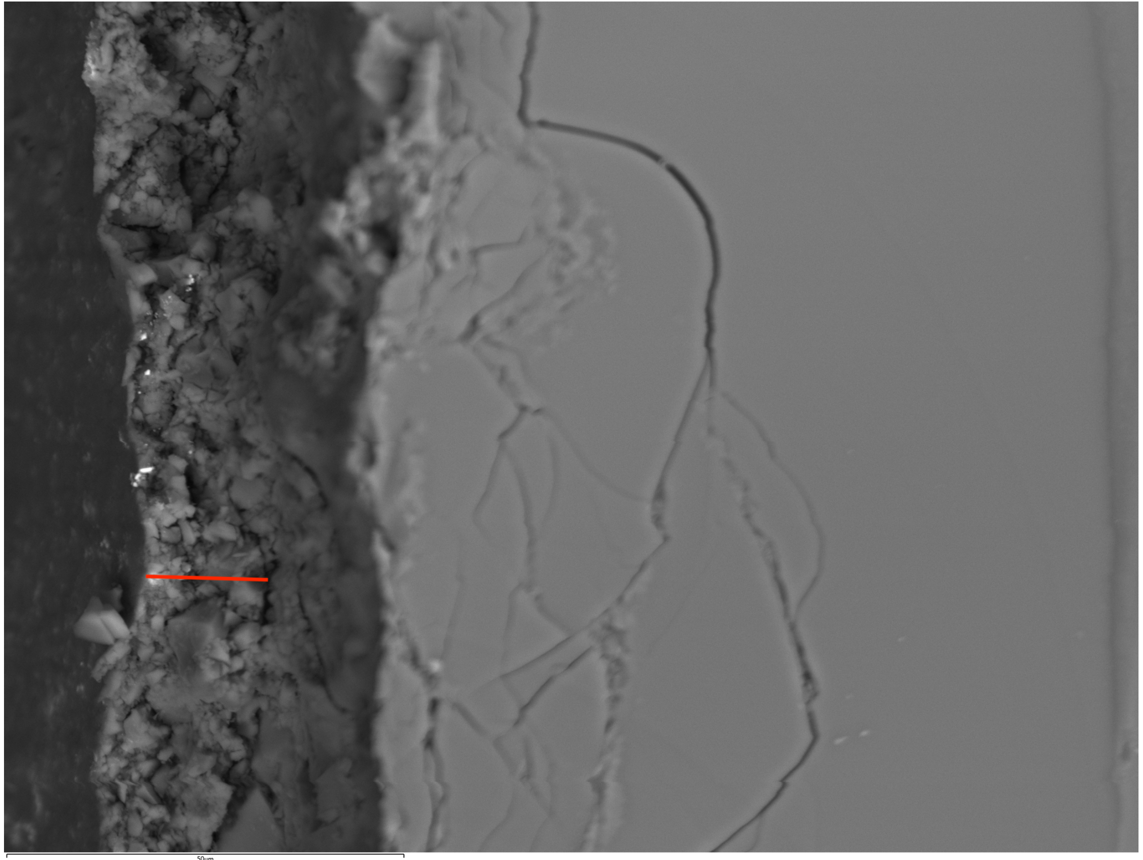

Figure 4.14. Cross section SEM image of NiO on FTO glass.

effect measurement was generated on nickel oxide deposited on quartz substrates. The measurements were conducted under ambient conditions with the thickness at 13.2 µm, a current of 1.0 nA and three sets of measurement were carried out and analysed. Table 4.7 below illustrates the resistivity, Hall mobility, bulk carrier concentration, Hall coefficient and Hall voltage. The Hall voltage values calculated for three of the four measurements where consistent A positive value for Hall voltage also demonstrates the analysed material is of *p*-type nature which holds true for nickel oxide.

Table 4.7. Hall effect measurements of NiO on quartz substrates at room temperature.

Measurements	ρ $\Omega\,cm^3$	μ $cm^2\,V^{-1}\,s^{-1}$	N_B cm^{-3}	R_H $cm^3\,C^{-1}$	V_H mV
A	4.17×10^6	50.96	2.94×10^{10}	2.12×10^8	9.33
B	4.10×10^6	80.81	1.89×10^{10}	3.31×10^8	14.55
C	3.03×10^6	115.2	1.79×10^{10}	3.49×10^8	15.33

Fujime[217] reported the Hall measurement for NiO, however there are differences in parameters used when measuring the Hall effect compared to the parameters used here. Fujime conducted the Hall measurement at a current of 200 mA, thickness of 0.1 cm and a temperature of 16 °C, similar to the temperature that was used for these measurements (300 K). A Hall voltage of 0.0004 mV was reported by Fujime, which is significantly smaller than the value calculated here (9 mV to 15 mV). The Hall coefficient was reported as 2.6×10^{4} cm^{3} C^{-1} compared to a average of 2.697×10^{8} cm^{3} C^{-1}. Carrier concentration was also different (2.7×10^{14} cm^{-3} vs an average of 2.21×10^{10} cm^{-3}). Other factors may also have an affect on the differences seen such as ohmic contact geometry and sample uniformity as explained previously.[217]

More recently, Ali[218] reported the analysis of Hall measurement on pure NiO thin films.[218] The thin films reported were annealed at 450 °C and have a reported values of $\rho = 5.15 \times 10^{4}\ \Omega$ cm, $R_H = 5.32 \times 10^{6}$ cm^{3} C^{-1}, $N_B = 1.2 \times 10^{12}$ cm^{-3} and $\mu = 98.19$ cm^{2} V^{-1} s^{-1}. The resistivity of NiO measured here is higher than the reported value but the average Hall mobility is relatively similar.

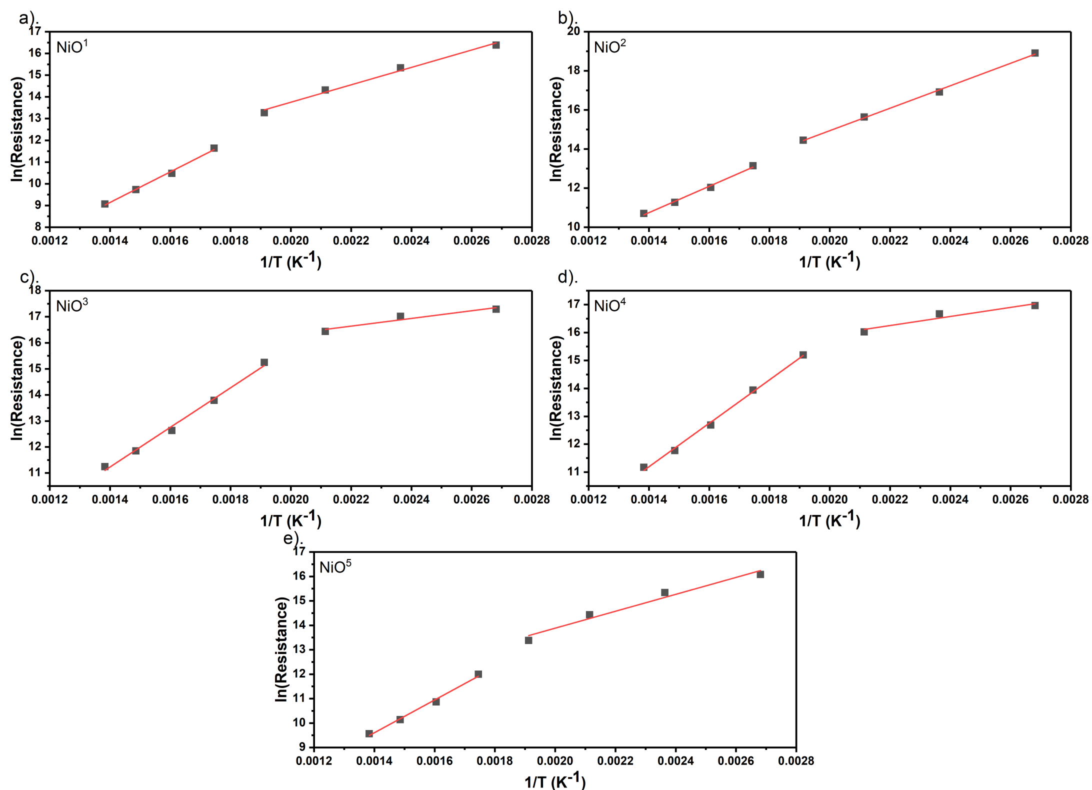

Figure 4.15. Arrhenius plots for the resistivity of NiO thin film under nitrogen.

Baseline resistance analysis under nitrogen at increasing temperatures (375 K to 725 K) were conducted on five different nickel oxide thin film on alumina sensor substrate samples. The activation energy levels were calculate from an arrhenius plot using the collected resistance values shown in figure 4.15. As shown in figure 4.16, two different activation energies are seen for the nickel oxide thin film samples. One at low temperature and another at high temperature region, where the transition point is between 475 K to 525 K. The activation energies at low temperature (375 K to 475 K) closely resembles the litereature value (0.46 eV) for samples NiO^1, NiO^2 and NiO^5. The activation energies at the higher temperature region demonstrates similar value to single crystal nickel oxide (0.75 eV) reported by Gray and Darby.[219,220]

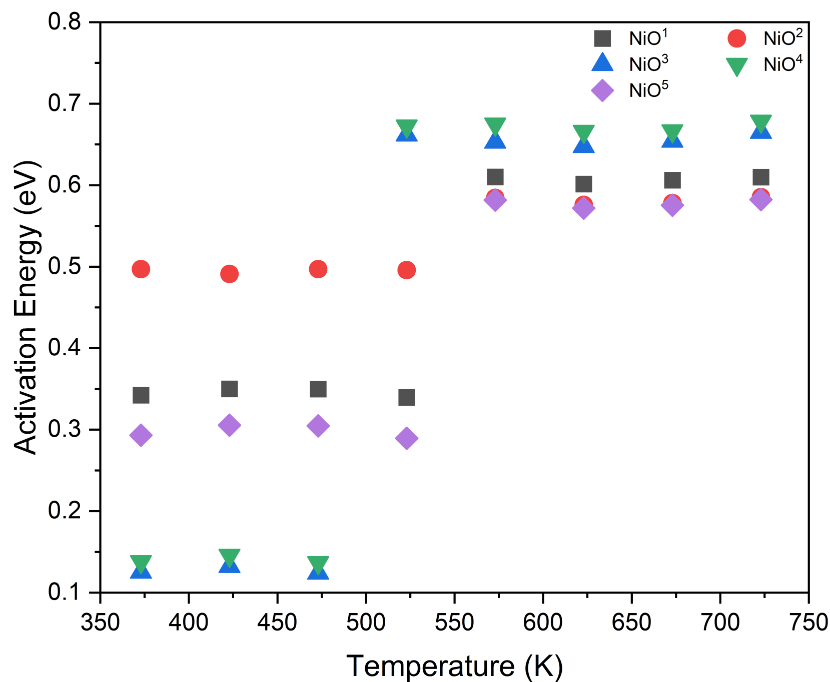

Figure 4.16. Nickel oxide activation energy against temperature under nitrogen.

4.3 Summary

In summary, Cr_2O_3 and NiO thin films were successfully deposited onto glass, alumina and sensing substrate via AACVD. Surface characterisation of Cr_2O_3 were successfully analysed (pXRD, XPS, Raman). The thickness of Cr_2O_3 film was measured to be at 33 µm

via SEM imaging. Using the thickness, the Hall voltage was calculated for Cr_2O_3. However, due to ohmic contact geometry, sample uniformity and accuracy of the thickness of the film, the measured voltage may have shifted due to ohmic drop given an inaccurate reading of the measurements and hence inaccurate Hall voltage. The activation energy was also calculated by measuring the baseline resistance of Cr_2O_3 sensors in a pure N_2 environment at elevated temperatures. Two distinct energy levels were measured, one above 500 K (0.46 eV, 0.54 eV and 0.56 eV) and one below 500 K (0.24 eV and 0.35 eV) for each of the sample. These values were relatively similar to Kofstad's reported energy value (0.2 eV) at 700 °C. Surface characterisation of NiO were also successfully analysed (pXRD, XPS, Raman). The thickness of the film was measured to be at 13.2 µm via SEM imaging. Again using the film thickness, the Hall voltage was calculated. The activation energy calculated coincides with literature values.

Chapter 5

Mixed Metal Oxide Thin Films

5.1 Chromium Titanium Oxide (CTO)

5.1.1 Introduction

CTO is a good *p*-type material for use in gas sensors due to its tolerance towards relative humidity, good baseline stability and reasonable sensitivity. CTO is already commercialised, however, herein CTO thin films are deposited via an AACVD and the structural and electronic properties of CTO is investigated.

Thin films deposited onto alumina sensing substrates were compared to deposited Cr_2O_3 and TiO_2 films on glass substrates and commercially made screen printed CTO sensors (from Alphasense). For the commercial CTO, two different types of sensor were analysed; one with a protective filter layer and one without the protective filter layer. The layer is a microporous, precious metal free ceramic oxide which is coated onto the sensing layer and is used to protect the sensing layer from contamination, reduce long term baseline drift and improve selectivity to certain gases due to its catalytic activity.

5.1.2 Film Characterisation

Structural analysis (pXRD) was conducted on different compositions ($x = 0.05 - 0.25$) of CTO thin films deposited via AACVD and annealed at 600 °C. Figure 5.1 illustrates

the patterns for the thin film samples and compared to TiO_2 and Cr_2O_3. Stick patterns for eskolaite (blue), anatase (olive), corundum (orange) and gold (yellow) are also shown.

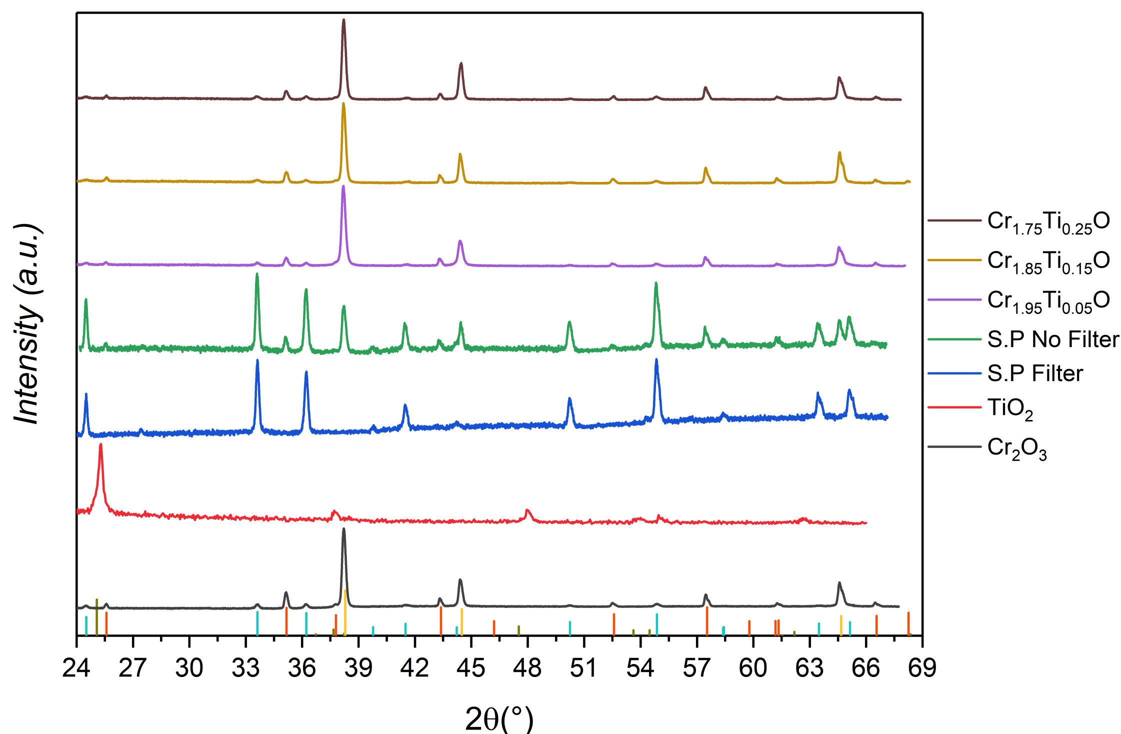

Figure 5.1. pXRD patterns of commercial screen printed CTO sensors, different titanium loading AACVD deposited CTO sensors annealed at 600 °C for 24 h, TiO_2 and Cr_2O_3.

The 2θ peaks indicated on the pattern of CTO films corresponds to the crystal structures of eskolaite (Cr_2O_3), corundum (Al_2O_3) and gold shown by the stick pattern. The occurrence of corundum and gold is due to the substrates used, i.e. corundum comes from the miniature alumina sensing platform and gold comes from the ink used on the sensing electrode. The CTO pattern was in close alignment with Cr_2O_3 films deposited and it was demonstrated as Ti dopant increased from 0.05 to 0.15 and 0.25, no measurable change in crystal structure was observed and anatase phase TiO_2 2θ peaks were not present. This indicated the full incorporation of Ti dopant into the lattice of Cr_2O_3 and no phase separation had occurred within the limit of detection of XRD. Figure 5.2 displays a low angle view of the pXRD samples. It can be seen that the titanium 2θ peak for [1 0 1] is not present in any of the CTO samples

Looking at the two screen printed commercial CTO sensors displayed in figure 5.1, it can be seen that the 2θ peaks for eskolaite are more intense than that of AACVD CTO,

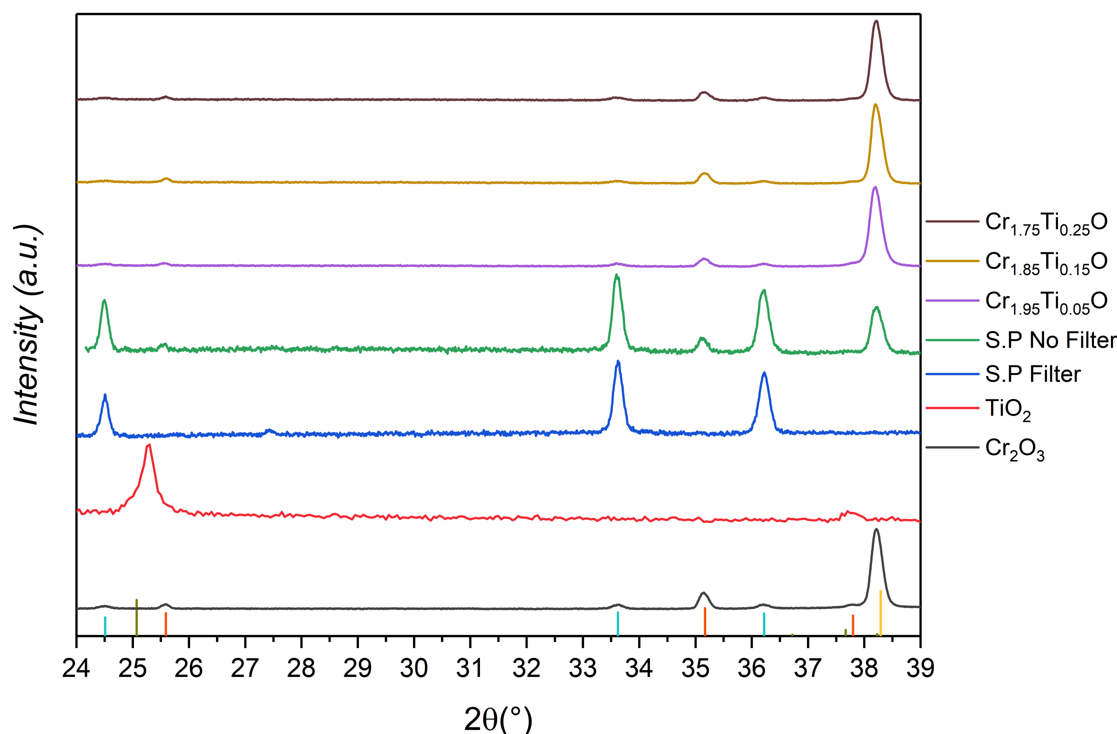

Figure 5.2. Low angle plot of pXRD patterns for commercial screen printed CTO sensors, different titanium loading AACVD deposited CTO sensors annealed at 600 °C for 24 h, TiO_2 and Cr_2O_3.

for example the 2θ peak at 24.5 for the [0 1 2] plane can clearly be seen (a sharp intense peak); whereas for AACVD samples, the peak is seen as a weak broad peak in figure 5.2. This could be due to the difference in thickness between the samples and also the reason why corundum is not present for the S.P filter sensor and barely present in the non filter S.P sensor. Table 5.1 displays the 2θ peaks CTO and its corresponding lattice planes in relation to eskolaite.

EDS mapping was performed to analyse the elements on the CTO films deposited by AACVD. Two areas were mapped on the miniature sensor substrates; on the gold electrode and on the alumina platform. As for screen printed CTO, the films were thick and hence the sensor substrate could not be seen under the microscope, therefore various spots were analysed on the thick film to see if the films were homogeneous and a average atomic percentage was calculated. Table 5.2 depicts the observed atomic percentage of the different compositions AACVD CTOs and screen printed CTO with and without the filter layer.

The atomic percentage of the AACVD CTO thin films shown in table 5.2 consist

Table 5.1. pXRD 2θ peaks and lattice planes of $Cr_{2-x}Ti_x$ annealed at 600 °C and screen printed CTO sensors.

pXRD 2θ peak (°)					Lattice Plane
$Cr_{1.75}Ti_{0.25}$	$Cr_{1.85}Ti_{0.15}$	$Cr_{1.95}Ti_{0.05}$	S.P Filter	S.P no Filter	
24.5	24.5	24.5	24.5	24.5	(012)
33.6	33.6	33.6	33.6	33.6	(104)
36.2	36.2	36.2	36.2	36.2	(110)
–	–	–	39.7	39.9	(006)
41.6	41.6	41.6	41.5	41.5	(113)
–	–	–	44.2	–	(202)
–	–	50.2	50.2	50.2	(024)
54.9	54.8	54.8	54.9	54.8	(116)
–	–	–	58.4	58.4	(122)
–	–	–	63.4	63.4	(214)
–	–	–	65.1	65.1	(300)

largely of both chromium and oxygen (an average of roughly 1 : 2 ratio), which was to be expected. Small amounts of titanium percentage was also observed. This seems to be the case for the commercial sensors as well, a chromium: oxygen ratio of about 1 : 2 and 1 : 1.7 for filter and non-filter respectively. The relative compositions were calculated using these observed atomic percentage which are displayed in table 5.3. The doping levels of titanium from AACVD samples are relatively similar to screen printed samples and hence can be comparable when analysing its gas sensing performance.

Trace amounts of Ca, Pb and Cd were seen on the AACVD deposited sensors. These trace elements could be from contamination during the annealing phase of the making of the sensor, i.e. contaminants were present inside the furnace or on the ceramic crucible. Another reason for the present of these elements is due to the gold ink on the electrode. Analysis of these trace amount is shown below in the analysis of XPS.

X-ray photoelectron spectroscopy (XPS) surface analysis was conducted using carbon 1*s* as calibration at 284.6 eV for charge shift corrections. The survey spectra of the dif-

Table 5.2. EDS analysis and atomic percentage comparison of CTO sensors.

Samples	Label	Cr	Ti	O	Al	Au	Ca	Pb	Cd
$Cr_{1.75}Ti_{0.25}$ (gold electrode)	CTO(0.25)G	25.65%	2.09%	67.02%	0.20%	4.19%	0.61%	0.01%	0.22%
$Cr_{1.75}Ti_{0.25}$ (alumina platform)	CTO(0.25)A	23.16%	1.83%	59.45%	15.50%	0%	0.05%	0.01%	0%
$Cr_{1.85}Ti_{0.15}$ (gold electrode)	CTO(0.15)G	19.86%	1.08%	69.21%	2.57%	5.95%	0.99%	0%	0.34%
$Cr_{1.85}Ti_{0.15}$ (alumina platform)	CTO(0.15)A	15.97%	0.89%	58.79%	24.17%	0%	0.13%	0%	0.06%
$Cr_{1.95}Ti_{0.05}$ (gold electrode)	CTO(0.05)G	24.03%	0.54%	68.86%	0.26%	5.18%	0.85%	0.01%	0.27%
$Cr_{1.95}Ti_{0.05}$ (alumina platform)	CTO(0.05)A	19.30%	0.45%	58.96%	21.13%	0%	0.06%	0.01%	0.08%
S.P with filter	–	32.64%	2.17%	65.19%	–	–	–	–	–
S.P without filter	–	36.25%	2.13%	61.16	0.15%	–	0.37%	–	–

Table 5.3. Theoretical and actual composition of AACVD CTO sensors.

Label	Targeted composition	Actual composition
CTO(0.25)G	$Cr_{1.75}Ti_{0.25}$ (gold electrode)	$Cr_{1.85}Ti_{0.15}$
CTO(0.25)A	$Cr_{1.75}Ti_{0.25}$ (alumina platform)	$Cr_{1.85}Ti_{0.15}$
CTO(0.15)G	$Cr_{1.85}Ti_{0.15}$ (gold electrode)	$Cr_{1.90}Ti_{0.10}$
CTO(0.15)A	$Cr_{1.85}Ti_{0.15}$ (alumina platform)	$Cr_{1.89}Ti_{0.11}$
CTO(0.05)G	$Cr_{1.95}Ti_{0.05}$ (gold electrode)	$Cr_{1.96}Ti_{0.04}$
CTO(0.05)A	$Cr_{1.95}Ti_{0.05}$ (alumina platform)	$Cr_{1.95}Ti_{0.05}$
S.P Filter	–	$Cr_{1.87}Ti_{0.13}$
S.P No Filter	–	$Cr_{1.89}Ti_{0.11}$

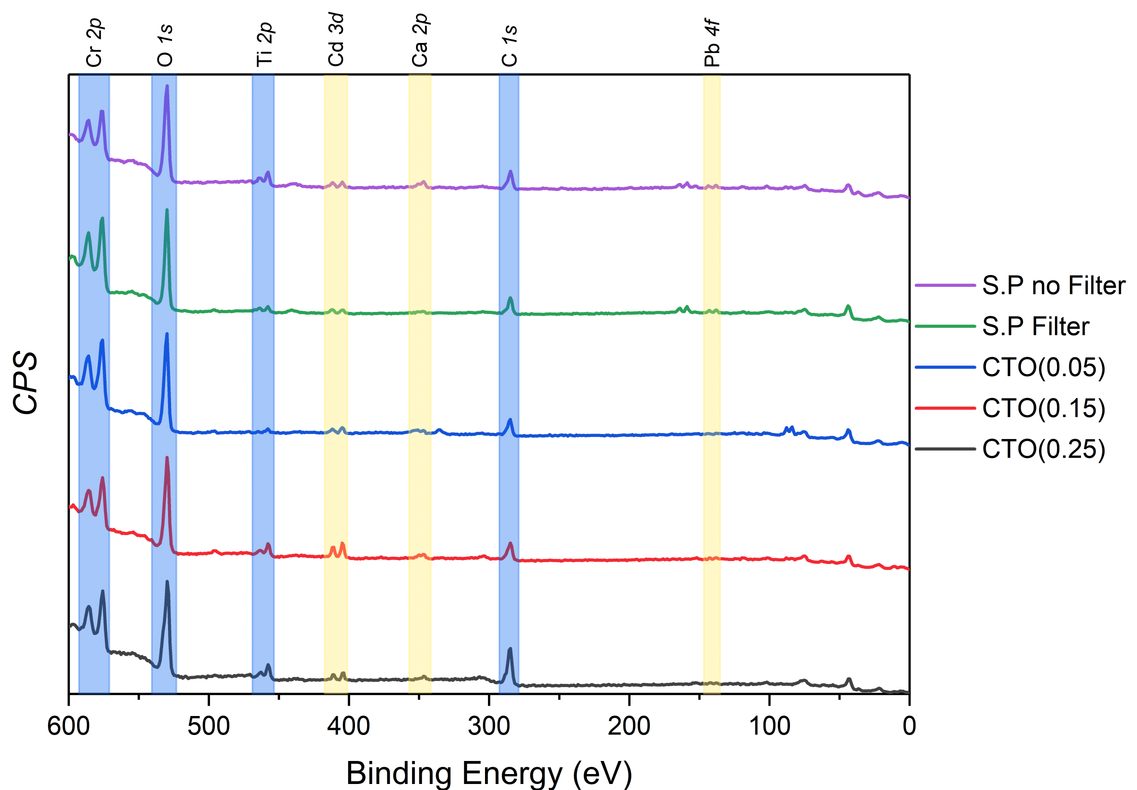

Figure 5.3. XPS survey spectrum of AACVD and screen printed CTO.

ferent CTO deposited onto alumina sensing platform and S.P sensors are illustrated in figure 5.3.The survey scan demonstrated sharp peaks attributed to Cr, Ti, O and C which are highlighted in blue. However, trace amounts of Ca, Cd and Pb were again present in the survey scan which are highlighted in yellow, which is in agreement with EDS analysis.

To confirm whether these trace amount are contaminants or not, CTO was deposited

onto FTO glass and annealed at 600 °C for 24 h. XPS analysis showed no Ca, Cd or Pb, which removed the possibility of contamination during annealing or from the ceramic crucible (figure 5.4). Therefore, the most probable explanation would be the contaminants coming from the gold ink of the electrode on the sensing substrate. Hence, samples were made on miniature blank alumina substrates made under the same conditions, annealing temperature and time. Figure 5.4 also shows the sample on a miniature blank alumina substrate does not contain any of the trace species seen in the sensor substrates. It can be concluded that these trace amount of species are solely due to the gold ink used to make the electrode. An interesting point to add, these 2^+ ions could have an affect on the gas sensing performance of these AACVD sensors, as they would act as a p-type dopant in the CTO matrix.

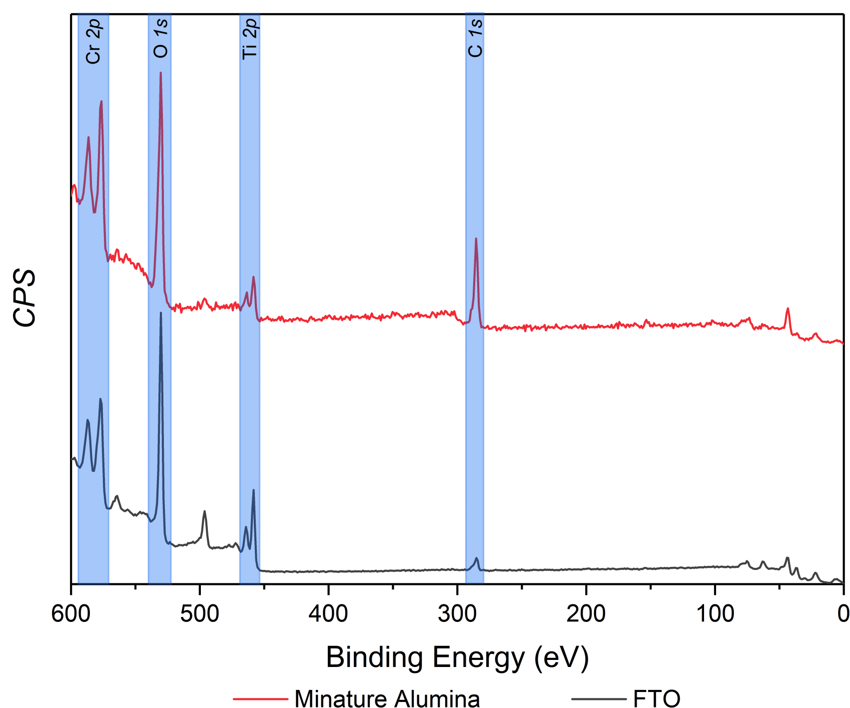

Figure 5.4. XPS survey spectrum of AACVD CTO on FTO and miniature alumina substrate.

Figure 5.5 illustrates both chromium and titanium 2*p* XPS spectra for AACVD samples. The peak for Cr $2p_{\frac{3}{2}}$ ranges from 575.7 eV to 576.1 eV which corresponds to Cr^{3+}. The values observed correlate to literature values for Cr_2O_3 (576.1 eV).[205] For the Ti 2*p* spectra, the Ti $2p_{\frac{3}{2}}$ ranged from 457.4 eV to 457.8 eV, corresponding to Ti^{4+} and similar

to the value reported by Ho *et al.* (458.7 eV).

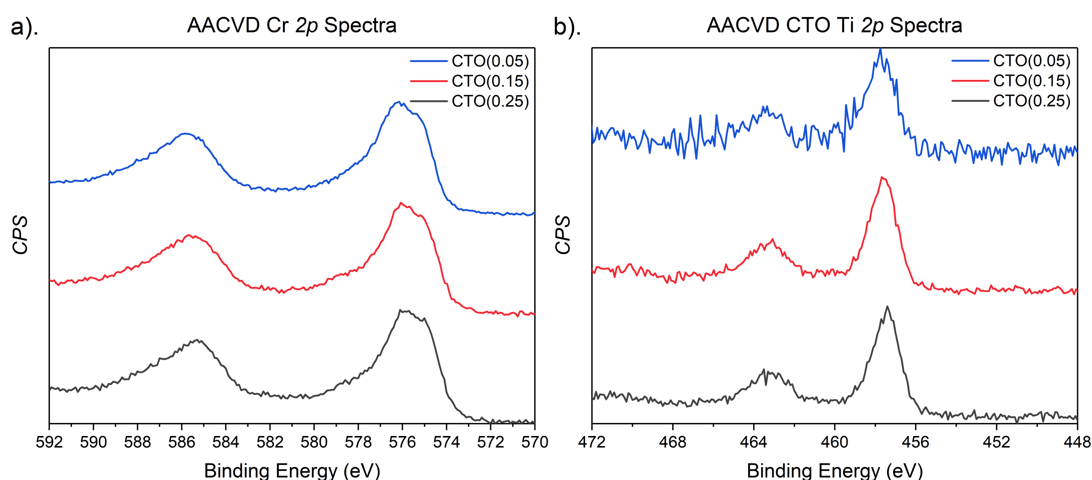

Figure 5.5. Cr 2*p* and Ti 2*p* spectra of AACVD CTO.

The survey scan shown in figure 5.3 of the commercially screen printed CTO sensors displayed peaks attributing to Cr, Ti, O, C, Ca, Cd, Pb and Figure 5.6 shows the Cr 2*p* and Ti 2*p* spectra for screen printed sensor. Again the binding energies with and without the ATF layer were similar to the deposited thin films and literature values for both Cr_2O_3 and TiO_2. The Cr $2p_{\frac{3}{2}}$ peak displayed in the chromium 2*p* scan corresponded to Cr^{3+} and no other oxidation states of chromium were observed. The same goes for the Ti 2*p* spectra; only Ti^{4+} was observed. The detection of Ca, Cd and Pb on commercial screen printed sensors correlates with the assumption that the gold ink used for the electrode contain these trace amount of metal elements.

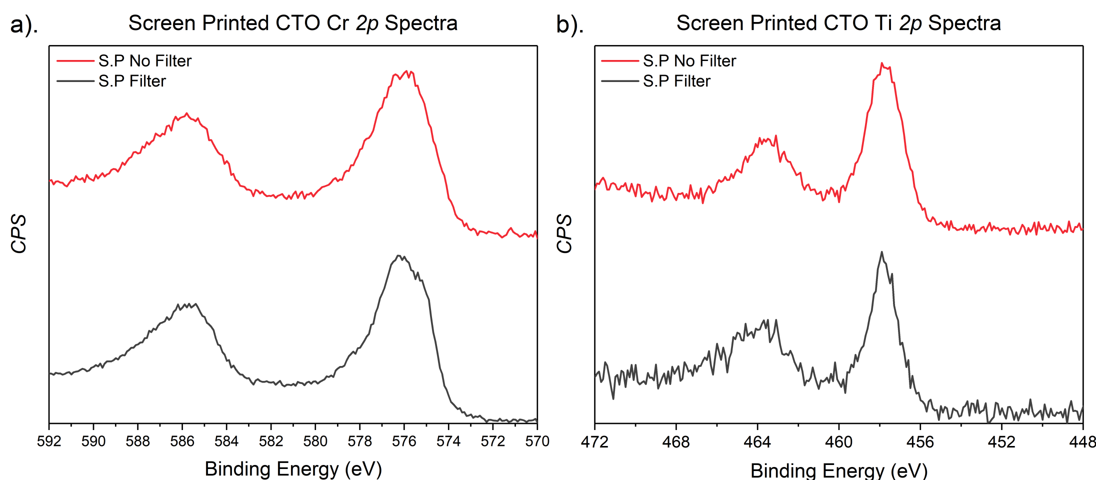

Figure 5.6. Cr 2*p* and Ti 2*p* spectra of screen printed CTO.

Figure 5.7 illustrates the O 1*s* spectra for the AACVD and screen printed CTO and displays intense peaks between 529.2 eV to 529.8 eV. The peaks correlates to lattice oxygen of the oxide. The O 1*s* also demonstrates a broad asymmetric peak which could be attributed to the overlapping of oxygen containing species peaks such as OH^-. Table 5.4 shows the binding energies of the sample and literature sources of Cr_2O_3 and TiO_2.

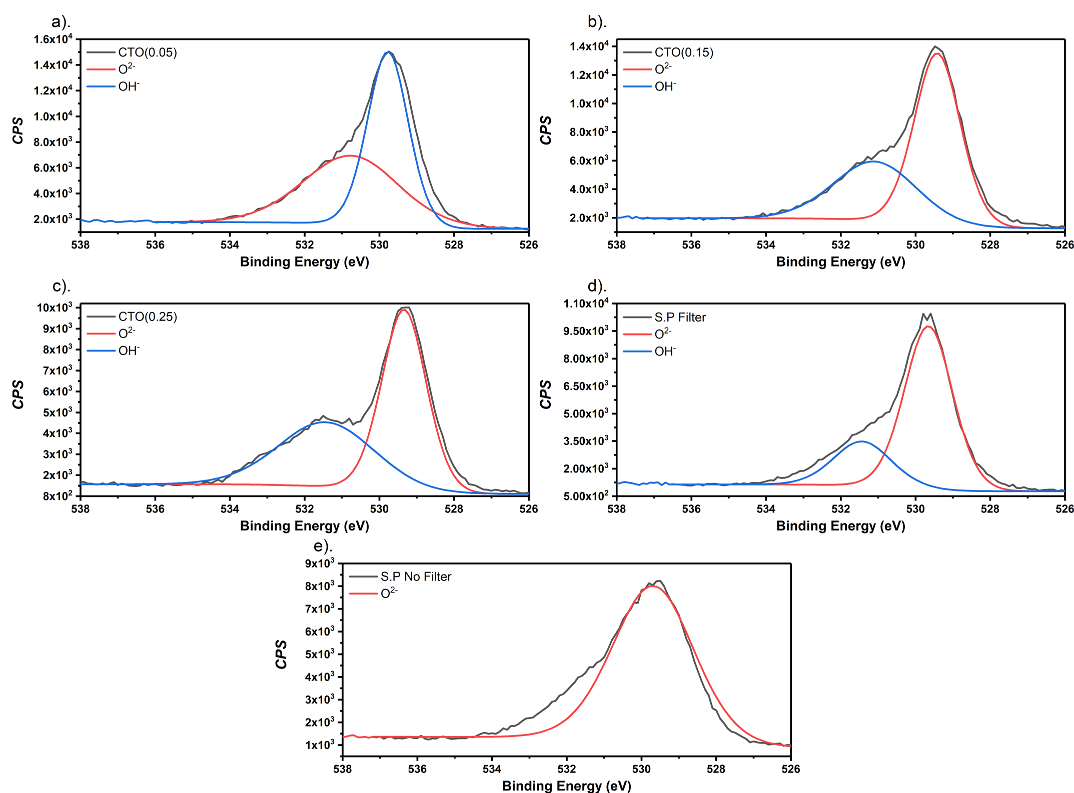

Figure 5.7. O 1*s* spectra of AACVD and screen printed CTO.

The composition ratio of deposited CTO could be calculated peak area and RSF values. Table 5.5 displays the peak area, ratio and relative composition of the samples. The composition ratio of chromium to titanium was calculated to be 1.62 : 0.38 for CTO(0.25), 1.61 : 0.39 for CrT(0.15) and 1.89 : 0.11 for CTO(0.05). The reason for the difference in values between EDS and XPS analysis is because EDS is an elemental analysis which gives the bulk concentration of elements present in the sample. Whereas for XPS, it gives the near surface region chemical composition of the sample.

Raman spectra of AACVD and screen printed CTO sensor substrates were analysed and compared to Cr_2O_3 and anatase TiO_2 on glass substrateas illustrated in figure 5.8.

Table 5.4. Binding energies (eV) of $Cr_{2-x}Ti_xO_3$ annealed at 600 °C (^{a,b}literature values).

Sample	Cr $2p_{\frac{3}{2}}$	Ti $2p_{\frac{3}{2}}$	O $1s$
CTO(0.25)	575.7	457.4	529.2
CTO(0.15)	576.1	457.7	529.5
CTO(0.05)	576.1	457.8	529.8
S.P CTO (ATF layer)	576.0	457.9	529.6
S.P CTO (no ATF layer)	576.4	458.1	530.2
$Cr_2O_3{}^a$	576.1	–	–
$TiO_2{}^b$	–	458.7	–

[a] Biesinger *et al.* referenced to Au $4f_{\frac{3}{2}}$ at 83.95 eV.[205]
[b] Ho *et al.*[221]

Table 5.5. Composition Ratio of CTO sensor substrates and screen printed sensors.

Sample	Area			Ratio
	Cr $2p_{\frac{3}{2}}$	Ti $2p_{\frac{3}{2}}$	O $1s$	
CTO(0.25)	13159.1	2066.2	13200.5	4.3 : 1 : 11.4
CTO(0.15)	15930.6	2581.9	18892.8	4.2 : 1 : 13
CTO(0.05)	23434.2	1003.6	18353.0	15.9 : 1 : 32.6
S.P Filter layer	16847.0	900.4	14552.2	12.7 : 1 : 28.8
S.P no Filter layer	12237.9	2503.4	19731.8	3.3 : 1 : 14

The absence of anatase phase TiO_2 peaks for the CTO samples correlates in good agreement with pXRD pattern demonstrating no phase separation on these films. The peaks observed for these samples resembles that of Cr_2O_3, in particular the intense peak around the 550 cm^{-1} is similar to the intense peak at 552 cm^{-1} for Cr_2O_3 which corresponds to the A_{1g} peak. The CTO samples are also comparable to literature values reported by Li[222] and Challagulla[223] as shown in figures 5.9 and 5.10 for Cr_2O_3 and TiO_2.[222,223] Table 5.6 illustrates the peak assignment for CTO and comparison to literature values of Cr_2O_3.

Cross section SEM imaging was taken to analyse the film thickness of CTO films. The image was taken from an equivalent deposition used for CTO(0.15) on a sensor sub-

Table 5.6. Raman shift assignment for AACVD and screen printed CTO sensors.

Observed Raman Shift (cm^{-1})					Literature [a,b] (cm^{-1})	
CTO(0.25)	CTO(0.15)	CTO(0.05)	S.P with filter	S.P wihout filter	Cr_2O_3	TiO_2
303	302	305	304	307	303	134
349	351	349	347	346	351	382
–	–	–	–	–	530	500
555	552	552	547	547	551	618
613	611	608	606	606	612	

[a] Beattie *et al.*[208]
[b] Challagulla *et al.*[223]

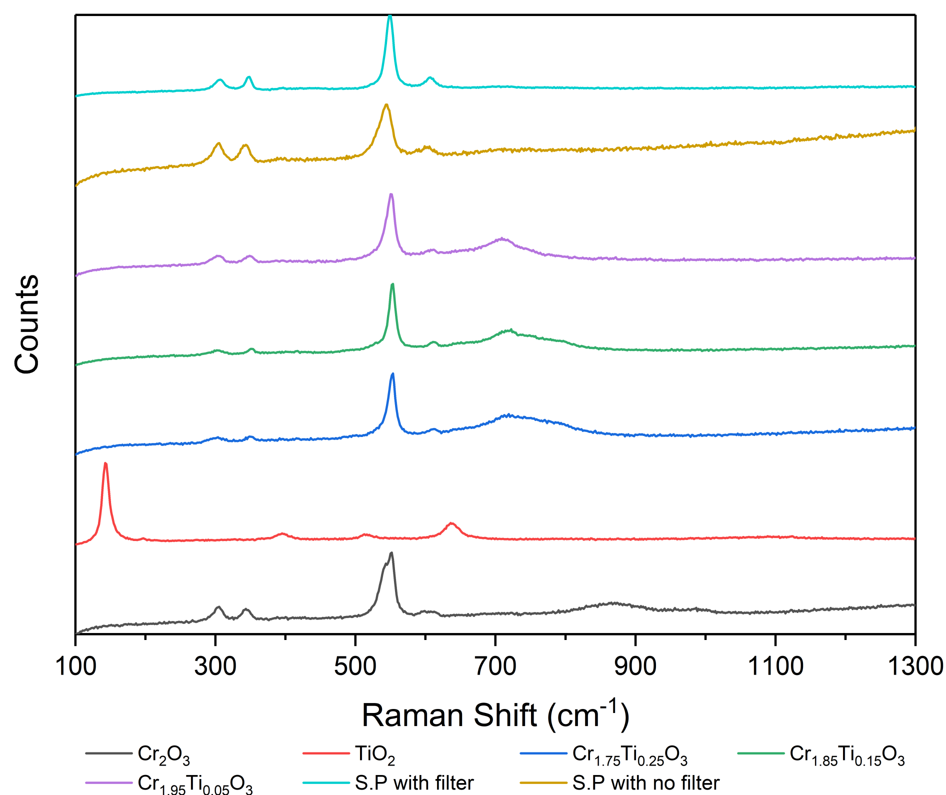

Figure 5.8. Raman spectra of Cr_2O_3, TiO_2, AACVD and screen printed CTO films.

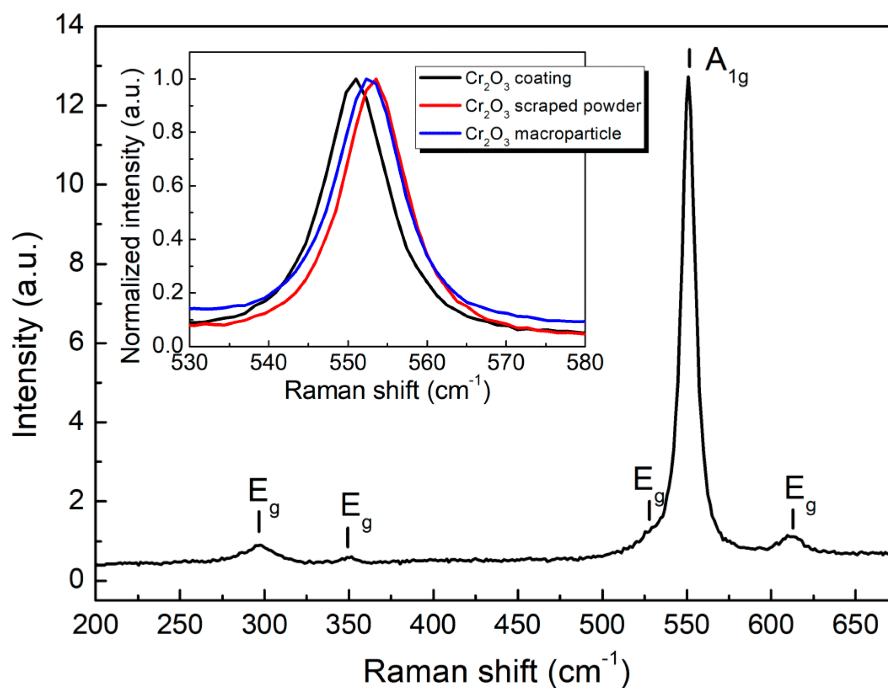

Figure 5.9. Cr_2O_3 raman spectra reported by Li.[222]

strate but on quartz substrate. The thickness of this film was determined to be 12.5 µm, which is about 20 µm thinner than Cr_2O_3 thickness measured previously. The thickness

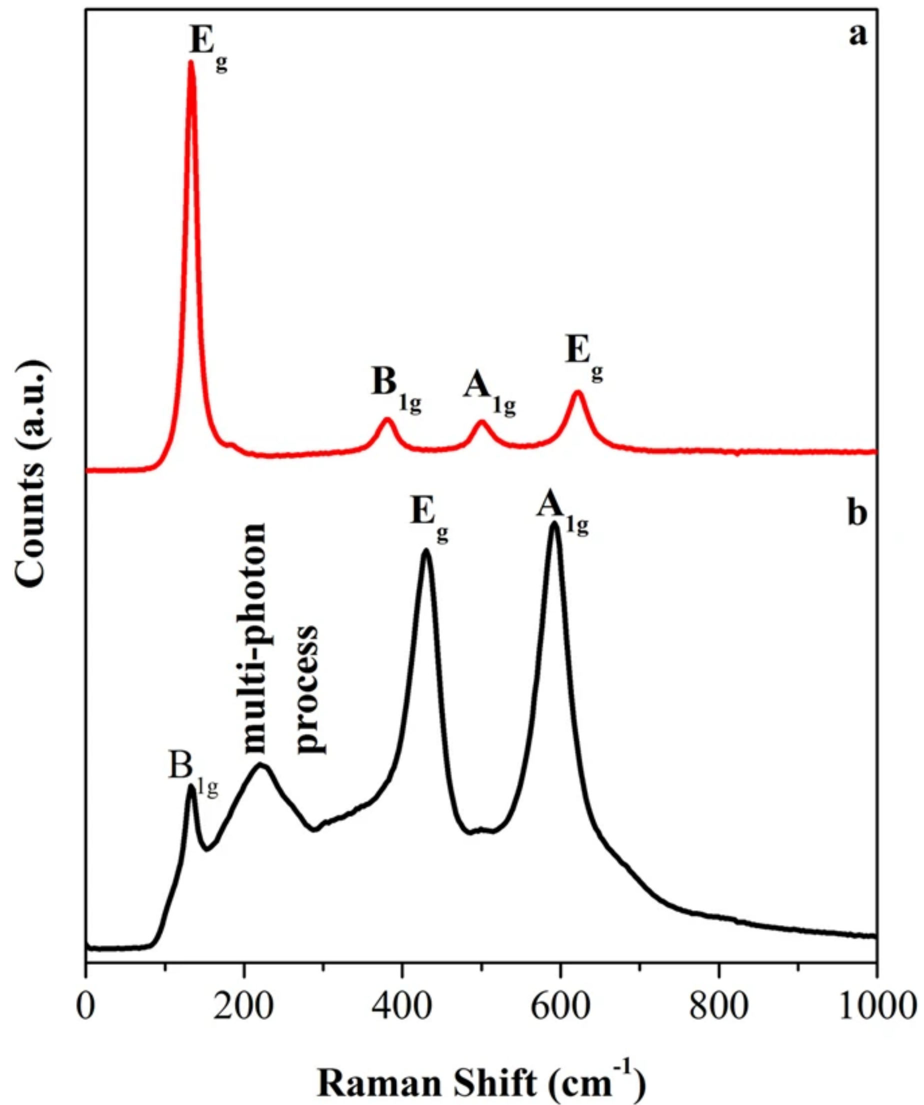

Figure 5.10. TiO_2 raman spectra reported by Challagulla.[223]

value obtained was then used for Hall measurement analysis. The measurements were conducted under ambient conditions at a current of 1.0 nA, where 4 measurements of the same sample was taken. Table 5.7 illustrates the Hall measurements and the calculated Hall voltage (V_H). The bulk carrier concentration displays negative values for most of the measurements, there are a number of factors for this such as poor ohmic contact geometry and accuracy of thickness of the film. It is therefore difficult to be certain if these measurements are correct for CTO. Conde-Gallardo[224] reported a resistivity value between $10^6\,\Omega$ cm to $10^7\,\Omega$ cm for CTO films deposited via AACVD on a sapphire substrate with a composition of $Cr_{1.83}Ti_{0.17}$.[224] The resistivity measurements recorded here are also the same as Conde-Gallardo's value. Conde-Gallardo also mentioned in the report that due

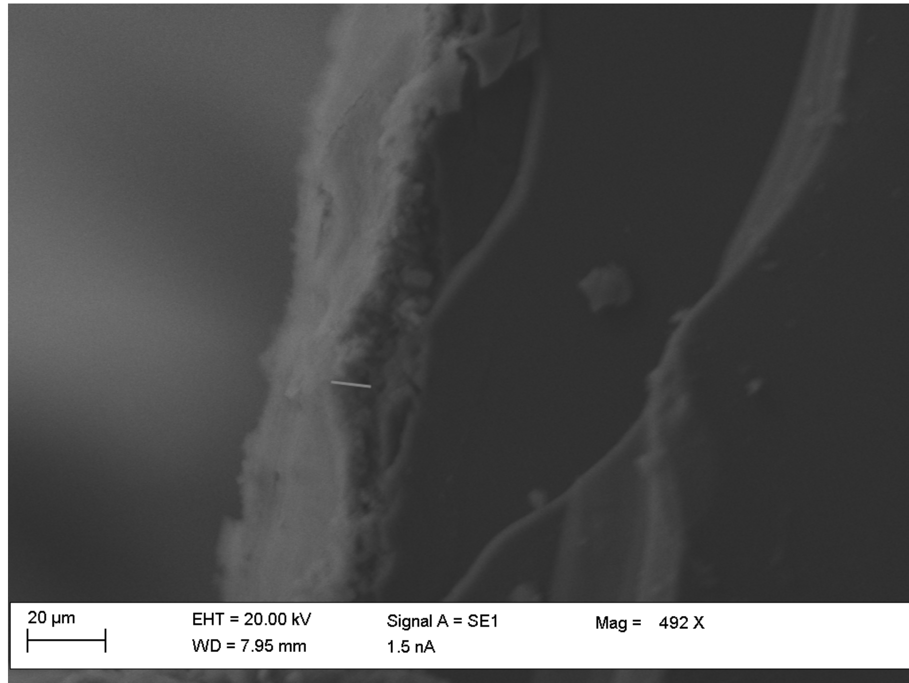

Figure 5.11. Cross section SEM image of CTO on quartz substrate.

to the high resistivity of CTO films Hall effect measurements could not be performed and hence they were unable to find the conduction type of the material, which may also be applicable here.

Table 5.7. Hall effect measurement of CTO sensors.

Measurements	ρ Ω cm	μ cm^2 V^{-1} s^{-1}	N$_B$ cm^{-3}	R$_H$ cm^3 C^{-1}	V$_H$ mV
A	4.97×10^6	4.53	-2.78×10^{11}	-2.25×10^7	−1.04
B	2.15×10^7	8.81	3.30×10^{10}	1.89×10^8	8.87
C	5.29×10^6	29.18	-4.05×10^{10}	-1.54×10^8	−7.15
D	3.18×10^{11}	1.45×10^{-3}	-1.35×10^{10}	-4.62×10^8	−21.45

An Arrhenius plot for two different CTO(0.15) sensors were plotted in figure 5.12. Figure 5.13 illustrates the activation energy of two different CTO(0.15) sensors. The two samples analysed demonstrated two different activation energies. At 475 K and below, the activation energy was 0.1 and 0.07 electronvolt for the two samples and above 475 K , the activation energies were 0.73 and 0.46 eV. Parkin[225] reported an activation energy value of 0.71 eV from a temperature range of 200 °C to 600 °C (473 K to 873 K) which closely

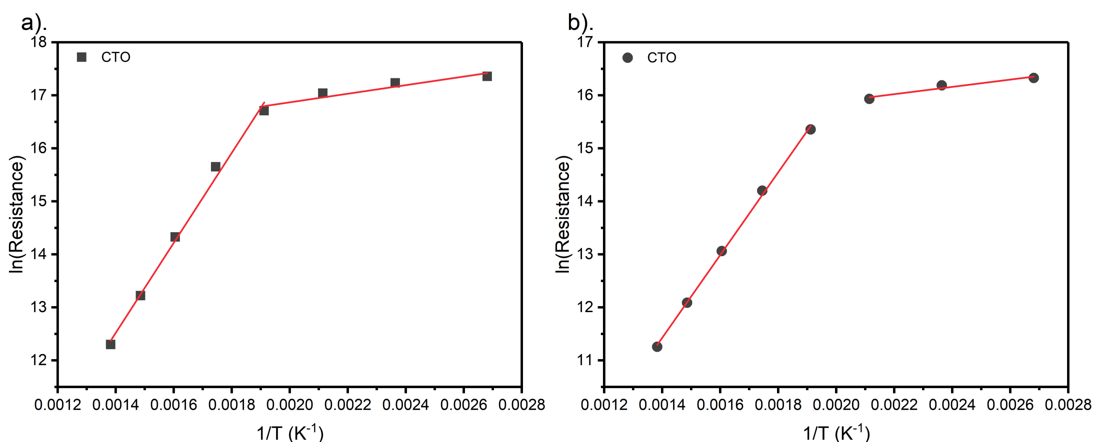

Figure 5.12. Chromium titanium oxide Arrhenius plot.

resembles to the values obtained here of temperatures above 475 K. However, the calculation for the activation energy differs slightly, Parkins calculation involves assessing the gas response of ethanol (80 ppm pulses) in dry air and 50 % relative humidity to formulate the activation energy calculations. Whereas in this case the values where calculated under pure nitrogen which may or maybe have an effect towards the energy calculations.[225] The activation energies calculated for CTO are roughly 0.1 eV and 0.2 eV different compared to those observed for Cr_2O_3 at high temperature conditions (0.46 eV and 0.73 eV vs 0.45 eV to 0.6 eV).

5.2 Tungsten Doped-chromium Oxide (CWO)

5.2.1 Introduction

In general *p*-type semiconductors are low in conductivity which makes investigating their response via resistance difficult. Doping can improve conductivity whilst maintaining favourable properties. Tungsten would be an ideal choice as another *n*-type dopant, as tungsten (VI) is similar in terms of ionic radii to chromium (III) (0.6 Å vs 0.615 Å) and hence can be substituted into the lattice; but it is a very strong dopant (6+ vs 3+), so small levels of substitution should improve resistance.[226]

Chromium hexacarbonyl was again chosen as the starting precursor for the formation of

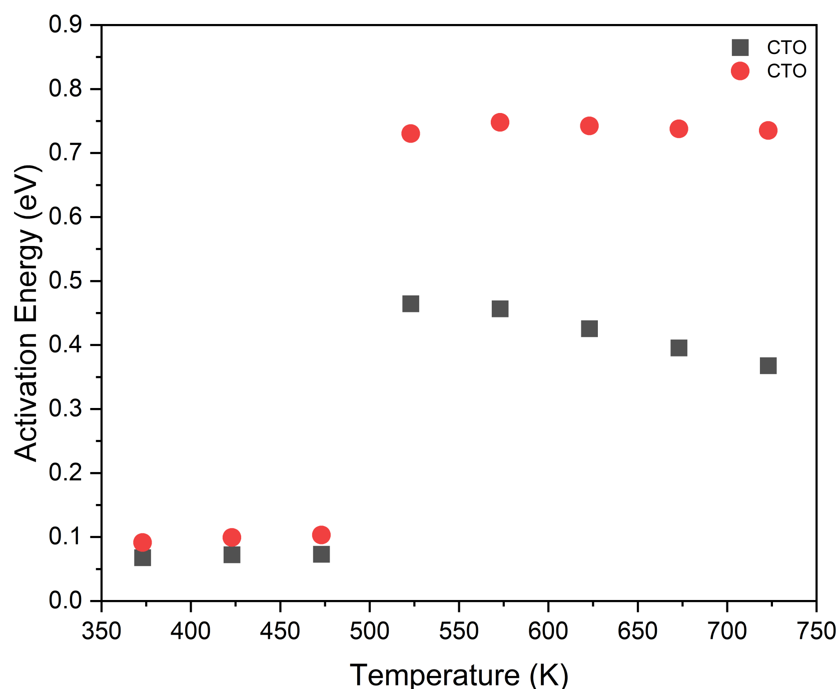

Figure 5.13. Chromium titanium oxide activation energy against temperature under nitrogen.

chromium oxide and tungsten hexacarbonyl ($W(CO)_6$) was chosen for the tungsten dopant precursor. Previous work conducted in our group showed $W(CO)_6$ displayed similar solubility as $Cr(CO)_6$ towards methanol and similar thermal profiles (DSC/TGA). They also display the same molecular structure. Therefore similar parameter ranges (heating temperature and flow rate) was used in the fabrication of CWO thin films via AACVD.

Various deposition temperature and flow rates were considered for the fabrication of CWO in order to find the optimum parameters for homogeneous deposition. Deposition temperatures between 330 °C to 360 °C and flow rates between 0.75 $L\,min^{-1}$ to 1.5 $L\,min^{-1}$ were investigated. The samples were all fabricated on glass and annealed at 500 °C for four hours.

5.2.2 Film Characterisation

Structural analysis (pXRD) was conducted and illustrated in figure 5.14 to see if there is a difference in crystal structure when flow rate and deposition temperature changes. The samples were plotted for each temperature at varying flow rate whilst compared with

deposited WO_3 and Cr_2O_3. Literature values (stick patterns) are of eskolaite and hexgaonal WO_3 (ICSD 32001).[227] The peaks highlighted in light green are of eskolaite. The patterns for CWO displayed no phase separation (i.e. no WO_3 peaks) and closely resemble the crystal structure of eskolaite. This indicates the full incorporation of tungsten dopant into the the lattice of chromium oxide. The pXRD pattern also indicates no change in crystal structure at different deposition temperature and flow rates.

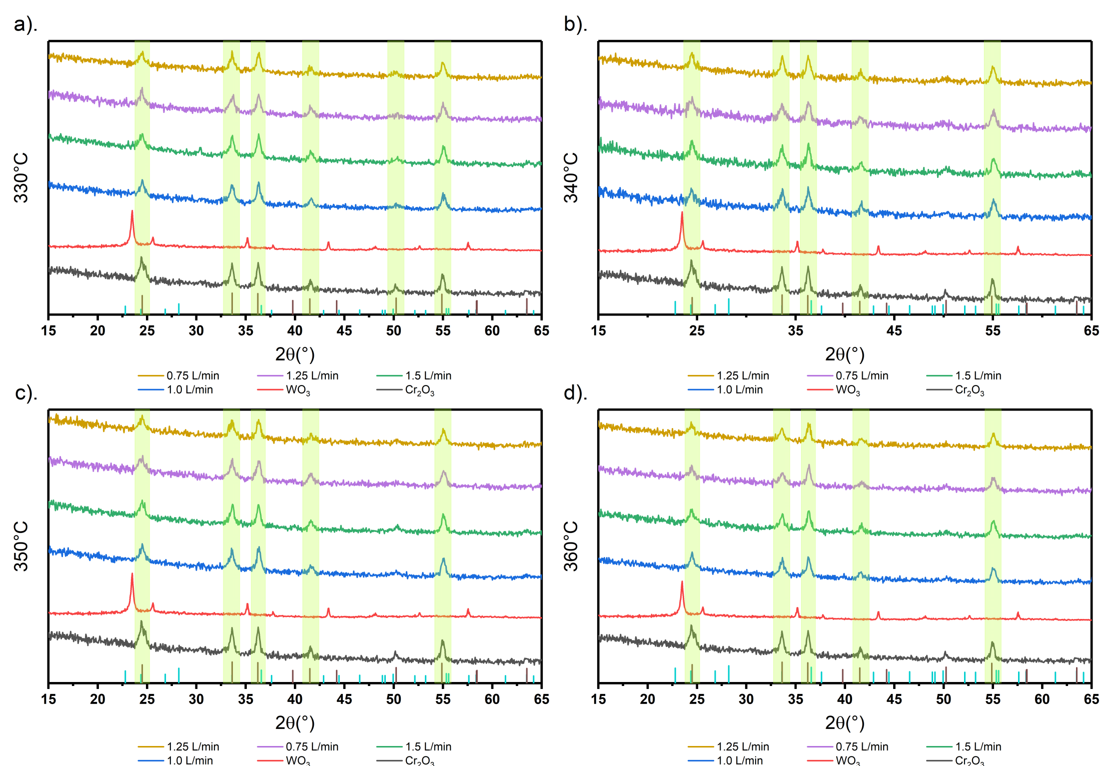

Figure 5.14. pXRD pattern of AACVD deposited CWO at various deposition temperature and flow rates.

EDS mapping was conducted on these samples to determine whether the films were homogeneous. The relative composition of these films was also calculated. Elemental analysis were collected along a diagonal line of the glass substrate (2.5 by 2.5 cm) where six points of analysis was taken, with each point four elemental scans were taken. Position one is the point closest to the inlet and position six is the point closest to the outlet.

Figure 5.15 illustrates the atomic percentage of chromium and tungsten from positions one to six for different deposition temperature. Atomic percentage of chromium shows a slight increase from inlet to outlet for all different parameters and the inverse is seen

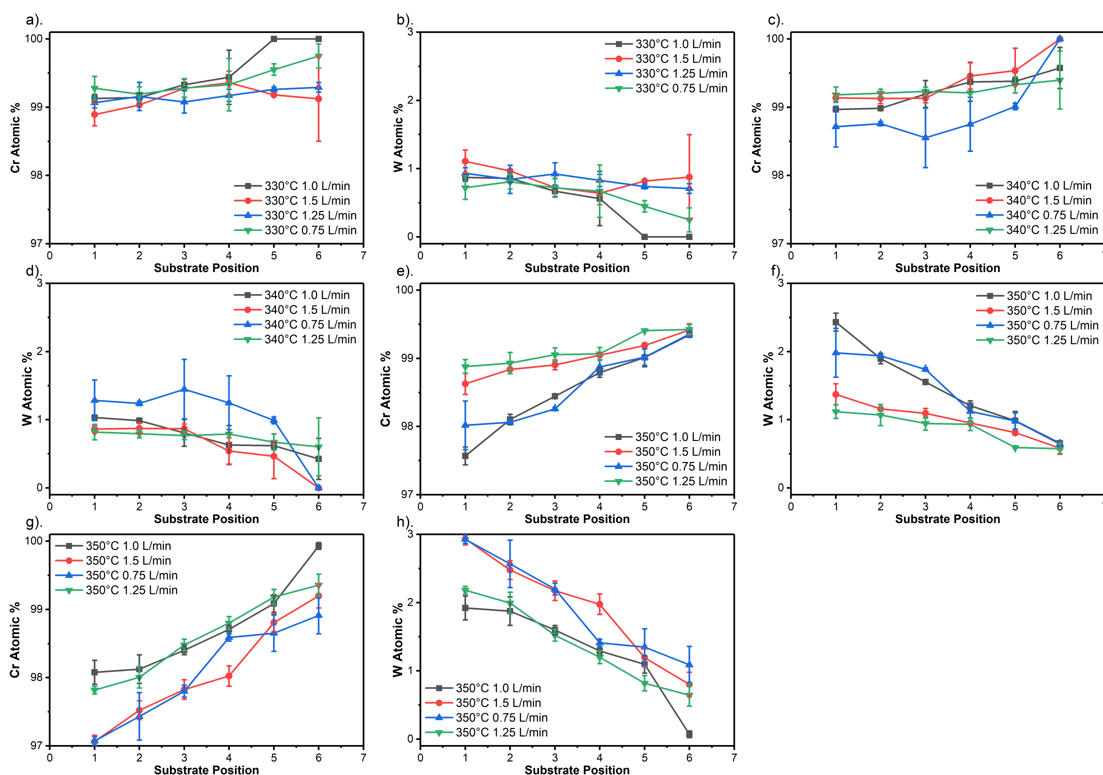

Figure 5.15. EDS elemental surface analysis of CWO at different deposition temperature and flow rate.

for tungsten. CWO thin film with the deposition parameters 360 °C and 1.0 L min^{-1} displayed the largest change in atomic percentage from inlet to outlet relative to other thin films fabricated, with a 2 % atomic percentage difference. Films fabricated at 340 °C and 1.5 L min^{-1} displayed the most linear curve with minimal changes in atomic percentage for both chromium and tungsten (roughly 0.25 % difference between substrate position) i.e. these parameters displayed a homogeneous film throughout the substrate compared to other deposition parameters. Therefore, these parameters were chosen for the deposition of CWO.

XPS analysis was conducted, with carbon 1s used as calibration at 284.6 eV for charge shift correction. The chromium 2p spectra for all deposition parameters were recorded and displayed in figure 5.16. The chromium $2p_{\frac{3}{2}}$ peak displayed a range from 572.5 eV to 581.9 eV. Three defined peaks were observed in this region where these peak environments are related to the binding energies of different oxidation states of chromium; Cr(III), Cr(IV) and Cr(VI) at roughly 576 eV, 575 eV and 579 eV. Again the survey spec-

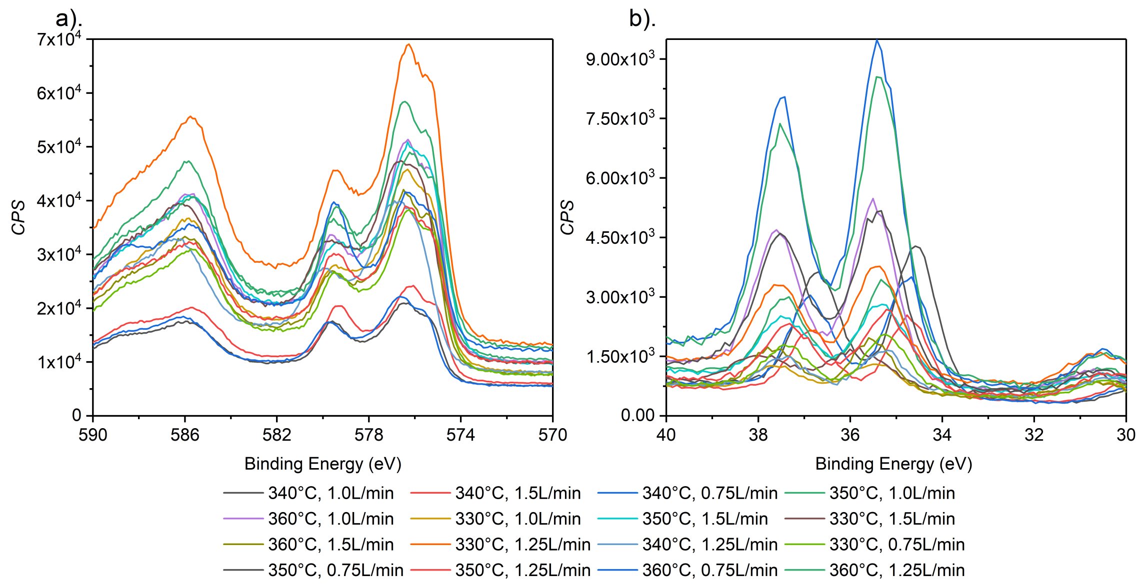

Figure 5.16. Cr $2p$ and W $4f$ spectra of CWO on glass substrate at different parameter deposition.

trum's were inspected and indicated the presence of sodium at roughly 1070 eV. EDS analysis also saw small atomic percentage of sodium (shown in table 5.8). Analysis were conducted on the glass substrate itself and indicated the presence of sodium. Again the assumption for different oxidation states observed for chromium is due to the formation of Cr(III) → Cr(VI) during the annealing process; where sodium ions from the glass substrate migrates onto the deposition layer and diffuses into the film when heated at high temperatures under the presence of oxygen, forming sodium dichromate ($Na_2Cr_2O_7$) as shown in equation (5.1). Tungsten $4f$ spectra's were recorded and a peak was observed at $4f_{\frac{7}{2}}$ which corresponds to W(VI), no other peaks where observed as shown in figure 5.16.

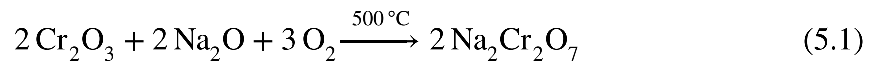

$$2\,Cr_2O_3 + 2\,Na_2O + 3\,O_2 \xrightarrow{500\,°C} 2\,Na_2Cr_2O_7 \tag{5.1}$$

Once optimum parameters were established for the deposition of CWO on glass substrates, alumina substrates were used rather than glass due to sodium migration for the investigation of dopant concentration and to find the correct loading of tungsten, i.e. theoretical composition to actual composition. The samples were also annealed at different temperatures (500 °C to 700 °C) for 24 hours. Figure 5.17 illustrates the pXRD pattern of CWO with different compositions and annealed at different temperatures on alumina

Table 5.8. Atomic percentage of sodium in CWO on glass substrate.

Parameters	Na Avg. Atomic %	Parameters	Na Avg. Atomic %
340 °C, 1.0 L min^{-1}	2.35	360 °C, 1.5 L min^{-1}	2.16
340 °C, 1.5 L min^{-1}	2.27	330 °C, 1.25 L min^{-1}	2.17
340 °C, 0.75 L min^{-1}	2.28	340 °C, 1.25 L min^{-1}	1.70
350 °C, 1.0 L min^{-1}	2.60	330 °C, 0.75 L min^{-1}	2.37
360 °C, 1.0 L min^{-1}	2.32	350 °C, 0.75 L min^{-1}	2.20
330 °C, 1.0 L min^{-1}	2.65	350 °C, 1.25 L min^{-1}	2.06
350 °C, 1.5 L min^{-1}	2.29	360 °C, 0.75 L min^{-1}	2.33
330 °C, 1.5 L min^{-1}	2.28	360 °C, 1.25 L min^{-1}	2.87

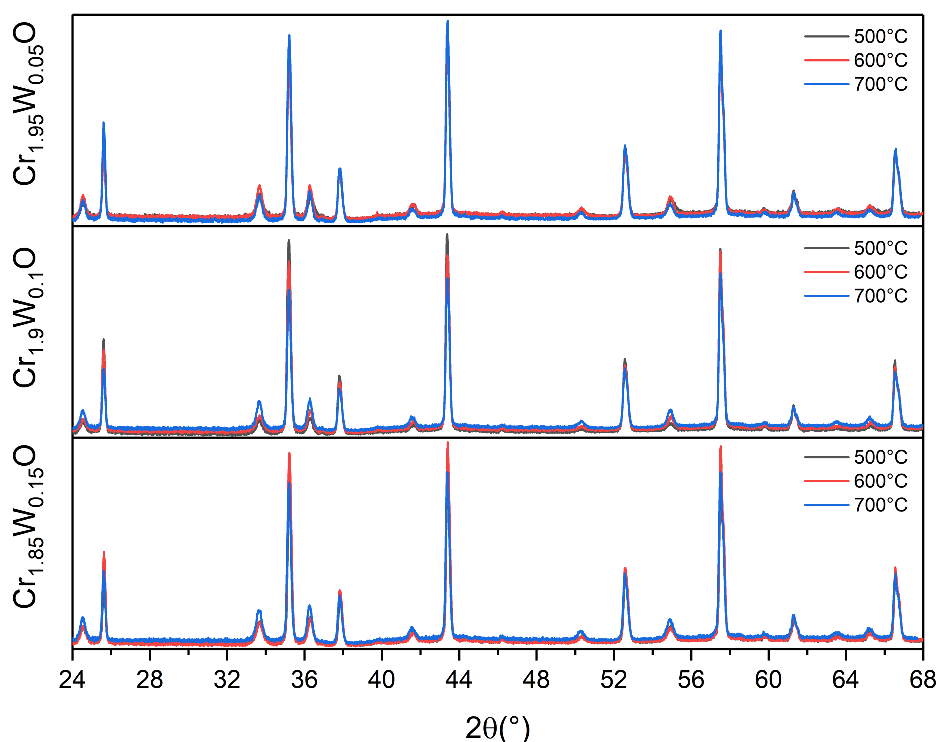

Figure 5.17. XRD pattern of CWO at different compositions and annealing temperatures.

substrates. Again, structural analysis were conducted on the samples with the patterns corresponding to eskolaite (Cr_2O_3) and corundum (Al_2O_3). No pattern of tungsten trioxide was observed which indicated the full incorporation of tungsten dopant into the lattice of chromium oxide and again no phase separation occurred within the limit of detection of XRD. Different annealing temperatures were investigated for each composition. The

crystallography pattern displayed no shifts in 2θ peaks at different annealing temperature, there were also no changes with different loading of tungsten dopant. Table 5.9 displays the 2θ peaks of CWO and its corresponding lattice planes with respect to eskolaite. Due to charging issues with the alumina substrate, XPS analysis could not be performed.

As previously stated in section 5.1.2, chromium oxide adopts a corundum structure with seven active raman modes.

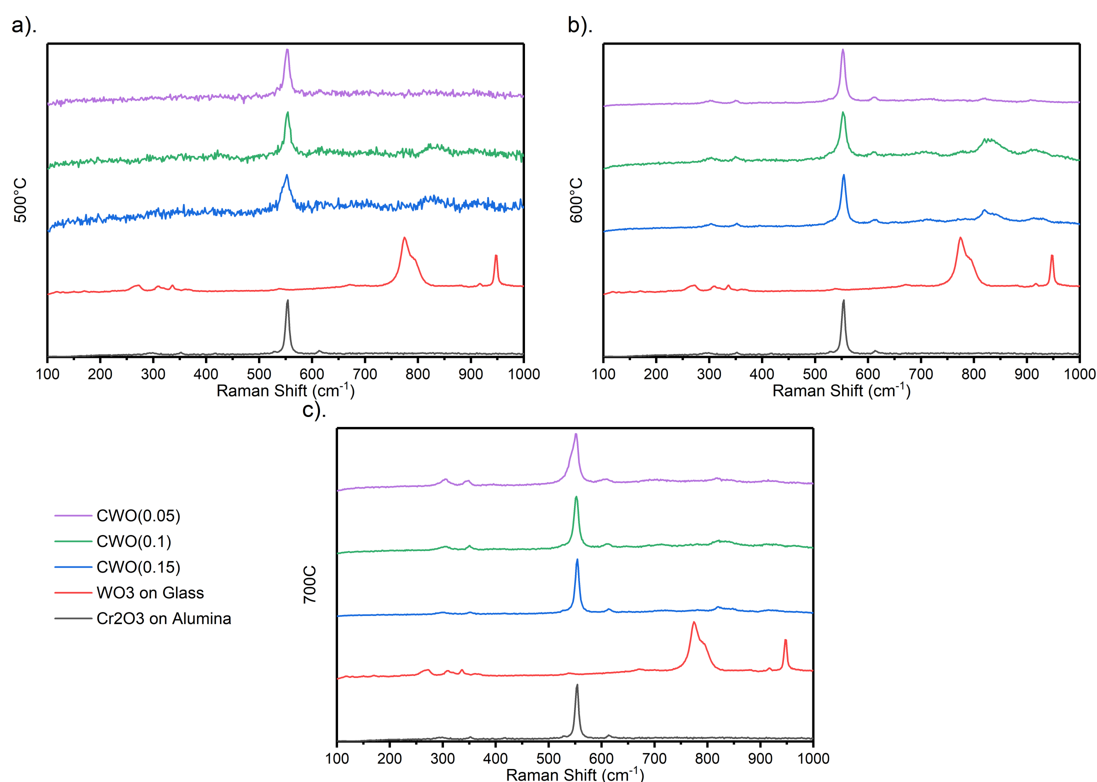

Figure 5.18. Raman spectra of CWO deposited on at different compositions and annealing temperatures.

As previously stated in section 5.1.2, chromium oxide adopts a corundum structure with seven active raman modes. Raman analysis was conducted and the bonding and stretching modes of CWO were compared to chromium oxide, tungsten trioxide and literature sources. Figure 5.18 depicts the Raman spectrum of different tungsten dopant levels at different annealing temperatures. Only one peak is observed for all three dopant's when annealed at 500 °C, whereas at temperatures of 600 °C and 700 °C, multiple peaks are observed. At low levels of tungsten doping ($W_{0.05}$), peaks between 700 cm^{-1} to 950 cm^{-1} are less intense than that of $W_{0.1}$ and $W_{0.15}$. These peaks are related to the W–O–W bonding

Table 5.9. pXRD 2θ peaks and lattice planes of $Cr_{2-x}W_xO$ on alumina and annealed at different temperatures.

pXRD 2θ peak (°)									Lattice Plane
$Cr_{1.85}W_{0.15}O$			$Cr_{1.9}W_{0.1}O$			$Cr_{1.95}W_{0.05}O$			
500 °C	600 °C	700 °C	500 °C	600 °C	700 °C	500 °C	600 °C	700 °C	
24.5	24.5	24.5	24.5	24.5	24.5	24.5	24.5	24.5	(012)
33.6	33.6	33.6	33.6	33.6	33.6	33.6	33.6	33.6	(104)
36.2	36.2	36.2	36.3	36.3	36.2	36.3	36.3	36.3	(110)
41.6	41.6	41.6	41.6	41.6	41.5	41.6	41.6	41.6	(113)
50.4	50.3	50.2	50.3	50.3	50.3	50.3	50.3	50.3	(024)
54.9	54.9	54.9	54.9	54.9	54.9	55.0	54.9	54.9	(116)
63.6	63.6	63.5	63.4	63.5	63.5	63.6	63.6	63.5	(214)
65.3	65.3	65.1	65.3	65.2	65.3	65.3	65.2	65.2	(300)

modes, where the 710 cm^{-1} relates to W−O bending mode and W−O stretching mode at 820 cm^{-1}. The peak at 915 cm^{-1} is associated with W=O stretching mode and is compareable to the WO_3 Raman spectra of Huirache-Acuna[227] represented in figure 5.19. The four peaks displayed between 250 cm^{-1} to 650 cm^{-1} are related to chromium oxide. The raman shifts and its assignments are illustrated in table 5.10. A reasonable assumption for the visible tungsten trioxide bands is because Raman is more of an surface analysis technique rather than looking into the bulk of the material, as in pXRD.

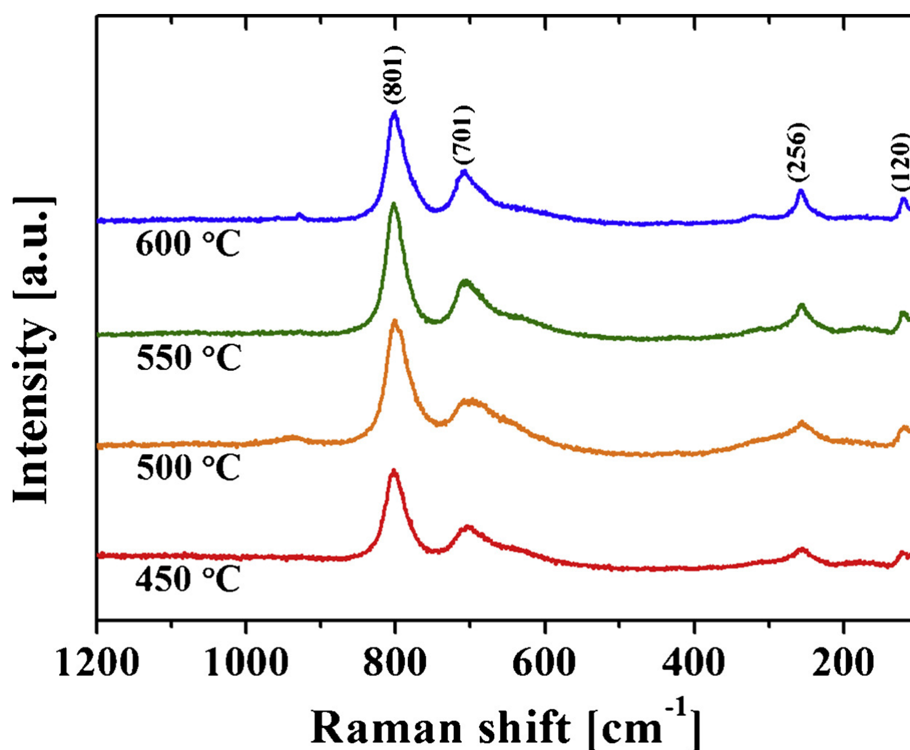

Figure 5.19. Raman spectra of WO_3 reported by Huirache-Acuna.[227]

Due to XPS charging issues seen on alumina substrates and the need to identify whether WO_3 was present as a separate phase, quartz substrates were used. pXRD analysis was conducted on two different levels of dopant of CWO and were compared to Cr_2O_3 and WO_3. As shown in figure 5.20, no pattern of tungsten trioxide was observed, which suggest the full incorporation of tungsten dopant into the lattice of chromium oxide, hence no indication of phase separation occurred within the detection limit of XRD. The pXRD pattern again closely resembles that of eskolaite.

Figure 5.21 depicts chromium 2*p* and tungsten 4*f* XPS spectra's. Carbon 1*s* at 284.6 eV was used for calibration for charge shift correction. CWO was compared to deposited chro-

Table 5.10. Raman shift assignment of CWO on alumina.

Raman Shift (cm^{-1})									Literature (cm^{-1})		Assignment	
$Cr_{1.85}W_{0.15}O$			$Cr_{1.9}W_{0.1}O$			$Cr_{1.95}W_{0.05}O$			Cr_2O_3	WO_3	Cr_2O_3 [a]	WO_3 [b,c,d]
500 °C	600 °C	700 °C	500 °C	600 °C	700 °C	500 °C	600 °C	700 °C				
–	–	–	–	–	–	–	–	–	–	275		W−O deformation
–	302	301	–	304	303	–	306	304	303	–	E_g	
–	350	351	–	351	349	–	349	349	351	–	E_g	
–	–	–	–	–	–	–	–	–	530	–	E_g	
552	554	554	554	552	552	554	552	552	551	–	A_{1g}	
–	614	613	–	613	613	–	611	606	612	–	E_g	
–	714	713	–	708	713	–	715	704	–	722		W−O bend
–	820	820	–	828	820	–	820	818	–	810		W−O stretch
–	925	916	–	912	921	–	906	917	–	950		W=O stretch

[a] Beattie *et al.*[208]
[b] Beattie *et al.*[228]
[c] Hercules *et al.*[229]
[d] Rougier *et al.*[230]

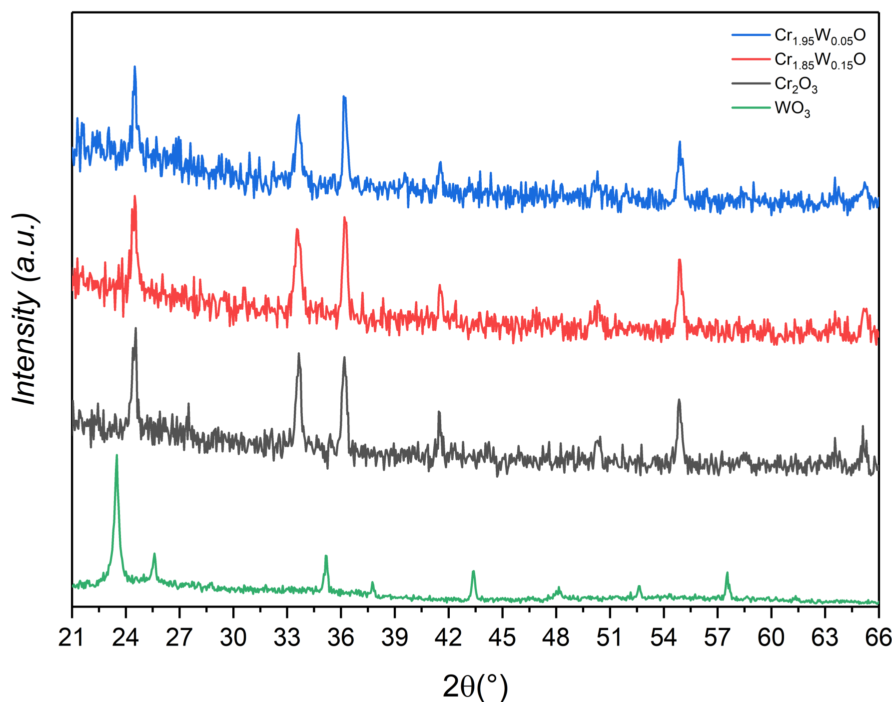

Figure 5.20. CWO pXRD pattern deposited on quartz substrate annealed at 600 °C.

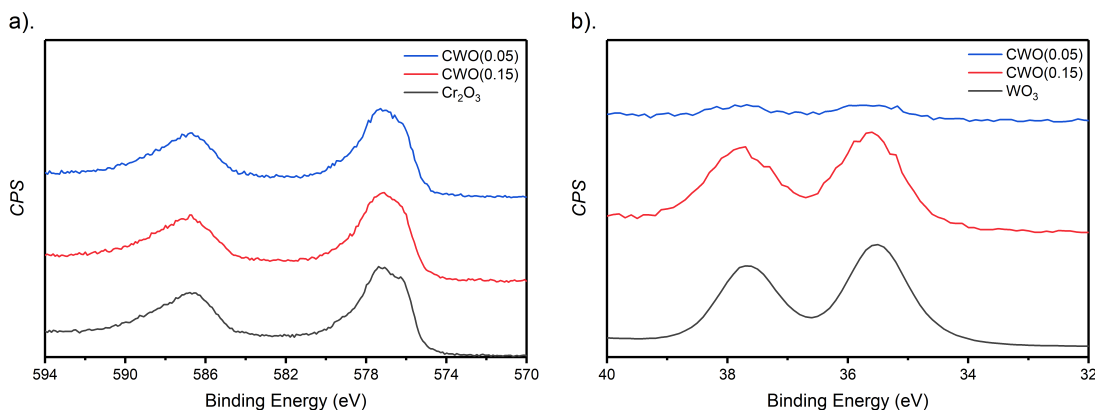

Figure 5.21. (a). Cr $2p$ and (b). W $4f$ spectra of CWO on quartz.

mium oxide and tungsten trioxide as well as literature values of chromium oxide, tungsten dioxide and trioxide. For the chromium $2p$ spectra, only one peak is observed in the $2p_{\frac{3}{2}}$ region which correlates to Cr(III) as the substrates used was quartz, hence Cr(VI) is not expected to be observed. For tungsten $4f$, one distinct peak was also observed at the $4f_{\frac{7}{2}}$ region, corresponding to W(VI). Oxygen $1s$ spectra correlates to lattice oxygen of the oxide. Composition ratio of CWO was calculated via the area of the peak and RSF

values. Again calculations demonstrated an excess amount of oxygen which is owed to adsorbed water, hydrocarbons, siloxanes as previously mentioned. The composition ratio of chromium to tungsten was shown to be 1.80 : 0.2 for CWO(0.15) and 1.98 : 0.02 for CWO(0.05). Table 5.11 illustrates the binding energies of CWO and its comparison to literature values.

Table 5.11. Binding energies (eV) of CWO on quartz ([a,b]literature values).

Composition	Cr $2p_{\frac{3}{2}}$	W $4f_{\frac{7}{2}}$	O 1*s*
$Cr_{1.85}W_{0.15}O$	577.1	35.6	530.7
$Cr_{1.95}W_{0.05}O$	577.3	35.5	530.6
Cr_2O_3	577.0	–	530.6
WO_3	–	35.5	530.2
Cr_2O_3[a]	576.1	–	–
WO_3[b]	–	35.7	–
WO_2[b]	–	33.0	–

[a] Biesinger *et al.* referenced to Au $4f_{\frac{3}{2}}$ at 83.95 eV.[205]
[b] Hercules *et al.*[229]

Raman of the films deposited onto quartz was measured and shown in figure 5.22. Again four bands are observed between 300 cm^{-1} to 620 cm^{-1} which correlates to chromium oxide. As explained previously, the bands observed between 700 cm^{-1} to 950 cm^{-1} are due to tungsten doping and relates to the bending and stretching modes of the W−O−W bonds.

Cross section SEM imaging was again taken to calculate the thickness of the deposited film. The thickness of CWO(0.15) films on quartz substrate was measured to be around 23.3 µm. The thickness of CWO(0.15) is thicker than CTO(0.15) (12.5 µm) but thinner than Cr_2O_3 (33 µm) Hall measurement were conducted at ambient conditions and a a current of 1.0 nA where the Hall voltage was calculated. Four measurements were taken for the two tungsten dopant analysed which is depicted in table 5.12. Some of the bulk concentration values recorded for both dopant levels displayed a negative value, which is again

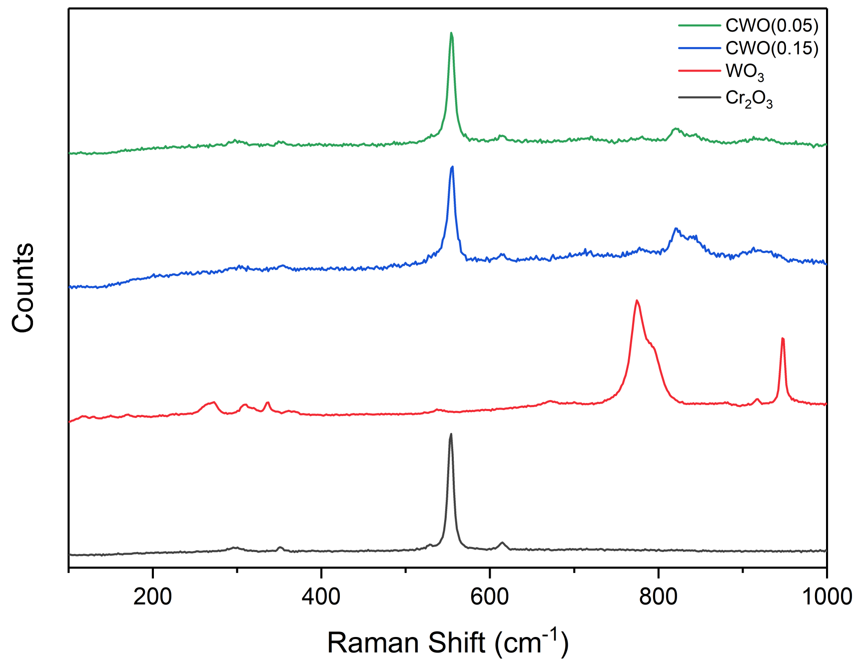

Figure 5.22. Raman spectra of CWO deposited on quartz substrate.

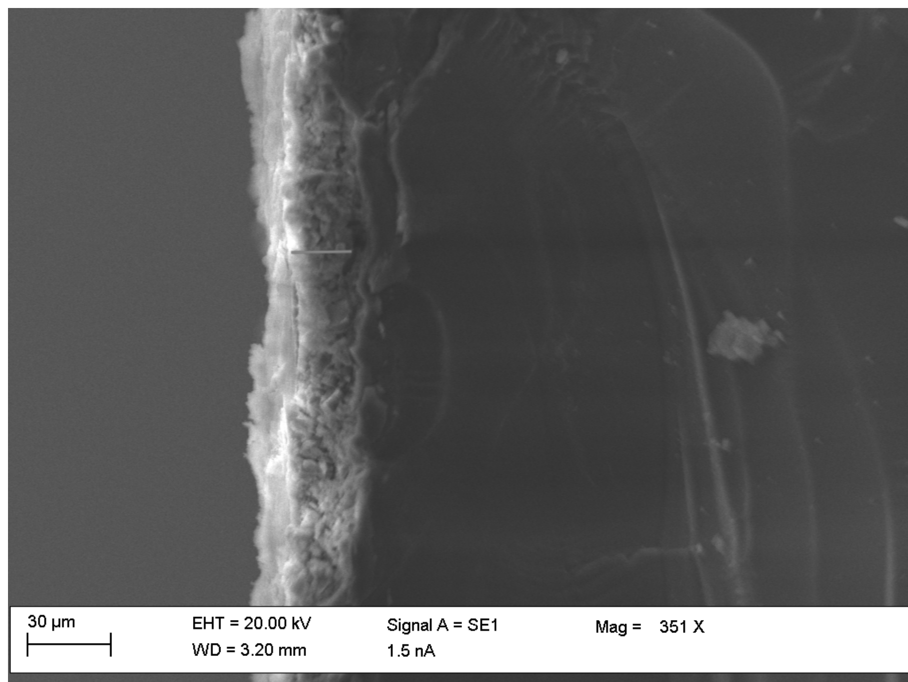

Figure 5.23. Cross section SEM image of CWO on quartz substrate.

which could be due to certain factors such as ohmic contact geometry, thickness accuracy and high resistivity of the film. Hence it is difficult to accurately calculate the Hall voltage and determine the films conduction type. The resistivity, compared to CTO measured in the section above are in general higher ($10^6\ \Omega$ cm to $10^9\ \Omega$ cm vs$10^6\ \Omega$ cm to $10^7\ \Omega$ cm).

Table 5.12. Hall effect measurements of CWO on quartz substrates.

Samples	ρ Ω cm	μ cm^2 V^{-1} s^{-1}	N_B cm^{-3}	R_H cm^3 C^{-1}	V_H mV
CWO(0.15) A	2.87×10^7	8.36	2.61×10^{10}	2.48×10^8	5.96
CWO(0.15) B	1.24×10^9	0.63	-8.05×10^9	-7.75×10^8	−19.30
CWO(0.15) C	7.43×10^9	0.02	4.85×10^{10}	1.29×10^8	3.20
CWO(0.15) D	9.08×10^6	130.7	5.26×10^9	1.19×10^9	29.55
CWO(0.05) A	3.90×10^6	106.2	1.51×10^{10}	4.14×10^8	10.31
CWO(0.05) B	4.37×10^{10}	5.28×10^{-3}	2.70×10^{10}	2.31×10^8	5.74
CWO(0.05) C	8.81×10^6	6.91	-1.03×10^{11}	-6.09×10^7	−1.51
CWO(0.05) D	7.91×10^7	13.41	-5.88×10^9	-1.06×10^9	−26.41

CWO(0.15) denotes $Cr_{1.85}W_{0.15}O$ and CWO(0.05) denotes $Cr_{1.95}W_{0.05}O$.

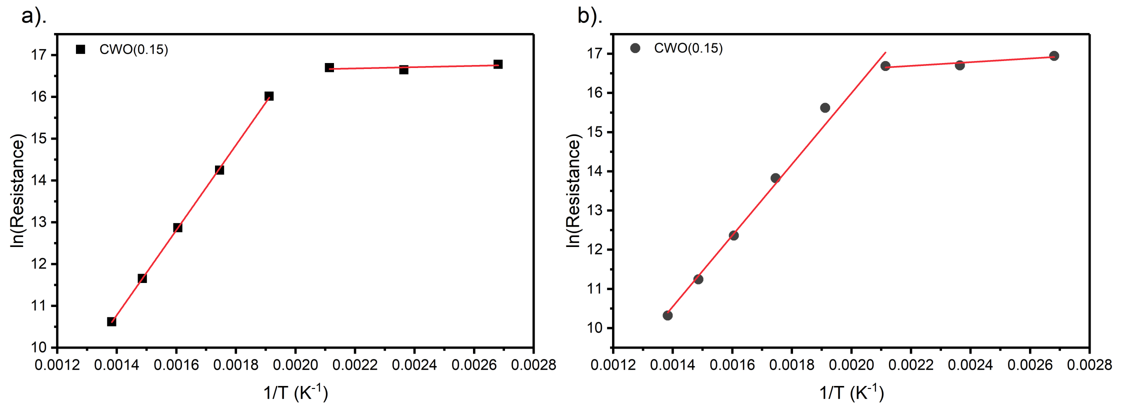

Figure 5.24. CWO(0.15) Arrhenius plot.

The activation energy of two CWO(0.15) sensors was measured by first recording the baseline resistance of the sensor in dry air and then under pure nitrogen at elevated temperatures (100 °C to 450 °C). An Arrhenius plot (shown in figure 5.24) was plotted and the activation energy was calculated. The activation energy plot is relatively similar to that of both chromium oxide and titanium doped-chromium oxide. The activation energies recorded were slightly lower compared to CTOs activation energy at low temperature and slighly higher energy level at high temperature. Below a temperature environment of 475 K, the energy calculated for CWO was 0.03 eV and 0.04 eV, whereas for CTO the energy was 0.06 eV and 0.1 eV. And at temperatures above 475 K, the energy was calcu-

lated to be at 0.8 eV and 0.9 eV (CWO) vs 0.45 eV and 0.73 eV (CTO). When compared to the activation energies of Cr_2O_3 samples in the previous chapter, the activation energies are lower for CWO (0.24 eV and 0.35 eV vs 0.06 eV and 0.1 eV) at lower temperature settings. At high temperature, CWO has a larger activation energy than Cr_2O_3, 0.8 eV and 0.9 eV vs 0.46 eV to 0.55 eV. This shows that the addition of a n-type dopant decreases the activation energy of oxide at low temperature and increases it at high temperature levels.

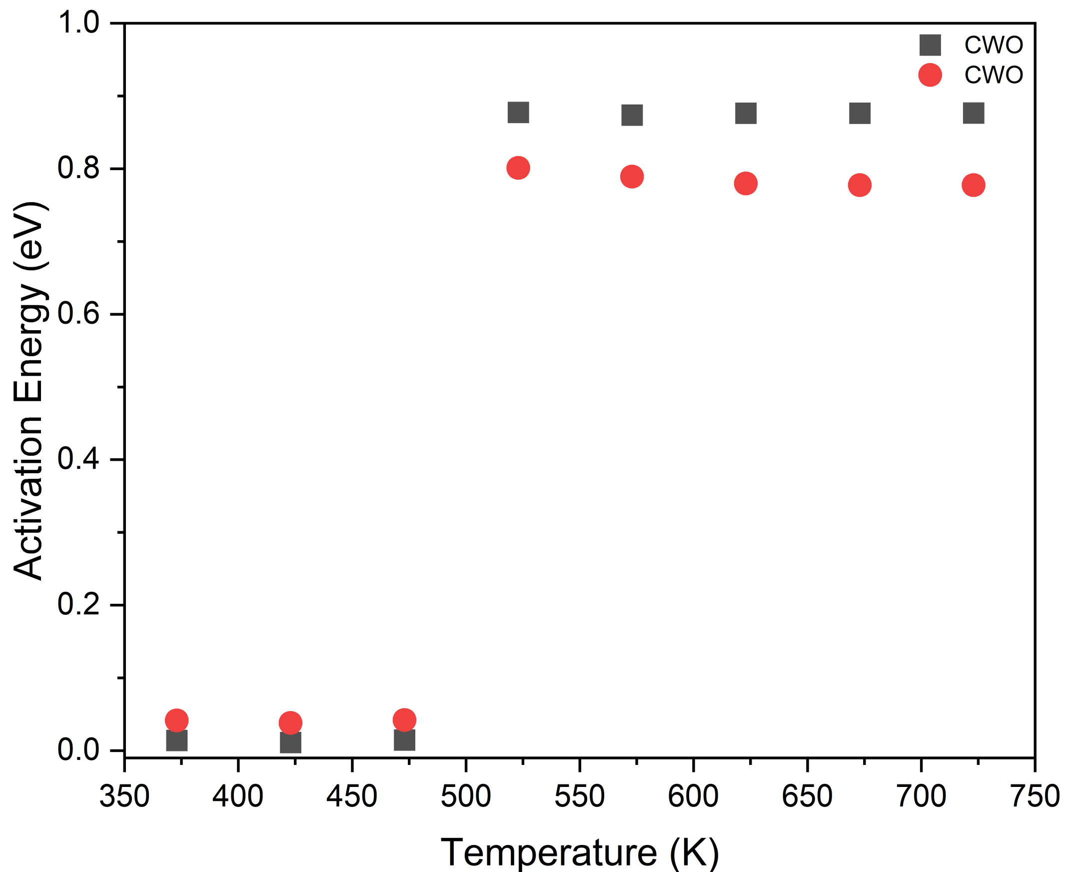

Figure 5.25. Tungsten doped-chromium oxide activation energy against temperature under pure nitrogen.

5.3 Nickel Doped-chromium Oxide

5.3.1 Film Characterisation

As previously described from the sections above, chromium and nickel oxide thin films can be fabricated via AACVD method using optimal parameters. Therefore small dop-

ing levels of nickel were used to fabricate nickel doped chromium oxides (1.85 : 0.15 ratio) using the parameters of 340 °C reactor temperature, a flow rate of 1.5 L min^{-1} using methanol as solvent of choice. Samples CNO(1 G), CNO(2 G) are samples deposited onto glass substrates and CNO(A600C), CNO(A700C), CNO(A800C) are samples deposited onto alumina annealed at three different temperatures, 600 °C, 700 °C and 800 °C respectively.

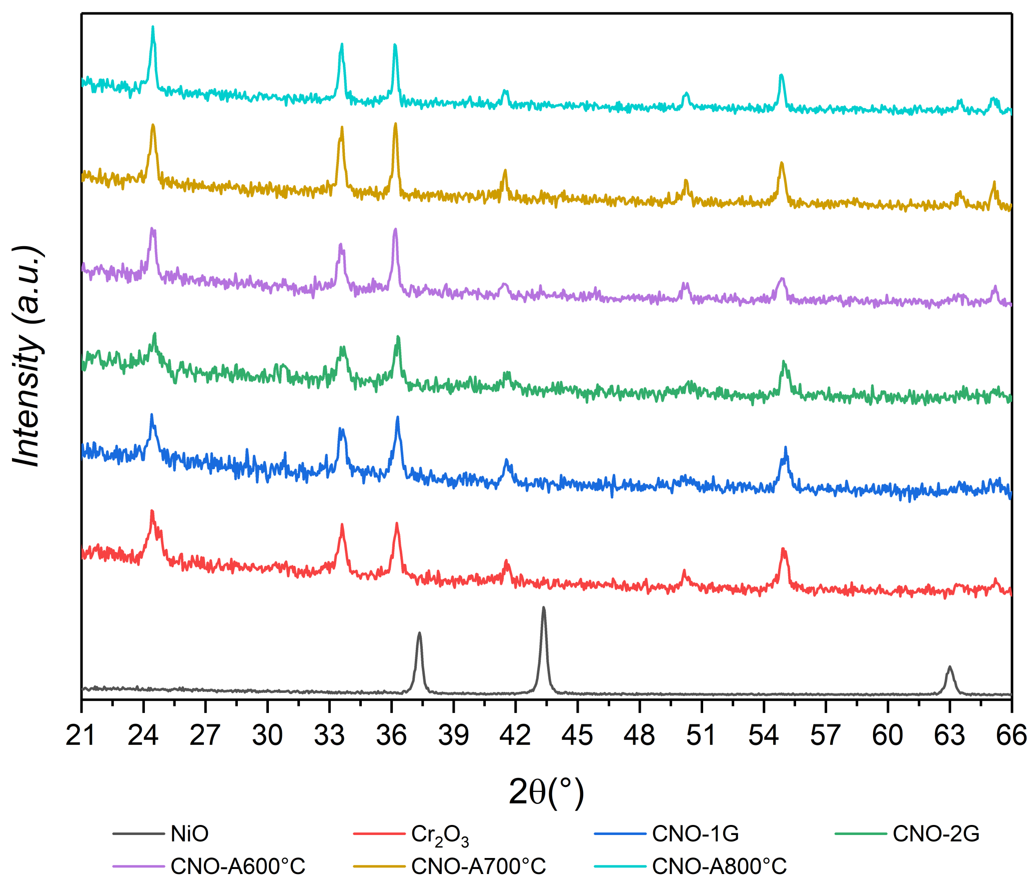

Figure 5.26. XRD pattern of CrNiO deposited onto glass and alumina.

Structural analysis (pXRD) was conducted on nickel doped-chromium oxide (CNO) films deposited on both glass and alumina annealed at 500 °C for glass and 600 °C, 700 °C and 800 °C for alumina, as shown in figure 5.26. The samples were compared to both nickel and chromium oxide. The 2θ peaks observed in the patterns correlates to eskolaite for both glass and alumina substrate samples. Neither displayed any peaks for bunsenite, hence no phase separation has occurred within the detection limit. This also suggests the full incorporation of Ni dopant into the lattice of chromium oxide. Changes to annealing

temperature on alumina substrate samples demonstrated no peak shifting, indicating no structural changes between the temperatures analysed. The table below depicts the 2θ bands to their corresponding lattice planes of eskolaite.

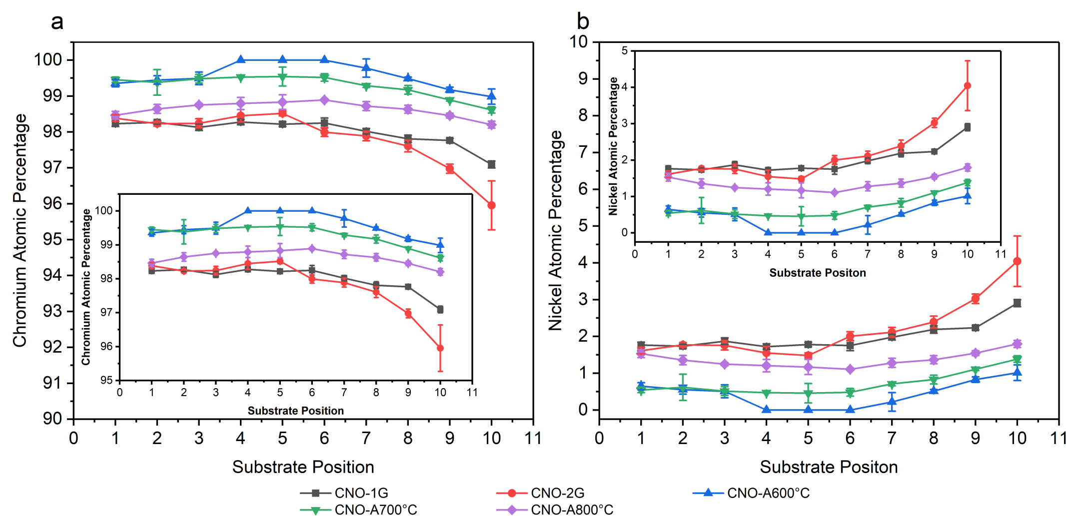

Figure 5.27. EDS elemental surface analysis of CNO where (a). Chromium atomic percentage; (b). Nickel atomic percentage.

EDS mapping analysis of CNO on glass and alumina annealed at different temperatures is shown in figure 5.27, where figure 5.27a). refers to chromium atomic percentage and b). refers to nickel atomic percentage. The relative composition of (chromium:nickel ratio) across the film on a 2.5 by 2.5 cm was calculated and used to determine the films homogeneity. Substrate positon one refers to the area closest to the outlet side of the reactor chamber and position ten is where the film is closest to the inlet. In figure 5.27a). the five sampled analysed all exhibited a relativity linear plot with small error margins demonstrating an homogeneous film. A slight decrease in chromium atomic percentage towards the inlet points towards nickel depositing preferentially near the inlet at these deposition parameters for the glass samples. Therefore the samples deposited on alumina were rotated by 180° after half of the aerosol solution mixture was deposited onto the substrate. This was shown to minimise the change in chromium and nickel atomic percentage throughout the substrate. Given that the plots demonstrates a homogeneous film at the deposition parameters of 340 °C and 1.5 L min^{-1} on alumina substrates, these conditions were used for the fabrication of CNO thin films on sensor substrates.

Table 5.13. pXRD 2θ peaks and lattice planes of CNO on different substrates.

pXRD 2θ peak (°)						Lattice Plane
Cr_2O_3	CNO−1 G	CNO−2 G	CNO−A600 °C	CNO−A700 °C	CNO−A800 °C	
24.5	24.4	24.5	24.5	24.5	24.5	(012)
33.6	33.7	33.6	33.5	33.6	33.6	(104)
36.3	36.3	36.3	36.2	36.2	36.2	(110)
41.6	41.6	41.6	41.4	41.5	41.5	(113)
50.2	–	–	50.2	50.3	50.2	(024)
54.9	55.1	54.9	54.9	54.9	54.9	(116)
63.6	–	–	63.4	63.5	63.6	(214)
65.2	–	–	65.2	65.2	65.1	(300)

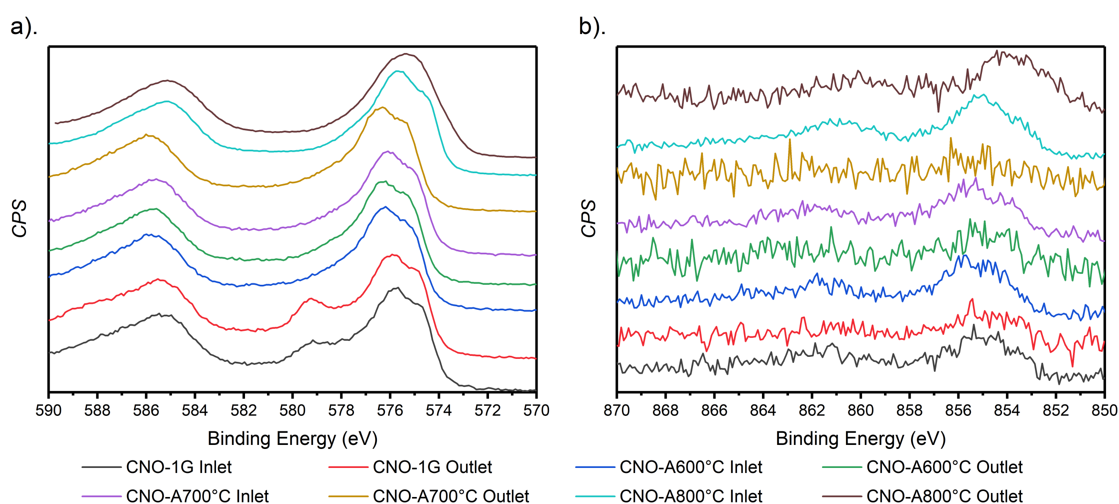

Figure 5.28. Chromium and nickel 2*p* spectra of nickel doped-chromium oxide.

XPS surface analysis was generated and the 2*p* spectra of chromium and nickel is shown in figure 5.28. Analysis of the film towards the outlet and inlet of the reactor chamber was performed to look for any differences in the levels of nickel dopant. Plots labelled with inlet is where the sample is at front of the reactor chamber and analysis was done in that section and ones labelled as outlet is where the sample is close to the back of the chamber. For the chromium 2*p* spectra, a shoulder peak is seen for the samples on glass substrate at the Cr $2p_{\frac{3}{2}}$ and correlates to Cr(VI) which was expected due to the presence of sodium in the glass substrate as seen previously for pure Cr_2O_3 samples. The binding energies matches to pure Cr_2O_3 samples previously analysed. For the nickel 2*p* spectra for glass substrate sample, Ni was not detectable at the outlet side but a small presence of Ni was observed at the inlet side. This correlates with EDS data for the glass substrate as a lower atomic percentage of nickel was seen at the outlet end of the substrate compared to the inlet. For alumina substrate samples, the chromium 2*p* spectra only displays the Cr(III) and for nickel spectra, small presence of nickel was observed.

Raman spectrum of CNO(0.15) on different substrate samples were analysed and illustrated in figure 5.29. Table 5.15 depicted below are the band assignments in relation to chromium oxides band assignments and literature values. The bands between $100\,cm^{-1}$ to $700\,cm^{-1}$ closely resembles that of chromium oxide and no bands which correlate to nickel oxide were seen in Raman which indicates the full incorporation of nickel into the

Table 5.14. Binding energies (eV) of CNO compared to literature values.

Sample	Cr $2p_{\frac{3}{2}}$	Ni $2p_{\frac{3}{2}}$	O $1s$	Sample	Cr $2p_{\frac{3}{2}}$	Ni $2p_{\frac{3}{2}}$	O $1s$	Sample	Cr $2p_{\frac{3}{2}}$	Ni $2p_{\frac{3}{2}}$	O $1s$
Cr_2O_3[a]	576.1	–	–	A600 °C inlet	576.2	855.7	529.6	A800 °C inlet	575.5	855.0	529.6
NiO[b]	–	853.9	–	A600 °C middle	576.2	–	529.7	A800 °C middle	575.5	854.2	529.1
1 G inlet	575.7	855.2	529.4	A600 °C outlet	576.2	–	529.7	A800 °C outlet	575.0	–	529.4
1 G outlet	576.0	855.3	529.4	A700 °C inlet	576.1	855.3	529.5				
2 G inlet	575.7	855.4	529.3	A700 °C middle	576.3	–	529.7				
2 G outlet	575.7	–	529.4	A700 °C outlet	576.3	–	529.8				

[a] Biesinger *et al.* referenced to Au $4f_{\frac{3}{2}}$ at 83.95 eV.[205]

[b] Venezia *et al.*[215]

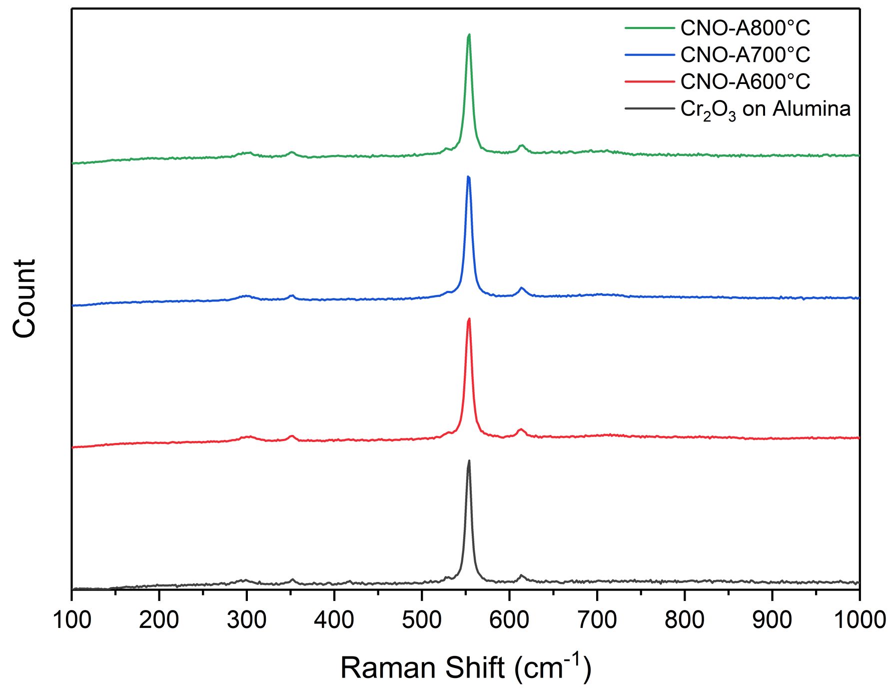

Figure 5.29. Raman specta of nickel doped chromium oxide.

chromium oxide structure. Verma *et al*. reported the Raman analysis of different dopant levels of nickel on Cr_2O_3 which is displayed in figure 5.30.[231] The spectra measured here are similar to that of Verma's reported analysis for dopant level of $x = 0.1$.

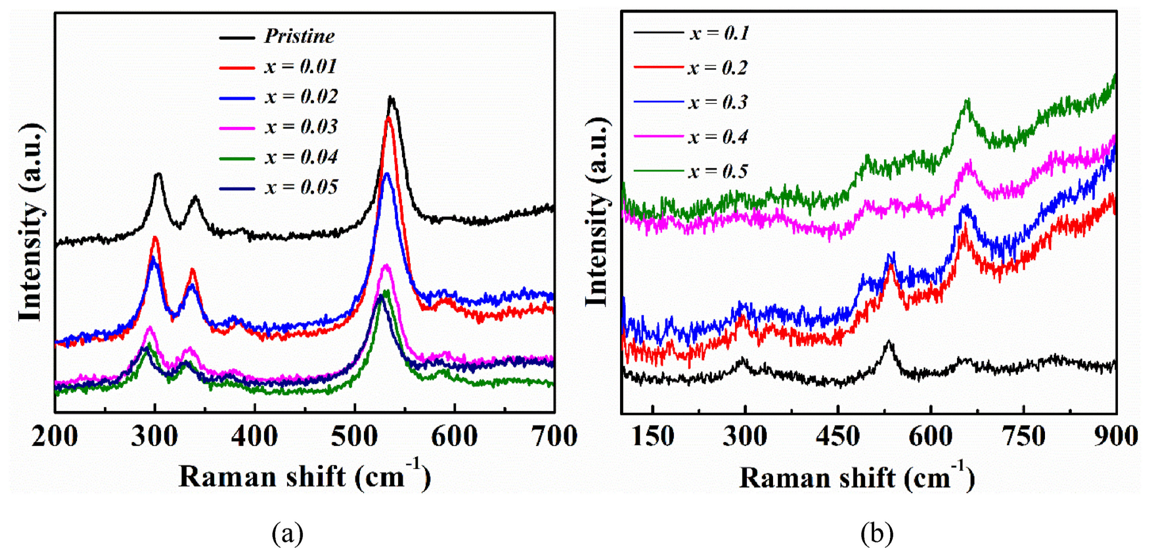

Figure 5.30. Raman spectra of nickel doped chromium oxide reported by Verma.[231]

Hall effect measurements were obtained for three different dopant levels of CNO on quartz substrate (0.25, 0.15, 0.05). The thickness used for the calculation was measured at 13.75 μm from the SEM image in figure 5.31, which is very similar to the thickness of

Table 5.15. Raman shift assignment for CNO thin films.

Observed Raman Shift (cm^{-1})					Assignment	Literature [a] (cm^{-1})
CNO−1 G	CNO−2 G	CNO−A600 °C	CNO−A700 °C	CNO−A800 °C		
303	302	305	304	307	E_g	303
349	351	349	347	346	E_g	351
–	–	–	–	–	E_g	530
555	552	552	547	547	A_{1g}	551
613	611	608	606	606	E_g	612

[a] Beattie *et al.*[208]

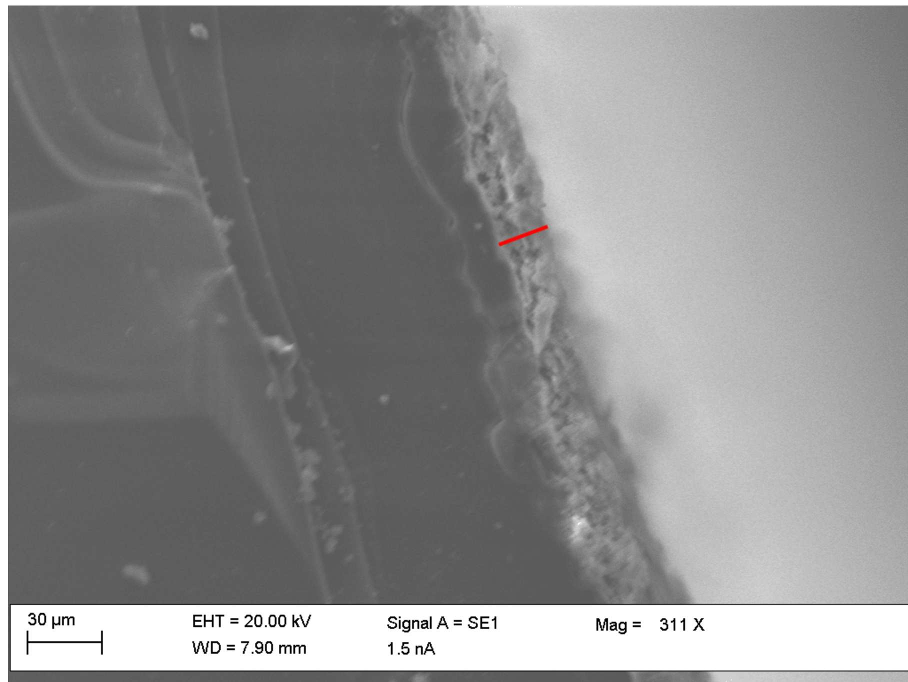

Figure 5.31. Cross section SEM image of CNO on quartz substrate.

NiO (13.2 µm) but different compared to Cr_2O_3 (33 µm). The measurements were conducted under ambient conditions at a current of 1.0 nA and results are displayed in table 5.16. Carrier concentration and Hall coefficient are comparable across the three different dopant levels. Hall mobility is larger at high doping level (CNO(0.25)) compared to the two other samples of doping level and the Hall voltage are all similar across samples. CNO shows similar Hall values when compared to NiO measurements. The average Hall voltage for NiO was 13.07 mV and 10.43 mV, 8.57 mV and 10.2 mV for CNO(0.25), CNO(0.15), CNO(0.05) respectively. The carrier concentration are also similar to NiO, i.e. similar order magnitude (10^{10} cm^{-3}). When compared to Cr_2O_3, resistivity is larger than for CNO(0.25) but similar for CNO(0.15) and CNO(0.05).

Baseline resistance analysis of three different CNO(0.15) on alumina sensor substrates samples was conducted under nitrogen and at variable operating temperature. The resistances measured were then used to calculate the activation energy via an Arrhenius plot (figure 5.32) as explained previously. Figure 5.33 illustrates the activation energy of CNO under nitrogen at elevated working temperature. Two distinct energy levels are seen, one at a low temperature range (0.15 eV and 0.35 eV) and another at a high temperature range

Table 5.16. Hall effect measurements of CNO on quartz substrates at room temperature.

Samples	ρ Ω cm	μ cm^2 V^{-1} s^{-1}	N_B cm^{-3}	R_H cm^3 C^{-1}	V_H mV
CNO(0.25) ^{A}	7.72×10^5	362.3	2.23×10^{10}	2.80×10^8	11.80
CNO(0.25) ^{B}	7.63×10^5	281.5	2.91×10^{10}	2.15×10^8	9.06
CNO(0.15) ^{A}	5.95×10^6	28.59	3.67×10^{10}	1.70×10^8	7.18
CNO(0.15) ^{B}	6.37×10^6	37.06	2.65×10^{10}	2.36×10^8	9.95
CNO(0.05) ^{A}	7.22×10^6	32.66	2.65×10^{10}	2.36×10^8	9.94
CNO(0.05) ^{B}	6.43×10^6	38.64	2.51×10^{10}	2.48×10^8	10.47

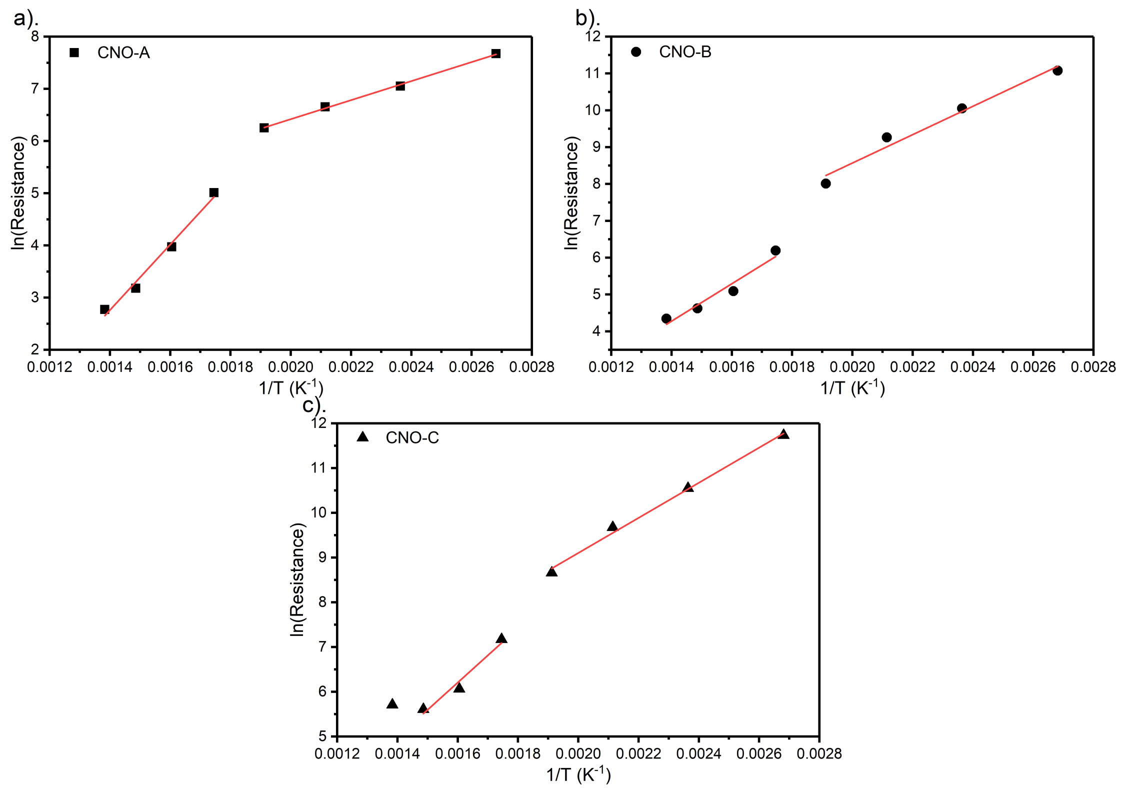

Figure 5.32. Nickel doped-chromium oxide activation energy against temperature under nitrogen.

(0.45 eV and 0.55 eV). The values calculated are similar to that of chromium oxide, at low temperature chromium oxides energy was 0.24 eV and 0.35 eV and at high temperature it was 0.45 eV and 0.55 eV.

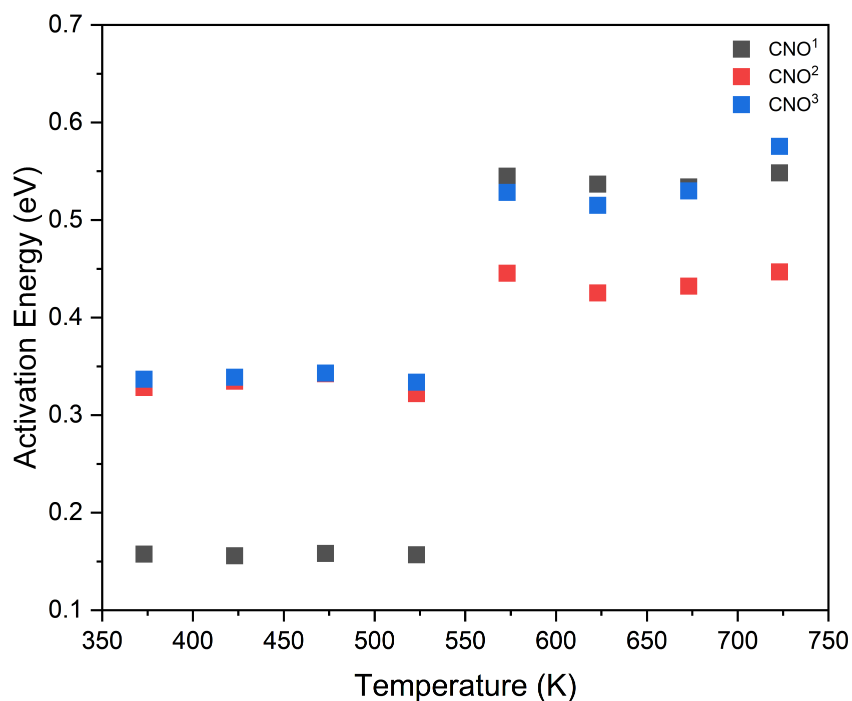

Figure 5.33. Nickel doped-chromium oxide activation energy against temperature under nitrogen.

5.4 Summary

To conclude, in this chapter the synthesis and structural analysis of the *n*-type and *p*-type doped chromium oxide were investigated. CTO was successfully deposited onto sensor substrates using previous deposition parameters within the group. The structural analysis of AACVD CTO was compared to commercial screen printed CTO sensors. pXRD pattern and XPS was similar to one another. Trace amounts of other elements were found (Pb, Ca and Cd) during XPS analysis. After further investigation, these trace elements were due to the gold ink that was used to make the gold electrode on the sensing substrate. SEM imaging was use to determine the thickness of AACVD CTO films, measuring at 12.5 µm. this was used to attempt the calculation of Hall voltage. Again, due to ohmic drop, the calculation of Hall voltage is not accurate. The activation energy of CTO was calculated and is similar to literature value reported by Parkin (0.73 eV vs 0.71 eV). The difference in activation energy between CTO and Cr_2O_3 could suggest that the films are true solid solution rather than a mixture of chromium and titanium particles.

CWO and CNO was successfully deposited onto sensor substrates. Optimum deposition parameters (flow rate and deposition temperature) were investigated and found that films fabricated at 340 °C and 1.5 L min^{-1} displayed minimal changes in atomic percentage. pXRD displayed no phase separation within the detection limit of pXRD for both materials. The film thickness was measured at 23.3 μm for CWO. The activation energy was determined and at temperature below 475 K, CWO energy was at 0.03 eV and 0.04 eV. Above 475 K, it was at 0.8 eV and 0.9 eV. This shows that the addition of an *n*-type dopant/ adding a stronger *n*-type dopant on a *p*-type metal oxide (Cr_2O_3) increases activation energy at high temperature settings and decreases at low temperature settings. The measured thickness of CNO was at 13.75 μm, similar to the thickness of NiO (13.2 μm). The activation energy observed here for CNO was very similar to that of Cr_2O_3 which is to be expercted as only small levels of doping was used and that NiO is a *p*-type.

Chapter 6

Thin Films Gas Sensing Analysis

In this chapter, mono and multi component MOS thin films synthesised in chapters 4 and 5 are used to test its sensitivity and selectivity towards a ranges of gases and VOCs. The sensitivity (S) can be defined as R_g/R_a and selectivity can usually be defined as the ability to discriminate the target from the interference molecules and display a target-specific sensor response. However, in this case selectivity will be defined as the number of response produced in reaction to different gas analyte, where gases were tested one at a time. R_g is the baseline resistance of gas analyte and R_a is the resistance of air. The detection limit can be defined as when the resistance or sensitivity response reaches a plateau or the minimum concentration of the target gas that can be reliably distinguished from the absence of the same gas. Response time is defined as the time required for a sensor to reach 90 % of the total response of the signal such as resistance upon exposure to the target gas.

6.1 Sensitivity towards isobutylene, ammonia and hydrogen sulfide

6.1.1 Chromium Oxide

Three Cr_2O_3 thin film sensors were deposited via standard AACVD synthesis and annealed at 600 °C for 24 hours. Multiple sensors were used for concordant result. The sensitivity

of these sensors towards isobutylene is illustrated in figure 6.1. Figure 6.1a) shows the resistance change of the the Cr_2O_3 sensors towards isobutylene and figure 6.1b) shows the sensitivity response (R_g/R_a). The test conditions was set at two different concentrations of isobutylene at 50% relative humidity and operating temperatures of 400 °C and 450 °C. These temperature were chosen as previous work done within the group showed CTO displays good sensitivity at these temperature settings. Each temperature was tested with three pulses of isobutylene (20 ppm-5 ppm-20 ppm) with a five minute recover time between each pulse. As shown figure 6.1a), there is a change in resistance value for all three samples which demonstrates the sensitivity towards isobutylene. Looking at the R_g/R_a responses, the sensors response displays very little change in response when concentration levels were changed from 20 ppm to 5 ppm (1.11 vs 1.07 for sensor Cr_2O_3-2) Response values remained stable as temperatures ramped from 400 °C to 450 °C and back down to 400 °C. In general, the sensitivity of Cr_2O_3 sensors towards isobutylene is relatively small, a response change of 0.11 at 400 °C and 20 ppm concentration.

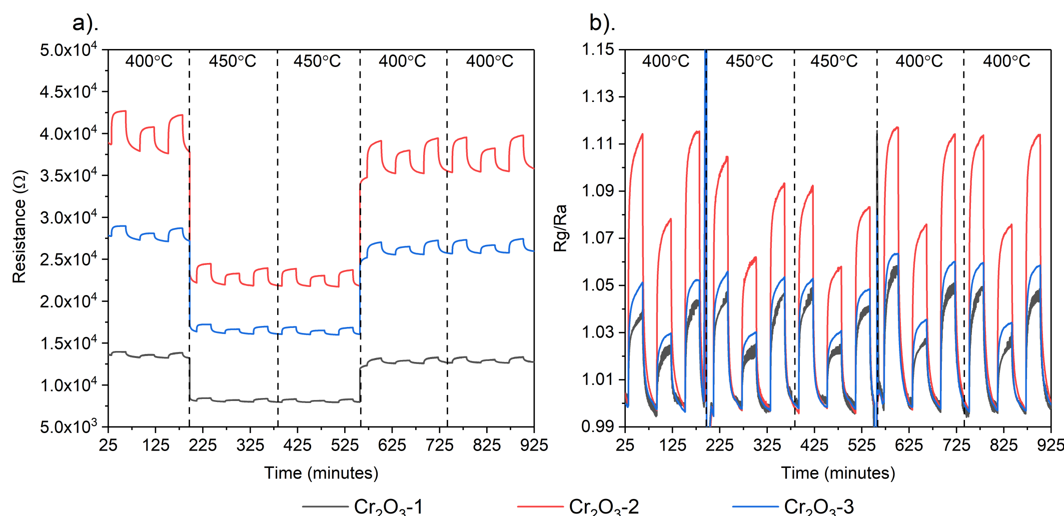

Figure 6.1. AACVD Cr_2O_3 gas sensor response towards isobutylene (20 ppm-5 ppm-20 ppm pulse) and working temperature of 400 °C and 450 °C; where a). Resistance response and b). R_g/R_a response.

Fang[232] reported a *n*-type ZnO sensor which displayed sensitivity towards isobutlyene at 50 % relative humidity and temperature of 25 °C at two concentration levels (10 ppm and 25 ppm). This is illustrated in figure 6.2. At a concentration of 25 ppm, a change of response (R/R_0) of 1.8 was seen with a response time of 20 seconds and displayed a higher

response compared to Cr_2O_3 sensors (response change of 0.11).[232] This was to be expected as ZnO have been widely used and researched as a gas sensor due to its fast response, low detection limit and high selectivity. At a concentration of 10 ppm, a slight drop in response was seen (from 2.8 to 2.2) and rapid recovery time. The response time for AACVD Cr_2O_3 sensors at 400 °C and pulse of 20 ppm was 20.4 s which is the same as the reported ZnO sensor and at a pulse of 5 ppm was 30.6 s.

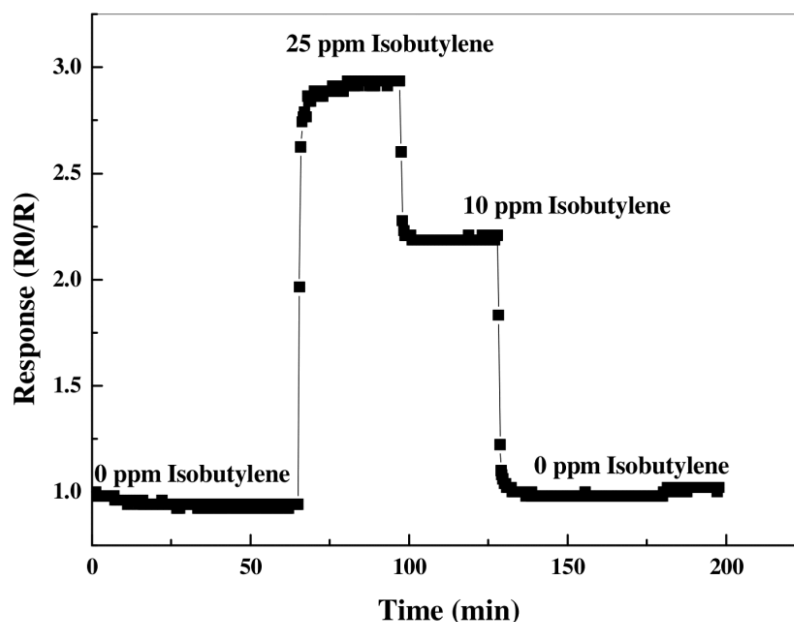

Figure 6.2. ZnO sensor response towards isobutylene.[232]

When looking at the mechanism of gas sensing (in terms of surface-traped limited), it is expected that the combustion of isobutylene analyte gas on the surface of the sensing layer reduces the concentration of surface acceptor oxygen (S_A) as it is oxidising isobutylene. Hence, S_A is now reduced, the electrons will be released and flow back into the valence band (as this is a p-type material) which causes the annihilation of holes and as a result increases the resistance of the material. As explained in chapter 2, for p-type materials, the sensitivity is independent of the amount of surface acceptors and can hypothesis the sensitivity of p-type is determined by where the valence band lies with respect to the surface acceptor and how readily electrons are accepted.

The sensors were next exposed to ammonia with similar test conditions as isobutylene, with only the different concentrations (25 ppm and 75 ppm). The resistance response and

R_g/R_a response are displayed in figure 6.3. The response seen for ammonia are similar to ones recorded for isobutylene. A R_g/R_a of 1.095 for the one of the sensors at a concentration of 75 ppm and 400 °C as compared to 1.11 seen for detection of isobutylene at 25 ppm. Again a decrease in response is observed when concentration was lowered from 75 ppm to 25 ppm, but recovers when increased back to 75 ppm. Temperature ramping (400 °C to 450 °C) displayed minimal effect towards response (R_g/R_a) values when compared. The response time for AACVD Cr_2O_3 sensors at 400 °C and pulse of 75 ppm was 62.8 s and at a pulse of 25 ppm was at 109.8 s.

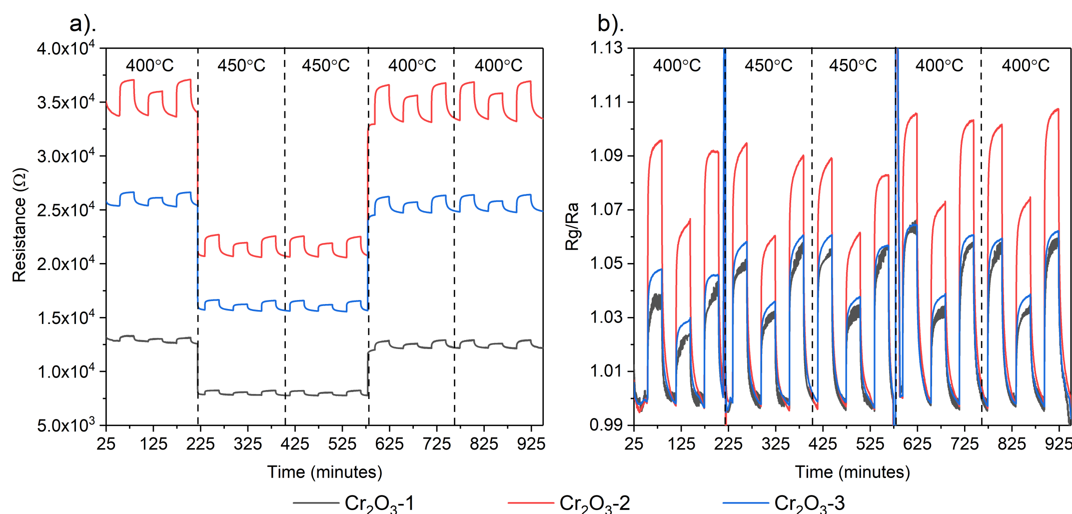

Figure 6.3. AACVD Cr_2O_3 gas sensor response towards ammonia (75 ppm-25 ppm-75 ppm pulse) and working temperature of 400 °C and 450 °C; where a). Resistance response and b). R_g/R_a response.

Almaev[233] reported the reponse of their Cr_2O_3 thin film sensors. A note to bear in mind, the reported sensors are thin films annealed at 450 °C with a grain size between 60 nm to 130 nm. A response of 90% was measured (response % = $[(R - R_0)/R_0] \times 100$) at a working temperature of 150 °C and 500 ppm of ammonia in a pure air environment and is displayed in figure 6.4.[233] For these sensors it can be seen that working temperatures has an effect on the response towards ammonia; as temperature increase towards 150 °C for the sample annealed at 450 °C, response increase exponentially but decreases once past 150 °C.

Compared to other types of MOX sensors for example tin coated indium oxide reported by Qi,[234] the Cr_2O_3 thin film sensors are outperformed by these *n*-type sensors and are dis-

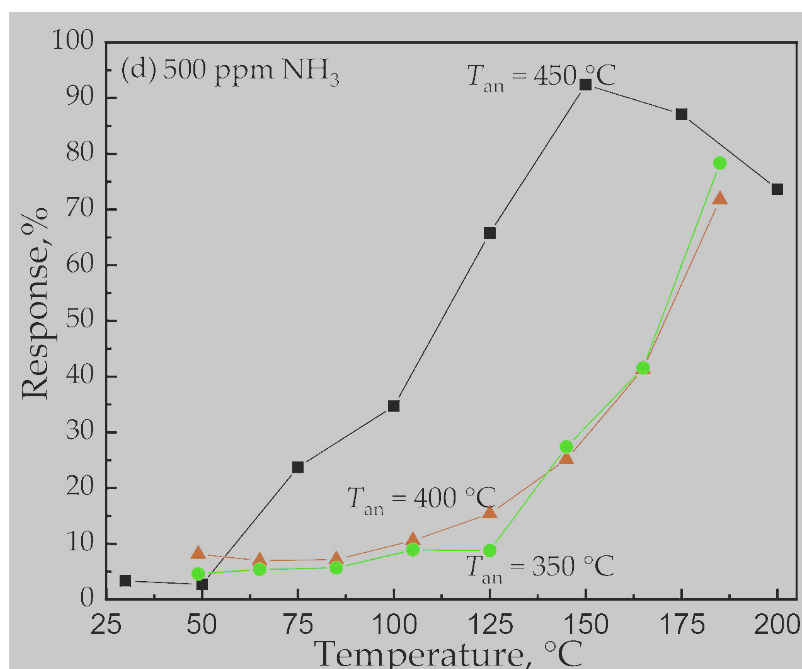

Figure 6.4. Cr_2O_3 response towards ammonia reported by Almaev.[233]

played in figure 6.5.[234] These sensors reported by Qi were exposed to 1 ppm of ammonia at room temperature where one of the sensors reported a sensitivity response of 21. which is significantly larger than the 1.095 seen for Cr_2O_3 thin film sensors. This could be due to the high surface area seen for these tin coated indium oxide sensors, with a BET surface area of 102 $m^2\,g^{-1}$, whereas uncoated indium oxide only has a BET surface area of 15 $m^2\,g^{-1}$. As described in chapter 2 gas sensing mechanism, n-type materials are dependent on surface acceptor states, hence a larger surface area would increase the response towards in this case ammonia as there would be more surface acceptors to interact with the target gas.

6.1.2 Nickel Oxide

Five NiO sensor samples, which were fabricated the same way were exposed to isobutylene at variable temperatures ranging from 300 °C to 450 °C, with a fixed concentration of 25 ppm and 50% relative humidity displayed in figure 6.6. The resistance and heater temperature profile is also shown. The resistance response towards 25 ppm of isobutylene for all sensor samples displayed little to no change across all tested operating temperature

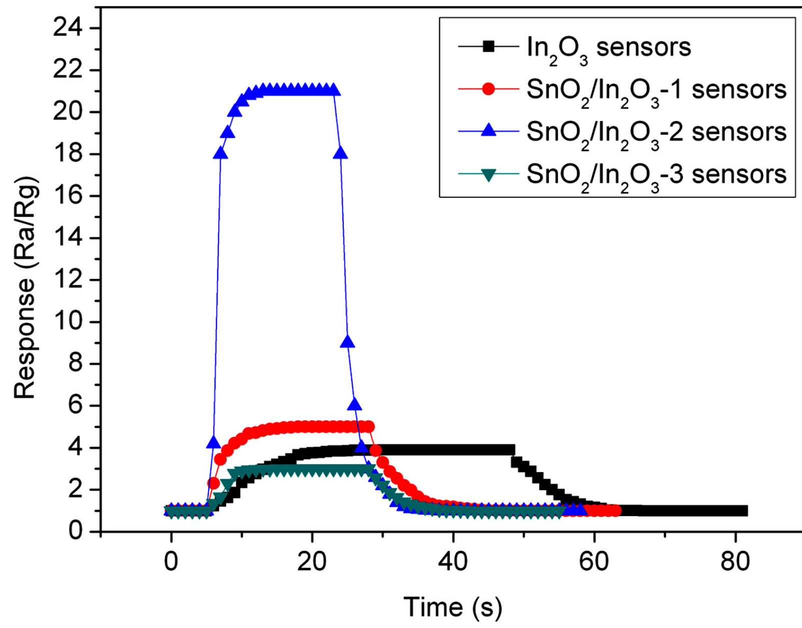

Figure 6.5. Indium and tin coated indium oxide response reported by Qi.[234]

(300 °C to 450 °C).

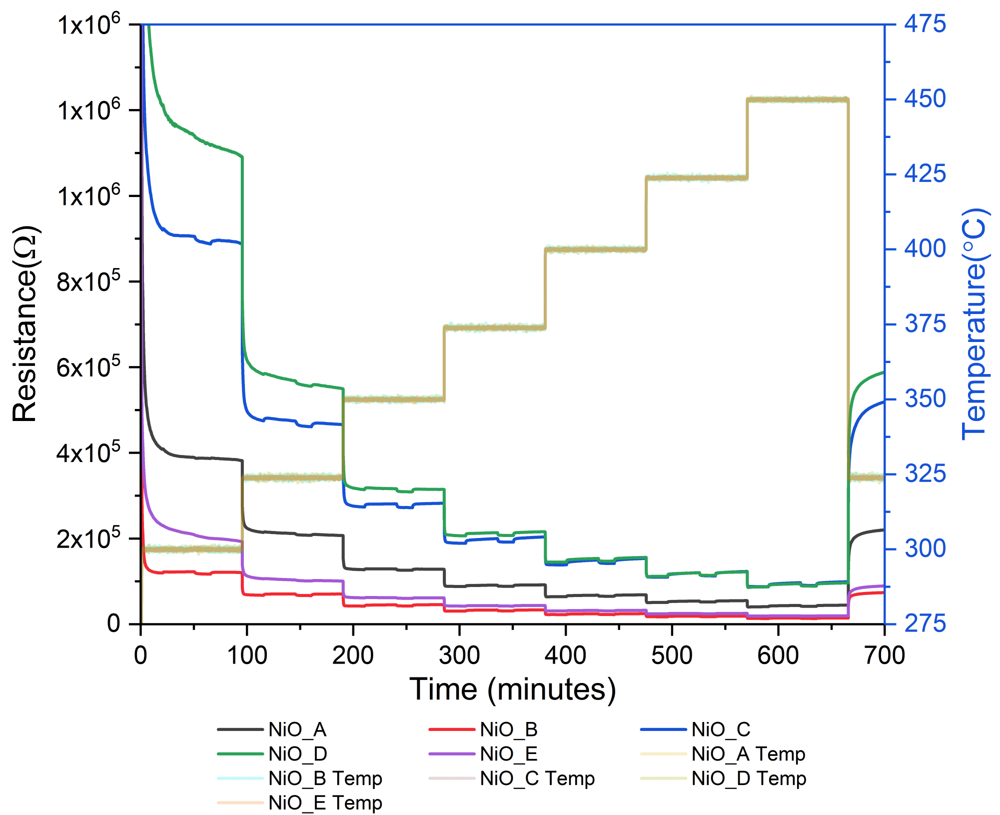

Figure 6.6. NiO sensor response (resistance in Ω) towards isobutylene at variable operating temperatures.

Convington and Ayyala reported the response of spin coated NiO sensors tested at

40% relative humidity and operating temperature of 350 °C.[235] The thickness of the film are comparable to ones deposited in this report (13.2 µm vs 5 µm and 10 µm). Figure 6.7 shows the literature measurements for NiO sensors. The literature also shows a weak resistance response towards isobutylene similar to the sensors reported here for NiO. NiO resistance response are also low compared to Cr_2O_3 sensors.

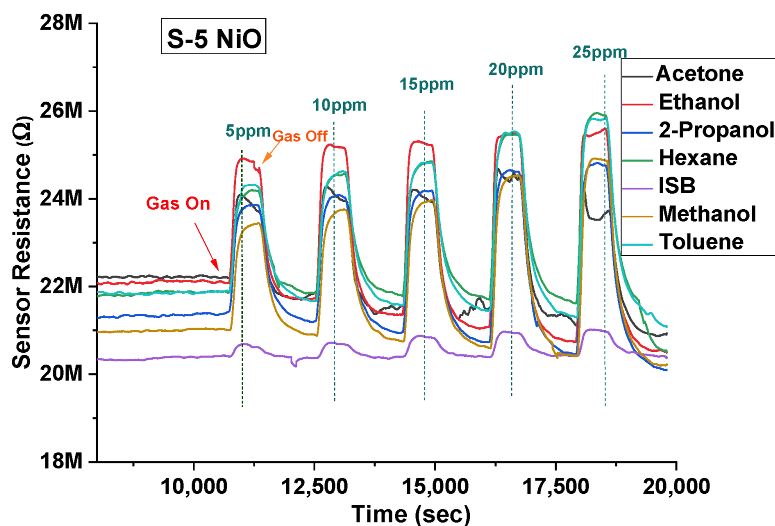

Figure 6.7. NiO sensor response (resistance in Ω) towards different gases reported by Ayyala.[235]

6.1.3 Chromium Titanium Oxide (CTO)

CTO(0.15) thin films were deposited onto alumina based substrate sensors via standard AACVD synthesis method and annealed at 600 °C. These sensors were then tested towards isobutylene, ammonia and hydrogen sulfide to compare to sensors deposited via the same method in a previous study to determine the reproducibility of the process. The CTO(0.15) gas sensors were annealed at 600 °C for 6 and 30 hours (CTO(0.15)A-6HR and CTO(0.15)A-30HR) and were compared to standard screen printed sensors made at Alphasense and AACVD-deposited ones made previously, annealed at 600 °C for 10 hours. Two of each sensors were used to test the material.

Gas sensing properties of the CTO(0.15) were measured and compared to screen printed CTO sensors at operating temperatures of 400 °C and 450 °C with two different concentration of isobutylene 5 ppm and 20 ppm. The sensors were also exposed to 50% relative

humidity and exposure time of each pulse towards the analyte was 30 min, then followed by 30 min of air and so on. This is illustrated in figure 6.8.

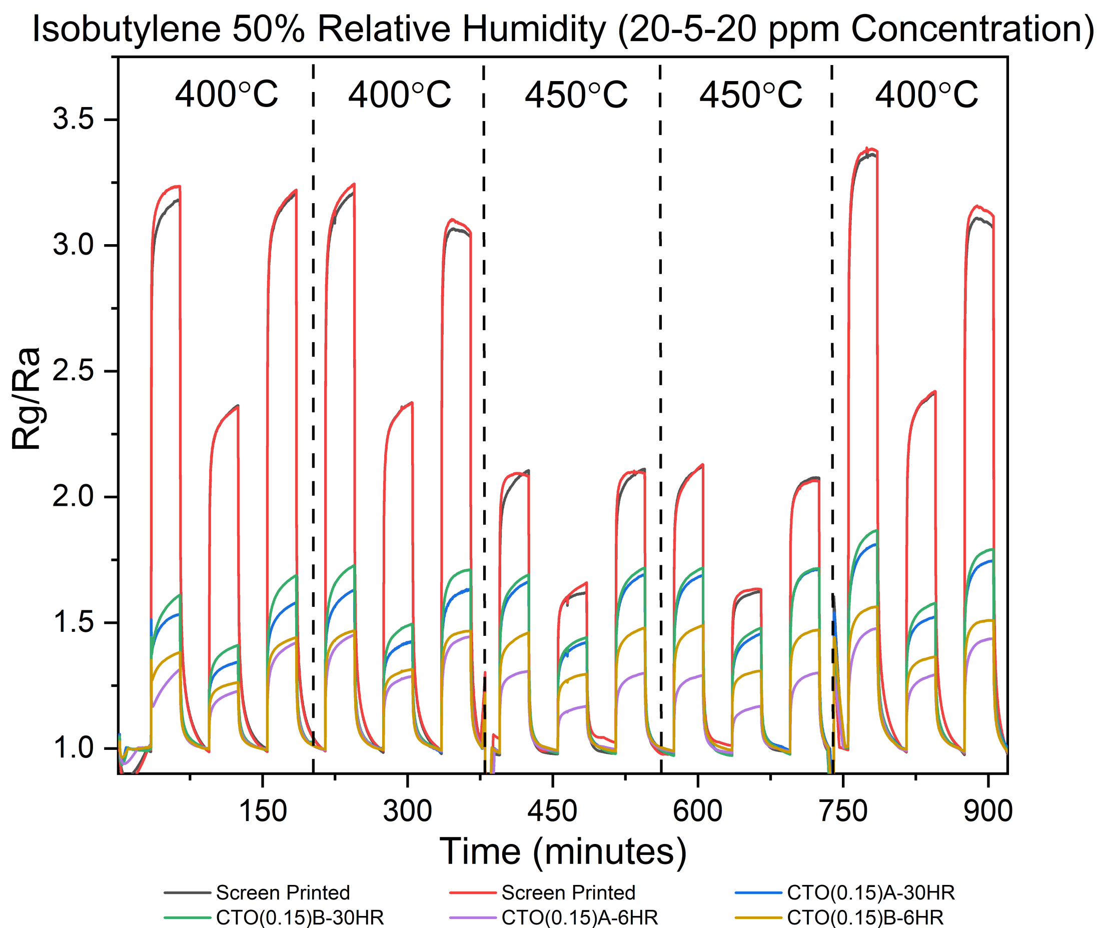

Figure 6.8. AACVD and screen printed CTO sensor gas response towards isobutylene (20 ppm-5 ppm-20 ppm pulse) and working temperature of 400 °C and 450 °C.

The sensors exhibited a *p*-type response towards the reducing gas (the resistance increased upon exposure to isobutylene) even at low concentrations (5 ppm with a response of ~ 2.38 for screen printed and ~ 1.4 for AACVD). These AACVD sensors displayed a slightly higher response than Cr_2O_3 sensors (~ 1.4 vs ~ 1.07) at 5 ppm concentration and 400 °C working temperature. When exposed to a concentration of 20 ppm and at a operating temperature of 400 °C, AACVD sensors annealed for six hours displayed a slightly lower response compare to ones annealed for 30 hours towards isobutylene (~ 1.4 vs ~ 1.22). In general, at a operating temperature of 400 °C, screen printed sensors displays a better response towards isobutylene than AACVD (~ 3.2 vs ~ 1.7). When concentration was decreased from 20 ppm to 5 ppm, response for screen printed sensors dropped to

∼ 2.1; however, for AACVD sensors remained relatively unchanged, displaying similar response even at low concentration levels, ∼ 1.6 and ∼ 1.4 for 20 ppm and 5 ppm respectively. When concentration increased back to 20 ppm, screen printed sensors response recovered back to ∼ 3.4. An increase in operating temperature to 450 °C demonstrated a decrease in response for screen printed sensors at a concentration of 20 ppm (∼ 3.2 vs ∼ 2.1). Whereas for AACVD sensors, at a concentration of 20 ppm, an increase in temperature displayed no changes in R_g/R_a response (∼ 1.7).

When the operating temperature was reduced back down to 400 °C, sensors response recovered back to ∼ 3.2 and ∼ 1.7 for screen printed and AACVD sensors respectively. It is also worth pointing out that the annealing temperature time has marginal effect on the sensors response towards isobutylene. Ones annealed for 30 hours displayed a only a slightly higher response than ones annealed for six hours.

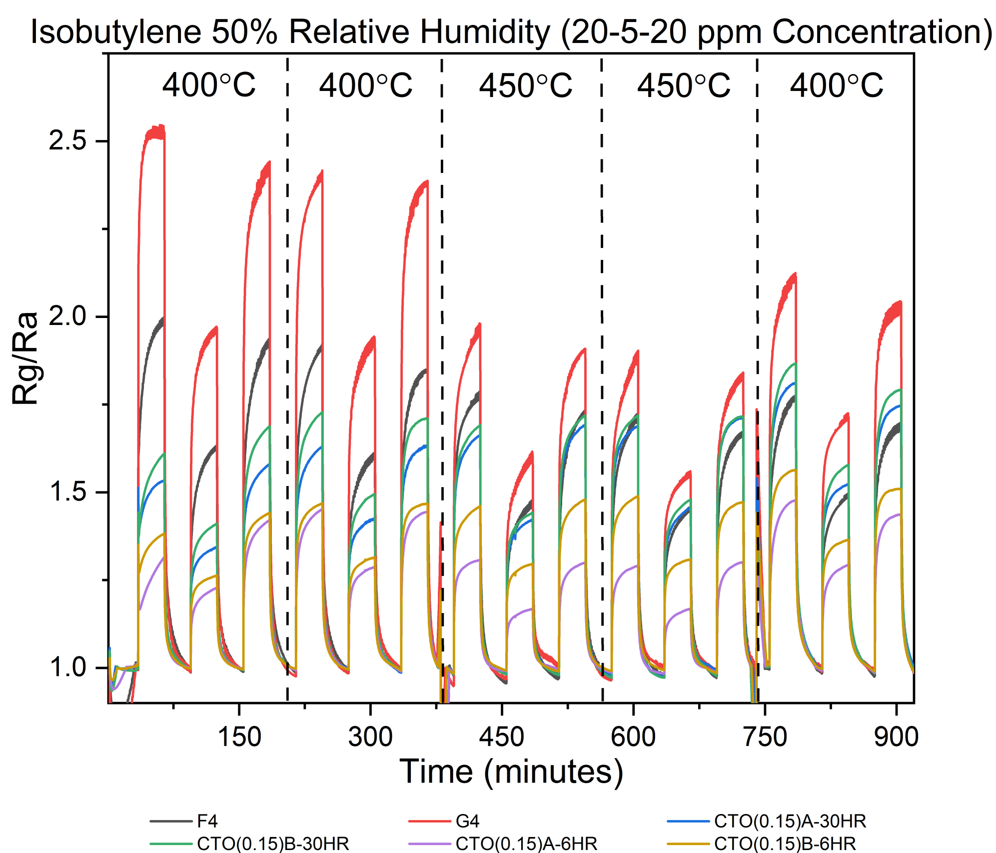

Figure 6.9. AACVD CTO sensor gas response towards isobutylene (20 ppm-5 ppm-20 ppm pulse) and working temperature of 400 °C and 450 °C in comparison with sensors previously made.

AACVD sensors were also compared to AACVD sensors in a previous study (F4 and G4) to demonstrate the reproducibility of the deposition technique. Figure 6.9 shows the comparison between the AACVD sensors. The sensors made by Dr Di Maggio are expected to be five times thicker (in terms of volume used for the deposition) and were annealed at 600 °C for ten hours. The F4 and G4 sensors typically displayed similar response values to one another; the three types of sensors analysed displayed a constant R_g/R_a response (∼ 1.6) at 20 ppm of isobutylene exposure at both 400 °C and 450 °C.

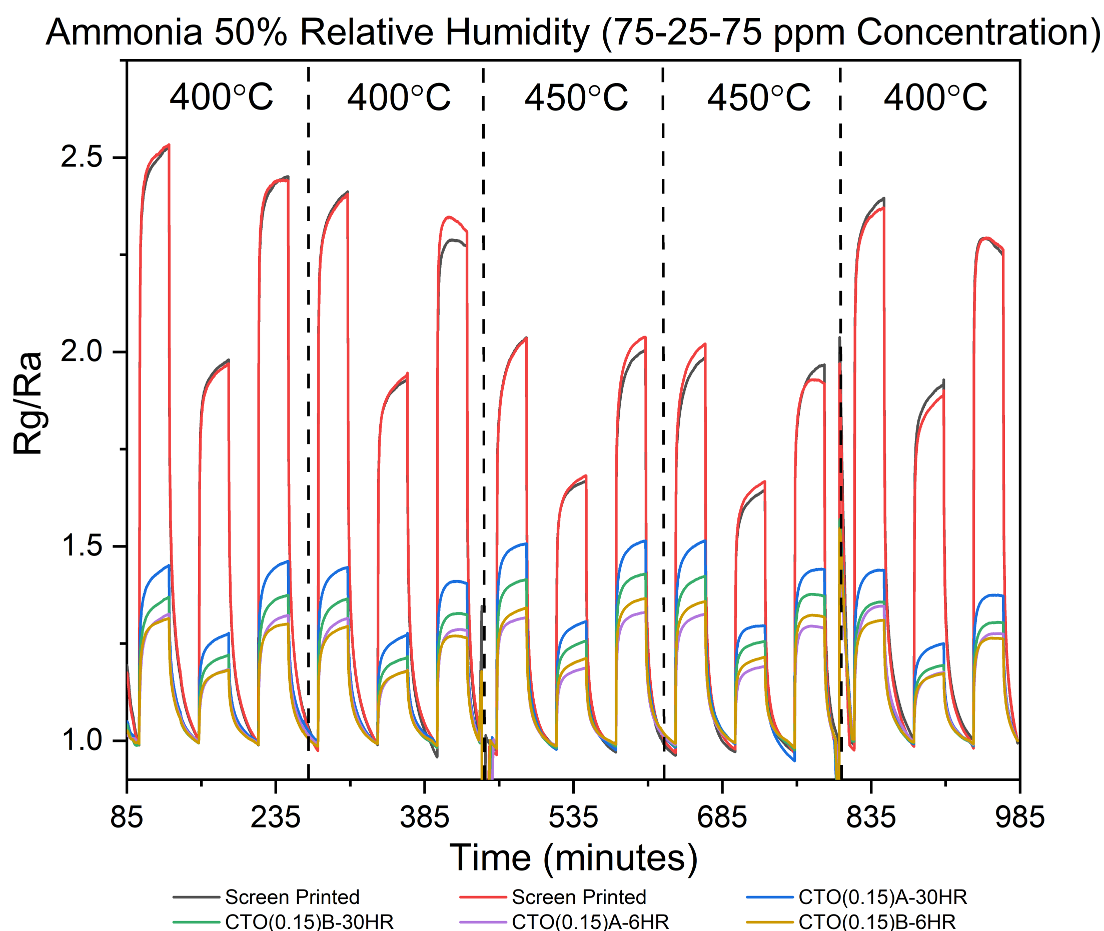

Figure 6.10. AACVD and screen printed CTO sensor gas response towards ammonia (75 ppm-25 ppm-75 ppm pulse) and working temperature of 400 °C and 450 °C.

Sensors were next exposed to ammonia at 50% relative humidity. Again the screen printed sensors displayed a better response than AACVD sensors annealed for 30 h at a operating temperature of 400 °C and 75 ppm of ammonia (∼ 2.55 vs ∼ 1.45). AACVD sensors annealed for six hours were comparable to ones annealed for 30 h (∼ 1.32). A decrease in concentration from 75 ppm to 25 ppm produced a decrease in response for

screen printed sensors (from ~ 2.55 to ~ 1.95) at 400 °C, a 24 % change. Whereas for AACVD sensors annealed for 30 hours,the R_g/R_a change was relatively smaller (~ 1.45 to ~ 1.26), a 13 % change. When operating temperature was increased to 450 °C, the sensing response decreased for both screen printed and AACVD for 75 ppm of ammonia. Screen printed sensors response decreased slightly from ~ 2.55 to ~ 2.1 (a change of 18 %) and for AACVD annealed for 30 hours, a slight increase in response was seen from ~ 1.45 to ~ 1.52 (a change of 5 %). A decrease in concentration from 75 ppm to 25 ppm at a operating temperature of 450 °C, screen printed sensors displayed a slight decrease in response from ~ 2 to ~ 1.7; whilst for AACVD sensors annealed for 30 hours, response dropped from ~ 1.52 to ~ 1.3. CTO sensors displayed a better response towards ammonia compared to Cr_2O_3 sensors. The highest response seen for Cr_2O_3 at 400 °C and 75 ppm of ammonia was ~ 1.09, whereas for CTO in the same conditions, the response was at ~ 1.45.

Sensors were exposed to hydrogen sulfide at 50% relative humidity at operating temperatures of 400 °C and 450 °C and concentrations of 8 ppm and 24 ppm shown in figure 6.11. At 400 °C and 24 ppm, AACVD CTO sensors displayed high response towards hydrogen sulfide, with the ones annealed for 30 h demonstrating the highest response (~ 50 and ~ 56). Whereas one annealed for six hours displayed a response of ~ 55 and ~ 30. Screen printed sensors displayed a significantly lower response than AACVD sensors, with a response of ~ 9.2 (AACVD are a factor of five more sensitive than screen printed). When concentration of H_2S decreased to 8 ppm AACVD sensors recorded a large drop in response from ~ 56 to ~ 10; whereas with the screen printed sensors, response decreased by a third, from ~ 9.2 to ~ 2.8. As concentration of the analyte increased back to 24 ppm, AACVD sensors response recovered. However two of the AACVD sensors showed a decrease in response. Over the course of the test, the sensors response at 24 ppm as it gradually goes through the cycle of operating temperature and recovery from a decrease of analyte. Whereas with screen printed sensors, the response remained stable throughout the test. In general, AACVD sensors displays better sensitivity towards H_2S than screen printed sensors, however, response reading varied and is less stable than screen printed

which is more constant.

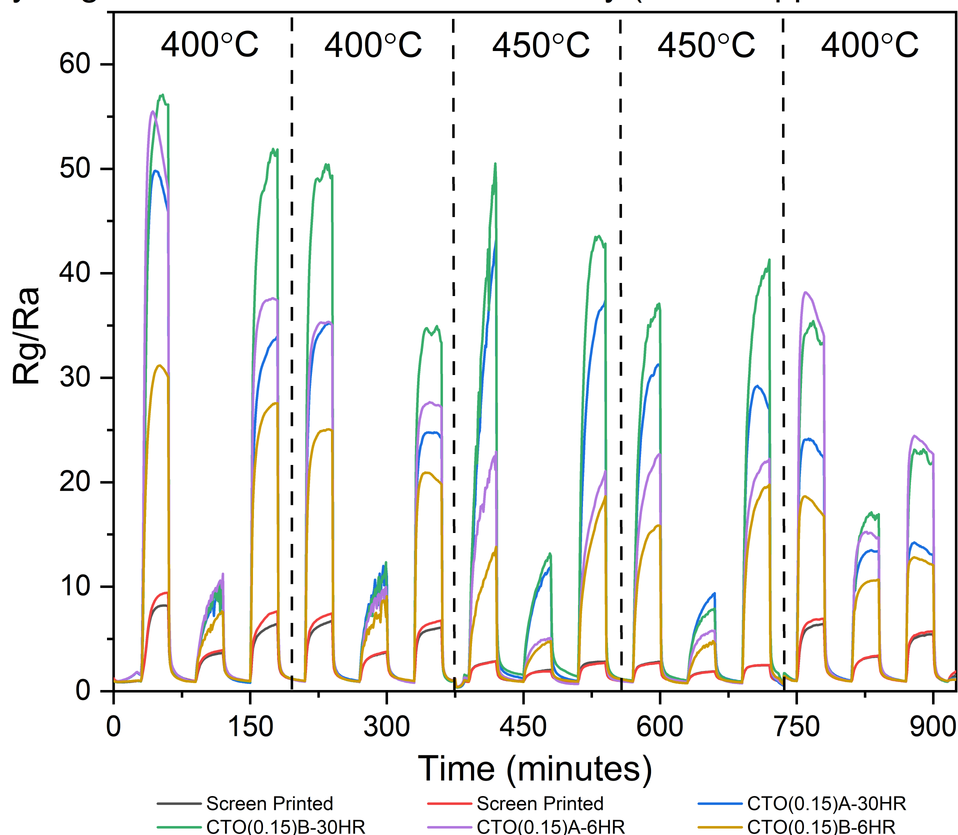

Figure 6.11. AACVD and screen printed CTO sensor gas response towards hydrogen sulfide (24 ppm-8 ppm-24 ppm pulse) and working temperature of 400 °C and 450 °C.

6.1.4 Tungsten Doped-chromium Oxide

AACVD CWO thin film sensors sensors were deposited by the similar method as CTO sensors. After in depth thin film characterisation, the optimum parameters for CWO thin film deposition via AACVD was at 340 °C and 1.5 L min^{-1} using methanol as the solvent and chromium hexacarbonyl and tungsten hexacarbonyl as the starting precursors. For a doping level of CWO(0.15), the amount of tungsten hexacarbonyl needed was shown to be at 0.013 g.

CWO(0.15) sensors which were annealed for six hours were first exposed to isobutylene to analyse its gas sensing sensitivity and selectivity. The sensors were exposed to two different concentrations of isobutylene (5 ppm and 20 ppm) at two different operating

temperatures and at a relative humidity level of 50%. The exposure time of gas analyte was 30 minutes, then 30 minutes of air and so on. Two different operating temperatures where analysed to see if temperature had an effect on the sensitivity of the sensor towards isobutylene and to also see the recovery of the sensor when working temperature ramps up and down. This is shown in figure 6.12.

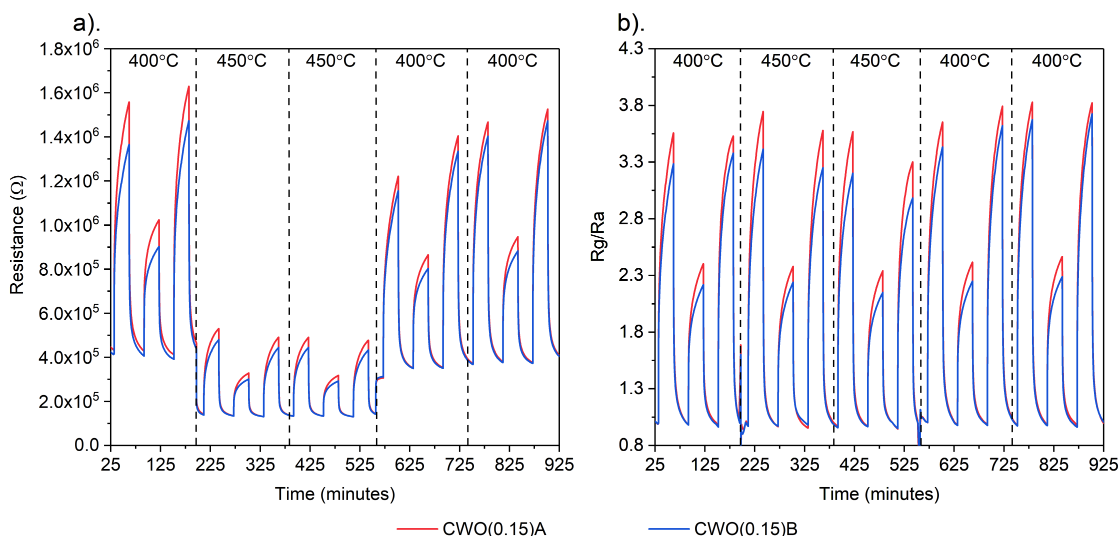

Figure 6.12. AACVD CWO gas sensor response towards isobutylene (20 ppm-5 ppm-20 ppm pulse) and working temperature of 400 °C and 450 °C; where a). Resistance response and b). R_g/R_a response.

CWO sensors displays a large change in resistance response towards 20 ppm of isobutylene at a operating temperature of 400 °C, with an R_g/R_a responses of 3.5. When concentration levels of isobutylene were decreased to 5 ppm, response also decreases which is to be expected as concentration levels were decreased by a factor of four, but the response only dropped by less than halve (2.3). When concentration levels of isobutylene increased back to 20 ppm, response recovered back to original value. When operating temperatures increased to 450 °C, resistance drops significantly; but the R_g/R_a response was unaffected, with the response recorded to be similar to that of when operated at 400 °C. This indicate that the sensors response could be stable at high temperature. When compared to screen printed CTO sensors, the R_g/R_a response are comparable if not better. At 20 ppm of isobutylene and operating temperature of 400 °C is 3.5 for CWO(0.15) and 3.2 for screen printed CTO. For operating temperature of 450 °C and 20 ppm of isobutylene, CTO only

had a response of 2.2, whereas it was unchanged for CWO. When compared to AACVD CTO(0.15) sensors annealed for six hours, the R_g/R_a response for CWO was almost two times larger than CTO(0.15) (3.5 vs 1.35 at 20 ppm and 400 °C). The improved sensor response between CTO and CWO is due to the difference in dopant, as there are more *n*-type carrier concentration than *p*-type due to *n*-type doping and hence may exhibit a more *n*-type like behaviour.

The sensors were next exposed to different concentrations of ammonia (25 ppm and 75 ppm), again at two different operating temperatures (400 °C and 450 °C) and at a relative humidity level of 50%. CWO sensors displayed sensitivity towards ammonia as shown in figure 6.13. Decreasing the concentration had a minimal effect on the response towards ammonia with the R_g/R_a response dropping from 1.5 to 1.3 at an operating temperature of 400 °C. When the operating temperature ramped up to 450 °C, resistance values showed a decrease but the R_g/R_a response remained similar, again displaying the minimal effect temperature has towards the sensors response. Throughout the 18 hour test, the sensors maintained a stable response towards ammonia. When compared to screen printed sensors, CWO are less sensitive to ammonia than screen printed CTO 1.5 vs 2.5 at 400 °C and gas analyte exposure of 75 ppm. The CWO sensors are comparable to AACVD CTO sensors annealed for six hours,1.5 vs 1.3 at the same test conditions.

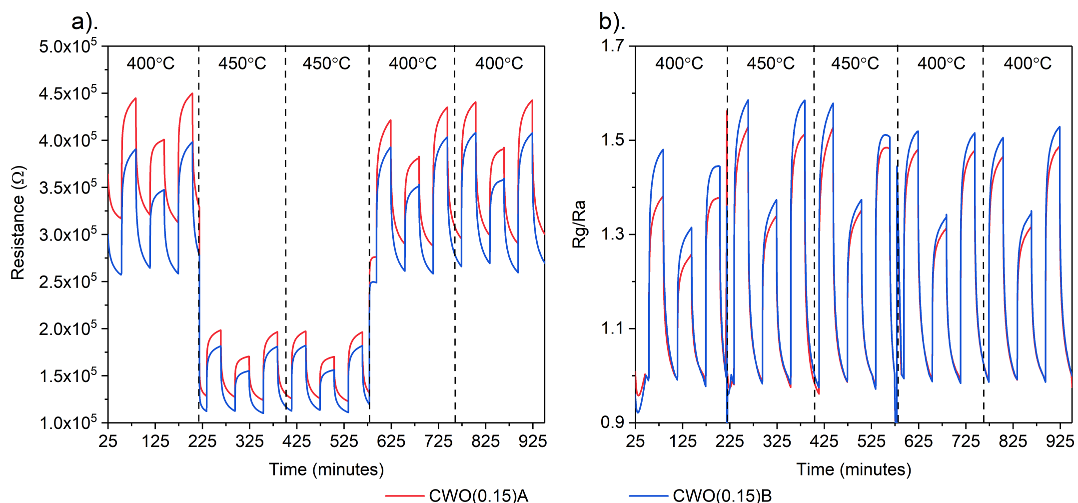

Figure 6.13. AACVD CWO gas sensor response towards ammonia (75 ppm-25 ppm-75 ppm pulse) and working temperature of 400 °C and 450 °C; where a). Resistance response and b). R_g/R_a response.

6.1.5 Summary

In general Cr_2O_3, NiO, CTO and CWO were successfully deposited onto alumina sensor substrates and demonstrated sensing capabilities towards isobutylene, ammonia and hydrogen sulfide. For Cr_2O_3 sensors, they demonstrated a relatively low response towards both isobutylene and ammonia with a response of roughly 1.07 at 400 °C; whereas screen printed displayed a value of 3.2 and 2.5 for isobutylene and ammonia respectively at 400 °C. NiO also displayed a low change in resistance response towards isobutylene across various temperatures. Compared to the literature, the resistance response were comparable.

For CTO(0.15), the sensors show that the response was reproducible when compared to previously made CTO sensors. Response towards isobutylene and ammonia was higher than pure Cr_2O_3 sensors (1.7 vs 1.07 for isobutylene) which shows that *n*-type doping has an effect on the sensitivity of the sensor. When compared to screen printed, the CTO(0.15) has a response two times smaller than screen printed at a temperature of 400 °C, 1.7 vs 3.2 and 2.4 (isobutylene and ammonia respectively). Despite the low sensitivity towards isobutylene and ammonia, AACVD CTO(0.15) displays outstanding sensitivity towards hydrogen sulfide. At 400 °C and 24 ppm, the sensors (annealed for 30 hours) displayed a response of $\sim$ 50 and $\sim$ 56. Whereas screen printed only displayed a response of $\sim$ 9.2 under the same conditions.

For CWO(0.15), the sensors displayed comparable response to screen printed CTO sensors towards isobutylene and was two times more responsive than AACVD CTO(0.15) sensors. Towards ammonia, the response was lower than screen printed but against AACVD CTO(0.15) the response was the same.

In terms of sensing mechanism, the combustion of reducing gases on the surface of the sensing layer is expected to reduce the concentration of surface acceptor oxygen (S_A) whilst oxidising the gas. Therefore, as S_A is reduced electrons are released back to the valence band, annihilating holes and hence increasing resistance of the sensor.

6.2 Sensitivity towards VOCs

In this section, several different types of VOCs were tested to analyse the sensitivity and selectivity of doped and undoped AACVD deposited thin film metal oxide sensors. Gases such as aldehydes, ketones, alcohols and aromatics were used to test these sensors. These tests were all done in the ppb concentration levels due to the upper limit of the gas analysis system.

6.2.1 Toluene

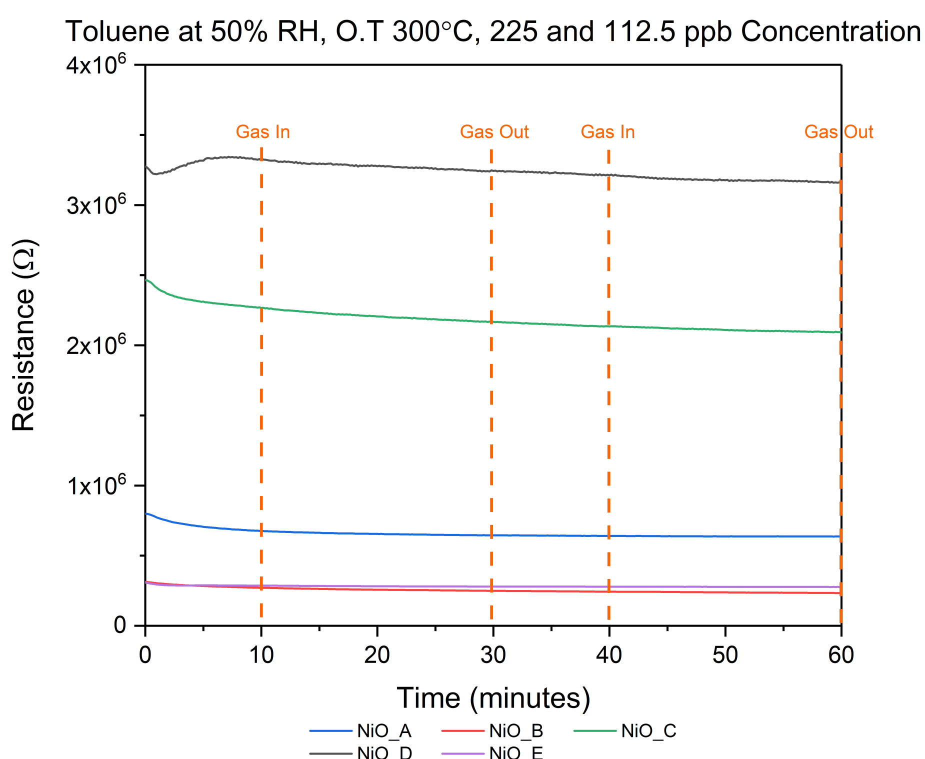

Figure 6.14. AACVD NiO sensors resistance response (Ω) against time (minutes) towards two pulses of toluene (225 ppb and 112.5 ppb) at operating temperature of 300 °C and 50 % relative humidity.

Five NiO sensor samples sensitivity were tested towards two pulses of toluene 225 ppb and 112.5 ppbm with the first pulse to be 225 ppb. The results are displayed in figure 6.14. The sensors were tested at an operating temperature of 300 °C and 50% relative humidity. The five NiO sensors tested gave no change in resistance response towards toluene at two different concentrations. However in the literature, as seen in figure 6.7 Covington

and Ayyala reported the sensitivity towards toluene between a concentration of 5 ppm to 25 ppm at 350 °C and 40% relative humidity with a R_g/R_a response of 1.15.[235] A reason for the samples not being able to detect toluene could be the detection limit. The concentration was in the ppb levels whereas the literature was at ppm levels. Another reason could be the operating temperature was not set at the optimum for NiO sensors.

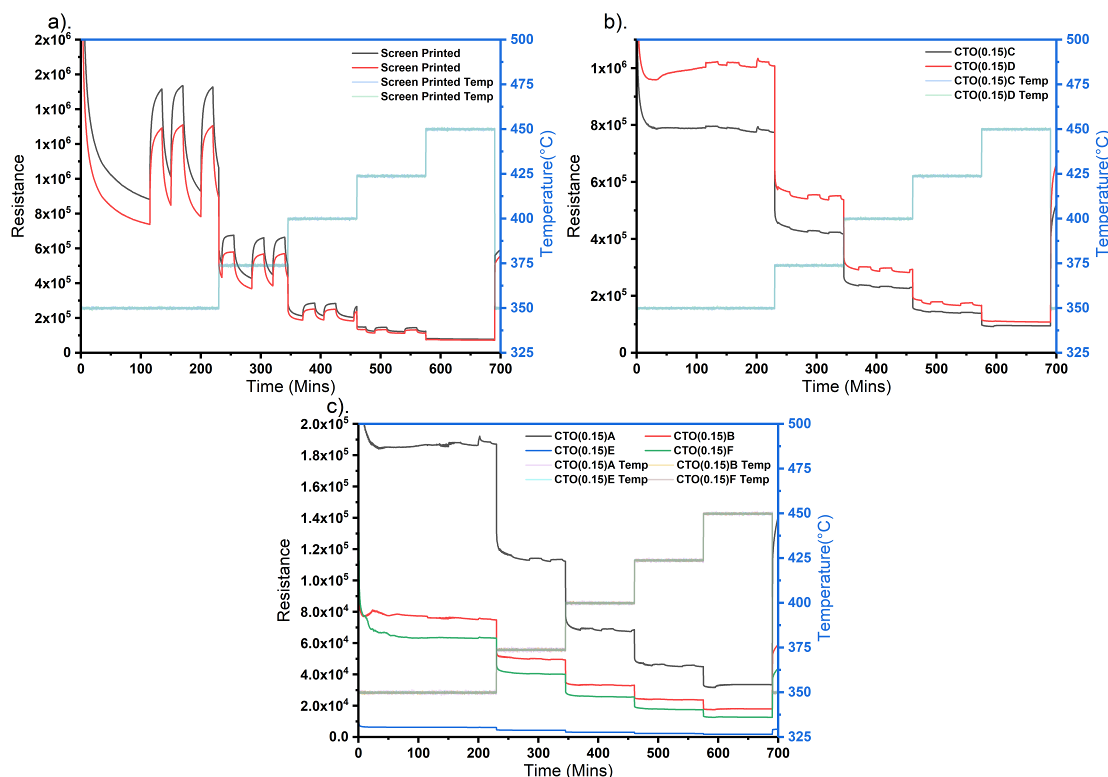

Figure 6.15. CTO sensor response (resistance in Ω) and operating temperature (°C) against time (minutes) when exposed to 210 ppb toluene at 50 % relative humidity, where; a) Screen printed sensors, b) AACVD sensors and c) AACVD sensors.

The sensors CTO(0.15) presented in this study for the detection of VOCs listed below have been annealed at 600 °C for 24 hours. The sensors were exposed to a concentration of 210 ppb toluene at 50% relative humidity and different operating temperatures. Operating temperatures between 350 °C and 450 °C were studied. This is illustrated in figure 6.15 which shows the resistance and the temperature profiles of the sensors. Screen printed sensors displayed a change in resistance (Ω) when exposed to toluene, which indicates CTO is sensitive towards toluene. However, as operating temperature increases, resistance response drops and the sensors became unable to detect toluene once temperature reached

450 °C. This shows that screen printed CTO works better at lower temperature when detecting toluene. For AACVD sensors, small changes in resistance was seen on some of the samples (CTO(0.15) A, CTO(0.15) C and CTO(0.15) D) displaying sensitivity towards toluene. However the response was far weaker than screen printed sensors. On a positive note, response towards toluene seem stable between an operating temperature of 350 °C to 425 °C whereas for screen printed sensors, the sensors response declines when operating temperature increases.

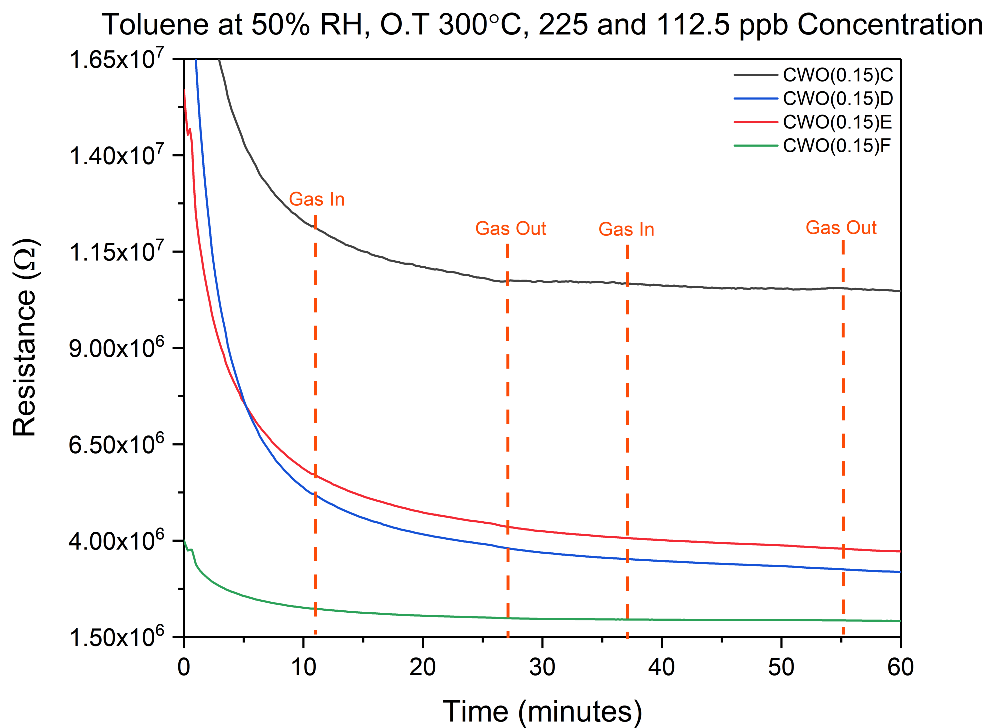

Figure 6.16. AACVD CWO sensors resistance response (Ω) against time (minutes) towards two pulses of toluene (225 ppb and 112.5 ppb) at operating temperature of 300 °C and 50 % relative humidity.

A new batch of sensors with the same composition (CWO(0.15)) were used for the detection of toluene. The sensors used the same deposition parameter as previously stated. Figure 6.16 displays the CWO sensor response towards two pulses of toluene (225 ppm and 112.5 ppm) at an operating temperature of 300 °C and 50% relative humidity. CWO sensors displayed no changes in resistance response towards toluene at these parameter settings. An increase in operating temperature may see a change in resistance response. For screen printed CTO sensors, the greatest response was recorded at the lowest tem-

perature measured 350 °C and a further decrease to 300 °C might be expected to increase the response further. The sensors also needs some time initially for it to stabilise as the sensors are not fully saturated in an humid environment.

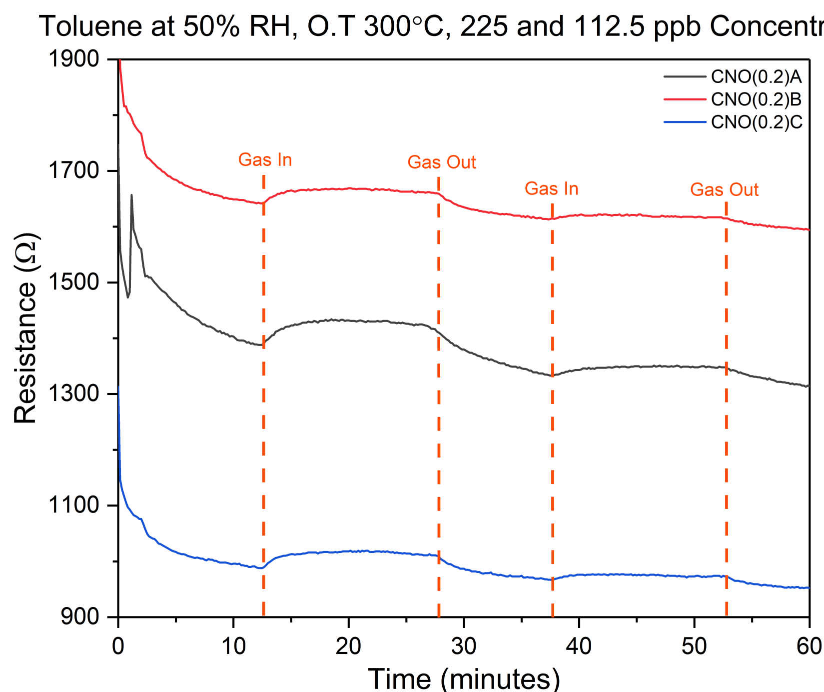

Figure 6.17. AACVD CNO sensors resistance response (Ω) against time (minutes) towards two pulses of toluene (225 ppb and 112.5 ppb) at operating temperature of 300 °C and 50 % relative humidity.

Nickel doped chromium oxide (CNO) thin films were deposited onto sensors with a doping level of $Cr_{1.8}Ni_{0.2}O$ via standard AACVD synthesis. This was to see what effect does *p*-type doping has on a already *p*-type metal oxide material. CNO sensors were first exposed to two pulses of toluene at different concentrations, 225 ppb and 112.5 ppb at an operating temperature of 300 °C and 50% relative humidity as described in figure 6.17. The sensors showed a change in resistance response towards both pulses of toluene, indicating that CNO is able to detect toluene, whereas for it was undetectable for CTO and CWO sensors. Also a point of interest is that the resistance values are significantly lower than all the sensors tested above. It is intriguing to see that there is a significant difference between an undoped Cr_2O_3 *p*-type material, CTO or CWO an *n*-type doped material and CNO a *p*-type doped material. This could suggest that the sensor could operate at low operating temperatures. With such a low resistance, the Hall mobility and carrier concentration

would be expected to be high. However, from Hall measurement the carrier concentrations are similar to other materials tested.

6.2.2 Formaldehyde

A new batch of sensors were used for the sensitivity analysis of Cr_2O_3 sensors towards formaldehyde, synthetic conditions were the same as before, so was for the annealing temperature and time. Cr_2O_3 sensors were exposed to two pulses of formaldehyde (95 ppb and 47.5 ppb) at 300 °C and 50% relative humidity. The two sensors analysed observed a small change in resistance response towards the exposure of formaldehyde, displaying sensitivity towards formaldehyde. No literature sources for the detection of formaldehyde using Cr_2O_3 were found.

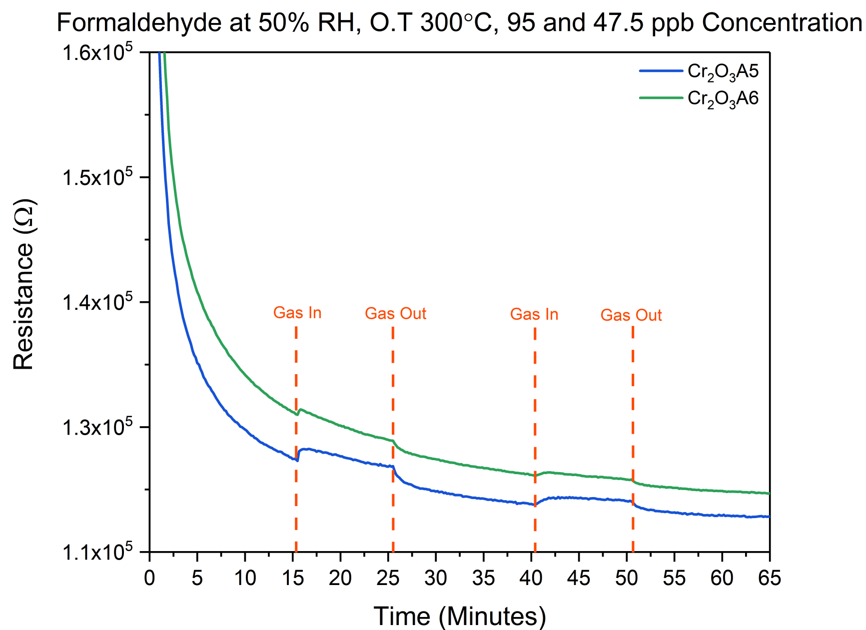

Figure 6.18. AACVD Cr_2O_3 sensors resistance response (Ω) against time (minutes) towards two pulses of formaldehyde (95 ppb and 47.5 ppb) at operating temperature of 300 °C and 50 % relative humidity.

NiO sensors sensitivity were next tested towards two pulses of formaldehyde 95 ppb and 47.5 ppb. The results are displayed in figure 6.19. The sensors were tested at an operating temperature of 300 °C and 50% relative humidity. The five NiO sensors tested observed no changes in resistance response towards the exposure of formaldehyde at two different concentrations.

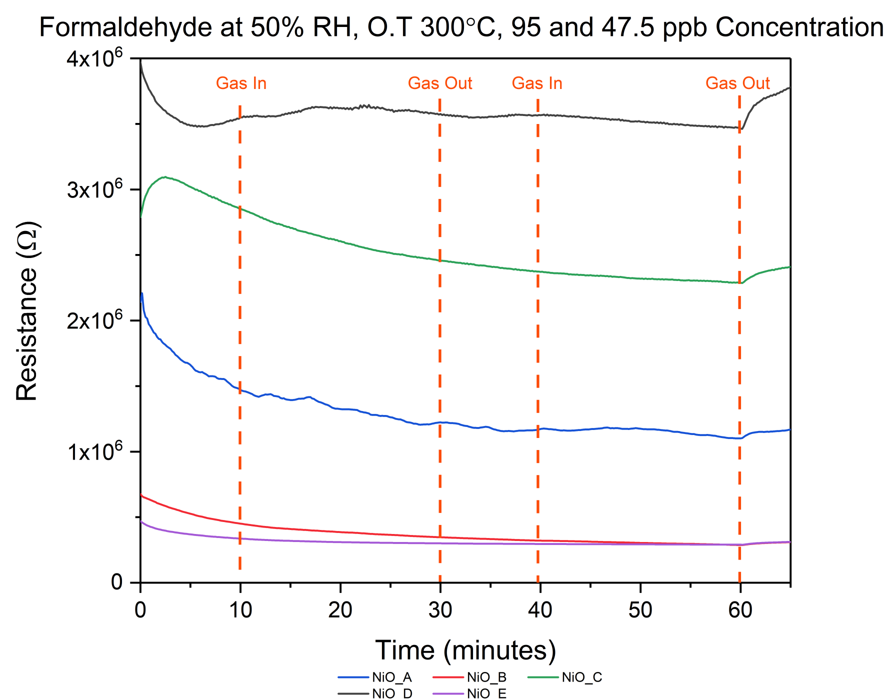

Figure 6.19. AACVD NiO sensors resistance response (Ω) against time (minutes) towards two pulses of formaldehyde (95 ppb and 47.5 ppb) at operating temperature of 300 °C and 50 % relative humidity.

Lai[236] reported the synthesis of mesoporous NiO for the detection of formaldehyde. Different pore thickness demonstrated different response towards formaldehyde which ranges from 2 to 20 R_g/R_a at 380 ppm concentration and is shown in figure 6.20. The condition for this measurement was conducted in ambient air and at 300 °C.[236] The reason for it to be undetected for these samples could be due to the detection limit of NiO thin films. It is also worth noting the concentration tested in Lai sample were 3 orders of magnitude higher in concentration than the thin film samples.

CTO(0.15) sensors were exposed to one pulse of formaldehyde at 350 °C and 50% relative humidity with a concentration of 50 ppb shown in figure 6.21. Small to no changes were seen for screen printed sensors. For AACVD sensors, two of the sensors (CTO(0.15) C and CTO(0.15) D) displayed a small change in resistance response, demonstrating sensitivity towards formaldehyde.The drop in resistance at the start of the test is due to humid air purging through the system for the first 15 minutes.

CWO(0.15) sensors were next tested towards formaldehyde which is shown in figure 6.22. The sensors were exposed to two pulses of gas analyte at 95 ppb and 47.5 ppb,

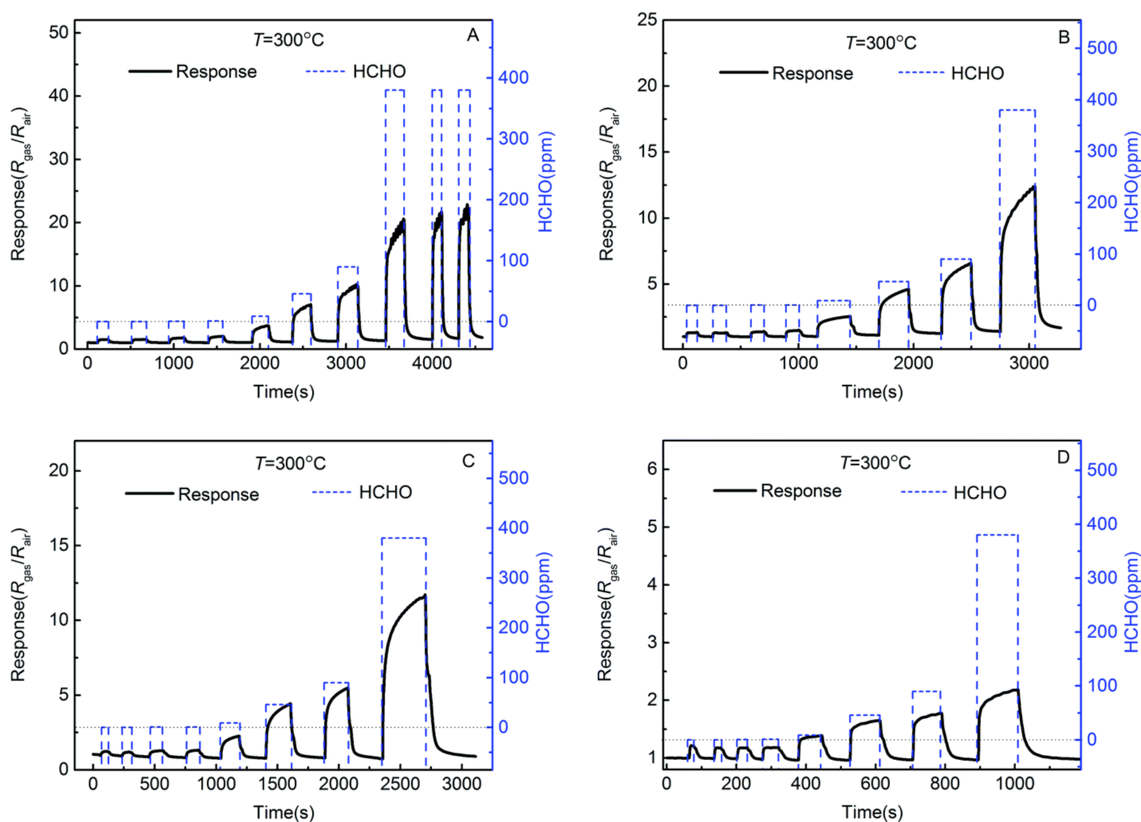

Figure 6.20. Typical dynamic response curves of gas sensors fabricated from (A) NiO-40, (B) NiO-80, (C) NiO-130 and (D) bulk NiO particle, during cycling between increasing concentration of HCHO and ambient air at 300 °C.[236]

again at an operating temperature of 300 °C and 50% relative humidity. CWO sensors displayed minimal changes in resistance response towards formaldehyde at this operating temperature. Again an increase in operating temperature and increase in concentration may see a better change in resistance response.

CNO sensors sensitivity were next tested towards two pulses of formaldehyde 95 ppb and 47.5 ppb at an operating temperature of 300 °C and 50% relative humidity. The results are shown in figure 6.23; as described in the graph, the first pulse of formaldehyde which is at 95 ppb was detectable i.e. a change in resistance response was seen for all three sensors tested. The pulse at 47.5 ppb had minimal changes in the resistance response. This again shows that doping chromium oxide with nickel changes the sensitivity and selectivity of the metal oxide as neither nickel oxide, chromium oxide and even *n*-type doped chromium oxide (CTO and CWO) displayed a change in resistance value. Again a significant low resistance vales are seen for CNO sensors.

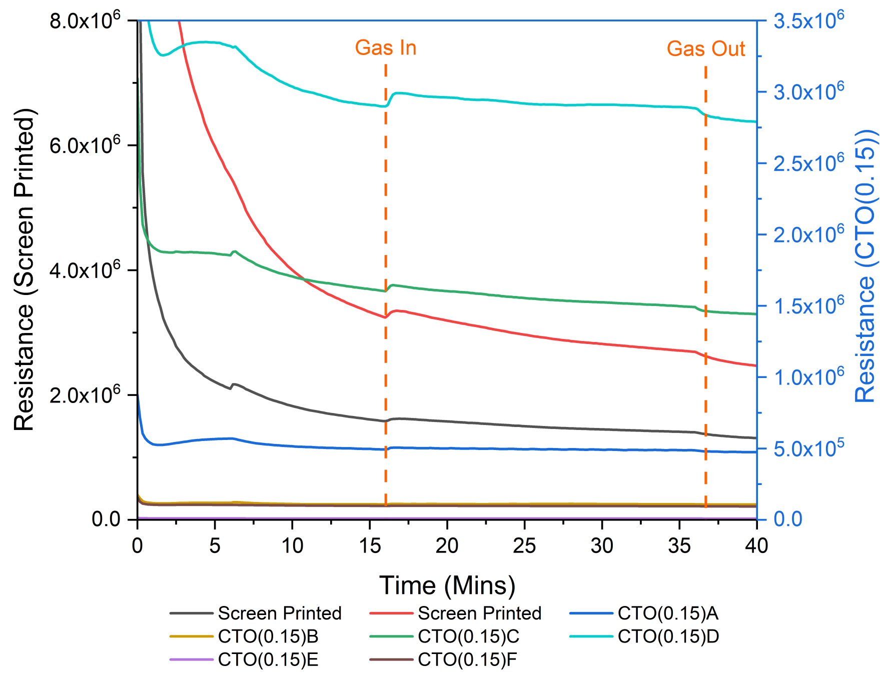

Figure 6.21. Screen printed and AACVD CTO sensors resistance response (Ω) against time (minutes) towards one pulses of formaldehyde (95 ppb) at operating temperature of 300 °C and 50 % relative humidity.

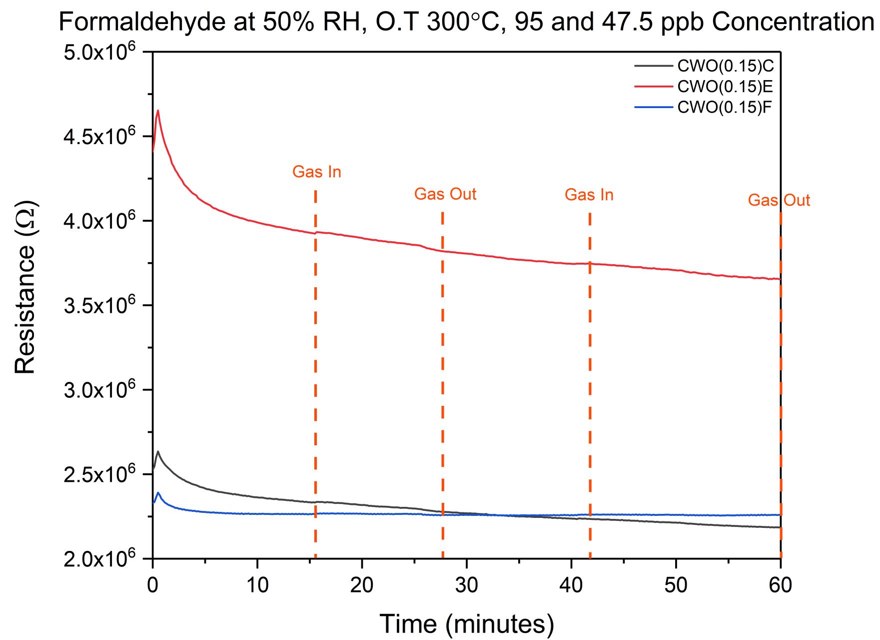

Figure 6.22. AACVD CWO sensors resistance response (Ω) against time (minutes) towards two pulses of formaldehyde (95 ppb and 47.5 ppb) at operating temperature of 300 °C and 50 % relative humidity.

6.2.3 Isopropanol

NiO sensors was lastly exposed to two pulses of isopropanol along with screen printed

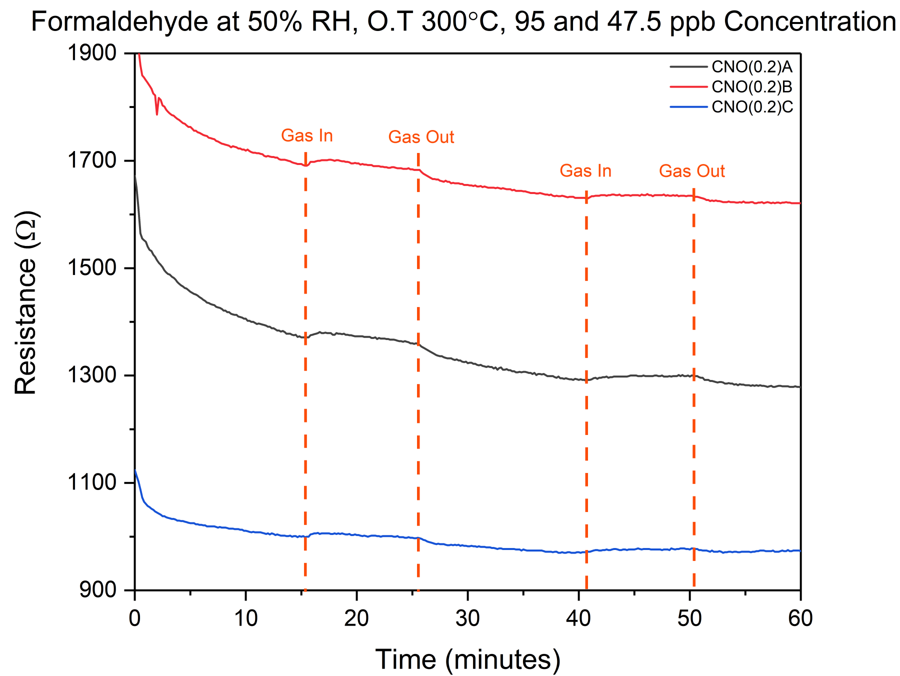

Figure 6.23. AACVD CNO sensors resistance response (Ω) against time (minutes) towards two pulses of formaldehyde (95 ppb and 47.5 ppb) at operating temperature of 300 °C and 50 % relative humidity.

CTO sensors at an operating temperature of 300 °C, concentration of 500 ppb and 250 ppb and 50% relative humidity which is illustrated in figure 6.24. The two types of sensors were compared with one another. NiO sensors displayed little to no change in resistance response when exposed to isopropanol. Literature source by Covington and Ayyala demonstrated the sensitivity of NiO towards isopropanol, giving a response of 1.21 R_g/R_a, again with a concentration range of 5 ppm to 25 ppm. Once more, this is probably due to the detection limit and the concentration levels tested are at ppb levels, whereas in the literature it is tested in the ppm range.

Two pulses of isopropanol were exposed to CTO sensors at 350 °C and 50% relative humidity with the concentration levels, 250 ppb and 500 ppb as shown in figure 6.25. Screen printed sensors displayed a good response towards isopropanol, with only a small drop in resistance response when concentration is halved. For AACVD sensors, most of the sensors display weak responses towards isopropanol at the high end concentration level (500 ppb) whereas there was minimal changes in the low concentration level (250 ppb). Binions[237] reported a response of 25 R_g/R_a for CTO sensors under dry air and 400 °C

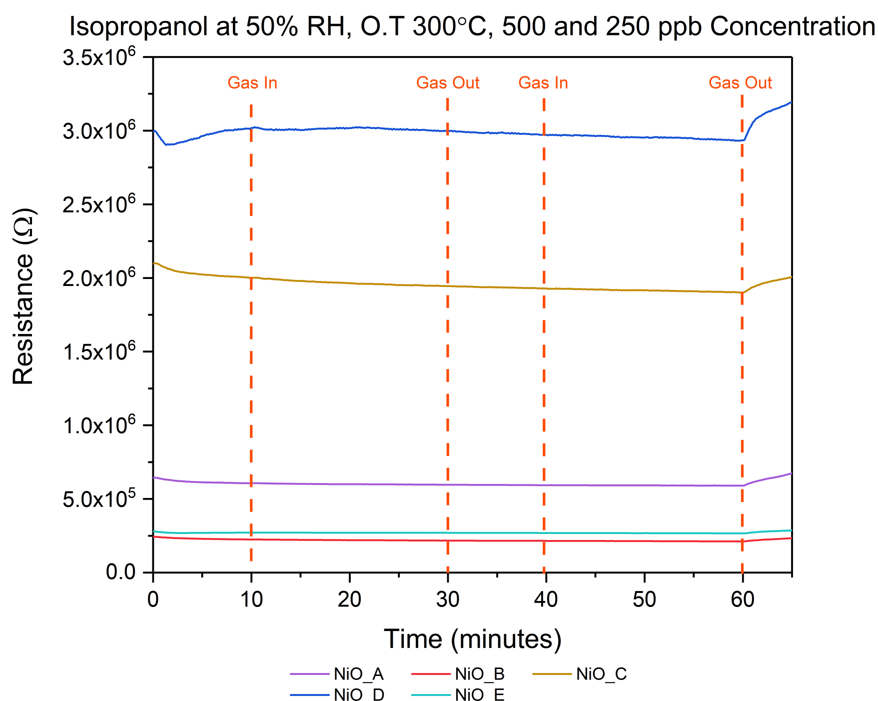

Figure 6.24. AACVD NiO sensors resistance response (Ω) against time (minutes) towards two pulses of isopropanol (500 ppb and 250 ppb) at operating temperature of 300 °C and 50 % relative humidity.

operating temperature. The concentration level used for that measurement was 80 ppm, roughly 200 times larger than what was tested.[237]

The sensor were last tested towards isopropanol illustrated in figure 6.26. Again the sensors were exposed to two pulses of gas analyte at 500 ppb and 250 ppb, operating temperature of 300 °C and 50% relative humidity. Three of the four sensors tested, displayed a small change in resistance response and hence displaying sensitivity towards isopropanol. An adjustment in parameter settings to find the optimum operating temperature may increase the sensors response towards isopropanol. The response compared to CTO looks comparable, both sensors are able to detect low levels of isopropanol.

CNO sensors were lastly tested towards two pulses of isopropanol at an operating temperature of 300 °C, concentration of 500 ppb and 250 ppb and 50% relative humidity. This is shown in figure 6.27 and it is seen that the three sensors tested observes a change in resistance response towards isopropanol at both concentration levels. The sensitivity of CNO towards isopropanol looks better than both CWO and CTO sensors. And again the resistance of these sensor are very low compared to CTO and CWO.

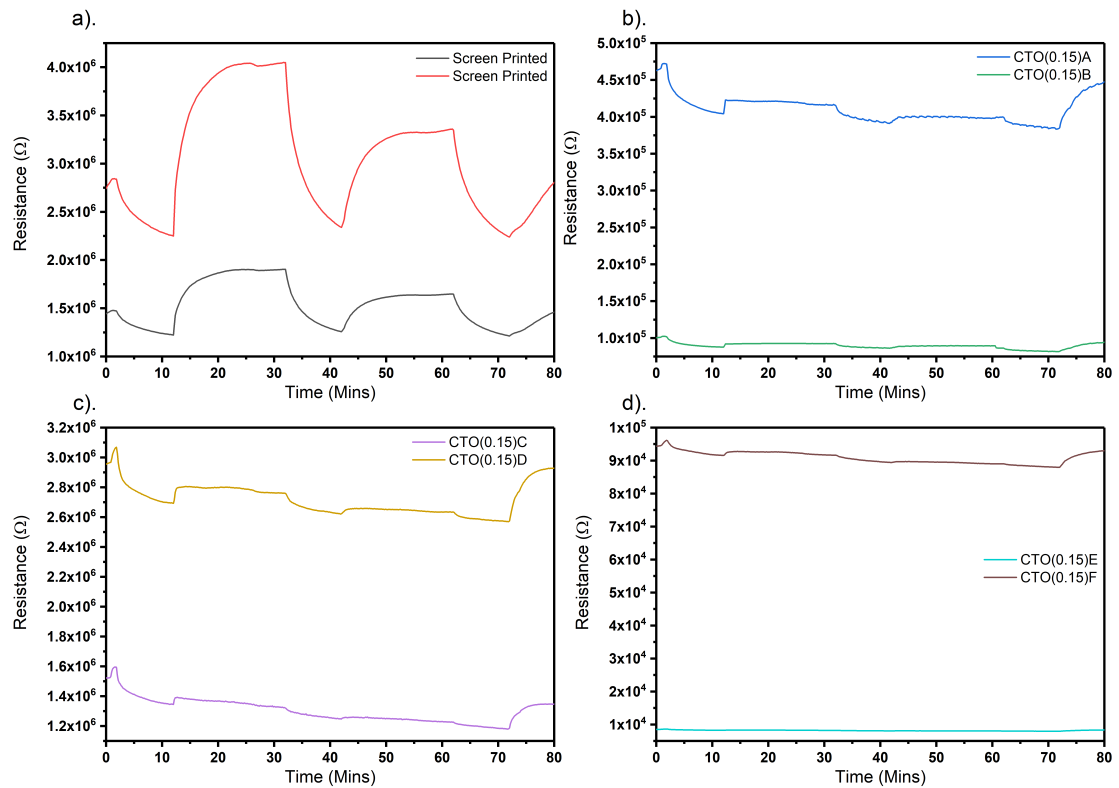

Figure 6.25. Sensor response (resistance in Ω) against time (minutes) when exposed to propan-2-ol at 350 °C and 50% relative humidity, 450 ppb and 225 ppb concentration, where a. Screen printed sensor response and b. AACVD sensor response.

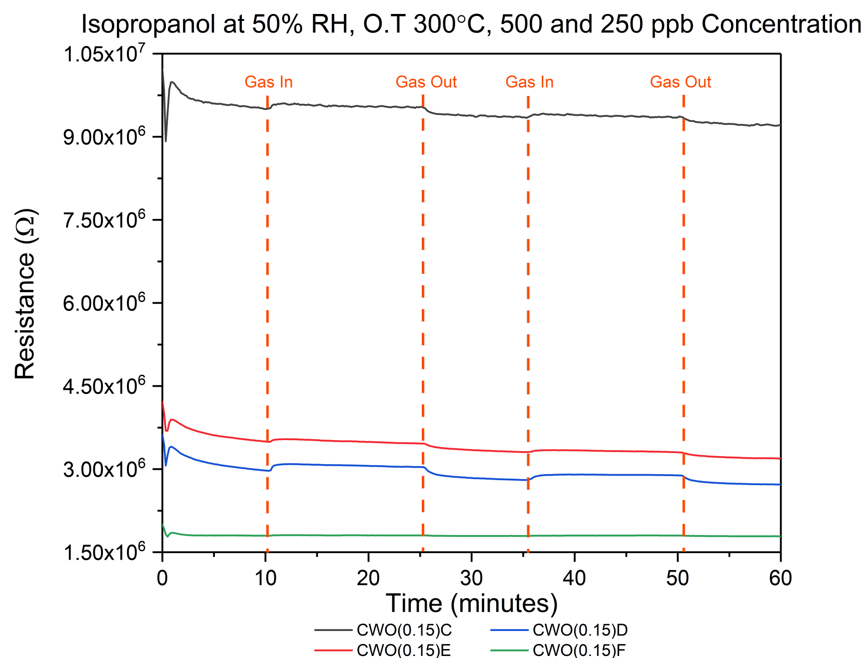

Figure 6.26. AACVD CWO sensors resistance response (Ω) against time (minutes) towards two pulses of isopropanol (500 ppb and 250 ppb) at operating temperature of 300 °C and 50 % relative humidity.

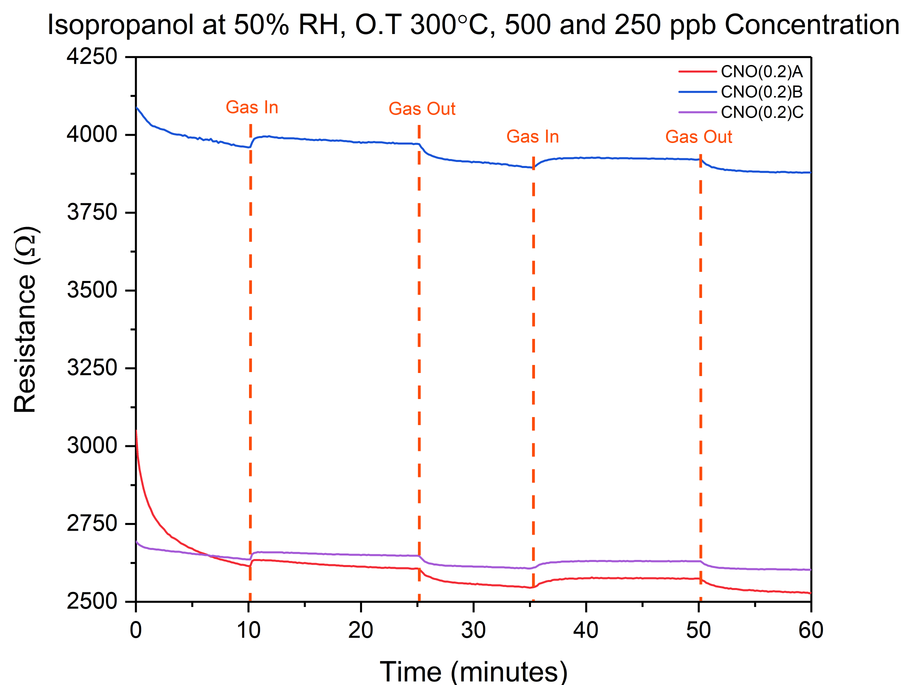

Figure 6.27. AACVD CNO sensors resistance response (Ω) against time (minutes) towards two pulses of isopropanol (500 ppb and 250 ppb) at operating temperature of 300 °C and 50 % relative humidity.

6.2.4 Benzene and 2-Butanone

Similarly to the toluene test, CTO sensors were exposed to 210 ppb of benzene at 50% relative humidity and increasing operating temperatures which is illustrated in figure 6.28. Screen printed sensors displayed minimal response changes in resistances when exposed to benzene between the temperatures of 300 °C and 425 °C. Temperatures above 375 °C displayed no changes in resistance for the screen printed sensors. As for AACVD deposited CTO sensors, no change in resistance response was seen throughout the whole test.

Two pulses of 2-Butanone at 250 ppb and 500 ppb were exposed to the sensor to analyse its behaviour towards ketones. The analyte gas was exposed at 50% relative humidity and 350 °C, shown in figure 6.29. Small changes in resistance response was recorded at both concentrations when 2-butanone was exposed towards screen printed sensors. For AACVD sensors, minimal to no changes in resistance response was displayed upon exposure towards 2-butanone.

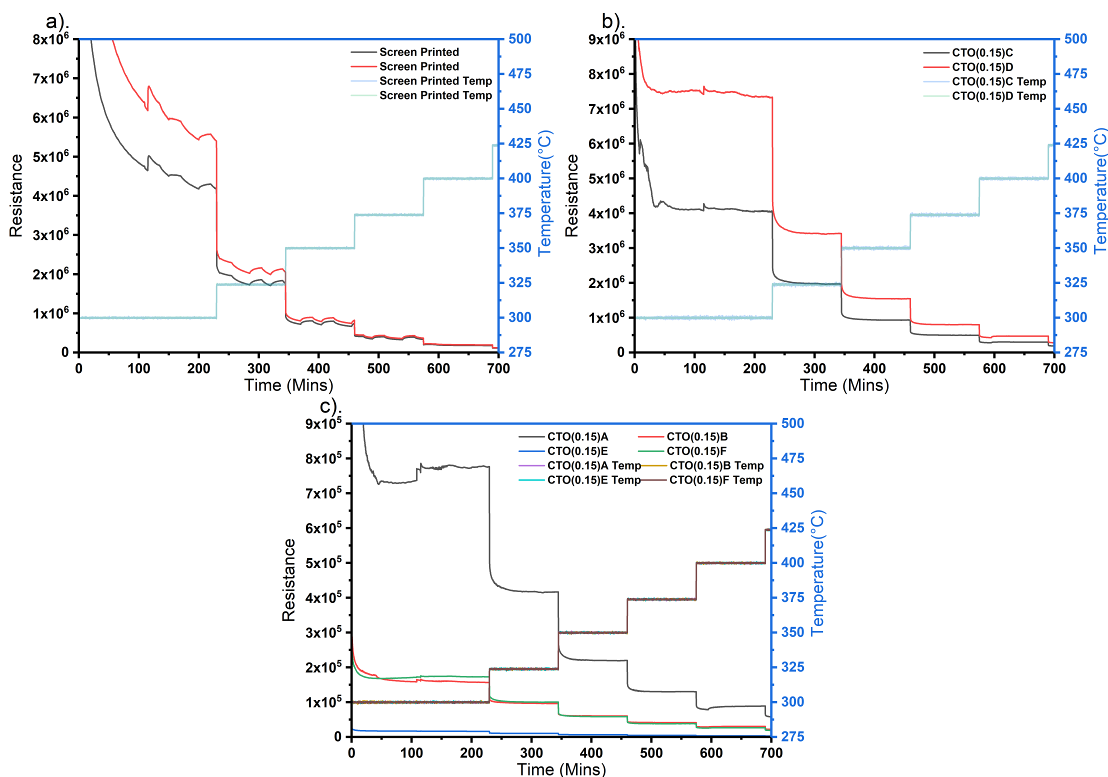

Figure 6.28. Sensor response (resistance in Ω) against time (minutes) when exposed to benzene at 50% relative humidity, 210 ppb and variable temperatures.

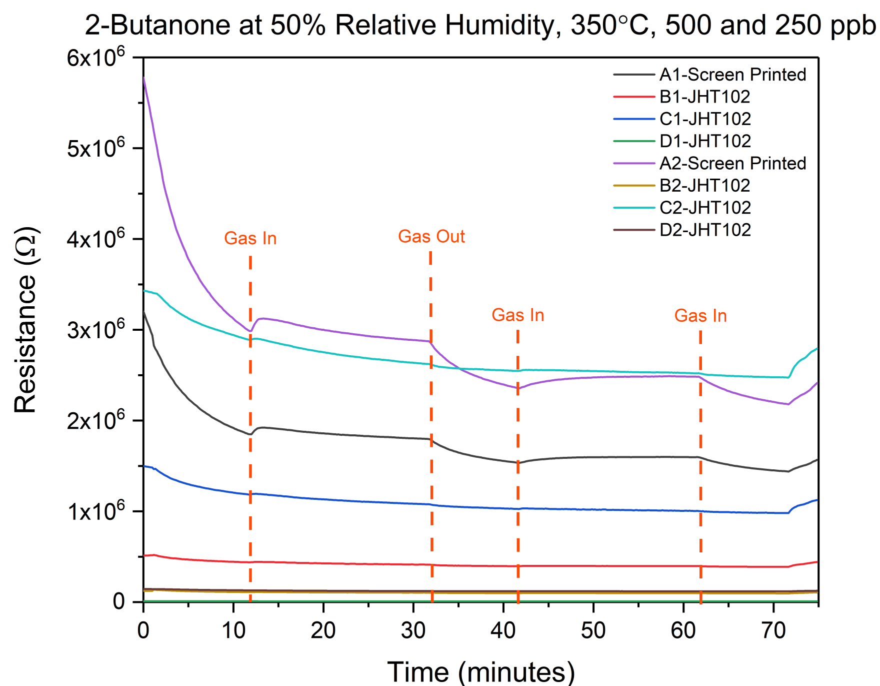

Figure 6.29. AACVD sensor response (resistance in Ω) against time (minutes) when exposed to 2-butanone at 350 °C and 50% relative humidity, 500 ppb and 250 ppb concentration.

6.2.5 Summary

Looking at figure 6.30 it can be hypothesise that for a *p*-type material (curve 3), Cr_2O_3 will lie within the curve, when a *n*-type dopant is added onto Cr_2O_3, an increase of resistance would be seen as a reduction in *p*-type carriers are available and hence the material will shift right of the curve; which is true as the resistance for pure Cr_2O_3 was observed at $10^4\ \Omega$ and $10^5\ \Omega$, $10^6\ \Omega$ for CTO and CWO respectively. As tungsten is a stronger dopant than titanium i.e. more readily to release electrons, CWO will lie more to the right than CTO. Conversely, when a *p*-type dopant is added (i.e. Ni), the material would move up the curve. A decrease in resistance would be seen as there are now more *p*-type carriers. The data records supports this as resistance levels were low for CNO sensors when detecting VOCs ($10^3\ \Omega$).

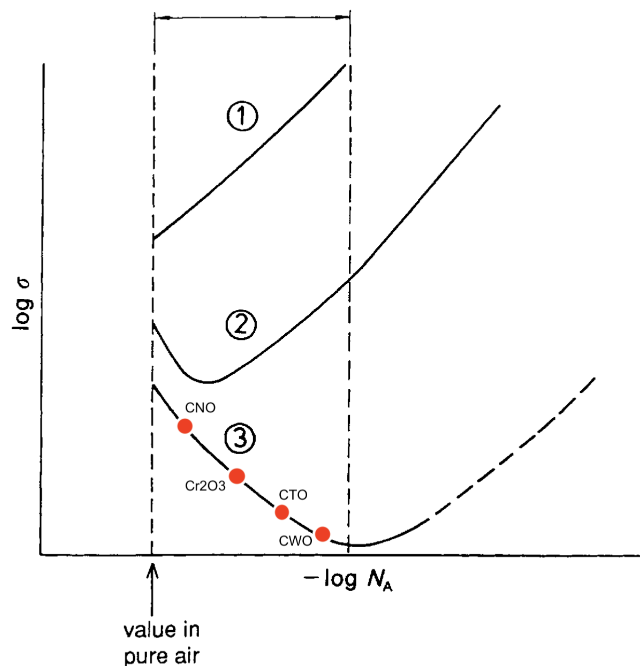

Figure 6.30. Schematic diagram of three curves with decreasing bulk donor density. Where N_A is equal to the surface acceptor density which is described as N_S in the equations above. The x-axis is the surface acceptor density; and the y-axis is the conductivity.[188]

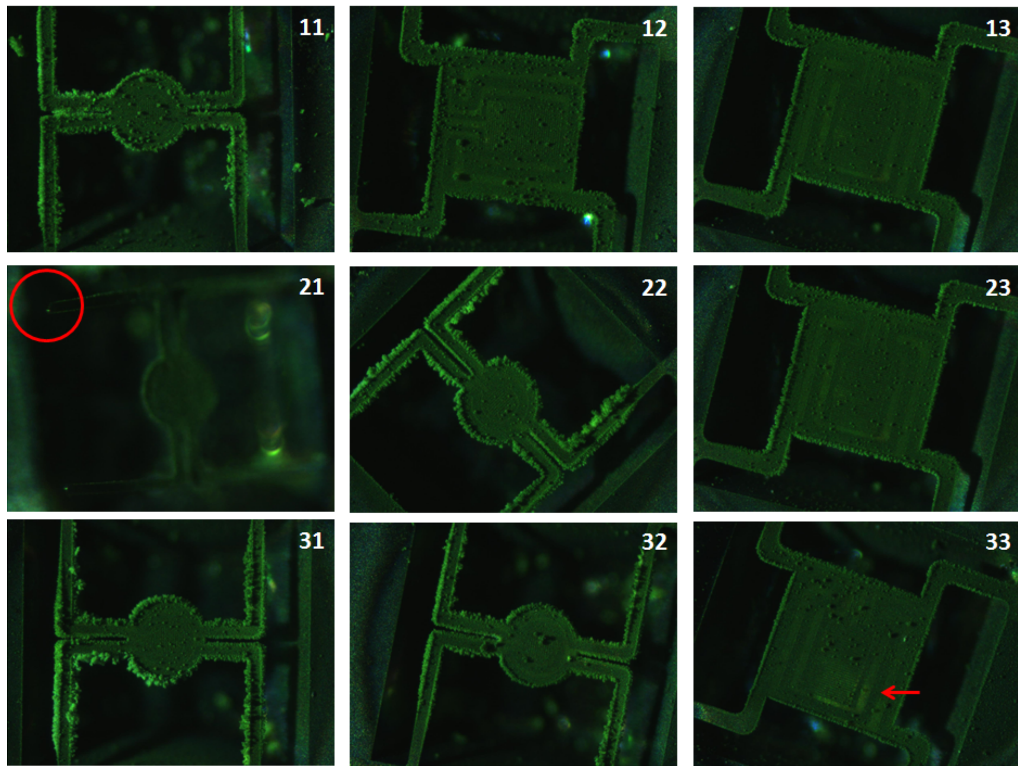

Figure 6.31. Microscopic images of AACVD deposited CTO thin films on MEMs devices.

6.3 MEMs Devices

As previously mentioned in section 1.6 the use of MEMs gas sensing platforms have been extensively researched due to their miniaturised heating element (micro-hotplates) which can operate at high temperatures quickly and preserve power consumption (mW ranges) due to its low thermal mass which are advantageous in comparison to alumina based sensors. It is however, very difficult to screen print on the top of these platforms due to the fragile membrane that has to be covered by the metal oxide material. In addition to this, micro-hotplates element are very fragile at high temperatures which is typically used in the screen printing sintering process, which cause the membrane to break. By using AACVD is it possible to deposit metal oxide materials at relatively low temperature without damaging the MHP membrane. Deposition of metal oxide materials using AACVD technique normally requires the use of a mask to cover the heater and detection pads to avoid short circuits and to isolate the deposition on the centre of the platform, however as the deposited materials are relatively thin, during the welding process the metal oxide material could be easily removed. Figure 6.31 depicts the microscopic images AACVD deposited CTO thin

films onto MEMs devices.

The MEMs used for the tests in this report are 2 by 2 mm micralyne MEMs coated with AACVD CTO thin films which were compared to ceramic AACVD and screen printed CTO sensors. The operating temperatures for the micralyne device were set at 350 °C and 375 °C, for screen printed it was at 375 °C and for AACVD it was at 350 °C. The micralynes were not annealed because the micralyne platforms were thermally unstable above 400 °C, whereas for screen printed and AACVD they were annealed at 825 °C and 600 °C respectively.

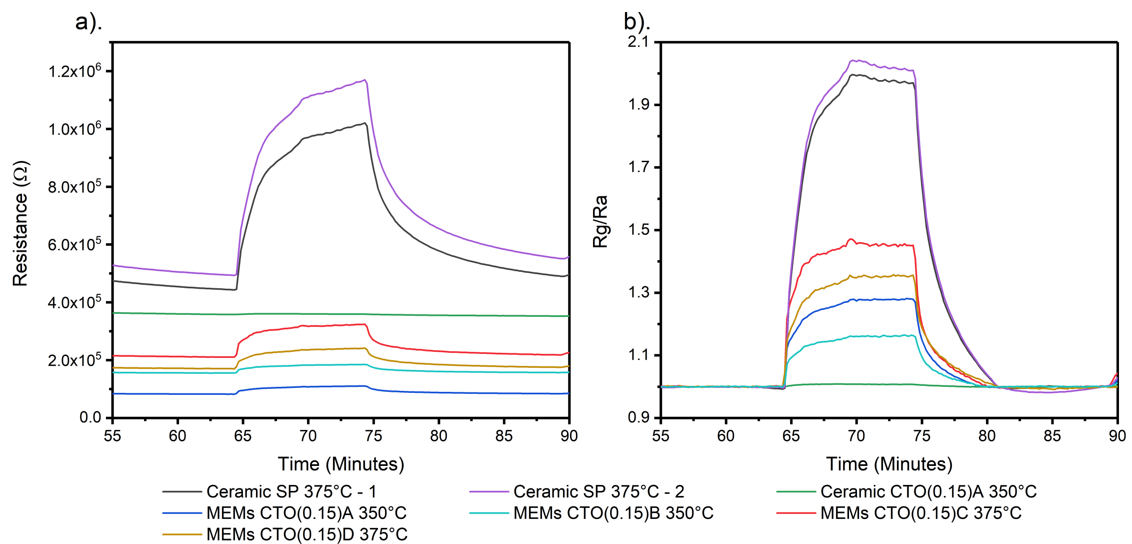

Figure 6.32. Resistance response to 200 ppb toluene in 50% relative humidity.

The MEMs devices were exposed to one pulse of toluene at 200 ppb in 50% relative humidity and at their respected operating temperatures and is illustrated in figure 6.32. The MEMs devices demonstrated the detection of toluene with a response ranging between 1.1 and 1.45 R_g/R_a at two different operating temperature (350 °C and 375 °C). The MEMs operating at 375 °C displayed the better response between the two MEMs, with a response of 1.35 and 1.45. Screen printed sensors observed a strong resistance response towards toluene with a response of 2, whereas no response was seen for the AACVD sensors.

Figure 6.33 displays the response of the tested sensors towards 200 ppb of toluene at an increasing rate of relative humidity. For ceramic screen printed sensors, the response were high at 10 % humidity (2.3 and 2.4). The response decreased when humidity was raised

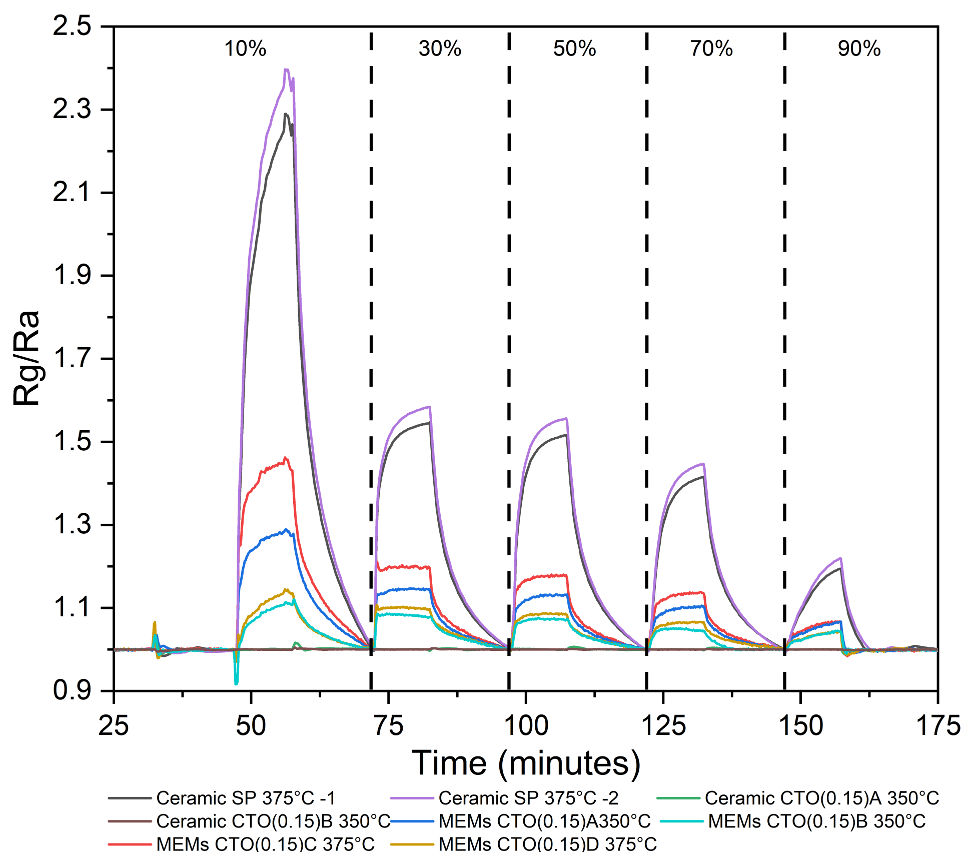

Figure 6.33. MEMs, screen printed and ceramic AACVD sensors response to 200 ppb of toluene in increasing relative humidity.

to30 % to a reading of 1.6. The sensors response remained at that level when humidity was raised to 50 % and 70 %. Once humidity was raised to 90 %, the sensors response dropped to below 1.3. For the ceramic AACVD sensor, no response was observed as humidity level increased. For the micralynes, a response were seen for all four sensors. The same trend like the screen printed sensors was seen, at 10 % humidity the response was at 1.45 and a decrease to 1.2 for humidity levels of 30 %, 50 % and 70 %.

Micralynes sensors sensitivity towards acetone were analysed after a seven hour burn in period in 50% relative humidity in air at their respected operating temperatures. Figure 6.34 displays the resistance response towards two pulses of acetone at 900 ppb concentration. The micralynes displayed a resistance response towards acetone for both operating temperatures. The resistance response were comparatively lower than of screen printed sensors, which is to be expected of as screen printed sensors are thick film sensors. Ceramic AACVD sensors displayed no response towards acetone.

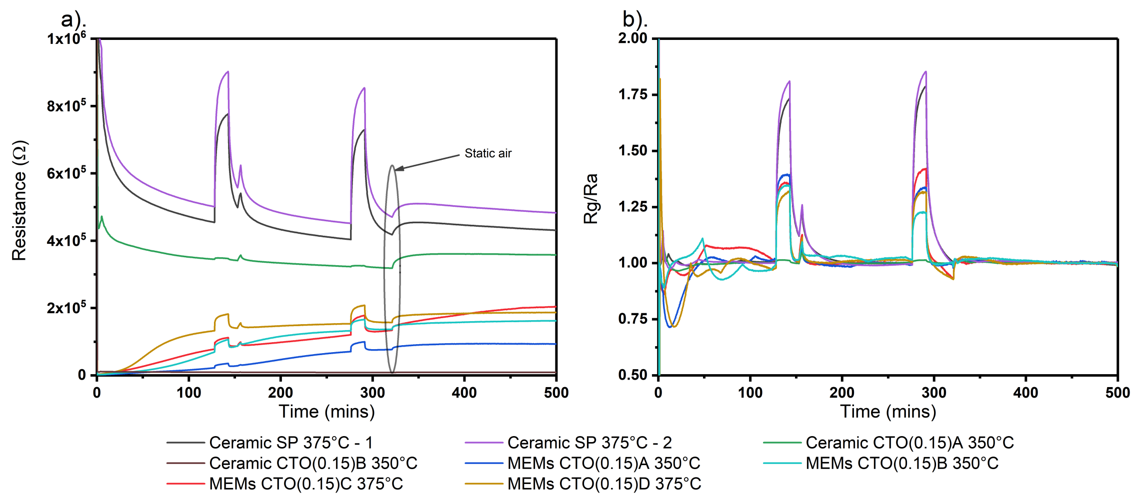

Figure 6.34. Resistance response to 900 ppb acetone in 50% relative humidity.

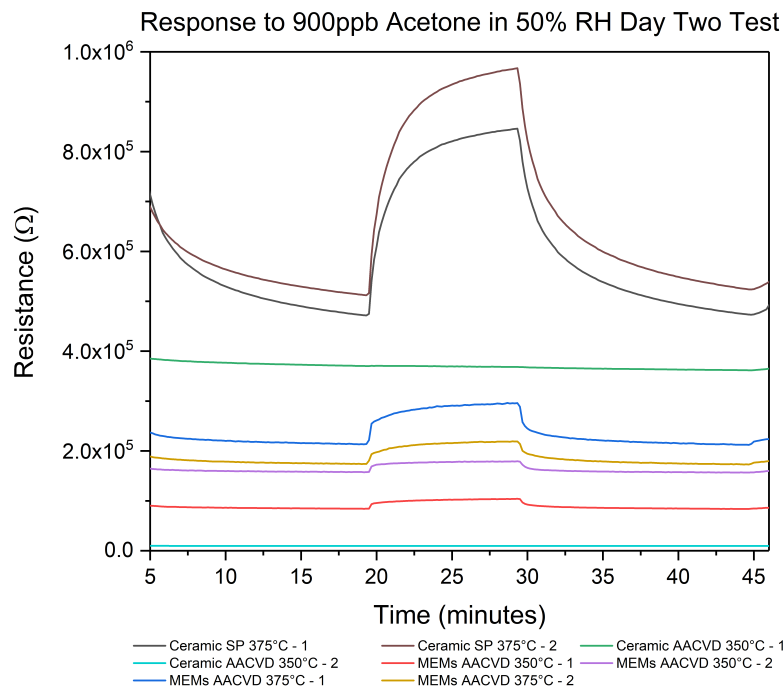

Figure 6.35. Resistance response to 900 ppb acetone in 50% relative humidity day two test.

The micralynes were re-exposed to 900 ppb of acetone on the second day to look at the stability of the sensor and to see if the results were comparable. The results are shown in figure 6.35. Again the ceramic AACVD sensors displayed no response towards acetone. Screen printed sensors observed a strong resistance response towards the acetone and the micralynes again demonstrates a small change in resistance which were comparable to the test which was ran previously.

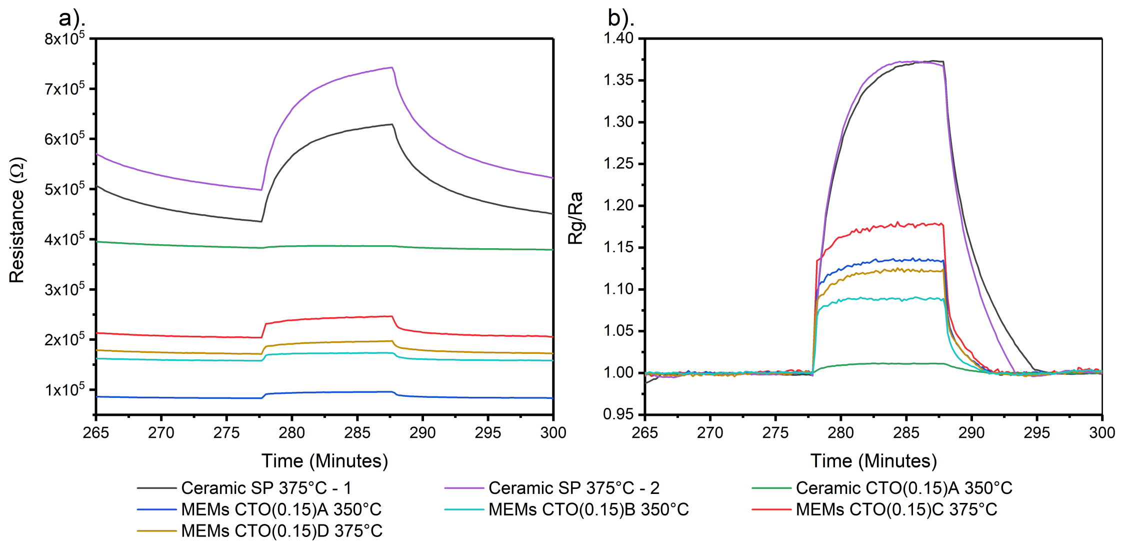

Figure 6.36. MEMs response to 400 ppb ethanol in 50% relative humidity.

Micralynes were next exposed to one pulse of 400 ppb ethanol in 50% relative humidity. A small change in resistance was recorded. The micralynes which operated at 375 °C displayed a slightly higher resistance response than the ones operated at 350 °C. Again ceramic AACVD displayed no response and screen printed sensors observed a large change in response compared to the micralynes.

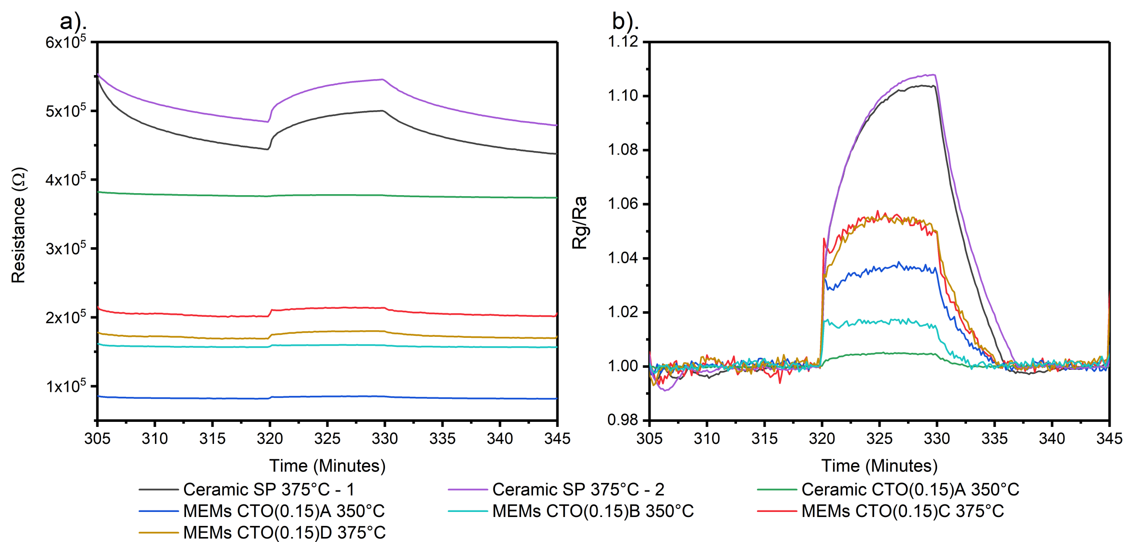

Figure 6.37. MEM sensors response towards 500 ppb dichlorobenzene in 50% relative humidity.

Micralynes were lastly exposed to one pulse of 500 ppb dichlorobenzene in 50% relative humidity. A small change in resistance was recorded for the micralynes which op-

erated at 375 °C, whereas for the ones operated at 350 °C displayed minimal to no change in resistance. Again ceramic AACVD displayed no response and screen printed sensors observed a larger change in response compared to the micralynes.

6.3.1 Summary of MEMs Devices

CTO was successfully deposited onto MEMS devices via AACVD synthesis and several types of VOCs (toluene, acetone, ethanol and dichlorobenzene) were used to test its sensitivity. The table 6.1 below displays the R_g/R_a response towards the mentioned VOCs at two different operating temperatures. The response times of these sensors are also depicted in this table. MEMs, compared to ceramic screen printed sensors have a relatively lower response (roughly 0.1 to 0.4 difference in response) but are still comparable to screen printed sensors. The response time for screen printed sensors towards toluene was at 120 s, whereas for MEMs the response time was a quarter of that at22.2 s. For acetone, screen printed sensors has a response time of 169.8 s and for MEMs it was at 10.2 s and 20.4 s. Towards ethanol, the response time for screen printed sensors was 150 s and for MEMS it was 19.8 s. Finally towards dichlorobenzene, screen printed sensors had a response time of 30 s and for MEMs this was 10.2 s and 19.8 s. This demonstrates that although screen printed sensors have stronger response towards the tested VOCs, MEMs sensors displays a superior response time towards this gases.

Table 6.1. MEMs gas response towards VOCs.

Gas (Concentration)	Temperature (°C)	R_g/R_a	Response Time (seconds)
Toluene 200 ppb	350	1.27	22.2
	375	1.32	22.2
Acetone 900 ppb	350	1.375	10.2
	375	1.28	20.4
Ethanol 400 ppb	350	1.08	19.8
	375	1.175	19.8
Dichlorobenzene 500 ppb	350	1.02	10.2
	375	1.055	19.8

Chapter 7

Conclusion and Future Work

7.1 Conclusion

There has been a growing demand for more accurate and low cost metal oxide based gas detectors. Commercially, screen printing technique is commonly used for the production of sensors on ceramic platforms, but is not a viable option on MEMS platforms, which offer advantages of lower power consumption and thermal mass and miniaturised heating element as compared to ceramic devices.

This thesis has investigated the making of several different types of metal oxide thin films (Cr_2O_3, NiO, CTO, CWO and CNO) by using aerosol-assisted chemical vapour deposition. The films were successfully deposited onto several different types of substrates; glass, quartz, FTO, alumina, alumina sensing platforms and MEMS. Various analytical techniques were used to characterise the films; such as EDS, XRD, XPS, SEM, Raman, Hall measurement and activation energies.

XRD patterns for the doped chromium oxides (CTO, CWO, CNO) only displayed eskolaite (chromium oxide), with no formation of the dopants seen and hence showing no indication of phase separation. XPS and EDS analysis confirmed the presence of Cr(III), Ti(IV), W(VI) and Ni(II) for AACVD and Cr(III) and Ti(IV) for screen printed sensors. SEM images was obtained for AACVD thin films to find the thickness of the films which showed to be in the range of 10 µm to 35 µm. This was then used for the calculation off

Hall effect. Due to ohmic contact geometry, sample uniformity and accuracy of thickness determination, Hall effect measurements are inconclusive. However, in general when Hall voltage is positive, this can be seen that the material is of *p*-type nature and if it's negative, it is of *n*-type nature. The measured film all displayed positive Hall voltage. Activation energies were calculated by looking into the baseline resistance values of the thin film sensors under pure nitrogen condition and temperatures between 100 °C to 450 °C. For all films, two different activation energies were calculated, one at low temperature and one at high temperature levels.

Gas sensing analysis were performed at different operating and ramping temperatures and different concentrations towards C_4H_8, NH_3 and H_2S at 50% relative humidity for Cr_2O_3, NiO, CTO and CWO. In general Cr_2O_3 sensors displayed weak responses towards isobutylene and ammonia compared to screen printed CTO and slightly weaker response compared to AACVD CTO. For NiO, there was minimal resistance response towards isobutylene (25 ppm). For CTO, sensitivity towards isobutylene and ammonia were weaker than screen printed, however when tested towards hydrogen sulfide, AACVD CTO a factor of five more sensitive than screen printed at 400 °C and 24 ppm (56 vs 9.2 R_g/R_a). For CWO sensors, the response towards isobutylene are comparable if not better than screen printed CTO sensors which are commercially available (3.5 vs 3.2 R_g/R_a) at 400 °C and 20 ppm of isobutylene. They are however, less sensitive towards ammonia than isobutylene and shows a weaker response than screen printed. The response is comparable to AACVD CTO sensors.

Sensitivity towards various VOCs were also performed on Cr_2O_3, NiO, CTO , CNO and CWO sensors. Cr_2O_3 sensors were only tested towards formaldehyde and displayed a resistance response. NiO sensors were tested towards toluene, formaldehyde and isopropanol which displayed no response towards these gases at their give concentration levels. AACVD CTO was tested towards toluene, formaldehyde, isopropanol, benzene and butanone. Minimal changes or no changes in resistance response was seen for the detection of toluene, benzene and butanone. Small resistance changes were seen towards isopropanol and formaldehyde. However screen printed CTO sensors were able to detect

all mentioned VOCs. This demonstrates that CTO are sensitive towards these VOCs but is undetectable for AACVD deposited CTO could be due to thickness or pore size of the film. CWO only display sensitivity towards isopropanol. Surprisingly, CNO sensors displayed sensitivity towards toluene, formaldehyde and isopropanol at very low resistance values. Finally, CTO was successfully deposited onto MEMS platforms via AACVD synthesis and its sensitivity towards VOCs (toluene, acetone, ethanol and dichlorobenzene) was analysed. MEMS sensor was able to detect all the gases analysed and in general displayed a better response at an operating temperature of 375 °C than 350 °C.

7.2 Future Work

We would like to further investigate on the sensitivity of CWO and CNO sensors on ceramic and onto MEMS platforms. Look into its optimum operating temperature towards VOCs as CNO displayed very low resistance reading could therefore be able to work at a much lower temperature than what was tested here. Look into other *p*-type dopants on chromium oxide to see if the sensitivity and resistance vales are similar to CNO. Investigate and see if these sensors are able to work in different humidity settings, its detection limits and selectivity to other VOCs such as dichlorobenzene. To accurately calculate the Hall voltage to determine if the materials are *p*-type or *n*-type. Finally to look further into the gas sensing mechanism of MOS sensors and how it is interacting with pure and *n*-doped *p*-type materials.

References

1. K. J. Albert, N. S. Lewis, C. L. Schauer, G. A. Sotzing, S. E. Stitzel, T. P. Vaid and D. R. Walt, *Chemical Reviews*, 2000, **100**, 2595–2626.

2. T. Seiyama, A. Kato, K. Fujiishi and M. Nagatani, *Analytical Chemistry*, 1962, **34**, 1502–1503.

3. J. Wollenstein, G. Plescher, G. Kuhner, H. Bottner, D. Niemeyer and D. Williams, *IEEE Sensors Journal*, 2002, **2**, 403–408.

4. D. Dawson, G. Henshaw and D. Williams, *Sensors and Actuators B: Chemical*, 1995, **26**, 76–80.

5. G. S. Henshaw, D. H. Dawson and D. E. Williams, *J. Mater. Chem.*, 1995, **5**, 1791–1800.

6. H. Liu, L. Zhang, K. Li and O. Tan, *Micromachines*, 2018, **9**, 557.

7. N. Yamazoe, *Sensors and Actuators B: Chemical*, 2005, **108**, 2–14.

8. S. R. Kolian, S. A. Porter, P. W. Sammarco, D. Birkholz, E. W. Cake and W. A. Subra, *Environmental Science and Pollution Research*, 2015, **22**, 12073–12082.

9. Duk-Dong Lee and Dae-Sik Lee, *IEEE Sensors Journal*, 2001, **1**, 214–224.

10. M. Kampa and E. Castanas, *Environmental Pollution*, 2008, **151**, 362–367.

11. S. K. Brown, M. R. Sim, M. J. Abramson and C. N. Gray, *Indoor Air*, 1994, **4**, 123–134.

12. T. Lin, X. Lv, Z. Hu, A. Xu and C. Feng, *Sensors*, 2019, **19**, 233.

13. A. Mirzaei, S. Leonardi and G. Neri, *Ceramics International*, 2016, **42**, 15119–15141.

14. F. Teimoori, K. Khojier and N. Z. Dehnavi, *Journal of Theoretical and Applied Physics*, 2017, **11**, 157–163.

15. C. Elosua, I. Matias, C. Bariain and F. Arregui, *Sensors*, 2006, **6**, 1440–1465.

16. S. Wang, H. Ang and M. O. Tade, *Environment International*, 2007, **33**, 694–705.

17. N. L. Nagda and H. E. Rector, *Indoor Air*, 2003, **13**, 292–301.

18. A. Jones, *International Journal of Environmental Research and Public Health*, 2017, **14**, 1286.

19. Z. Zhu and R.-J. Wu, *Journal of the Taiwan Institute of Chemical Engineers*, 2015, **50**, 276–281.

20. O. Bunkoed, F. Davis, P. Kanatharana, P. Thavarungkul and S. P. Higson, *Analytica Chimica Acta*, 2010, **659**, 251–257.

21. P. Patnaik, *A Comprehensive Guide to the Hazardous Properties of Chemical Substances*, John Wiley & Sons, Inc., Hoboken, NJ, USA, 2007.

22. M.-T. Ke, M.-T. Lee, C.-Y. Lee and L.-M. Fu, *Sensors*, 2009, **9**, 2895–2906.

23. Z. Shen, X. Zhang, X. Ma, R. Mi, Y. Chen and S. Ruan, *Sensors and Actuators B: Chemical*, 2018, **262**, 86–94.

24. K. Kawamura, M. Vestergaard, M. Ishiyama, N. Nagatani, T. Hashiba and E. Tamiya, *Measurement*, 2006, **39**, 490–496.

25. *Hawley's Condensed Chemical Dictionary*, ed. R. J. Lewis, John Wiley & Sons, Inc., Hoboken, NJ, USA, 2007.

26. R. A. Kadir, R. A. Rani, A. S. Zoolfakar, J. Z. Ou, M. Shafiei, W. Wlodarski and K. Kalantar-zadeh, *Sensors and Actuators B: Chemical*, 2014, **202**, 74–82.

27. *Handbook of Machine Olfaction*, ed. T. C. Pearce, S. S. Schiffman, H. T. Nagle and J. W. Gardner, Wiley-VCH Verlag GmbH & Co. KGaA, Weinheim, FRG, 2002.

28. K. Arshak, E. Moore, G. Lyons, J. Harris and S. Clifford, *Sensor Review*, 2004, **24**, 181–198.

29. A. Hulanicki, S. Glab and F. Ingman, *Pure and Applied Chemistry*, 1991, **63**, 1247–1250.

30. C. Hagleitner, A. Hierlemann, D. Lange, A. Kummer, N. Kerness, O. Brand and H. Baltes, *Nature*, 2001, **414**, 293–296.

31. P. N. Bartlett and S. Guerin, *Analytical Chemistry*, 2003, **75**, 126–132.

32. A. D. Wilson and M. Baietto, *Sensors*, 2009, **9**, 5099–5148.

33. D. Kohl, *Journal of Physics D: Applied Physics*, 2001, **34**, R125–R149.

34. G. Korotcenkov, *Materials Science and Engineering: B*, 2007, **139**, 1–23.

35. S. Lee, D. Dyer and J. Gardner, *Microelectronics Journal*, 2003, **34**, 115–126.

36. S. Fanget, S. Hentz, P. Puget, J. Arcamone, M. Matheron, E. Colinet, P. Andreucci, L. Duraffourg, E. Myers and M. Roukes, *Sensors and Actuators B: Chemical*, 2011, **160**, 804–821.

37. Z. Shen, M. Huang, C. Xiao, Y. Zhang, X. Zeng and P. G. Wang, *Analytical Chemistry*, 2007, **79**, 2312–2319.

38. L. Pirondini and E. Dalcanale, *Chem. Soc. Rev.*, 2007, **36**, 695–706.

39. D. Matatagui, O. V. Kolokoltsev, N. Qureshi, E. V. Mejía-Uriarte and J. M. Saniger, *Nanoscale*, 2015, **7**, 9607–9613.

40. J. Hodgkinson and R. P. Tatam, *Measurement Science and Technology*, 2013, **24**, 012004.

41. R. Knake and P. C. Hauser, *Analytica Chimica Acta*, 2002, **459**, 199–207.

42. R. Knake, R. Guchardi and P. C. Hauser, *Analytica Chimica Acta*, 2003, **475**, 17–25.

43. G. Korotcenkov, *Handbook of Gas Sensor Materials*, Springer New York, New York, NY, 2013.

44. P. F. Weller, *Journal of Chemical Education*, 1967, **44**, 391.

45. P. F. Weller, *Journal of Chemical Education*, 1971, **48**, 831.

46. M. Batzill and U. Diebold, *Progress in Surface Science*, 2005, **79**, 47–154.

47. C. Wang, L. Yin, L. Zhang, D. Xiang and R. Gao, *Sensors*, 2010, **10**, 2088–2106.

48. E. Comini, *Analytica Chimica Acta*, 2006, **568**, 28–40.

49. A. Tischner, T. Maier, C. Stepper and A. Köck, *Sensors and Actuators B: Chemical*, 2008, **134**, 796–802.

50. Y. Liu, E. Koep and M. Liu, *Chemistry of Materials*, 2005, **17**, 3997–4000.

51. S. J. Chang, W. Y. Weng, C. L. Hsu and T. J. Hsueh, *Nano Communication Networks*, 2010, **1**, 283–288.

52. A. P. Chatterjee, P. Mitra and A. K. Mukhopadhyay, *Journal of Materials Science*, 1999, **34**, 4225–4231.

53. S. Lin, D. Li, J. Wu, X. Li and S. Akbar, *Sensors and Actuators B: Chemical*, 2011, **156**, 505–509.

54. J. Moon, J.-A. Park, S.-J. Lee, T. Zyung and I.-D. Kim, *Sensors and Actuators B: Chemical*, 2010, **149**, 301–305.

55. A. Dey, *Materials Science and Engineering: B*, 2018, **229**, 206–217.

56. A. Berna, *Sensors*, 2010, **10**, 3882–3910.

57. J. Prasek, S. Vancik, V. Svatos, J. Klempa, I. Gablech, Z. Pytlicek and V. Levek, 2018 41st International Spring Seminar on Electronics Technology (ISSE), 2018, pp. 1–5.

58. J. Huang and Q. Wan, *Sensors*, 2009, **9**, 9903–9924.

59. D. Lee, J. Ondrake and T. Cui, *Sensors*, 2011, **11**, 9300–9312.

60. Y.-F. Sun, S.-B. Liu, F.-L. Meng, J.-Y. Liu, Z. Jin, L.-T. Kong and J.-H. Liu, *Sensors*, 2012, **12**, 2610–2631.

61. G. Di Francia, B. Alfano and V. La Ferrara, *Journal of Sensors*, 2009, **2009**, 1–18.

62. A. Mirzaei, K. Janghorban, B. Hashemi and G. Neri, *Journal of Nanoparticle Research*, 2015, **17**, 371.

63. A. DeHennis and K. Wise, Technical Digest. MEMS 2002 IEEE International Conference. Fifteenth IEEE International Conference on Micro Electro Mechanical Systems (Cat. No.02CH37266), 2002, pp. 252–255.

64. R. Moos, K. Sahner, M. Fleischer, U. Guth, N. Barsan and U. Weimar, *Sensors*, 2009, **9**, 4323–4365.

65. P. Feng, F. Shao, Y. Shi and Q. Wan, *Sensors*, 2014, **14**, 17406–17429.

66. M. Carminati, *Journal of Sensors*, 2017, **2017**, 1–15.

67. R. Ahmad, N. Tripathy and Y.-B. Hahn, *Biosensors and Bioelectronics*, 2013, **45**, 281–286.

68. D. J. Wales, J. Grand, V. P. Ting, R. D. Burke, K. J. Edler, C. R. Bowen, S. Mintova and A. D. Burrows, *Chem. Soc. Rev.*, 2015, **44**, 4290–4321.

69. C. Gattinoni and A. Michaelides, *Surface Science Reports*, 2015, **70**, 424–447.

70. D. Nunes, A. Pimentel, P. Barquinha, P. A. Carvalho, E. Fortunato and R. Martins, *Journal of Materials Chemistry C*, 2014, **2**, 6097.

71. N. R. Dhineshbabu, V. Rajendran, N. Nithyavathy and R. Vetumperumal, *Applied Nanoscience*, 2016, **6**, 933–939.

72. C. H. B. Ng and W. Y. Fan, *The Journal of Physical Chemistry B*, 2006, **110**, 20801–20807.

73. A. V. Korshunov and A. P. Il'in, *Russian Journal of Applied Chemistry*, 2009, **82**, 1164–1171.

74. B. Gleeson, in *Shreir's Corrosion*, Elsevier, 2010, pp. 180–194.

75. G. Eranna, *Metal Oxide Nanostructures as Gas Sensing Devices*, CRC Press, 1st edn., 2016, pp. 1–336.

76. D. Oosthuizen, D. Motaung and H. Swart, *Applied Surface Science*, 2019, **466**, 545–553.

77. A. Aslani and V. Oroojpour, *Physica B: Condensed Matter*, 2011, **406**, 144–149.

78. V. Figueiredo, J. V. Pinto, J. Deuermeier, R. Barros, E. Alves, R. Martins and E. Fortunato, *Journal of Display Technology*, 2013, **9**, 735–740.

79. Y.-T. Xu, Y. Guo, H. Jiang, X.-B. Xie, B. Zhao, P.-L. Zhu, X.-Z. Fu, R. Sun and C.-P. Wong, *Energy Technology*, 2015, **3**, 488–495.

80. Y.-S. Kim, I.-S. Hwang, S.-J. Kim, C.-Y. Lee and J.-H. Lee, *Sensors and Actuators B: Chemical*, 2008, **135**, 298–303.

81. R. Zhang, X. Liu, T. Zhou and T. Zhang, *Journal of Colloid and Interface Science*, 2019, **535**, 58–65.

82. A. Umar, A. Alshahrani, H. Algarni and R. Kumar, *Sensors and Actuators B: Chemical*, 2017, **250**, 24–31.

83. B. Urasinska-Wojcik and J. W. Gardner, *IEEE Sensors Journal*, 2018, **18**, 3502–3508.

84. L. Hou, C. Zhang, L. Li, C. Du, X. Li, X.-F. Kang and W. Chen, *Talanta*, 2018, **188**, 41–49.

85. S.-Y. Cho, H.-W. Yoo, J. Y. Kim, W.-B. Jung, M. L. Jin, J.-S. Kim, H.-J. Jeon and H.-T. Jung, *Nano Letters*, 2016, **16**, 4508–4515.

86. A. Bashir, S. Shukla, J. H. Lew, S. Shukla, A. Bruno, D. Gupta, T. Baikie, R. Patidar, Z. Akhter, A. Priyadarshi, N. Mathews and S. G. Mhaisalkar, *Nanoscale*, 2018, **10**, 2341–2350.

87. S. Vladimirova, V. Krivetskiy, M. Rumyantseva, A. Gaskov, N. Mordvinova, O. Lebedev, M. Martyshov and P. Forsh, *Sensors*, 2017, **17**, 2216.

88. A. Miquelot, M. Despotopoulou, C. Vahlas, C. Villeneuve, N. Dragoe, N. Prud'homme and O. Debieu, *Materials Chemistry and Physics*, 2020, **240**, 122059.

89. M. Ebadi, M. A. Mat-Teridi, M. Y. Sulaiman, W. J. Basirun, N. Asim, N. A. Ludin, M. A. Ibrahim and K. Sopian, *RSC Advances*, 2015, **5**, 36820–36827.

90. P. Sahoo, H. Djieutedjeu and P. F. P. Poudeu, *Journal of Materials Chemistry A*, 2013, **1**, 15022.

91. Y. Mao, W. Li, P. Liu, J. Chen and E. Liang, *Materials Letters*, 2014, **134**, 276–280.

92. Y. Gui, L. Yang, K. Tian, H. Zhang and S. Fang, *Sensors and Actuators B: Chemical*, 2019, **288**, 104–112.

93. P. L. Quang, N. D. Cuong, T. T. Hoa, H. T. Long, C. M. Hung, D. T. T. Le and N. V. Hieu, *Sensors and Actuators B: Chemical*, 2018, **270**, 158–166.

94. P. Moseley and D. Williams, *Sensors and Actuators B: Chemical*, 1990, **1**, 113–115.

95. J. Du, Y. Wu, K.-L. Choy and P. H. Shipway, *Thin Solid Films*, 2010, **519**, 1293–1299.

96. D. Niemeyer, D. E. Williams, P. Smith, K. F. E. Pratt, B. Slater, C. R. A. Catlow and A. Marshall Stoneham, *Journal of Materials Chemistry*, 2002, **12**, 667–675.

97. V. Jayaraman, K. Gnanasekar, E. Prabhu, T. Gnanasekaran and G. Periaswami, *Sensors and Actuators B: Chemical*, 1999, **55**, 175–179.

98. J. Du, Y. Wu and K.-L. Choy, *Thin Solid Films*, 2006, **497**, 42–47.

99. A. Atkinson, M. Levy, S. Roche and R. Rudkin, *Solid State Ionics*, 2006, **177**, 1767–1770.

100. S. Pokhrel, Y. Ming, L. Huo, H. Zhao and S. Gao, *Sensors and Actuators B: Chemical*, 2007, **125**, 550–555.

101. J. Zheng, Z.-Y. Jiang, Q. Kuang, Z.-X. Xie, R.-B. Huang and L.-S. Zheng, *Journal of Solid State Chemistry*, 2009, **182**, 115–121.

102. D. Nunes, A. Pimentel, A. Gonçalves, S. Pereira, R. Branquinho, P. Barquinha, E. Fortunato and R. Martins, *Semiconductor Science and Technology*, 2019, **34**, 043001.

103. A. Mirzaei, J.-H. Lee, S. M. Majhi, M. Weber, M. Bechelany, H. W. Kim and S. S. Kim, *Journal of Applied Physics*, 2019, **126**, 241102.

104. M. Hübner, C. Simion, A. Tomescu-StÄČnoiu, S. Pokhrel, N. Bârsan and U. Weimar, *Sensors and Actuators B: Chemical*, 2011, **153**, 347–353.

105. X. Pan and X. Zhao, *Sensors*, 2015, **15**, 8919–8930.

106. P. Shihabudeen and A. Roy Chaudhuri, *Sensors and Actuators B: Chemical*, 2020, **305**, 127523.

107. H. Duan, L. Yan, Y. He, H. Li, L. Liu, Y. Cheng and L. Du, *Materials Research Express*, 2017, **4**, 095022.

108. C. Zhao, B. Huang, E. Xie, J. Zhou and Z. Zhang, *Sensors and Actuators B: Chemical*, 2015, **207**, 313–320.

109. M. J. Piotrowski, P. Tereshchuk and J. L. F. Da Silva, *The Journal of Physical Chemistry C*, 2014, **118**, 21438–21446.

110. M. F. GarcíÂŋa-Sánchez, A. Ortiz, G. Santana, M. Bizarro, J. Peña, F. Cruz-Gandarilla, M. A. Aguilar-Frutis and J. C. Alonso, *Journal of the American Ceramic Society*, 2010, **93**, 155–160.

111. J.-D. Cafun, K. O. Kvashnina, E. Casals, V. F. Puntes and P. Glatzel, *ACS Nano*, 2013, **7**, 10726–10732.

112. T. Hu, S. Xiao, H. Yang, L. Chen and Y. Chen, *Chemical Communications*, 2018, **54**, 471–474.

113. N. A. Joy, M. I. Nandasiri, P. H. Rogers, W. Jiang, T. Varga, S. V. N. T. Kuchibhatla, S. Thevuthasan and M. A. Carpenter, *Analytical Chemistry*, 2012, **84**, 5025–5034.

114. R. Bene, I. Perczel, F. Réti, F. Meyer, M. Fleisher and H. Meixner, *Sensors and Actuators B: Chemical*, 2000, **71**, 36–41.

115. N. Izu, W. Shin, I. Matsubara and N. Murayama, *Journal of The Electrochemical Society*, 2005, **152**, H111.

116. D. Van Dao, T. T. Nguyen, S. M. Majhi, G. Adilbish, H.-J. Lee, Y.-T. Yu and I.-H. Lee, *Materials Chemistry and Physics*, 2019, **231**, 1–8.

117. M. Cristina, A. Giberti, V. Guidi, C. Malagù, B. Vendemiati and G. Martinelli, *MRS Proceedings*, 2004, **828**, A4.6.

118. G. Eranna, B. C. Joshi, D. P. Runthala and R. P. Gupta, *Critical Reviews in Solid State and Materials Sciences*, 2004, **29**, 111–188.

119. R. Verma, J. Gangwar and A. K. Srivastava, *RSC Advances*, 2017, **7**, 44199–44224.

120. J. Ovenstone and K. Yanagisawa, *Chemistry of Materials*, 1999, **11**, 2770–2774.

121. W.-D. Lin, C.-T. Liao, T.-C. Chang, S.-H. Chen and R.-J. Wu, *Sensors and Actuators B: Chemical*, 2015, **209**, 555–561.

122. S. Panigrahi, S. Jana, T. Calmeiro, D. Nunes, R. Martins and E. Fortunato, *ACS Nano*, 2017, **11**, 10214–10221.

123. M. Ni, M. K. Leung, D. Y. Leung and K. Sumathy, *Renewable and Sustainable Energy Reviews*, 2007, **11**, 401–425.

124. J. Yu, J. Low, W. Xiao, P. Zhou and M. Jaroniec, *Journal of the American Chemical Society*, 2014, **136**, 8839–8842.

125. Z. Zhu, S.-J. Lin, C.-H. Wu and R.-J. Wu, *Sensors and Actuators A: Physical*, 2018, **272**, 288–294.

126. Y.-T. Wang, W.-T. Whang and C.-H. Chen, *ACS Applied Materials & Interfaces*, 2015, **7**, 8480–8487.

127. M. Wu, X. Zhang, S. Gao, X. Cheng, Z. Rong, Y. Xu, H. Zhao and L. Huo, *CrystEngComm*, 2013, **15**, 10123.

128. M. Abbasi, S. Rozati, R. Irani and S. Beke, *Materials Science in Semiconductor Processing*, 2015, **29**, 132–138.

129. Y. Vijayakumar, G. K. Mani, M. R. Reddy and J. B. B. Rayappan, *Ceramics International*, 2015, **41**, 2221–2227.

130. R. Binions and A. Naik, in *Semiconductor Gas Sensors*, Elsevier, 2013, pp. 433–466.

131. O. D. Renedo, M. Alonso-Lomillo and M. A. Martínez, *Talanta*, 2007, **73**, 202–219.

132. G. F. Fine, L. M. Cavanagh, A. Afonja and R. Binions, *Sensors*, 2010, **10**, 5469–5502.

133. S. Limmer and G. Cao, *Advanced Materials*, 2003, **15**, 427–431.

134. Y. Choi, J. Kim and S. Bu, *Materials Science and Engineering: B*, 2006, **133**, 245–249.

135. M. Tong, G. Dai and D. Gao, *Materials Chemistry and Physics*, 2001, **69**, 176–179.

136. R. S. Devan, R. A. Patil, J.-H. Lin and Y.-R. Ma, *Advanced Functional Materials*, 2012, **22**, 3326–3370.

137. A. Mirzaei and G. Neri, *Sensors and Actuators B: Chemical*, 2016, **237**, 749–775.

138. S. C. Motshekga, S. K. Pillai, S. Sinha Ray, K. Jalama and R. W. M. Krause, *Journal of Nanomaterials*, 2012, **2012**, 1–15.

139. A. B. Panda, G. Glaspell and M. S. El-Shall, *Journal of the American Chemical Society*, 2006, **128**, 2790–2791.

140. A. Cirera, A. Vilà, A. Diéguez, A. Cabot, A. Cornet and J. Morante, *Sensors and Actuators B: Chemical*, 2000, **64**, 65–69.

141. X. Chen, X. Jing, J. Wang, J. Liu, D. Song and L. Liu, *CrystEngComm*, 2013, **15**, 7243.

142. F. Solzbacher, in *Semiconductor Manufacturing Handbook*, ed. H. Geng, McGRAW-HILL, London, 2005, ch. 13, pp. 175–196.

143. J. Singh and D. E. Wolfe, *Journal of Materials Science*, 2005, **40**, 1–26.

144. F. Böke, I. Giner, A. Keller, G. Grundmeier and H. Fischer, *ACS Applied Materials & Interfaces*, 2016, **8**, 17805–17816.

145. A. Banerjee, C. Ghosh, K. Chattopadhyay, H. Minoura, A. K. Sarkar, A. Akiba, A. Kamiya and T. Endo, *Thin Solid Films*, 2006, **496**, 112–116.

146. T. Lindgren, J. M. Mwabora, E. Avendaño, J. Jonsson, A. Hoel, C.-G. Granqvist and S.-E. Lindquist, *The Journal of Physical Chemistry B*, 2003, **107**, 5709–5716.

147. B. Lin, Z. Fu and Y. Jia, *Applied Physics Letters*, 2001, **79**, 943–945.

148. K. Choy, *Progress in Materials Science*, 2003, **48**, 57–170.

149. O. A. Nerushev, M. Sveningsson, L. K. L. Falk and F. Rohmund, *Journal of Materials Chemistry*, 2001, **11**, 1122–1132.

150. F. E. Annanouch, S. Vallejos, T. Stoycheva, C. Blackman and E. Llobet, *Thin Solid Films*, 2013, **548**, 703–709.

151. X. Hou and K.-L. Choy, *Chemical Vapor Deposition*, 2006, **12**, 583–596.

152. J. L. Cholula-Díaz, J. Barzola-Quiquia, H. Krautscheid, U. Teschner and P. Esquinazi, *Carbon*, 2014, **67**, 10–16.

153. P. Biswas, W.-N. Wang and W.-J. An, *Frontiers of Environmental Science & Engineering in China*, 2011, **5**, 299–312.

154. P. Marchand, I. A. Hassan, I. P. Parkin and C. J. Carmalt, *Dalton Transactions*, 2013, **42**, 9406.

155. C. E. Knapp and C. J. Carmalt, *Chem. Soc. Rev.*, 2016, **45**, 1036–1064.

156. K. Choy, in *Handbook of Nanostructured Materials and Nanotechnology*, Elsevier, 2000, pp. 533–577.

157. R. J. Lang, *The Journal of the Acoustical Society of America*, 1962, **34**, 6–8.

158. G. Taylor, *Proceedings of the Royal Society A: Mathematical, Physical and Engineering Sciences*, 1964, **280**, 383–397.

159. P. Bhattacharyya, *IEEE Transactions on Device and Materials Reliability*, 2014, **14**, 589–599.

160. M. Ghasemi-Varnamkhasti, S. S. Mohtasebi, M. Siadat and S. Balasubramanian, *Sensors*, 2009, **9**, 6058–6083.

161. J. W. Gardner, H. W. Shin and E. L. Hines, *Sensors and Actuators B: Chemical*, 2000, **70**, 19–24.

162. L. Zhang, F. Tian, H. Nie, L. Dang, G. Li, Q. Ye and C. Kadri, *Sensors and Actuators B: Chemical*, 2012, **174**, 114–125.

163. D. Barrettino, M. Graf, M. Zimmermann, A. Hierlemann, H. Baltes, S. Hahn, N. Barsan and U. Weimar, 2002 IEEE International Symposium on Circuits and Systems. Proceedings (Cat. No.02CH37353), 2002, pp. II–157–II–160.

164. F. Annanouch, I. Gràcia, E. Figueras, E. Llobet, C. Cané and S. Vallejos, *Sensors and Actuators B: Chemical*, 2015, **216**, 374–383.

165. K. Wetchakun, T. Samerjai, N. Tamaekong, C. Liewhiran, C. Siriwong, V. Kruefu, A. Wisitsoraat, A. Tuantranont and S. Phanichphant, *Sensors and Actuators B: Chemical*, 2011, **160**, 580–591.

166. B. Yuliarto, G. Gumilar and N. L. W. Septiani, *Advances in Materials Science and Engineering*, 2015, **2015**, 1–14.

167. M. Righettoni, A. Amann and S. E. Pratsinis, *Materials Today*, 2015, **18**, 163–171.

168. H.-W. Ra, K.-S. Choi, J.-H. Kim, Y.-B. Hahn and Y.-H. Im, *Small*, 2008, **4**, 1105–1109.

169. I.-D. Kim, A. Rothschild, B. H. Lee, D. Y. Kim, S. M. Jo and H. L. Tuller, *Nano Letters*, 2006, **6**, 2009–2013.

170. C. Wang, R. Sun, X. Li, Y. Sun, P. Sun, F. Liu and G. Lu, *Sensors and Actuators B: Chemical*, 2014, **204**, 224–230.

171. H.-R. Kim, K.-I. Choi, K.-M. Kim, I.-D. Kim, G. Cao and J.-H. Lee, *Chemical Communications*, 2010, **46**, 5061.

172. H.-R. Kim, A. Haensch, I.-D. Kim, N. Barsan, U. Weimar and J.-H. Lee, *Advanced Functional Materials*, 2011, **21**, 4456–4463.

173. H.-J. Kim and J.-H. Lee, *Sensors and Actuators B: Chemical*, 2014, **192**, 607–627.

174. P. Moseley, *Sensors and Actuators B: Chemical*, 1992, **6**, 149–156.

175. A. Rothschild and Y. Komem, *Journal of Applied Physics*, 2004, **95**, 6374–6380.

176. D.-J. Yang, I. Kamienchick, D. Y. Youn, A. Rothschild and I.-D. Kim, *Advanced Functional Materials*, 2010, **20**, 4258–4264.

177. W. Schottky, *Zeitschrift fur Physik*, 1939, **113**, 367–414.

178. W. Schottky, *Die Naturwissenschaften*, 1938, **26**, 843–843.

179. N. F. Mott, *Proceedings of the Royal Society of London. Series A. Mathematical and Physical Sciences*, 1939, **171**, 27–38.

180. N. F. Mott, *Mathematical Proceedings of the Cambridge Philosophical Society*, 1938, **34**, 568–572.

181. N. Barsan and U. Weimar, *Journal of Electroceramics*, 2001, **7**, 143–167.

182. Y. Li, N. Chen, D. Deng, X. Xing, X. Xiao and Y. Wang, *Sensors and Actuators B: Chemical*, 2017, **238**, 264–273.

183. N. Barsan, C. Simion, T. Heine, S. Pokhrel and U. Weimar, *Journal of Electroceramics*, 2010, **25**, 11–19.

184. P.-J. Yao, J. Wang, W.-L. Chu and Y.-W. Hao, *Journal of Materials Science*, 2013, **48**, 441–450.

185. Y. Zhang, J. Zhang, J. Chen, Z. Zhu and Q. Liu, *Sensors and Actuators B: Chemical*, 2014, **195**, 509–514.

186. T. Chen, Q. J. Liu, Z. L. Zhou and Y. D. Wang, *Nanotechnology*, 2008, **19**, 095506.

187. S. Pokhrel, C. Simion, V. Quemener, N. Bârsan and U. Weimar, *Sensors and Actuators B: Chemical*, 2008, **133**, 78–83.

188. D. E. Williams and P. T. Moseley, *Journal of Materials Chemistry*, 1991, **1**, 809.

189. K. Ellmer, *Hall Effect and Conductivity Measurements in Semiconductor Crystals and Thin Films*, John Wiley & Sons, Inc., Hoboken, NJ, USA, 2012.

190. G. Caruntu and C. Panait, 2009 IEEE International Workshop on Intelligent Data Acquisition and Advanced Computing Systems: Technology and Applications, 2009, pp. 323–326.

191. A. Rohrbach, J. Hafner and G. Kresse, *Physical Review B*, 2004, **70**, 125426.

192. M. Egashira, Y. Shimizu and Y. Takao, *Sensors and Actuators B: Chemical*, 1990, **1**, 108–112.

193. H. Yang, Q. Tao, X. Zhang, A. Tang and J. Ouyang, *Journal of Alloys and Compounds*, 2008, **459**, 98–102.

194. H. Sato, T. Minami, S. Takata and T. Yamada, *Thin Solid Films*, 1993, **236**, 27–31.

195. S. Akinkuade, B. Mwankemwa, J. Nel and W. Meyer, *Physica B: Condensed Matter*, 2018, **535**, 24–28.

196. R. H. Misho, W. A. Murad, G. H. Fatahalah, I. M. A. Aziz and H. M. Al-Doori, *Physica Status Solidi (a)*, 1988, **109**, K101–K104.

197. M. Z. Sialvi, R. J. Mortimer, G. D. Wilcox, A. M. Teridi, T. S. Varley, K. G. U. Wijayantha and C. A. Kirk, *ACS Applied Materials & Interfaces*, 2013, **5**, 5675–5682.

198. M. A. R. Abdullah, M. H. Mamat, A. S. Ismail, M. F. Malek, S. A. H. Alrokayan, H. A. Khan and M. Rusop, AIP Conference Proceedings, 2016, p. 020013.

199. M. M. Gomaa, G. RezaYazdi, M. Rodner, G. Greczynski, M. Boshta, M. B. S. Osman, V. Khranovskyy, J. Eriksson and R. Yakimova, *Journal of Materials Science: Materials in Electronics*, 2018, **29**, 11870–11877.

200. J. A. Dirksen, K. Duval and T. A. Ring, *Sensors and Actuators B: Chemical*, 2001, **80**, 106–115.

201. H. Steinebach, S. Kannan, L. Rieth and F. Solzbacher, *Sensors and Actuators B: Chemical*, 2010, **151**, 162–168.

202. A. M. Soleimanpour, A. H. Jayatissa and G. Sumanasekera, *Applied Surface Science*, 2013, **276**, 291–297.

203. P.-C. Chou, H.-I. Chen, I.-P. Liu, C.-C. Chen, J.-K. Liou, K.-S. Hsu and W.-C. Liu, *IEEE Sensors Journal*, 2015, **15**, 3711–3715.

204. I. Hotovy, V. Rehacek, P. Siciliano, S. Capone and L. Spiess, *Thin Solid Films*, 2002, **418**, 9–15.

205. M. C. Biesinger, C. Brown, J. R. Mycroft, R. D. Davidson and N. S. McIntyre, *Surface and Interface Analysis*, 2004, **36**, 1550–1563.

206. J. Zuo, C. Xu, B. Hou, C. Wang, Y. Xie and Y. Qian, *Journal of Raman Spectroscopy*, 1996, **27**, 921–923.

207. Y. Repelin, E. Husson and C. Proust, *Journal of Solid State Chemistry*, 1995, **116**, 378–384.

208. I. R. Beattie and T. R. Gilson, *Journal of the Chemical Society A: Inorganic, Physical, Theoretical*, 1970, 980.

209. M. Naito, in *High-Temperature Superconductors*, Elsevier, 2011, pp. 208–275e.

210. M. Julkarnain, J. Hossain, K. Sharif and K. Khan, *Journal of Optoelectronics and Advanced Materials*, 2011, **13**, 485–490.

211. A. Holt and P. Kofstad, *Solid State Ionics*, 1994, **69**, 127–136.

212. D. de Cogan and G. Lonergan, *Solid State Communications*, 1974, **15**, 1517–1519.

213. G. Subba Rao, B. Wanklyn and C. Rao, *Journal of Physics and Chemistry of Solids*, 1971, **32**, 345–358.

214. J. R. Vaišnys, *Journal of Applied Physics*, 1967, **38**, 2153–2156.

215. A. M. Venezia, R. Bertoncello and G. Deganello, *Surface and Interface Analysis*, 1995, **23**, 239–247.

216. N. Mironova-Ulmane, A. Kuzmin, I. Steins, J. Grabis, I. Sildos and M. Pärs, *Journal of Physics: Conference Series*, 2007, **93**, 012039.

217. S. Fujime, M. Murakami and E. Hirahara, *Journal of the Physical Society of Japan*, 1961, **16**, 183–186.

218. O. A. Ali, M. A. Hameed and Q. G. Al-Zaidi, *Transactions of the Indian National Academy of Engineering*, 2020, **5**, 27–31.

219. N. D. Hoa and S. A. El-Safty, *Chemistry - A European Journal*, 2011, **17**, 12896–12901.

220. T. J. Gray and P. W. Darby, *The Journal of Physical Chemistry*, 1956, **60**, 209–217.

221. W.-Y. Ho, M.-H. Chan, K.-S. Yao, C.-L. Chang, D.-Y. Wang and C.-H. Hsu, *Thin Solid Films*, 2008, **516**, 8530–8536.

222. Q. Li, Y. Gou, T.-G. Wang, T. Gu, Q. Yu and L. Wang, *Coatings*, 2019, **9**, 500.

223. S. Challagulla, K. Tarafder, R. Ganesan and S. Roy, *Scientific Reports*, 2017, **7**, 8783.

224. A. Conde-Gallardo, A. Cruz-Orea, O. Zelaya-Angel and P. Bartolo-Pèrez, *Journal of Physics D: Applied Physics*, 2008, **41**, 205407.

225. G. A. Shaw, I. P. Parkin and D. E. Williams, *J. Mater. Chem.*, 2003, **13**, 2957–2962.

226. R. D. Shannon, *Acta Crystallographica Section A*, 1976, **32**, 751–767.

227. R. Huirache-Acuña, F. Paraguay-Delgado, M. A. Albiter, L. Alvarez-Contreras, E. M. Rivera-Muñoz and G. Alonso-Núñez, *Journal of Materials Science*, 2009, **44**, 4360–4369.

228. I. R. Beattie and T. R. Gilson, *Journal of the Chemical Society A: Inorganic, Physical, Theoretical*, 1969, 2322.

229. L. Salvati, L. E. Makovsky, J. M. Stencel, F. R. Brown and D. M. Hercules, *The Journal of Physical Chemistry*, 1981, **85**, 3700–3707.

230. A. Rougier, F. Portemer, A. Quédé and M. El Marssi, *Applied Surface Science*, 1999, **153**, 1–9.

231. J. Singh, R. Kumar, V. Verma and R. Kumar, *Ceramics International*, 2020, **46**, 24071–24082.

232. F. Fang, J. Futter, J. Kennedy and A. Markwitz, 2011 Fifth International Conference on Sensing Technology, 2011, pp. 12–15.

233. A. V. Almaev, B. O. Kushnarev, E. V. Chernikov, V. A. Novikov, P. M. Korusenko and S. N. Nesov, *Superlattices and Microstructures*, 2021, **151**, 106835.

234. Q. Qi, P.-P. Wang, J. Zhao, L.-L. Feng, L.-J. Zhou, R.-F. Xuan, Y.-P. Liu and G.-D. Li, *Sensors and Actuators B: Chemical*, 2014, **194**, 440–446.

235. S. K. Ayyala and J. A. Covington, *Chemosensors*, 2021, **9**, 247.

236. X. Lai, G. Shen, P. Xue, B. Yan, H. Wang, P. Li, W. Xia and J. Fang, *Nanoscale*, 2015, **7**, 4005–4012.

237. R. Binions, A. Afonja, S. Dungey, D. W. Lewis, I. P. Parkin and D. E. Williams, *IEEE Sensors Journal*, 2011, **11**, 1145–1151.